



Chair of Ferrous Metallurgy

Doctoral Thesis



Evaluation of the Smelting Behavior of
Direct Reduced Iron

Dipl.-Ing. Andreas Pfeiffer, BSc

April 2023



EIDESSTÄTLICHE ERKLÄRUNG

Ich erkläre an Eides statt, dass ich diese Arbeit selbständig verfasst, andere als die angegebenen Quellen und Hilfsmittel nicht benutzt, und mich auch sonst keiner unerlaubten Hilfsmittel bedient habe.

Ich erkläre, dass ich die Richtlinien des Senats der Montanuniversität Leoben zu "Gute wissenschaftliche Praxis" gelesen, verstanden und befolgt habe.

Weiters erkläre ich, dass die elektronische und gedruckte Version der eingereichten wissenschaftlichen Abschlussarbeit formal und inhaltlich identisch sind.

Datum 29.04.2023

Unterschrift Verfasser/in
Andreas Pfeiffer

Kurzfassung

Wasserstoffbasierte Direktreduktion (DR) ist die vielversprechendste Technologie, hinsichtlich einer CO₂-neutralen Stahlproduktion. Während beim heute vorherrschenden Hochofenverfahren, Reduktion, Aufschmelzen und Abtrennen der Gangart simultan erfolgen, zeichnet sich die Direktreduktion durch eine Gas-Feststoffreaktion aus. Folglich entsteht ein Zwischenprodukt, welches in einem separaten Schritt aufgeschmolzen werden muss. Dieser Eisenschwamm oder Direct Reduced Iron (DRI) ist ein Verbund aus metallischem Eisen, Resteisenoxid, Gangart und üblicherweise Kohlenstoff. Als häufigste Form gilt DRI als Pellet, wobei verfahrensabhängig auch Briketts (Hot Briquetted Iron, HBI) oder Feinmaterial mit Korngrößen von <8 mm möglich sind. Stand heute, ist der Elektrolichtbogenofen (Electric Arc Furnace, EAF) das bevorzugte Einschmelzaggregat von DRI auf Erdgasbasis. Wenngleich die integrierte Route DR-EAF im Vergleich zur Kombination aus Hochofen (Blast Furnace, BF) und LD-Konverter (Basic Oxygen Furnace, BOF) eine quantitativ untergeordnete Rolle spielt, kann diese Strategie als industriell erprobt bezeichnet werden und ist vor allem in erdgasreichen Ländern – wie z. B. Iran, Saudi-Arabien, Vereinigte Arabische Emirate oder Mexiko – weit verbreitet. Betrachtet man die Umstellung europäischer BF-BOF Stahlwerke auf die Route DR-EAF, stößt man bei der Auswahl des Eisenträgers auf eine Herausforderung. Während erstere auf günstige Eisenerze, oftmals Sinterfeed, mit $58\% < Fe_{\text{tot}} < 65\%$ setzen, benötigen letztere sogenannte „DR-grades“. Dies sind hochqualitative Erze mit einem Eisengehalt $>67\%$, stellen jedoch bezogen auf die Gesamteisenerzproduktion eine teure Minderheit dar. Eine weitere Aufbereitung von günstigeren Erzen ist mit zusätzlichem Aufwand verbunden und verringert die Gesamteisenausbringung. Weiters beeinträchtigt ein Schwenk zu höherwertigen Erzen die Wirtschaftlichkeit einer Hütte maßgeblich. Folglich ist die Verarbeitung solcher weniger qualitativen Erzen zu Rohstahl eine der entscheidenden Fragestellungen für die Dekarbonisierung der Stahlindustrie.

Im Zuge dieser Arbeit werden einige Aspekte hinsichtlich des Einschmelzens von DRI zu Rohstahl oder Roheisen genauer beleuchtet. Massenbilanzrechnungen mit verschiedenen Modellfällen dienen einerseits zur Definition möglicher Verarbeitungsweisen und zeigen andererseits Stärken und Schwächen dieser Routen auf. Dabei zeigt sich, dass der Elektrolichtbogenofen das beste Aggregat bei hochqualitativem Eisenschwamm ist. Bei schlechterer Erzqualität ergeben sich Vorteile einer zweistufigen Verarbeitung, bestehend aus einem simultanen Einschmelzen, Ausreduzieren und Abschlacken in einem Smelter und einem Frischen des dabei entstehenden Smelter-Roheisens in einem LD-Konverter.

Weiters wird das Verhalten von Phosphor untersucht. P, im Erz als Apatit abgebunden, verbleibt während der Direktreduktion in dieser oxidischen Form im DRI. Im Vergleich zu BF-Roheisen, in dem der Phosphor reduziert und gelöst vorliegt, lässt sich dadurch ein Vorteil erwarten, da die Ausreduktion im Einschmelzaggregat mit einer kinetischen Verzögerung verbunden sein kann.

Im Zuge von Eintauchtests wird gezeigt, dass einerseits Kohlenstoff eine entscheidende Rolle bei der Auflösung von DRI spielt und andererseits ein großer Unterschied bei Kontakt mit Schlacke oder Schmelze herrscht. Während H₂-basiertes, kohlenstofffreies Material träge reagiert, beschleunigt C die Erweichung. Ergänzend ist ein Kontakt mit der Stahlschmelze zu bevorzugen, da der Kontakt mit Schlacke einen langsamen Wärmeeintrag nach sich zieht. Diese Beobachtungen korrelieren mit Ergebnissen aus Laborlichtbogeneinschmelzversuchen. Aufgekohltes DRI zeichnet sich durch die Abwesenheit von Lunkern und einer guten Separierung von der Gangart aus. Der Lichtbogen führt zu

einer intensiven Durchmischung des Bades. Daraus lässt sich schließen, dass das Rohmaterial möglichst im Hotspot aufgegeben werden soll, da dort am ehesten Kontakt mit der metallischen Phase eintritt.

Abschließend wird die Schaumslagbildung untersucht und bestätigt, dass eine BF ähnliche Schlacke bei reduktionsinduzierter Gasbildung nicht schäumbar ist. Im Gegensatz dazu zeigt sich bei einer EAF typischen Schlacke eine hervorragende Schaumbildung.

Abstract

Hydrogen-based direct reduction is the most promising technology for CO₂-neutral steelmaking. The gas-solid reduction reactions characterize these aggregates, producing sponge or direct reduced iron (DRI) consisting of metallic iron, residual iron oxide, and gangue. That is in contrast to the blast furnace (BF), which simultaneously reduces, melts, and deslags the iron ore. Therefore, a separate melting step is required for sponge iron, whether briquetted or pellet material or unagglomerated fines with particle sizes <8 mm. Nowadays, the electric arc furnace (EAF) is the preferred melting aggregate. Although quantitatively subordinated, this direct reduction reactor (DR) – EAF sequence is considered an industrially proven technology, especially in natural gas-rich regions such as Iran, Saudi Arabia, United Arab Emirates, and Mexico. When comparing it to the integrated BF – basic oxygen furnace (BOF) capacities in Europe, besides the reducing agent, also the iron carriers differ significantly. The latter uses lower grade materials, typically containing 58% < Fe_{tot} < 65%; the former rely on so-called DR-grades with Fe_{tot} > 67%. They are considered the highest-grade iron ores and an expensive minority compared to sinter or BF-grade concentrate. Further beneficiation decreases the total yield and means additional effort. Therefore, processing lower-grade iron ores via direct reduction is of great importance with regard to economically worthwhile and CO₂-neutral steel.

Various aspects of this question are examined in the scope of this thesis. Introductory mass balance calculations are used to define different DRI processing strategies and to compare their strengths and weaknesses. Looking at different cases, it is clear that the EAF is the unit of choice for sponge iron from DR-grade ore. Nevertheless, lower grades demand an alternative two-step melting process, using a smelter to produce hot metal and a BOF to refine it to crude steel.

Secondly, the behavior of phosphorus during direct reduction is investigated. BF hot metal contains phosphorus in reduced condition. Since phosphorus remains bound in apatite during direct reduction, this indicates an advantageous behavior during melting, as a kinetic rephosphorization delay can be expected.

Dipping tests highlight the role of carbon during DRI dissolution in a melt. While carbon-free H₂-based sponge iron melts slowly, carbon accelerates softening. Further, a significant difference in the behavior between contact with slag and steel is observed. Both observations correlate with lab-scale melting tests; the carbon-containing material results in a blister-free structure and pronounced separation from gangue and steel. A further test shows an intensive stirring effect in slag and steel induced by the electric arc. The primary conclusion can be made in case of the DRI charging spot. It should be fed directly into the arc, as the stirring increases the chance of contact with the metallic phase, which is essential for rapid DRI melting.

Last but not least, slag foaming is evaluated. Adding a carbon carrier generates gas, resulting from the reduction reactions with FeO. No foaming occurs in blast furnace-like slag, while EAF slag shows extensive foamability.

“The secrets of this earth are not for all men to see, but only for those who will seek them”
Ayn Rand, Anthem

Acknowledgment

Developing the data, methods, experiments, and results necessary for this dissertation was a three-year odyssey. Such a journey is not possible without the support of colleagues and experts. First of all, I would like to thank Prof. Johannes Schenk for his help, input, and challenges during this project. Further, a special thank goes to Prof. Helmut Antrekowitsch for mentoring this thesis.

Furthermore, I want to acknowledge the partners Primetals Technologies Austria, KI-MET, voestalpine Stahl, voestalpine Stahl Donawitz, and thyssenkrupp Steel Europe. That is especially true for Dr. Gerald Wimmer from Primetals Technologies Austria. He was always available for questions of all kinds and gave influential impulses for further tasks and questions.

Finally, I would like to thank my colleagues for their support and for making this time unforgettable. In this context, I would like to make special mention of Daniel, Harri, Heng, and Kathi, without whom central parts of the work would not have been possible.

Funding

This research was funded by KI-MET GmbH, metallurgical competence center (funding number FFG No. 869295). The research program of the KI-MET competence center is supported by COMET (Competence Center for Excellent Technologies), the Austrian program for competence centers. COMET is funded by the Federal Ministry for Climate Action, Environment, Energy, Mobility, Innovation, and Technology, the Federal Ministry for Labour and Economy, the provinces of Upper Austria, Tyrol, and Styria, and the Styrian Business Promotion Agency (SFG). In addition, this research work was partially financed by the industrial partners Primetals Technologies Austria GmbH, voestalpine Stahl GmbH, voestalpine Stahl Donawitz GmbH and thyssenkrupp Steel Europe AG, and the scientific partner Montanuniversität Leoben.

Nomenclature

Fe_{met} / wt.-%	metallic iron content
Fe_{tot} / wt.-%	total iron content
$x_{Fe_{tot}}$ / mol.-%	total iron content
$x_{O_{Fe}}$ / mol.-%	Oxygen in iron oxide
Σ / s	Slag foaming index
η / kg/(ms) or Pas	Dynamic viscosity
ν / m ² /s	kinematic viscosity
σ / kg/s ²	Surface tension
D / mm	Diameter
T / K	Temperature
E_{eff} / kg/s ²	Eff. Elasticity
F / N	Force
Mo / l	Morton number
g / m/s ²	gravity
ϵ / l	amount of solids
m / kg	Mass
Pr / l	Prandtl number
a / m ² /s	thermal diffusivity
c_p / J/(Kmol)	heat capacity
λ / W/(mK)	thermal conductivity
U / V	Voltage
I / A	Current
P / W	Power
L_P, L_{P^*} / l	Phosphorus partition coefficients
(abc)	slag phase
[abc]	iron phase
{abc}	gas phase

Abbreviations

AC	Alternate current
BF	Blast furnace
BOF	Basic oxygen furnace
CapEx	Capital expenditure
CDA	Carbon direct avoidance
CCS	Carbon capture and storage
CCU	Carbon capture and usage
CS	Crude steel
DC	Direct current
DR	Direct reduction
DRI	Direct reduced iron
DRP	Direct reduced product
EAF	Electric arc furnace
EBITDA	Earnings before interest, taxes, depreciation, and amortization
EDX	Energy dispersive x-ray analysis
EU	European union
HBI	Hot briquetted iron
HM	Hot metal (in this work, hot metal is defined as the output from a smelter)
HPSR	Hydrogen plasma smelting reduction
HRC	Hot rolled coil
HT-LSCM		High-temperature laser scanning confocal microscopy
ICP-OES	...	Inductive coupled plasma optical emission spectroscopy
IMCT	Ion-molecule coexistence theory
MD	Metallization degree
OES	Optical emission spectroscopy
OBM	Oxygen bodenblasend Maxhütte – bottom blowing converter
OpEx	Operational expenditure
OSBF	Open slag bath furnace
PC	Petrol coke
PCI	Pulverized coal injection
PI	Pig iron (in this work, pig iron is defined as the output from a blast furnace)
RD	Reduction degree

SAFSubmerged arc furnace
 SCRSilicon-controlled rectifier
 SEM.....Scanning electron microscope
 SR.....Smelting reduction
 SRA.....Substitute reducing agent
 VRF.....Vertical reduction furnace
 WPWorking package

Molecules

Al_2O_3 Aluminiumoxide
 CO_2 Carbon dioxide
 CaO Calcium oxide
 FeO Iron(II)oxide
 Fe_2O_3 Iron(III)oxide
 Fe_3O_4 Magnetite
 Fe_3C Cementite
 MgO Magnesium oxide
 P_2O_5 Phosphorus oxide
 SiO_2 Silicon dioxide
 TiO_2 Titanium oxide
 MnO Manganese oxide
 PO_4^{3-} Phosphate
 $\text{Ca}_5[(\text{F},\text{Cl},\text{OH})](\text{PO}_4)_3$. Apatite
 $\text{Ca}_3(\text{PO}_4)_2$. Calcium phosphate
 CuFeS_2 Chalcopyrite
 MA..... Magnesio-Alumina-Spinel
 MW, $(\text{Mg},\text{Fe})\text{O}$ Magnesiowustite

Table of Contents

Eidesstattliche Erklärung	II
Kurzfassung	III
Abstract	IV
Quote	V
Acknowledgment	VI
Funding	VI
Nomenclature	VII
Abbreviations	VIII
Molecules	IX
Table of Contents	X
List of Figures	XII
Appendix Figures	XVII
List of Tables	XVIII
1. Introduction – Target of this thesis	I
1.1. State of the art	I
1.2. Transformation of the Steel Industry towards CO ₂ -neutrality	3
1.3. Research Target	5
2. Theoretical Fundamentals	6
2.1. Direct reduced iron	6
2.2. DRI processing strategies	9
2.2.1. Electric arc furnace	9
2.2.2. Submerged arc- and open slag bath furnace – “smelter”	11
2.2.3. Blast furnace	13
2.2.4. Basic oxygen furnace	13
2.3. EAF slag properties	13
2.3.1. Behavior of trace elements	14
2.3.2. Slag foaming	17
3. Methodology	21
3.1. Definition and comparison of processing strategy	21
3.2. DRI Preparation	22
3.3. Slag Premelting	23
3.4. Phosphorus	24

3.4.1. Reduction part	25
3.4.2. Modeling part	26
3.5. Interaction between DRI and liquids (results see chapter 6)	28
3.6. Arc melting behavior (results see chapter 7)	32
3.7. Slag Foaming (results see chapter 8)	35
3.8. Sample Investigation Techniques	40
4. Definition and comparison of processing strategies	41
4.1. Check with Emirates Steel data	45
4.2. Results	46
4.3. Discussion	52
5. Phosphorus	53
5.1. Phosphorus behavior in direct reduction conditions	53
5.2. Phosphorus distribution	65
5.3. Discussion	69
6. Interaction between DRI and liquids	70
6.1. Results	71
6.2. Discussion	79
7. Arc melting behavior	81
7.1. Results	81
7.2. Discussion	91
8. Slag foaming	92
8.1. Experimental slag foaming investigation	92
8.1.1. Optical microscope evaluation	93
8.1.2. SEM-EDX distribution mappings and chemical analyses	95
8.2. Slag foaming index – sensitivity analysis	110
8.3. Discussion	117
9. Conclusion and outlook	119
10. References	121
Appendix	A-I
a) Publications related to this thesis	A-I
b) Conference contributions	A-I
c) Other publications	A-I

List of Figures

Figure 1: Annual crude steel production ^[1]	1
Figure 2: Currently applied steelmaking routes ^[10] ©VDEH.....	2
Figure 3: Iron ore price since 1960 ^[42]	4
Figure 4: Price for hot rolled coil (HRC) since 2009 ^[48]	4
Figure 5: Comparison of the DRI melting time in slag/steel melts with slag melts; T=1617°C; initial particle size: 12 mm ^[59]	8
Figure 6: Colakoglu melt shop with a Primetals Ultimate EAF ©Primetals ^[70]	9
Figure 7: (%FeO) vs. [%C] – comparison of BOF, EAF, and OBM (“Oxygen Bodenblasend Maxhütte” – bottom blowing converter) ^[32, 80]	10
Figure 8: Empirical (%FeO)-[C] partition in the EAF ^[81]	11
Figure 9: Operational resistance vs. electrode tip position ^[82, 95]	12
Figure 10: OSBF schematic process behavior ^[82] ; ©Pasquale Cavaliere.....	12
Figure 11: OSBF schematic process behaviors ^[96] ; ©Gerald Wimmer, Primetals.....	13
Figure 12: Phosphorus partition vs. [%C] in BOF and OBM („Oxygen Bodenblasend Maxhütte” – bottom blowing converter) ^[80]	16
Figure 13: Rephosphorization experiment acc. to Manning, Fruehan ^[109] ; B2=0.9; (FeO)=18%; (MgO)=17%; (%P) ₀ =2.6%; T=1600°C.....	16
Figure 14: Isothermal solubility diagram @ 1600°C; calculated by FactSage™ 8.2.....	19
Figure 15: Influence of effective viscosity on the slag foaming index ^[119]	19
Figure 16: Calculation flow for a one-step melting sequence.....	21
Figure 17: Calculation flow for a two-step melting sequence.....	21
Figure 18: Lab-scale vertical reduction furnace ^[139]	22
Figure 19: Lab-scale 68 mm fluidized bed reactor 1 – gas storage; 2 – evaporator; 3 – gas distributor; 4 – internal cyclone; 5 – dust filter; 6 – pressure regulator; 7 – differential pressure measurement; 8 – scale; 9 – reactor; 10 – heating furnace; 11 – process control; 12 – off-gas; T – thermocouples.....	23
Figure 20: MU900 induction furnace.....	24
Figure 21: A) Conditions (T, N ₂ , H ₂) during reduction of DRI 1 – lump; B) m, RD, and MD during reduction of DRI 1 – lump.....	25
Figure 22: A) Conditions (T, N ₂ , H ₂) during reduction of DRI 2 – fine; B) m, RD, and MD during reduction of DRI 2 – fine.....	26
Figure 23: FactSage™ input scheme.....	27
Figure 24: Goodness of polynomial fit; A) L _p ; B) L _p *; different lines represent different FeO-contents; circles: calculated values, solid blue lines: polynomial fit, degree 4; red dashed line: cubic-spline fit.....	28
Figure 25: Gero® vertical tube furnace.....	28
Figure 26: Test setup A) series I ^[140] ; B) series II.....	29
Figure 27: Prereduction of pellets A) I-0%C; B) Prereduction for I-C750 and I-C800; just reduction period shown => timescale does not start at 0.....	30
Figure 28: Carburizing of series I samples A) I-C750, and B) I-C800; just carburization period shown => timescale does not start at 0.....	31
Figure 29: Prereduction of pellets for series II; A) II-0%C.2, and B) II-C800.2; just reduction period shown => timescale does not start at 0.....	31

Figure 30: Flowsheet of the hydrogen plasma smelting reduction facility ^[142, 143]	32
Figure 31: Batchwise pellet feed	33
Figure 32: m, RD, and MD during reduction of 0%C-DRI-DR; just reduction period shown => timescale does not start at 0	34
Figure 33: A) RD and MD during reduction of C-DRI-DR; B) mass evolution during carburizing; just reduction and carburization periods shown => timescale does not start at 0	34
Figure 34: m, RD, and MD during reduction of 0%C-DRI-Fines; just reduction period shown => timescale does not start at 0	35
Figure 35: Location of the cutted cross-sections	35
Figure 36: Test setup for slag foaming tests	36
Figure 37: Phase diagram of SAF (smelter) slags, calculated by FactSage™ 8.2.....	38
Figure 38: Phase diagram of EAF slags, calculated by FactSage™ 8.2; T = 1600°C.....	39
Figure 113: Foaming height measurement.....	39
Figure 39: Flow sheet for the three defined melting strategies	41
Figure 40: Sankey diagram of the mass flow for route 1	42
Figure 41: Sankey diagram of the mass flow for routes 2 and 3.....	43
Figure 42: A) Scrap rates-; B) EAF/BOF tapping temperatures for the calculated cases (assignment see Table 26).....	46
Figure 43: Pig iron rates and carbon contents for the calculated cases (assignment see Table 26)	46
Figure 44: Composition of A) hot metal and B) crude steel (assignment see Table 26)	47
Figure 45: A) Basicities and B) (FeO), (MgO) in smelter slags (assignment see Table 26)	47
Figure 46: A) B2 and B) (FeO), (MgO) in EAF/BOF slags (assignment see Table 26).....	48
Figure 47: Electrical Energy consumption A) per t hot metal; B) per t crude steel for the calculated cases (assignment see Table 26).....	48
Figure 48: Electrical Energy consumption per t vs. the carbon content of the DRI (cases 3-5; assignment see Table 26)	49
Figure 49: Electrical Energy consumption per t vs. MD (cases 5-7; assignment see Table 26).....	49
Figure 50: Phosphorus contents for crude steel and smelter hot metal for the calculated cases (assignment see Table 26).....	50
Figure 51: Slag amount in EAF, smelter, EAF-smelter, and BOF for the calculated cases (assignment see Table 26); 200 and 350 kg/t are considered as critical values in EAF and smelter/ EAF-smelter	50
Figure 52: Fe-yield and Fe-losses for the calculated cases (assignment see Table 26).....	51
Figure 53: Additive consumption, A) total oxides and carbon; B) type-specific, for the calculated cases (assignment see Table 26).....	51
Figure 54: Oxygen potential vs. Temperature (Richardson-Jeffes diagram) for iron- and phosphorus oxides; standard conditions; data from FactSage™ 8.2, reaction and equilib modes, FactPS database; $1p_{H_2}/p_{H_2O}=10^8$; $2p_{H_2}/p_{H_2O}=10^2$	54
Figure 55: Digital microscope images of raw Kiruna lump samples.....	54
Figure 56: Digital microscope images of reduced Kiruna lump samples; marked spot: porous metallic iron phase, growing into dense magnetite	55
Figure 57: Digital microscope images of raw Kiruna fine ore; 250-500 μm ; marked particle: chalcopyrite (CuFeS_2).....	55
Figure 58: Digital microscope images of oxidized Kiruna fine ore; 250-500 μm ; market spot: residual magnetite bars.....	55
Figure 59: Digital microscope images of reduced Kiruna fine ore; 125-500 μm	56
Figure 60: SEM image of an apatite-containing particle; Kiruna fines 250-500 μm , raw	56
Figure 61: EDX-mapping of an apatite-containing particle; Kiruna fines 250-500 μm , raw; corresponding SEM image see Figure 60	57
Figure 62: SEM image of an apatite-containing particle; Kiruna fines 250-500 μm , oxidized.....	58

Figure 63: EDX-mapping of an apatite-containing particle; Kiruna fines 250-500 μm , oxidized; corresponding SEM image see Figure 62	59
Figure 64: SEM image of an apatite-containing particle; Kiruna fines 250-500 μm , reduced	59
Figure 65: EDX-mapping of an apatite-containing particle; Kiruna fines 125-500 μm , reduced; corresponding SEM image see Figure 64	60
Figure 66: SEM image of an apatite-containing particle; Kiruna lump, raw	61
Figure 67: EDX-mapping of an apatite-containing particle; Kiruna lump, raw; corresponding SEM image see Figure 66	62
Figure 68: SEM image of an apatite-containing particle; Kiruna lump, reduced	62
Figure 69: EDX-mapping of an apatite-containing particle; Kiruna lump, reduced; corresponding SEM image see Figure 68	63
Figure 70: Apatite EDX-line scan; A) Kiruna fines 250-500 μm , raw; B) Kiruna fines 250-500 μm , oxidized	64
Figure 71: Apatite EDX-line scan; Kiruna fines reduced, 150-500 μm	65
Figure 72: Apatite EDX-line scan; Kiruna lump; A) raw; B) reduced	65
Figure 73: Surface- and contour chart of phosphorus partition in EAF/BOF; A) Partition according to equation 8; B) Phosphorus content in the melt, based on equation 8, with an initial [%P] content of 0.3%	66
Figure 74: Surface- and contour chart of phosphorus partition in the smelter (based on HISMELT); A) Partition according to equation 9; B) Phosphorus content in the melt, based on equation 9, with an initial [%P] content of 0.3%	67
Figure 75: Surface- and contour chart of phosphorus partition in BOF/EAF and smelter at an increased temperature of 1650°C	68
Figure 76: Surface- and contour chart of phosphorus equilibrium partition; dots represent the calculated values; A) L_P ; $L_{P,EAF,Mod}$, $L_{P,BOF,Mod}$... acc. to equation 8 ; B) L_P^* ; $L_{P,HIS,Mod}$ acc. to equation 9, $L_{P,HIS,Ref}$ acc. to [19]	69
Figure 77: Macroscopic photographs of selected series I 0%C samples A) I-0%C-ULC-1; B) I-0%C-SAF-1; C) I-0%C-EAF-2 ^[140]	71
Figure 78: Macroscopic photograph of sample I-0%C-ULC-3-10s ^[140]	72
Figure 79: Macroscopic photograph of sample I-C750-ULC-3 ^[140]	72
Figure 80: Macroscopic photographs of selected series I C800 samples A) I-C800-ULC-4; B) I-C800-SAF-1; C) I-C800-EAF-1 ^[140]	73
Figure 81: Macroscopic photograph of sample I-HBI-ULC-2 ^[140]	73
Figure 82: Macroscopic photograph of series II 0%C.2 samples A) 3 s; B) 6 s; C) 9 s; D) 21 s	74
Figure 83: Macroscopic photograph of series II C800.2 samples A) 3 s; B) 6 s; C) 9 s; D) 14 s	75
Figure 84: Digital microscope images of A) I-0%C-ULC-1; B) I-0%C-ULC-10s-3; dipped into liquid ULC steel ^[140]	76
Figure 85: Digital microscope images of A) I-0%C-SAF-2; B) I-0%C-EAF-2; dipped into EAF/SAF slag ^[140]	76
Figure 86: Digital microscope images of A) I-C750-ULC-2; B) I-C800-ULC-4; both dipped into liquid ULC steel ^[140]	76
Figure 87: Digital microscope images of A) I-C800-SAF-1; B) I-C800-EAF-1; dipped into slag ^[140]	77
Figure 88: Digital microscope image of the I-HBI-ULC-1 sample, dipped into ULC ^[140]	77
Figure 89: Digital microscope images of series II 0%C.2 samples A) 3 s; B) 6 s; C) 9 s; D) 21 s	78
Figure 90: Digital microscope images of series II C800.2 samples A) 3 s; B) 6 s; C) 9 s; D) 14 s	78
Figure 91: U, I, P vs. time for all arc melting tests	84
Figure 92: Voltage as a function of current as a cloud of points for all arc melting tests	84
Figure 93: Screenshots from the thermal camera during the 0%-C-DRI-Test (Test 1 - pretest); time progressing from A) to D)	85
Figure 94: Screenshots from the thermal camera during the 0%-C-DRI-DR (Test 2); time progressing from A) to D)	85

Figure 95: Screenshots from the thermal camera during the C-DRI-DR (Test 3); time progressing from A) to D	86
Figure 96: Screenshots from the thermal camera during the 0%-C-DRI-Fines (Test 4); time progressing from A) to D)	86
Figure 97: Screenshots from the thermal camera during the 0%-C-DRI-BF-slag (Test 5); time progressing from A) to D)	87
Figure 98: off-gas analyses of C-DRI-DR (Test 3) with two different y-scales; measurement started already before igniting the arc.....	87
Figure 99: off-gas analyses of 0%-C-DRI-Fines (Test 4) with two different y-scales; measurement started already before igniting the arc.....	88
Figure 100: off-gas analyses of 0%-C-DRI-BF-slag (Test 5) with two different y-scales; measurement started already before igniting the arc.....	88
Figure 101: Digital microscope image of the 0%-C-DRI-Test (Test 1 - pretest) cross-section.....	88
Figure 102: Photograph from the top and digital microscope image of the 0%-C-DRI-DR (Test 2) cross-section.....	89
Figure 103: Photograph from the top and digital microscope image of the C-DRI-DR (Test 3) cross-section.....	89
Figure 104: Photograph from the top and digital microscope image of the 0%-C-DRI-Fines (Test 4) cross-section.....	89
Figure 105: Photograph from the top and digital microscope image of the 0%-C-DRI-BF-slag (Test 5) cross-section.....	90
Figure 106: Cover layer of sample C-DRI-DR from both sides after melting.....	90
Figure 107: Surface profile of the C-DRI-DR cover layer.....	90
Figure 108: Digital microscope images of slag foaming A) Test 2; B) Test 10; see Table 37	93
Figure 109: Digital microscope images of A) Test 1; B) Test 6; see Table 37	93
Figure 110: Digital microscope images of slag foaming A) Test 5; B) Test 3; see Table 37	94
Figure 111: Digital microscope images of slag foaming A) Test 4; B) Test 7; see Table 37	94
Figure 112: Digital microscope images of slag foaming A) Test 8; B) Test 9; see Table 37	95
Figure 114: Normalized increase in volume	95
Figure 115: SEM image of foaming sample 1 EAF-sat, upper part of the crucible; A) see Table 38	96
Figure 116: EDX-mapping of foaming sample 1 EAF-sat, upper part of the crucible; corresponding SEM image see Figure 115	97
Figure 117: SEM image of foaming sample 1 EAF-sat, lower and outer part of the crucible.....	97
Figure 118: EDX-mapping of foaming sample 1 EAF-sat, lower and outer part of the crucible; corresponding SEM image see Figure 117	98
Figure 119: SEM image of foaming sample 1 EAF-sat, lower and central part of the crucible.....	99
Figure 120: EDX-mapping of foaming sample 1 EAF-sat, lower and central part of the crucible; corresponding SEM image see Figure 119	100
Figure 121: SEM image of foaming sample 4 EAF-sat-reference, upper and central part of the crucible.....	100
Figure 122: EDX-mapping of foaming sample 4 EAF-sat-reference, upper and central part of the crucible; corresponding SEM image see Figure 121	101
Figure 123: SEM image of foaming sample 4 EAF-sat-reference, lower and central part of the crucible; A) and B) see Table 38	102
Figure 124: EDX-mapping of foaming sample 4 EAF-sat-reference, lower and central part of the crucible; corresponding SEM image see Figure 123	103
Figure 125: SEM image of foaming sample 6 EAF, part of the foam; A), B), and C) see Table 38	103
Figure 126: EDX-mapping of foaming sample 6 EAF, part of the foam; corresponding SEM image see Figure 125	104
Figure 127: SEM image of foaming sample 6 EAF, lower and central part of the crucible.....	104

Figure 128: EDX-mapping of foaming sample 6 EAF, lower and central part of the crucible; corresponding SEM image see Figure 127	105
Figure 129: SEM image of foaming sample 10 SAF, lower and outer part of the crucible	106
Figure 130: EDX-mapping of foaming sample 10 SAF, lower and outer part of the crucible; corresponding SEM image see Figure 129	107
Figure 131: Schematic description of the different slag foaming crucible zones; A) non-foaming samples 4,10; B) foaming samples 1,3,5,6,7,8,9	108
Figure 132: Surface plot and horizontal sections of viscosity η , neglecting solid particles; A) based on fitted FactSage™ data; B) acc. to Urbain ^[123] model with parameters from ^[129] ; Emirates steel data from ^[105]	111
Figure 133: Surface plot and horizontal sections of the solid fraction ϵ in wt.-% based on fitted FactSage™ data; Emirates steel data from ^[105]	112
Figure 134: Surface plot and horizontal sections of effective viscosity η_{eff} , A) based on equation 13 ^[95] ; B) based on equation 14 ^[124] ; Emirates steel data from ^[105]	113
Figure 135: Surface plot and horizontal sections of the surface tension σ based on ^[147] ; Emirates steel data from ^[105]	114
Figure 136: Surface plot and horizontal sections of the density ρ based on ^[147] ; Emirates steel data from ^[105]	115
Figure 137: Surface plot and horizontal sections of Slag foaming index Σ ; A) for bath smelting slags; B) for MgO_{sat} slags; C) for CaO-based slags; Emirates steel data from ^[105]	116
Figure 138: Surface plot and horizontal sections of the Morton number Mo ; Emirates steel data from ^[105]	117

Appendix Figures

Figure A- I: SEM image of foaming sample 4 EAF-sat reference, lower and outer part of the crucible.....	A-II
Figure A- II: EDX-mapping of foaming sample 4 EAF-sat reference, lower and outer part of the crucible; corresponding SEM image see Figure A- I.....	A-II
Figure A- III: SEM image of foaming sample 6 EAF, lower and outer part of the crucible.....	A-III
Figure A- IV: EDX-mapping of foaming sample 6 EAF, lower and outer part of the crucible; corresponding SEM image see Figure A- III.....	A-III
Figure A- V: SEM image of foaming sample 7 EAF-sat, lower and outer part of the crucible.....	A-IV
Figure A- VI: EDX-mapping of foaming sample 7 EAF-sat, lower and outer part of the crucible; corresponding SEM image see Figure A- V	A-IV
Figure A- VII: SEM image of foaming sample 7 EAF-sat, part of the foam.....	A-V
Figure A- VIII: EDX-mapping of foaming sample 7 EAF-sat, part of the foam; corresponding SEM image see Figure A- VIII	A-V
Figure A- IX: SEM image of foaming sample 7 EAF-sat, lower and central part of the crucible....	A-VI
Figure A- X: EDX-mapping of foaming sample 7 EAF-sat, lower and central part of the crucible; corresponding SEM image see Figure A- IX	A-VI
Figure A- XI: SEM image of foaming sample 8 EAF, part of the foam.....	A-VII
Figure A- XII: EDX-mapping of foaming sample 8 EAF, part of the foam; corresponding SEM image see Figure A- XI	A-VII
Figure A- XIII: SEM image of foaming sample 10 SAF, lower and central part of the crucible....	A-VIII
Figure A- XIV: EDX-mapping of foaming sample 10 SAF, lower and central part of the crucible; corresponding SEM image see Figure A- XIII	A-VIII
Figure A- XV: Linescans of sample no. 1 EAF-sat.....	A-IX
Figure A- XVI: Linescans of sample no. 4 EAF-sat ref.....	A-IX
Figure A- XVII: Linescans of sample no. 6 EAF.....	A-X
Figure A- XVIII: Linescans of sample no. 7 EAF-sat.....	A-X
Figure A- XIX: Linescans of sample no. 8 EAF.....	A-XI
Figure A- XX: Linescans of sample no. 9 EAF.....	A-XI
Figure A- XXI: Linescans of sample no. 10 SAF.....	A-XII
Figure A- XXII: Surface plot and horizontal sections of viscosity η , neglecting solid particles; 10% MgO, 1500°C; A) based on fitted FactSage™ data; B) acc. to Urbain ^[123] model with parameters from ^[129] ; Emirates steel data from ^[105]	A-XII
Figure A- XXIII: Surface plot and horizontal sections of the solid fraction ϵ in wt.-% based on fitted FactSage™ data; 10% MgO, 1500°C; Emirates steel data from ^[105]	A-XIII
Figure A- XXIV: Surface plot and horizontal sections of effective viscosity η_{eff} ; 10% MgO, 1500°C; A) based on equation 13 ^[95] ; B) based on equation 14 ^[124] ; Emirates steel data from ^[105]	A-XIII
Figure A- XXV: Surface plot and horizontal sections of the surface tension σ based on ^[147] ; 10% MgO, 1500°C; Emirates steel data from ^[105]	A-XIV
Figure A- XXVI: Surface plot and horizontal sections of the density ρ based on ^[147] ; 10% MgO, 1500°C; Emirates steel data from ^[105]	A-XIV
Figure A- XXVII: Surface plot and horizontal sections of the Morton number Mo ; 10% MgO, 1500°C; Emirates steel data from ^[105]	A-XV

Figure A- XXVIII: Surface plot and horizontal sections of Slag foaming index Σ ; 10% MgO, 1500°C; A) for bath smelting slags; B) for MgO _{sat} slags; C) for CaO-based slags; Emirates steel data from ^[105]	A-XVI
Figure A- XXIX: Surface plot and horizontal sections of viscosity η , neglecting solid particles; 5% MgO, 1600°C; A) based on fitted FactSage™ data; B) acc. to Urbain ^[123] model with parameters from ^[129] ; Emirates steel data from ^[105]	A-XVII
Figure A- XXX: Surface plot and horizontal sections of the solid fraction ϵ in wt.-% based on fitted FactSage™ data; 5% MgO, 1600°C; Emirates steel data from ^[105]	A-XVII
Figure A- XXXI: Surface plot and horizontal sections of effective viscosity η_{eff} ; 5% MgO, 1600°C; A) based on equation 13 ^[95] ; B) based on equation 14 ^[124] ; Emirates steel data from ^[105]	A-XVIII
Figure A- XXXII: Surface plot and horizontal sections of the surface tension σ based on ^[147] ; 5% MgO, 1600°C; Emirates steel data from ^[105]	A-XVIII
Figure A- XXXIII: Surface plot and horizontal sections of the density ρ based on ^[147] ; 5% MgO, 1600°C; Emirates steel data from ^[105]	A-XIX
Figure A- XXXIV: Surface plot and horizontal sections of the Morton number Mo; 5% MgO, 1600°C; Emirates steel data from ^[105]	XIX
Figure A- XXXV: Surface plot and horizontal sections of Slag foaming index Σ ; 5% MgO, 1600°C; A) for bath smelting slags; B) for MgO _{sat} slags; C) for CaO-based slags; Emirates steel data from ^[105]	A-XX

List of Tables

Table 1: Comparison of different iron ore products ^[36, 38–40] ; *in 2018.....	3
Table 2: DRI properties ^[50]	6
Table 3: HBI properties ^[52]	7
Table 4: Transformation strategies of European steelmakers; CO ₂ neutral means a significant emission reduction of approx. 90%, def. by the company; *Transformation strategy is just published for the first period until 2027.....	9
Table 5: Emirates steel slag composition ^[105] ; B2 according to equation 4	14
Table 6: Summary of slag foaming index correlations from various authors; Σ ... Slag foaming index / s; η ... dynamic viscosity / kg/(m·s); σ ... surface tension / kg/s ² ; ρ ... density / kg/m ³ ; D _b ... bubble diameter / mm; T... Temperature / K.....	17
Table 7: Slag foaming models from Ghag et al. ^[130, 135, 136] ; Σ ... Slag foaming index / s; η ... dynamic viscosity / kg/(m·s); σ ... surface tension / kg/s ² ; ρ ... density / kg/m ³ ; D _b ... bubble diameter / mm; E _{eff} ... effective elasticity / kg/s ²	18
Table 8: Compositions of applied slag forming oxides; CaO-95, SiO ₂ -99, Al ₂ O ₃ -99, MgO-99... technically pure oxides, composition according to Carl Roth GmbH.+ Co KG (Karlsruhe, Germany); *FeO-prered... composition determined by mass balance, based on the ore composition and the weight loss during reduction.....	24
Table 9: Chemical composition of Kiruna ore samples, before and after oxidation / wt.-%.....	25
Table 10: particle sizes of the mixtures.....	25
Table 11: Boundary conditions for the phosphorus partitions, shown in Figures 72 to 75	26
Table 12: Test setup components ^[140]	29
Table 13: Pellet compositions applied in test series I and II / wt.-%.....	30

Table 14: DRI compositions; C... measured by LECO; Fe _{met} , Fe ²⁺ ... measured by titration methods; Fe ³⁺ ... determined by mass balance with Fe _{tot} ; *based on mass balance; xcarburization time lost..	30
Table 15: ULC composition; determined by optical emission spectroscopy (OES) ^[140]	31
Table 16: HM composition; determined by OES ^[140]	31
Table 17: Slag compositions determined by inductively coupled plasma optical emission spectroscopy (ICP-OES); *by SEM-EDS ^[140]	32
Table 18: Composition of the iron ores; *determined by mass balance calculation, wt.-%.....	33
Table 19: Composition of premelts for slag foaming tests in chapter 8, determined by SEM-EDX..	36
Table 20: Slag mixtures for 100 g; Premelt no. according to Table 19	36
Table 21: Target slag compositions for slag foaming tests; ρ, σ acc. to ^[147] ; η _l , ε, T _{Liquidus} acc. to FactSage™ 8.2; η ₂ acc. to Urbain model ^[123, 129] ; *Σ for bath smelting slags; xΣ for MgO _{sat} slags; ✓ for CaO based slags ... see Table 6 ; Mo acc. to equation 12	37
Table 22: Additive compositions	42
Table 23: External iron carrier compositions / wt.-%.....	43
Table 24: Ores considered for the calculations / wt.-%.....	43
Table 25: Boundary conditions for melting aggregates.....	44
Table 26: Calculated case studies	45
Table 27: Comparison between published and calculated Emirates Steel data; *coal for 90% hot and 10% cold DRI.....	45
Table 28: List of DRI dipping tests; *pretests, which were cooled in flushed nitrogen and not further examined ^[140]	70
Table 29: Calculated dimensionless Prandtl numbers, incl. literature data for the parameters ^[163]	79
Table 30: List of arc melting tests.....	81
Table 31: Mass balance of arc melting test 1	82
Table 32: Mass balance of arc melting test 2	82
Table 33: Mass balance of arc melting test 3	82
Table 34: Mass balance of arc melting test 4	83
Table 35: Mass balance of arc melting test 5	83
Table 36: Chemical composition based on the element distribution, determined by SEM-EDX, wt.-%.....	91
Table 37: List of slag foaming tests; m _{PC} ... mass petrol coke; m _{Slag} ... mass of slag mixture; t... foaming time (from PC addition to quenching); *Outer diameter x Inner diameter x Outer height.....	92
Table 38: Analyses of the Figures' detailed spots; * If not metallic, Fe was assumed to be 100% FeO.; x Balanced by traces of oxides, possibly resulting from margin blur.....	107
Table 39: Chemical analyses of selected foaming samples, determined by SEM-EDX; *Fe assumed to be 100% FeO	109

I. Introduction – Target of this thesis

Due to its widespread properties, steel is one of the most important materials in all industry sectors. The scope of application ranges from low alloyed construction steels to high alloyed corrosion-protected or tool steels. **Figure 1** shows the annual crude steel production for the last 70 years. Although the amount stagnated in the 90s, China's strong economic growth accelerated crude steel production in 2000. Since then, the amount has increased steadily, interrupted by the global financial crisis in 2008/2009 and the Euro crisis in 2011/12, leading to more than 1.9 billion tons in 2021^[1, 2].

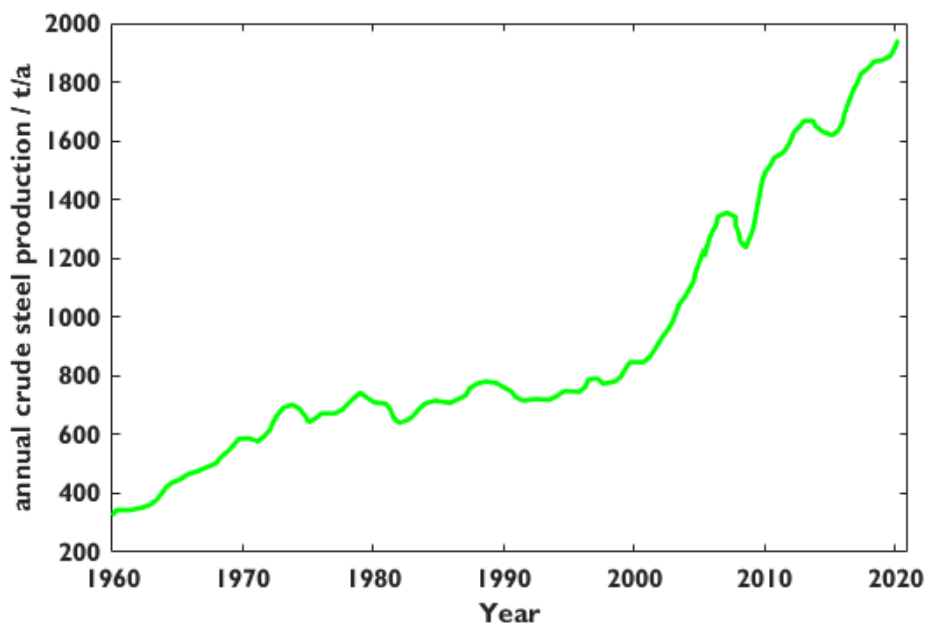


Figure 1: Annual crude steel production^[1]

Nowadays, the steel industry is responsible for 5% of the CO₂ emissions in the EU and 7% on a global scale. Since the Paris Agreement sets an ambitious framework, the European steel industry must reduce its emissions by 55% compared to 1990 until 2030 and get CO₂ neutral until 2050. Carbon direct avoidance (CDA), carbon capture and usage (CCU), and carbon capture and storage (CCS) are three approaches to reducing emissions. Therefore, European steelmakers work out different solutions, leading to estimated capital expenditures (CapEx) of €31 billion and operating expenditures (OpEx) of €54 billion^[3-5]. Therefore, further research into this transformation is of great interest.

I.1. State of the art

Figure 2 shows the most important steelmaking routes. With a share of ≈71% of the global steel output, the integrated blast furnace (BF) – basic oxygen furnace (BOF) is the primary strategy. The BF is a counter-current flow shaft furnace. Its raw materials are lumpy ores in the form of lump ore, sinter or pellets, lumpy coke, hot blast, as well as substitute reducing agents (SRA) such as pulverized coal

(PCI) or hydrogen^[6], which are injected via the tuyeres. The output products are top gas, slag, and hot metal, which is further processed in the BOF to crude steel. Since all by-products can be reused, the BF is a highly effective process. Nevertheless, it relies on a minimum amount of coke to guarantee permeability; therefore, it cannot be driven CO₂ neutrally. Currently, approx. 1900 kg of CO₂ is emitted per t crude steel via the BF-BOF steelmaking route^[7–9].

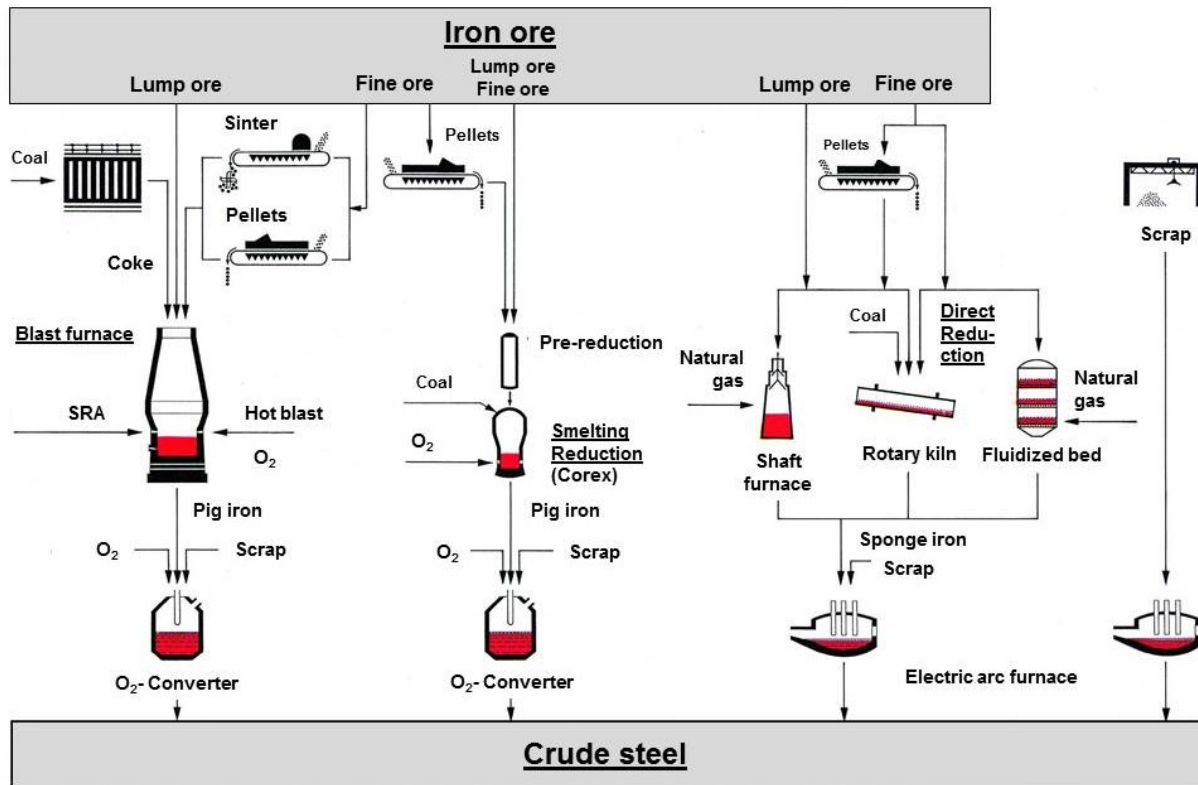


Figure 2: Currently applied steelmaking routes^[10] ©VDEH

Electric steelmaking in the electric arc furnace (EAF) accounts for 29% of global steel production. The EAF is a flexible aggregate usually operated with up to 100% scrap but also direct reduced iron (DRI), hot briquetted iron (HBI), or pig iron. Applying such metallic charging materials reduces the typical CO₂ emissions to approx. 401 kg per t crude steel, also considering indirect emissions from electricity generation. Although this seems promising at first sight, and the EAF will gain greater importance in the future, the global steel demand cannot be fully satisfied by recycling steel. The supply of scrap, in general, is increasing, but the availability of high-quality ones is limited as tramp elements, such as Cu, accumulate with each recycling step^[4, 5, 8, 11, 12].

Alternative ironmaking technologies can be divided into direct reduction (DR) and smelting reduction (SR). SR processes are analogs to the BF, characterized by producing a carbon-saturated hot metal directly from the ore. Examples are Corex^[7, 9, 13, 14], Finex^[7, 9, 15, 16], Hisarna^[17–20], or Hismelt^[9, 21]. DR reduces the iron ore in a gas-solid reaction to a so-called direct reduced iron (DRI) without any liquid phase. As shown in **Figure 2**, DR plants exist as shaft furnaces, fluidized bed reactors, and rotary kilns:

- Shaft furnaces: Midrex[®]^[7, 9, 22–25], HyL Energiron[®]^[7, 9, 26]
- Fluidized bed reactors: Finmet[®]/Finored[®]^[7, 9, 27], Circored[™]^[7, 9, 28, 29], Hyfor[®]^[30, 31]
- Rotary kilns: SL/RN^[32]

In 2021, 119,2 million t DRI were produced^[33]. Although this is just a minor share of global steel production, gas-based DR is an industrially proven technology, especially in countries rich in natural gas, such as Iran, Russia, Saudi Arabia, or Mexico^[33]. Further, DR provides excellent potential to reduce CO₂ emissions compared to the BF-BOF route. Based on natural gas, a DR plant with an EAF saves 35-45% of the CO₂. With hydrogen as the reducing agent and CO₂-neutrally generated electricity, the emissions can be reduced by 80%^[8, 34]. Therefore, the reduction step from iron ore to DRI and the further processing of DRI are of great interest. This thesis focuses on the latter, the melting, and processing of DRI.

1.2. Transformation of the Steel Industry towards CO₂-neutrality

Hydrogen-based direct reduction is a promising technology for CO₂-neutral steel production. Industrial-scale DR shafts with capacities of up to 2.5 million tons^[35] are planned to replace coal-based blast furnaces. However, a simple replacement of existing integrated plants with DR-EAF facilities, similar to existing plants, is challenging.

One aspect is the market for iron carriers. In 2018, the seaborne supply of iron ore was approx. 1.5 billion tons^[36]. As seen in **Table 1**, most of it is sinter feed, characterized by a relatively low total iron content of 58%. Next to sinter feed, which is usually agglomerated in sinter plants for BF application, there are lump ores and pellets. The former has a wide property spectrum and can be used as a direct charge for BF and sometimes DR. The latter is a ball-shaped agglomerate and consists of pelletized so-called pellet feed or concentrate, a fine material with a particle size <150µm^[37].

Table 1: Comparison of different iron ore products^[36, 38–40], *in 2018

	DR-pellet	BF-pellet	Lump ore	Sinter (feed)
Fe_{tot} / wt.-%	>67	62-65	58-68	≈58
Seaborne supply p.a. / Mt*	35	90	240	1165
Gangue / wt.-%	1-4	3-8	2-10	>12
Grain size / mm	6,3-16	6,3-16	6,3-40	6,3-40 (0-10) feed

The pellet category can be subdivided into BF-grades and DR-grades. While the blast furnace can handle a wide range of ores, the DR-EAF route relies on the highest possible qualities. The main reason is the absence of a deslagging mechanism in the DR-shaft, leading to significantly higher slag quantities in the EAF as the gangue content of the raw material increases. Further, sulfur and phosphorus contents must be low. The former poisons the Ni-catalyzed natural gas reformer; the latter is because of the dephosphorization in the EAF^[36, 38, 39].

Figure 3 shows the average iron-ore price since 1960. While it increased in a moderate order of magnitude between 1960 and 2000, as a result of the market entrance of China and a global commodity boom, the price rose to 160 \$/ton before the global financial crisis. After a couple of volatile years, the ore price increased significantly after the Covid pandemic. As mentioned, the chart shows a worldwide average. Ore price indices are based on the region and the total iron content. For the highest grade DR-pellets, the so-called DR-grade premium must be considered. E.g., in January 2021, DR-grade pellets were 46.3 \$/ton more expensive than 65% Fe iron fine ore, which cost appr. 190 \$/ton, representing an increase in ore cost of more than 20%^[41].

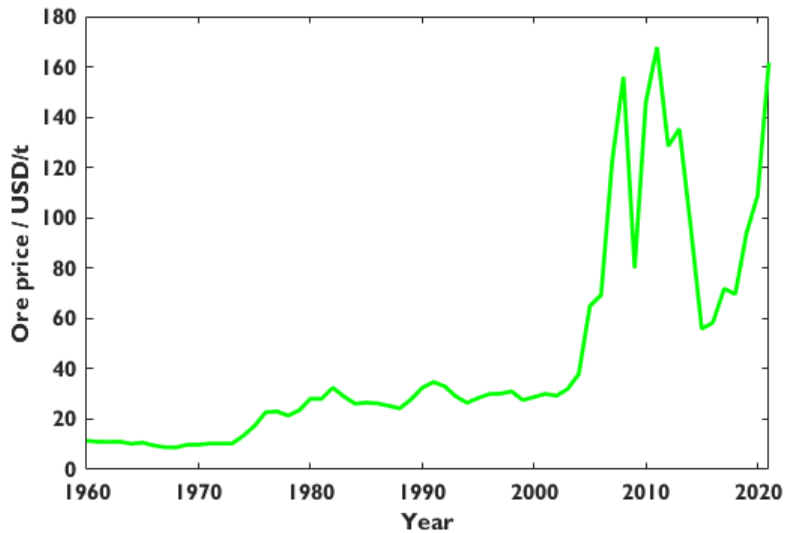


Figure 3: Iron ore price since 1960^[42]

Figure 4 shows prices for hot rolled coil (HRC) since 2009. Comparing ore costs with steel prices, the former is a critical parameter for profitability. The EBITDA margin for European steelmakers, like voestalpine or ArcelorMittal, in the last years was in the range of -2 and 29%^[43–47]. Further, the margins in the steel industry are highly volatile, depending on the economic cycles. Therefore, the switch from the integrated BF-BOF route to a DR-EAF, based on DR-grade pellets, must be critically questioned. Additionally, when more integrated plants transform, the DR-grade premium is expected to increase further due to the higher demand for the highest-grade iron ores.

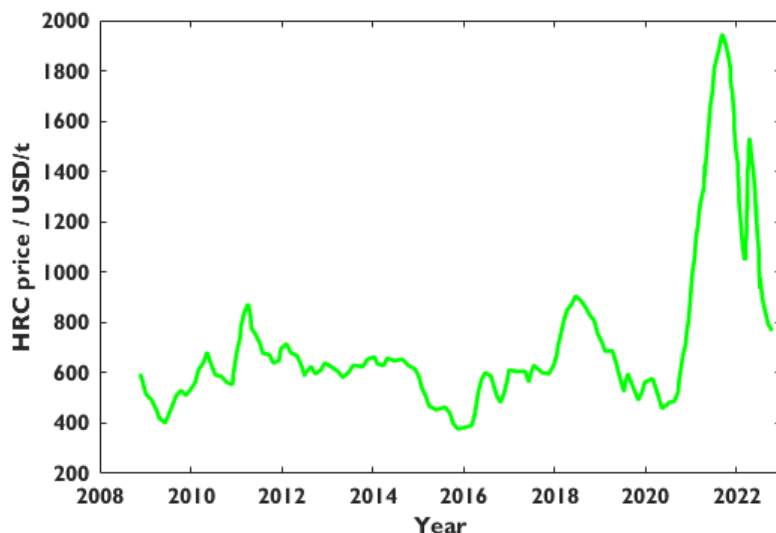


Figure 4: Price for hot rolled coil (HRC) since 2009^[48]

Therefore, applying BF-grade raw materials to guarantee an economical operation is of great interest. However, besides economic considerations, metallurgical aspects must be considered. DRI from lower-grade ores influences subsequent process steps as well as the final product quality in terms of yield, energy consumption, or unwanted tramp elements.

Consequently, European steelmakers are confronted with a major challenge. They demand a steelmaking strategy, which is CO₂-neutral, can be operated with BF-grade iron carriers, and delivers recyclable by-products. Furthermore, no compromises may be made with regard to product quality.

1.3. Research Target

Based on these recitals, some major research questions can be defined: *How could an appropriate path to CO₂-neutral steelmaking route look like? Which melting behavior shows DRI, based on BF-grade iron ores and reduced with hydrogen? How can DRI melting aggregates be operated with focus on high process efficiency and crude steel quality?* This PhD thesis aims to provide answers to these questions. The work described in this thesis can be subdivided into three working packages (WP).

The first one addresses a definition and evaluation of different DRI melting routes. This top-down view is essential to define a future plant layout. In this case, three possible routes are defined and compared using mass- and energy balance calculations. Considering different raw material grades, the strategies are evaluated.

The second WP analyses the behavior of DRI during the melting step. In this case, a method is developed, providing the possibility to characterize different sponge iron samples according to their interaction with slags, steel, and hot metal.

WP three focuses on process-specific topics. Firstly, an experimental study of the phosphorus behavior during direct reduction with hydrogen in a laboratory-scale vertical reduction furnace is performed. Based on these observations, the behavior in the melting stage is classified by means of thermodynamic and empirical approaches. Secondly, a method is developed to evaluate the slag foaming behavior, a critical aspect of efficient electric arc furnace operation. Different slag types are tested and assessed with the slag foaming index concept. This index is a widely used empirical approach from literature. Last but not least, different sponge iron samples are melted in a lab-scale arc furnace, providing the possibility to study its behavior in the electric arc and the morphology of the solidified sample.

Further, a thermal analysis of DRI was performed in the scope of a master thesis by Kern^[49], which could be assigned to WP II. Selected results are integrated into this work. Thus, this thesis provides a comprehensive overview of many aspects to be considered in processing direct reduced iron.

2. Theoretical Fundamentals

This chapter describes the theoretical background for the following practical part. Starting with the iron ore supply, an important aspect underscoring the research objective described above, a comprehensive literature review on this topic is given.

2.1. Direct reduced iron

Two aspects define the sponge iron properties: the raw materials (e.g., Fe_{tot} , gangue, particle size) and the reduction process (aggregate, conditions). The International Iron Metallics Association defines Direct reduced iron (DRI) according to **Table 2** made of iron ore with 65.5-68 wt.-% Fe_{tot} ^[50]. Such definitions are important to gain a standardized material quality for merchant DRI.

Table 2: DRI properties^[50]

Parameter	
MD / %	92.0-96.0
Fe_{tot} / wt.-%	86.1-93.5
Fe_{met} / wt.-%	81.0-87.9
C / wt.-%	1.0-4.5
S / wt.-%	0.001-0.03
P_2O_5 / wt.-%	0.005-0.09
Gangue / wt.-%	3.9-8.4
Size / mm	4-20
Apparent density / t/m³	3.4-3.6
Bulk density / t/m³	1.6-1.9

Next to the relatively low gangue content, which is a result of the high-grade ore, the following aspects can be noticed:

- The metallization degree (MD) of >92% indicates a highly reduced material. See equations **1** and **2** for the mathematical definitions of MD and reduction degree (RD)^[51], two important parameters for characterizing reduced ores regarding their reduction state.

$$MD / \% = \frac{Fe_{met}}{Fe_{tot}} \cdot 100 \quad \mathbf{1}^{[51]}$$

$$RD / \% = \left[1 - \frac{xO_{Fe}}{1.5 \cdot xFe_{tot}} \right] \cdot 100 \quad \mathbf{2}^{[51]}$$

- The grain size is >4 mm. Consequently, DRI fines from fluidized bed technologies do not consistently meet this definition^[7, 25, 37, 40, 51].

- According to this definition, DRI contains more than 1% C. Consequently, hydrogen-based DRI without any carbon also does not fit this criterium.

Theoretically, if the properties deviate, the term direct reduced product (DRP) should be used. The terms are used as synonyms in this work, as the precise specifications will always be given.

Hot briquetted iron (HBI), a premium form of DRI, was invented for easier shipping. The sponge iron is briquetted in hot condition, $>650^{\circ}\text{C}$. **Table 3** shows its major properties. Characteristic for HBI is the high apparent density of $>5 \text{ t/m}^3$, which leads to a lower specific surface. Therefore, shipping and handling are much easier since it is less susceptible to reoxidation and self-heating.^[52]

Table 3: HBI properties ^[52]

Parameter	
MD / %	94
Fe _{tot} / wt.-%	88.3-94.0
Fe _{met} / wt.-%	83.0-88.4
C / wt.-%	0.5-1.6
S / wt.-%	0.001-0.03
P ₂ O ₅ / wt.-%	0.005-0.09
Gangue / wt.-%	3.9-8.6
Size / mm ³	(90-140)x(48-58)x(32-34)
Apparent density / t/m ³	>5.0
Bulk density / t/m ³	2.5-3.3

Kern^[49] performed extensive thermal analyses with various DRI, DRP, and HBI samples as part of a master thesis in this project's scope. Three methods were applied to study the influence of gangue and carbon on the high-temperature behavior. The following general conclusions can be drawn: Carbon-free DRI/DRP softens and melts at the melting point of pure iron. Although small liquid spots are observed in the high-temperature confocal microscope (HT-LSCM) from gangue phases, it shows a stable structure up to approximately 1539°C . Further, in the simultaneous thermal analysis (STA), small peaks can be seen at lower temperatures, which could result from gangue phases. Nevertheless, these signals are weak, so it cannot be ruled out that they are artifacts. Although higher than expected, carbon-containing samples show characteristic peaks at the liquidus and solidus temperatures. Further, a significant mass loss is observed, indicating a reduction of residual iron oxides with either carbon in the sample or CO from reduction with solid carbon. Nevertheless, the high-temperature microscopy indicated a hemispheric temperature of 1549°C for DRP with 1.9% carbon. Two conclusions can be made based on these observations: Firstly, the internal carbon is reactive and reduces residual iron-oxides. This effect is so distinctive that the characteristic temperatures move to higher values. Secondly, the metal framework stabilizes the sample. So, significant softening happens at around 1538°C , the Fe liquidus temperature^[53].

Kim et al.^[54] performed similar tests with fully metalized samples to study the influence of carbon and its bonding state. The differences between carbon as graphite and cementite were relatively small, so the authors concluded that heat transfer was the determining mechanism in industrial processes. Memoli^[55] reports that in zero reformer DR processes, such as HYL-Energiron, up to 95% of carbon was bound as cementite. Further, he indicates that high C DRI benefits the EAF process due to its chemical energy and better reoxidation behavior. If carbon is bound as cementite, on the one hand,

the Fe_3C dissociation delivers additional chemical energy, and the resistance against carbon losses due to dust formation is decreased.

The behavior of DRI when in contact with liquids was investigated broadly. Sharifi and Barati^[56] dropped commercial DRI pellets into steelmaking slag in an isochor reactor. Due to the reduction of iron oxides in pellets and slag, the pressure increased. The authors noted that firstly, carbon reacts with iron oxide in the DRI and afterward with FeO in the slag. An intermediate step sometimes separates the two stages depending on the conditions. Ramírez-Argàez et al.^[57–60] used mathematical models to study the behavior of DRI in contact with liquid steel and slag. The authors describe a two-stage sequence, starting with forming a solid layer. The driving force is heat transfer; if the temperature in the layer gets high enough, it starts to melt. Since the thermal conductivity in the shell is higher for steel, melting rates in steel baths are significantly higher than in slags. **Figure 5** highlights this comparison. Two aspects can be noticed. A steel melt forms a thicker solid shell than case two, with a top slag layer. Due to the higher thermal conductivity, the steel shell melts much faster, leading to a significantly higher melting rate relative to the slag case^[59].

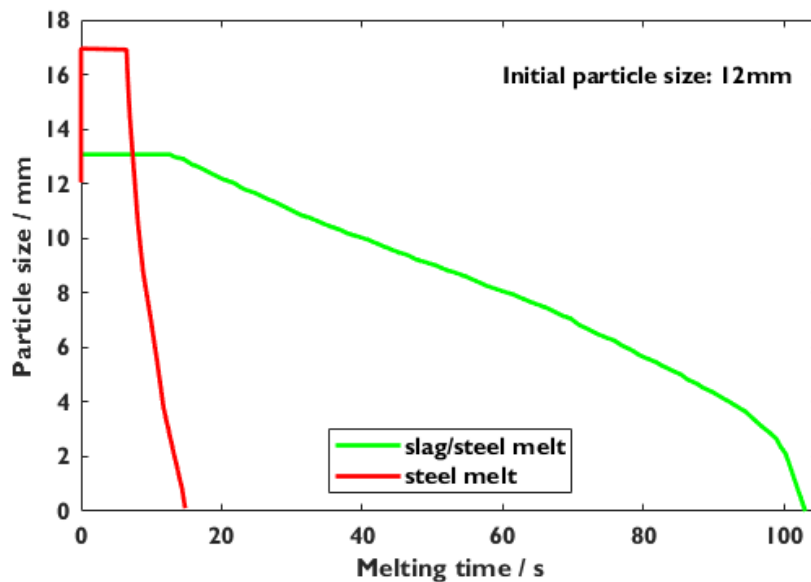


Figure 5: Comparison of the DRI melting time in slag/steel melts with slag melts; $T=1617^{\circ}\text{C}$; initial particle size: 12 mm^[59]

Another aspect being considered is fluid flow. Forced convection drastically reduces the shell thickness, resulting in lower melting times. For the actual EAF process, e.g., a long electric arc was beneficial since it leads to better stirring^[57, 59]. The authors also analyzed the influence of the particle size and its porosity on the melting behavior. On the one hand, increasing porosity decreases the thermal conductivity and the melting rate. However, as Sadrnezhaad^[61] found out, this may not be valid in the system solid particle – liquid slag – liquid steel. If the density, dependent on porosity, exceeds the slag density, the molten steel penetrates the particle instead of the slag, resulting in much faster melting. The particle size is positively correlated with the melting time and the maximum shell thickness since the mass to melt also increases. Therefore, from a melting perspective, the DRI pellets should be small in diameter and have a high density. A smaller particle size leads to a larger total solid area based on the specific pellet mass. Highly porous pellets may not reach the metal pool, leading to slow melting^[59].

2.2. DRI processing strategies

The first MIDREX shaft was installed in Hamburg and inaugurated in 1972. The main goal of this facility was to replace scrap in the minimills of Willi Korff^[23]. Besides this EAF route, also other DRI melting strategies were developed. The transformation process from the integrated BF-BOF to a CO₂-neutral process is highly individual for European steelmakers. **Table 4** gives a short overview of selected projects:

Table 4: Transformation strategies of European steelmakers; CO₂ neutral means a significant emission reduction of approx. 90%, def. by the company; *Transformation strategy is just published for the first period until 2027

Company	Project name	Strategy	CO ₂ neutral in:	Comment
Salzgitter	Salcos®	DR-EAF	2033	[62]
SSAB	Hybrit	DR-EAF	2030	[63]
Tata Steel Ijmuiden		DR-smelter-BOF	2045	[64]
thyssenkrupp Steel		DR-smelter-BOF	2045	[65]
voestalpine*	Greentec Steel	DR-EAF	2050	[66]

2.2.1. Electric arc furnace

As seen in **Figure 2**, the electric arc furnace (EAF) is one of the major steelmaking methods. Although it is mainly considered a scrap recycling aggregate, it is very flexible regarding raw materials. It can be operated with scrap, DRI/HBI, and up to 40% hot metal. The furnace typically consists of a transformer, flexible cables to the electrodes, the cooled furnace roof, the furnace shell, and the bottom. The bottom can be equipped with inert stirring plugs. DC or AC furnaces are possible; the former consists of one cathode with a bottom anode, the latter of three electrodes through the roof. An EAF melt shop can be seen in **Figure 6**. Various tapping methods are applied, e.g., excentric bottom tapping or offset bottom tapping^[32, 67–69].



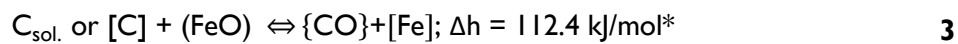
Figure 6: Colakoglu melt shop with a Primetals Ultimate EAF ©Primetals^[70]

For charging scrap, the roof can be opened and rotated. Alternative charging methods are:

- Scrap preheating by conveyor “Tenova Consteel”^[71]
- Scrap preheating by shaft “Primetals Quantum”^[72, 73]
- DRI direct hot feeding “MIDREX Hotlink”^[74] or “Tenova Hytemp”^[75]

Typical charging rates are 28-30 kg/(MW·min) HBI, 34-44 kg/(MW·min) cold DRI and 50-65 kg/(MW·min) hot DRI. These values vary with changing composition, temperature, and carbon content. If these values are exceeded, so-called iceberg formation occurs^[76].

Electrical as well as chemical energy contribute to the heat input. Due to high electricity prices, the former is kept as low as possible. Minimum values of approximately 340 kWh/t can be achieved with extensive chemical energy input, which can exceed 50% of the total energy consumption^[77]. That means charged and injected carbon, up to 18 kg/t, for Primetals Ultimate furnace^[70]. Further, C in DRI, HBI, or hot metal also contributes in this case; see equation 3. A second form of chemical energy is natural gas, added through refining combined burners (RCB) and oxygen^[68, 69, 78].



*calculated by FactSage 8.2 @ 1500°C

High-capacity plants, like Colakoglu in Turkey, reach up to 205 MW power input during the melting phase and 160 MW during the refining phase for a scrap charge^[78].

This theoretical introduction provides a brief overview of the EAF. More detailed information can be found in the literature^[32, 67–69, 79]. The following text, as well as chapter 2.3, describe three aspects relevant to this thesis in detail: the behavior of carbon, phosphorus, and the slag foaming practice.

The equilibrium between melt and slag is decisive regarding process modeling, steel- and slag quality. Turkdogan^[80] shows this in **Figure 7** by the iron oxide – carbon partition in different aggregates. While the bottom blowing converter (OBM – “Oxygen Bodenblasend Maxhütte”) provides the possibility of lowest carbon contents with moderate iron losses, the EAF is limited depending on the furnace design in this case. The top-blowing BOF is somewhere in the middle.

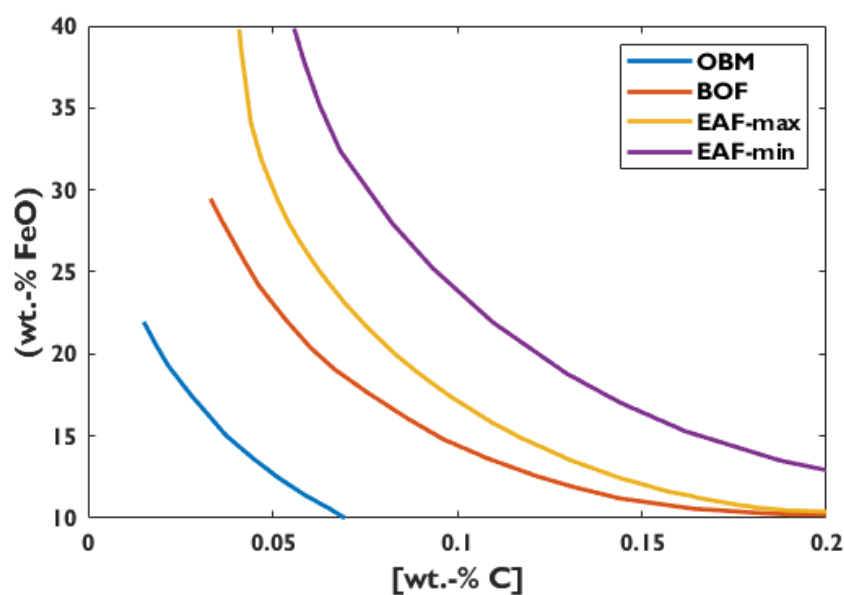


Figure 7: (%FeO) vs. [%C] – comparison of BOF, EAF, and OBM (“Oxygen Bodenblasend Maxhütte” – bottom blowing converter)^[32, 80]

Elkoumy et al.^[81] studied this topic in detail by analyzing numerous melts in an industrial EAF in Egypt. One of their results is the relationship in **Figure 8** which corresponds with **Figure 7** above. The central message of this chart is the importance of the demanded steel grade for the EAF process. Since a decreasing carbon content increases Fe in the slag, the yield decreases massively, influencing the refractory lifetime and the slag foaming behavior.

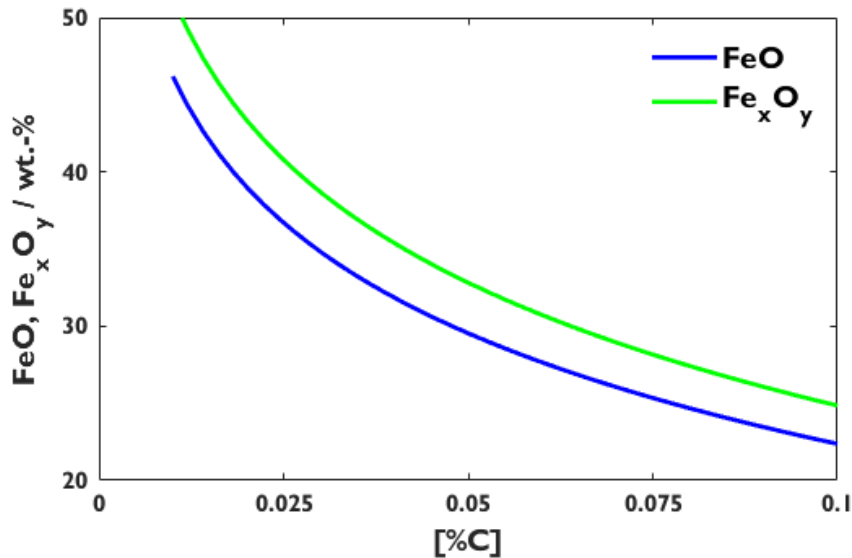


Figure 8: Empirical (%FeO)-[C] partition in the EAF^[81]

2.2.2. Submerged arc- and open slag bath furnace – “smelter”

As mentioned above, the DR-EAF route can be limited in applying lower-grade ores. A possible alternative can be the DRI-based hot metal production in an electrical smelting furnace. The idea is to separate the steelmaking process into two steps, a melting, deslagging, and final reduction step and a decarburizing and refining step. For existing integrated plants, this strategy provides further the advantage of using their existing BOF meltshop^[82, 83].

2.2.2.1. Smelter – State of the art

Such furnaces have been primarily used in ferroalloy production, e.g., Ferrosilicon, Ferrochrome, or Ferromanganese^[79, 84–91]. A second application is smelting sponge iron, made of titanomagnetite, e.g., at New Zealand Steel^[92] and Highveld Steel and Vanadium^[93–95]. Since extensive literature has been published about the latter, some basic information is described here. The plant consists of a prerelution step in rotary kilns. This reduced material is melted in submerged arc furnaces (SAF), partly updated to open slag bath furnaces (OSBF). The main characteristics of these concepts are described below. The hot metal with 3.2% C, 1.29% V, and 0.2% Ti is charged into shaking ladles under the slight addition of oxygen, anthracite, and scrap. Oxygen is used to bring Vanadium into the slag; scrap acts as a coolant, and anthracite replaces unintentionally burned carbon. Afterward, the slag is transported to the vanadium plant, while the hot metal is further processed in a BOF. Compared to the EAF, these furnaces have a low power input of 36 MW. The annual hot metal production of Highveld’s furnace 6 after the conversion to an OSBF was approximately 12000 t/month, which means 144000 t/a. This low melting capacity explains the high number of furnaces; for 900000 t_{Steel}/a, five OSBF are necessary. Nevertheless, a comparison to EAF data must be viewed critically since the smelter is operated with a reducing atmosphere. The low prerelution degree of 30-40% at the Highveld plant explains that 21 of 36 MW are for reduction. Further, the energy consumption of >1500 kWh/t is significantly higher than in the EAF^[93, 94].

2.2.2.2. Smelter - Furnace concepts

As mentioned above, two principal furnace concepts exist: the submerged arc furnace (SAF) and the open slag bath furnace (OSBF). The design is similar; the only difference is the arc operation. While the SAF works with electrodes submerged into the slag (resistance heating), the OSBF is operated in the so-called brush arc mode, a short electric arc.

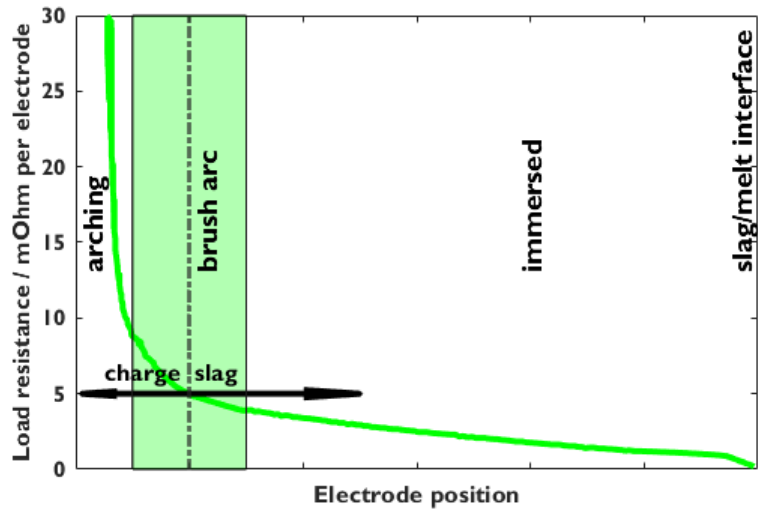


Figure 9: Operational resistance vs. electrode tip position^[82, 95]

Figure 9 gives the electric resistance as a function of the electrode position relative to the slag layer. Since these aggregates are operated in a reducing atmosphere, carbon must be charged. Such carbon sources can be coke in the burden and excess carbon in the sponge iron. The amount has to be balanced according to the remaining reduction work (FeO, SiO₂, MnO) and the target hot metal composition. The electrical energy is induced via self baking Söderbergh-electrodes^[79, 82, 93–95].

The following Figures 10 and 11 show the OSBF process in principle. One crucial aspect is the burden structure. Because the brush arc causes radiation losses, applying a loose burden on the outer areas and electric arcs is essential. This cover protects the refractory material and preheats the added coke – sponge iron mixture.

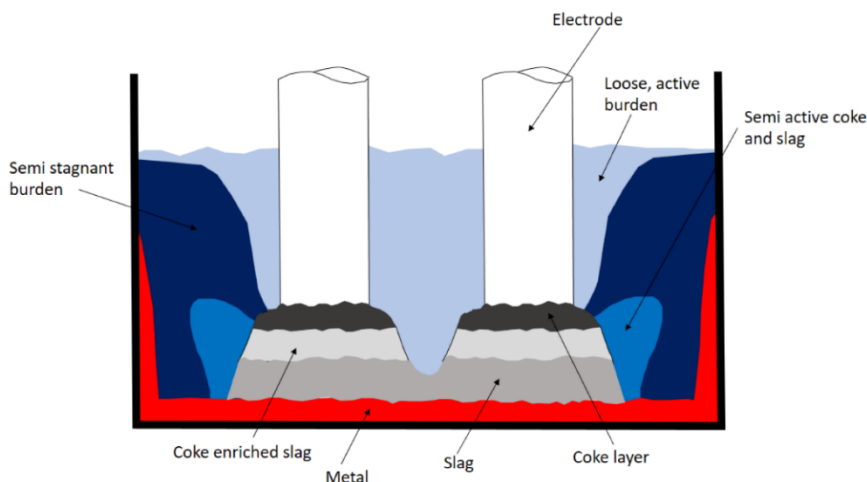


Figure 10: OSBF schematic process behavior^[82]; ©Pasquale Cavaliere

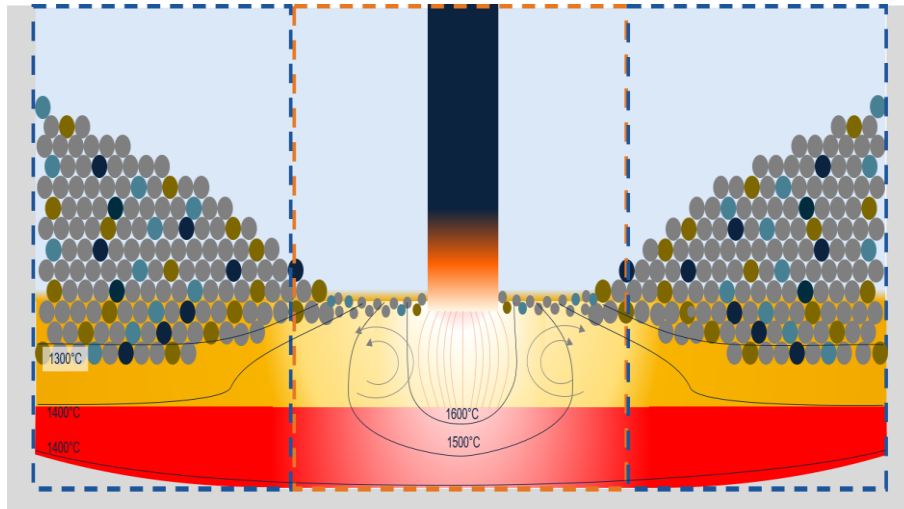


Figure 11: OSBF schematic process behaviors^[96]; ©Gerald Wimmer, Primetals

2.2.3. Blast furnace

In the BF, DRI, and HBI can increase productivity and cut reducing agents. It was used in blast furnaces worldwide, e.g., in Austria, USA, Japan, and Canada. Up to 30% of the iron-bearing charge in a full-scale commercial unit were replaced. One example is AK Steel in Ohio. They reported an increase in productivity by 1.2% and a decrease in fuel consumption by 0.8% for a 30% DRI/HBI charge^[34, 97–99]. Griesser and Bürgler^[34] evaluated the influence of HBI addition on the process characteristics at voestalpine Stahl Linz. They noticed a decrease of approximately 20kg/tHM in consumption of reducing agents, a lower sulfur but a higher carbon in the hot metal.

Although the BF is little sensitive in the case of gangue in the raw materials, the charge mixture has some other limitations. The BF burden needs a high strength to resist the burden load and a high resistance against abrasion to avoid the formation of fines^[100]. Further, reoxidation in the upper BF section can be an issue^[101–103]. In these cases, HBI shows benefits compared to DRI.

2.2.4. Basic oxygen furnace

DRI or HBI can be added as a scrap substitute in the BOF. Since DRI shows a high porosity, thermal conductivity may be limited, leading to incomplete dissolution when higher amounts of DRI are charged. Further, heavy flame shooting and high-end carbons are observed. Therefore, the optimum sponge iron amount is approximately 70 kg/tCS^[32, 104].

Since the application of DRI in BF or BOF can reduce CO₂ emissions just by a small amount, these strategies are not further considered in this thesis.

2.3. EAF slag properties

This chapter focuses on the properties of EAF slag as the smelter is a relatively new aggregate and there is little empirical experience with processing conventional iron ore-based DRI. From an economic perspective, the final smelter slag should be as close as possible to BF-slag with a basicity of typically 1.1 and a low FeO^[100] content to enable similar further processing.

The EAF has a wide range of applications. DRI, hot metal, and scrap can be applied from a raw material perspective. From the product view, rebar, quality low carbon steel, as well as high alloyed steel must be distinguished. This thesis refers to processing DRI to low-carbon crude steel instead of high-alloyed steel. Therefore, this chapter spotlights slags for this target.

Table 5 gives a slag composition from Emirates steel directly before tapping. The high FeO content, the high MgO content, and the basicity of ≈ 1.6 -2.2 are typical in this case. These properties provide a compromise for the following goals:

- MgO saturation: It reduces refractory consumption and is beneficial for slag foaming.
- CaO level: It should be as low as possible regarding the total slag amount and, on the other hand, high for improved dephosphorization.
- FeO content: Needs to be at a certain level to gain the demanded tapping carbon composition; compare **Figure 7**^[32, 68, 105].

Table 5: Emirates steel slag composition^[105]; B2 according to equation 4

Component	wt.-%
CaO	37.7
SiO ₂	17.9
Al ₂ O ₃	4.2
MgO	10.8
FeO	28.3
MnO	0.9
B2	2.1

$$B2 / 1 = \frac{(\text{wt.-%CaO})}{(\text{wt.-%SiO}_2)} \cdot 100 \quad 4$$

2.3.1. Behavior of trace elements

Trace elements are a critical factor concerning the final steel properties. These elements can be subdivided into residual elements from iron ore or coke, like S and P, and tramp elements from scrap, like Cu or Pb. Mostly, they are considered harmful due to the formation of unwanted inclusions or a detrimental effect on mechanical properties. Nevertheless, this must not be concluded generally. E.g., machining steels require S^[106], weatherproof steels Cu and P^[107]. The following subchapter describes the behavior of P in detail, as dephosphorization is a central metallurgical task. Other elements like Cu have a lower affinity to oxygen than Fe and must be controlled by carefully selecting input materials^[11, 12, 108].

Equation 5 gives the dephosphorization reaction, with Ca²⁺ usually being the counterpart for the negatively loaded ions. High basicity and oxygen activity shift the equilibrium to the right-hand side, meaning beneficial conditions for low P contents in the steel phase. The reaction is exothermic; hence, lower temperatures improve dephosphorization from a thermodynamic perspective.



The so-called partition constant describes the distribution of Phosphorus between slag and steel. Various authors give different definitions, with equations 6 and 7 representing two of them.

$$L_P = \frac{(\%P)}{[\%P]} \quad 6^{[109-111]}$$

$$L_P^* = \frac{(\%P_2O_5)}{[\%P]^2} \quad 7^{[112]}$$

The partition between slag and steel melt has been analyzed since the 1940s. The history of the model development is documented in [110] and [109]. Basu et al. [113, 114] investigated the influence of basicity, (%FeO), and (%MgO) on high- and low-FeO steelmaking slags. The authors generally suggest high basicity, up to 2.5, for improved dephosphorization. Higher values do not show any improvements in the partition coefficient. Additionally, a higher FeO content further shifts phosphorus into the slag. Nevertheless, excessive FeO, above 20-21%, shows the opposite effect since more and more CaO gets dissolved, influencing the dephosphorization negatively.

De- and rephosphorization rates were investigated by Manning and Fruehan [109]. Mass transfer is considered the rate-limiting step. The rates are comparably high in the first 20 min, leading to a linear increase of [%P] for the rephosphorization and vice versa for the dephosphorization. The mass transfer decreases toward the end of the reaction, slowing the reaction rate.

Hereafter, two partition models are described, with these equations being applied in chapters 4 and 5.2:

Assis et al. [110, 111] performed melting tests with a 10 h holding time, representing equilibrium near conditions. Based on these experiments, the authors develop the correlation in equation 8 [110, 111], with components in wt.-% and temperature T in K. The approach focuses on the EAF, but the given validity ranges also suit the BOF.

$$\log \frac{L_P}{(\%Fe_{tot})^{2.5}} = 0.073 \cdot [(\%CaO) + 0.148 \cdot (\%MgO) + 0.96 \cdot (\%P_2O_5) + 0.144 \cdot (\%SiO_2) + 0.22 \cdot (\%Al_2O_3)] + \frac{11570}{T} - 10.46 \quad 8^{[110, 111]}$$

Li et al. [112] developed a distribution model for Hismelt, a smelting reduction technology. In contrast to the approach above, this model is representative of reducing conditions. While the correlation from Assis et al. is based on laboratory tests, Li et al. mathematically derivates equation 9 using the ion-molecule coexistence theory (IMCT).

$$\log L_P^* = 4.568 \cdot \log \left[\frac{(\%CaO) + (\%MgO)}{(\%SiO_2)} \right] - 0.051 \cdot (\%Al_2O_3) + 0.54 \cdot [(\%FeO) + (\%Fe_2O_3)] + \frac{2000}{T} - 9.276 \quad 9^{[112]}$$

Although these approaches act as an indicator, their transfer to industrial conditions must be considered carefully. As can be seen from the measurements in **Figure 12**, the values fluctuate significantly. Further, the OBM equilibrium curve approximates the phosphorus partition. Especially at higher carbon contents, a systematic underestimation of L_P occurs.

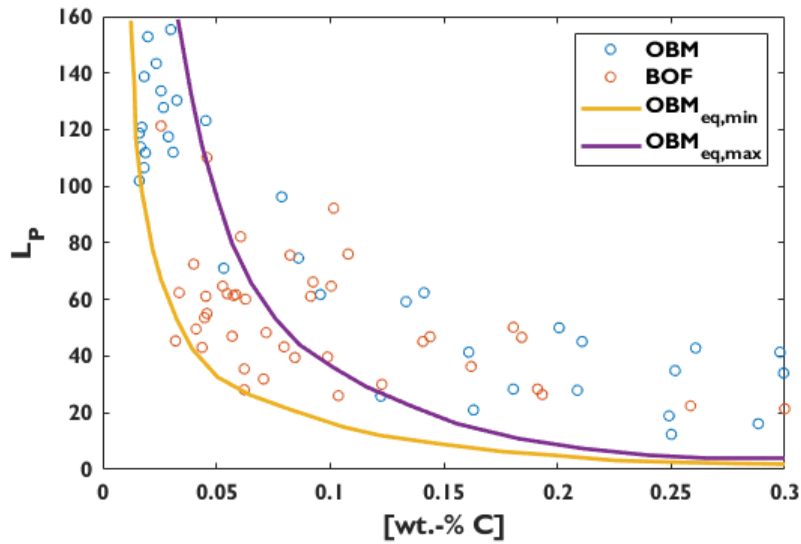


Figure 12: Phosphorus partition vs. [%C] in BOF and OBM (*Oxygen Bodenblasend Maxhütte* – bottom blowing converter)^[80]

Besides steady state partitions, the reaction kinetics of equation 5 is worth a closer look. Some literature^[115, 116] focuses on reducing BOF slag and cannot be directly related to this topic. Nevertheless, Manning and Fruehan^[109] studied the kinetics of slag in contact with liquid iron, considering dephosphorization as well as rephosphorization. Looking at DRI melting, the second case is more relevant. **Figure 13** shows their results and a modeled approach. That indicates a rapid rephosphorization until an equilibrium is reached after approximately 30-40 min. Although this is an interesting result, the relevance for industrial operations must be checked carefully. On the one hand, the initial phosphorus content is very high. Further, the slag basicity inspired by gangue is relatively low. Therefore, more research is necessary with variations in basicity and initial phosphorus contents.

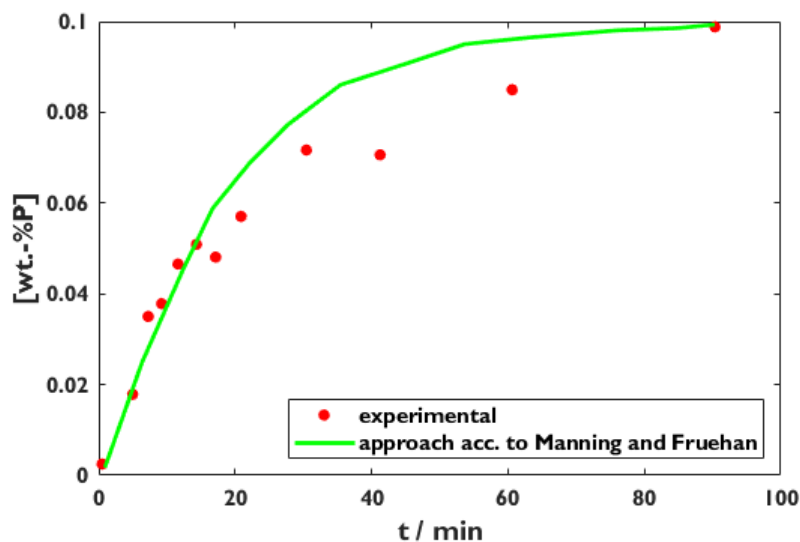


Figure 13: Rephosphorization experiment acc. to Manning, Fruehan^[109]; B2=0.9; (FeO)=18%; (MgO)=17%; (%P)₀=2.6%; T=1600°C

2.3.2. Slag foaming

Slag foaming is a phenomenon that occurs in EAF as well as in BOF. While in the latter, it accompanies the period of maximum decarburization, in the former, it is a critical factor for an efficient process. It covers the electric arc, reducing radiation losses and refractory consumption. That leads to an increase in efficiency up to 60-90% for foamy slag operation, compared to 40% without^[32, 117]. Two aspects must be considered: The slag composition has to meet specific demands, and gas has to be delivered. Reactions **10** and **11** give some gas-forming reactions with solid carbon, dominant in the EAF, and dissolved carbon, dominant in the BOF. The reaction enthalpy is highly endothermic (+124.9 kJ/mol; calculated using FactSage™ 8.2).



The slag foaming behavior and the role of the slag have been intensively investigated in the last few years. Liukkonen et al.^[118] and Pretorius^[119] give broad overviews of the physicochemical influences on slag foaming. This chapter describes major aspects based on the slag foaming index Σ . The idea behind this index is the characterization of slags regarding their composition and foaming behavior. Ito and Fruehan^[120, 121] describe Σ as the gas retention time in the slag. The authors flushed slag samples with Ar and measured the height gain. With the help of dimensional analyses, correlations between Σ vs. viscosity η , density ρ , and surface tension σ can be made from these results. **Table 6** lists literature approaches for Σ , based on high-temperature slag experiments. All equations are functions from η , ρ , and σ ; most differ only by the prefactor and indicate the viscosity as the crucial parameter. Nevertheless, some equations deviate strongly, e.g., compare the diameter-dependent equations from Zhang and Fruehan with Stadler et al. The latter indicates that bubble diameter and surface tension are decisive. The temperature equations indicate Arrhenius functions. Nevertheless, viscosity, surface tension, and density are themselves temperature dependent^[122, 123], so these Arrhenius equations must be handled as slag-specific correlations.

Table 6: Summary of slag foaming index correlations from various authors; Σ ... Slag foaming index / s; η ... dynamic viscosity / kg/(m·s); σ ... surface tension / kg/s²; ρ ... density / kg/m³; D_b ... bubble diameter / mm; T ... Temperature / K

Author	Correlation	Comment
Ito, Fruehan ^[121]	$\Sigma = 570 \cdot \frac{\eta}{\sqrt{\sigma \cdot \rho}}$	CaO-SiO ₂ -FeO slag
Jiang, Fruehan ^[124]	$\Sigma = 115 \cdot \frac{\eta}{\sqrt{\sigma \cdot \rho}}$	Bath smelting slag; B2 = 1-1.5
Zhang, Fruehan ^[125]	$\Sigma = 115 \cdot \frac{\eta^{1.2}}{\sigma^{0.2} \cdot \rho \cdot D_b^{0.9}}$	Incl. bubble diameter; also foaming induced by reaction with high C alloy was analyzed
Stadler et al. ^[126]	$\Sigma = 0.93 \cdot \frac{\eta^{1.2}}{\rho^{2/3} \cdot \sigma}$	Acidic slags; based on ^[124]
Stadler et al. ^[126]	$\Sigma = 10.3 \cdot 10^4 \cdot \frac{\sigma^{12}}{\eta^{0.4} \cdot \rho^{11.7} \cdot D_b^{23}}$	Acidic slags, based on ^[125]
Kim et al. ^[127]	$\Sigma = 214 \cdot \frac{\eta}{\sqrt{\sigma \cdot \rho}}$	for CaO-based slags
Kim et al. ^[127]	$\Sigma = 999 \cdot \frac{\eta}{\sqrt{\sigma \cdot \rho}}$	for MgO-saturated slags

Ozturk, Fruehan ^[128]	$\Sigma = 1.78 \cdot 10^{-5} \cdot e^{\left(\frac{16797}{T}\right)}$	Temperature dependency; 40% CaO; 40% SiO ₂ ; 10% Al ₂ O ₃ ; 10% FeO
Jung, Fruehan ^[129]	$\log \Sigma = \frac{6610}{T} - 3.90$	Temperature dependency; 35% CaO; 35% SiO ₂ ; 30% FeO; 10% MgO

Another characterization method is the application of cold models, used by many authors^[130–134]. Two correlations from Ghag et al. are shown in **Table 7**.

Table 7: Slag foaming models from Ghag et al.^[130, 135, 136]; Σ ... Slag foaming index / s; η ... dynamic viscosity / kg/(m·s); σ ... surface tension / kg/s²; ρ ... density / kg/m³; D_b ... bubble diameter / mm; E_{eff} ... effective elasticity / kg/s²

Author	Correlation	Comment
Ghag et al. ^[130, 135, 136]	$\Sigma = 1 \cdot 10^6 \left(\frac{\eta \cdot E_{eff}}{(\rho \cdot g)^2 \cdot D_b^3} \right)$	Water-glycerol solution with sodium dodecylbenzene sulphonate
Ghag, et al. ^[130, 135, 136]	$\Sigma = 2.02 \cdot 10^6 \cdot \eta \left(\frac{\Delta\sigma^{1.32}}{(\rho \cdot g)^{2.32} \cdot D_b^{3.64}} \right)$	Water-glycerol solution with sodium dodecylbenzene sulphonate

These correlations use the same parameters as those determined in hot tests. The similarity theory compares such cold models with EAF or BOF slags. Equation **12** gives the dimensionless Morton number. Mo describes the relationship between viscous forces F_V and forces from the surface tension F_O . Neglecting the small density of the gas bubbles ($\Delta\rho = \rho_{fluid} - \rho_{bubble} \approx \rho$) if the bubble density is approximately 1, it is only dependent on the fluid-specific parameters viscosity η , density ρ , surface tension σ and the gravity g . Comparing it with the slag foaming index approaches in **Table 6**, most equations look similar but with different exponents.

$$Mo = \frac{F_V}{F_O} = \frac{\eta^4 \cdot g \cdot \Delta\rho}{\sigma^3 \cdot \rho^2} \approx \frac{\eta^4 \cdot g}{\sigma^3 \cdot \rho} \quad \mathbf{12}^{[134, 137]}$$

EAF slag is usually saturated with MgO and therefore contains Magnesiowustite precipitations. That is another aspect influencing the foaming behavior. If the content is not too high, these particles promote slag foaming. Based on this knowledge, so-called isothermal stability diagrams are used. **Figure 14** shows an exemplary chart. The dashed line highlights the optimal area. In this part, a small but limited amount of solids is available. Compared to the other solid-containing regions, this one is relatively resilient regarding (FeO) fluctuations; this is beneficial due to the varying iron oxide content in the slag during an EAF charge^[119].

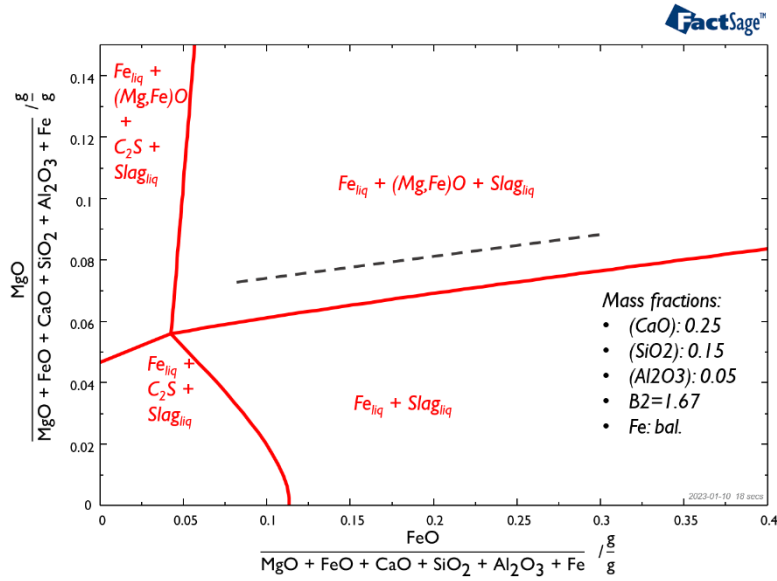


Figure 14: Isothermal solubility diagram @ 1600°C; calculated by FactSage™ 8.2

In slag foaming index calculations, these particles are considered using an effective viscosity corrected by the number of solids. Two modifications of this Einstein equation are given in 13 and 14, with ϵ representing the volume fraction of solid particles.

$$\eta_{\text{eff}} = \eta \cdot (1 - 1.35 \cdot \epsilon)^{-2.5} \tag{13}^{[95]}$$

$$\eta_{\text{eff}} = \eta \cdot (1 + 5.5 \cdot \epsilon) \tag{14}^{[124]}$$

The chart in Figure 15 describes the relationship between the foaming index and the effective viscosity qualitatively. In line with the isothermal solubility diagram, the curve forms a maximum at a certain number of solid particles. This condition would be called „fluffy“. The x-axis may be abstracted as MgO of an EAF slag or the basicity of a BOF slag. If totally liquid, the viscosity decreases as the SiO₂ network breaks up. Once the slag is saturated, solid particles of magnesiowustite or calcium-silicate precipitate. Then these solid particles define the effective viscosity, as seen in equations 13 and 14. However, these equations cannot describe the decreasing trend in the crusty region. Therefore, the slag foaming approaches are only valid in the composition range in which the model was developed.

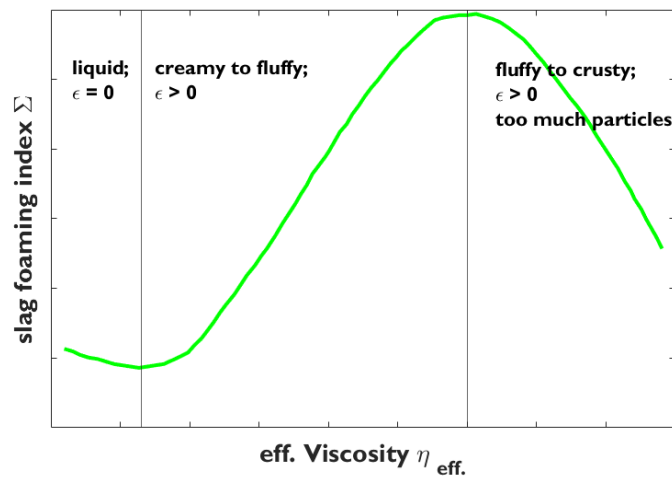


Figure 15: Influence of effective viscosity on the slag foaming index^[119]

However, looking more closely at the equations in **Tables 6** and **7**, modeling the slag foaming phenomenon must be viewed critically. While the sheer number of correlations is striking, a closer look reveals some contradictions. E.g., Stadler describes in one equation the surface tension with an exponent of 12 and directly proportional to the foaming index; the opposite is the case in Zhang and Fruehan's approach. This observation aligns with statistically insignificant correlations found by Stadler et al.^[126] for acidic slags. De Vos et al.^[138] compared acoustic measurements from BOF charges with the foaming indices calculated according to the slag compositions. No significant correlation could be observed, indicating that this laboratory scale concept is challenging to transform to industrial conditions. Some reasons for this could be:

- *Gas conditions:* In EAF and BOF, mainly CO, which arises from chemical reactions, is the driving foaming force. The reactions are either endothermal (reduction of FeO) or exothermal (oxidation of C_{sol} or [C]). On a laboratory scale, usually, inert gas injections are applied.
- *Inhomogeneities:* The industrial aggregate sizes inevitably lead to inhomogeneities regarding temperature, gas bubbles, and composition.
- *Interactions with refractory:* Since, on a laboratory scale, crucibles are very small, wetting of the refractory material may influence the observed results.

3. Methodology

This chapter describes the applied methods and facilities. A wide range of tools is used in this work, from thermodynamic software to laboratory furnaces and reduction aggregates.

3.1. Definition and comparison of processing strategy

Mass and energy balances are used to define and compare various DRI processing strategies, part of WPI. They are performed using FactSage™ macro calculations. Therefore, two calculation files were created, one for allothermal processes with a predefined end temperature, and one for autothermal processes, represented by an isenthalpic calculation. FactSage is a thermodynamic equilibrium calculation software. The input streams, e.g., slag, DRI, and additives, are defined in their composition and temperature, and the software calculates the composition and the phases at the given final state. This state may be defined as a final temperature or an enthalpy difference. One essential aspect is the definition of the databases. In this thesis, FactPS, FTOxid, and FSStel are applied.

These files are connected by an MS-Excel spreadsheet which acts as a dashboard. The spreadsheet allows for storing raw material compositions, predefining the boundary conditions, and compensating the thermodynamic equilibrium calculation if it deviates too much from reality. An integrated VBA macro in the spreadsheet precalculates the demanded additives to meet the predefined parameters and activates the separate FactSage-macro. **Figures 16** and **17** show the calculation flows for one- and two-step sequences. These steps are performed automatically.

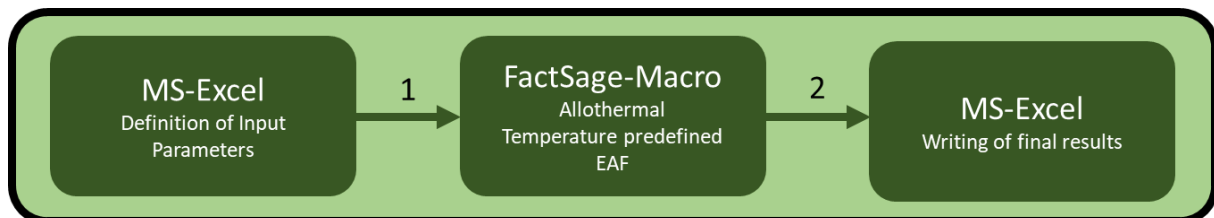


Figure 16: Calculation flow for a one-step melting sequence

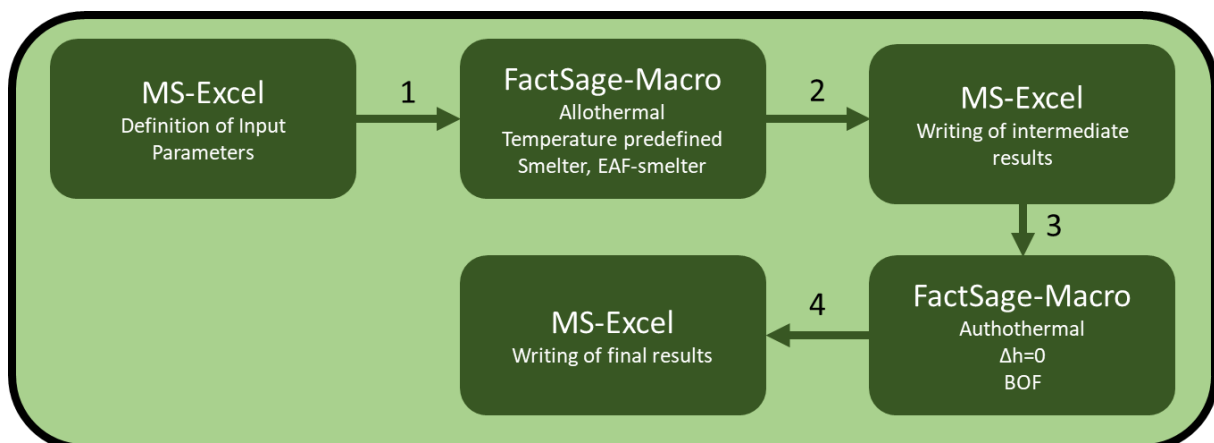


Figure 17: Calculation flow for a two-step melting sequence

Although it is a good approximation, the thermodynamic equilibrium approach of FactSage is not representative of industrial facilities. Therefore, some corrections were made in this case:

- The empirical equations $8^{[110, 111]}$ (in EAF and BOF) and $9^{[112]}$ (in smelter and EAF-smelter) correct the equilibrium phosphorus distribution.
- The approach from Elkoumy^[81], shown in **Figure 8**, approximates the [C]-(FeO) partition in the EAF.
- (%FeO) in the smelter is set to $\approx 1\%$, inspired by Highveld Steel and Vanadium, published by Steinberg et al.^[94, 95] and smelting reduction processes such as Hisarna^[17, 18]. For the EAF-smelter, respectively, a higher value of 5% is assumed.
- (%FeO) in the BOF is set to $\approx 25\%$; a widespread value in literature^[104, 129] for conventional one step converter processes.
- Since, in reality, equilibrium conditions will not be reached, leading to remaining iron oxide in the smelter slag, extensive Silicon reduction cannot be expected. Therefore, [%Si] was capped at 0.2% for the smelter and 0.05% for the EAF-smelter. In other words, if the FactSage result is below these limits, the thermodynamic values are used as the final result; if it is above, the maximum value of 0.2 or 0.05% is taken into account.

The derivation of the routes and the more specific parameters are described in chapter 4.

3.2. DRI Preparation

In the scope of various experimental investigations, prereduced materials are necessary. Such direct reduced iron samples are prepared using a vertical reduction furnace (VRF). Two retorts are applied, a 75 mm one for pellets, shown in **Figure 18**, and a 68 mm one for fines, shown in **Figure 19**. Temperatures up to 1100°C are possible; besides N₂, H₂, CO, and CO₂, also CH₄ or NH₃ can be applied through a separate gas supplier, which is not shown in the images. The online weight measurement enables the controllability of the reduction progress. That allows the production of DRI samples with predefined Reduction degrees.

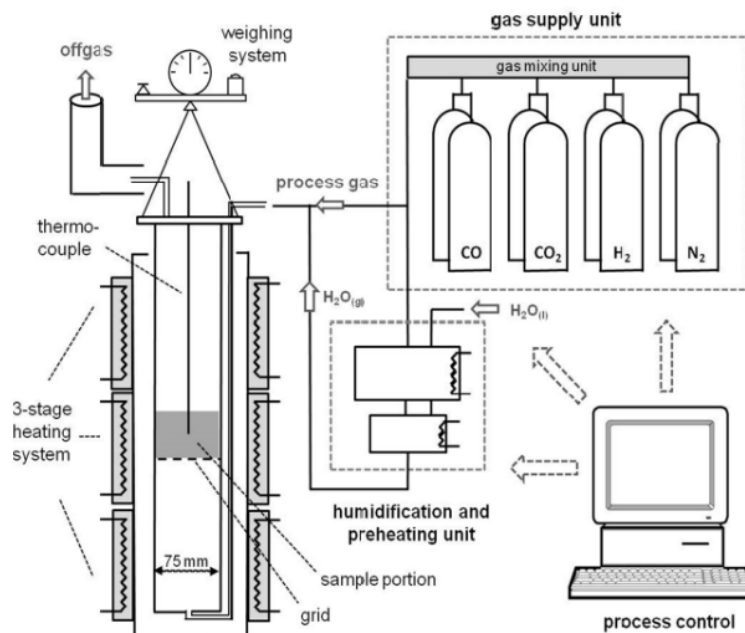


Figure 18: Lab-scale vertical reduction furnace^[139]

The preparation of DRI-fines is slightly different from that of pellets. On the one hand, the magnetic fines are preoxidized in a heat treatment furnace, to get a hematitic structure. That improves reducibility and fluidizability. On the other hand, the reactor is equipped with a second thermocouple. As shown in **Figure 19**, the upper one is placed in the bed, and the lower one is below the grid.

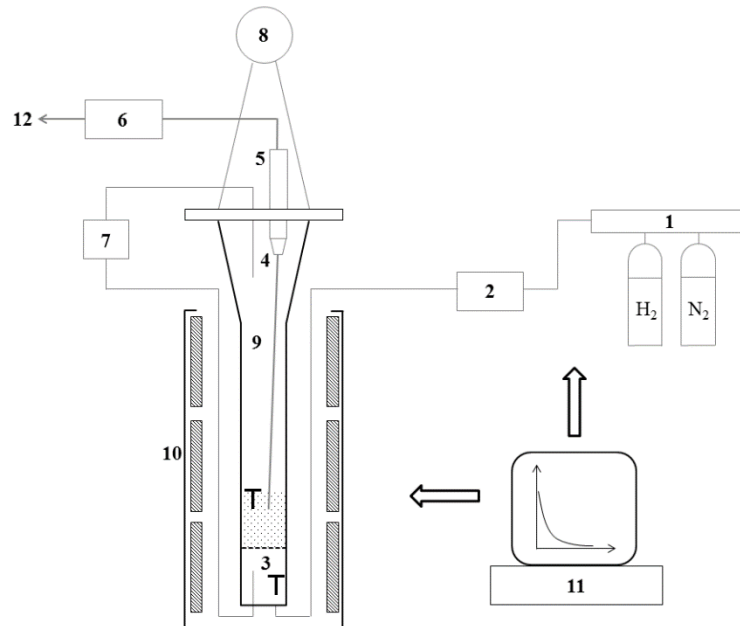


Figure 19: Lab-scale 68 mm fluidized bed reactor 1 – gas storage; 2 – evaporator; 3 – gas distributor; 4 – internal cyclone; 5 – dust filter; 6 – pressure regulator; 7 – differential pressure measurement; 8 – scale; 9 – reactor; 10 – heating furnace; 11 – process control; 12 – off-gas; T – thermocouples

The preparation process is subdivided into two steps if carbon-containing DRI is demanded. After prereducing the sample with hydrogen, it is carburized with methane. That enhances the process control since the mass loss during reduction is noted separately from the mass gain during carburization. Hanel^[139] and Spreitzer^[7] describe the aggregate more precisely in their PhD theses. The respective chapters describe the associated ore compositions and DRI preparation procedures.

3.3. Slag Premelting

The slag samples were partially premelted before the actual experiment, providing advantages in two respects. On the one hand, the volume decreases compared to pure oxide powders. On the other hand, liquefaction takes place more homogeneously since low-melting phases provide an early melt pool. The mixture was made of technically pure oxides for CaO, SiO₂, Al₂O₃, and MgO, see **Table 8**. FeO was made of hematitic iron ore and prerduced in the 68 mm fluidized bed reactor. The particle size was 100-200 µm; the reduction temperature was 750°C under 6 NI/min N₂, 7 NI/min H₂, and 5 NI/min H₂O_{vap}. Once the mass remained constant, indicative of pure FeO, reduction was stopped. The resulting composition in **Table 8** was determined by the mass balance and based on the initial ore composition, determined by x-ray fluorescence spectroscopy (XRF).

Table 8: Compositions of applied slag forming oxides; CaO-95, SiO₂-99, Al₂O₃-99, MgO-99... technically pure oxides, composition according to Carl Roth GmbH.+ Co KG (Karlsruhe, Germany); *FeO-prered... composition determined by mass balance, based on the ore composition and the weight loss during reduction

	CaO-95	SiO ₂ -99	Al ₂ O ₃ -99	MgO-99	FeO-prered.*
(CaO)	95				1.09
(SiO ₂)		99			6.54
(Al ₂ O ₃)			99		1.96
(MgO)				99	0
(FeO)					89.0
others	5				1.41

Slag premelting was performed in the MU900 induction furnace, see **Figure 20**. It provides 15 kW power and inductively heats a graphite crucible. The graphite either warms the slag mixture directly or indirectly through an additional refractory crucible.



Figure 20: MU900 induction furnace

The powder mixture for the demanded composition was heated to 1600°C; once it was totally liquid, more of the premixed powder was added. Afterward, it was slightly stirred to homogenize the slag and cast on steel plates to quench the slag. For DRI dipping tests in chapter 6, the exact slag was premelted in MgO crucibles and applied without any adjustments for the tests. However, slag foaming tests in chapter 8 consist of broader variations in slag compositions. Therefore, two premelts were made. Afterward, they were adjusted for the actual tests with additional powder. That can be considered a compromise between reducing the charging volume and limiting the workload. Since these premelts were FeO-free, this procedure was done directly in the graphite crucible.

3.4. Phosphorus

The behavior of phosphorus was investigated in two ways. On the one hand, the behavior in a DR plant is experimentally studied. That clarifies whether P occurs in the oxide or elementary state. The behavior in the DRI processing aggregates is studied based on published phosphorus partitions and

thermodynamical equilibrium calculations. Chapter 5 summarizes the reduction tests' results and partition calculations. This chapter describes experimental and modeling methodology.

3.4.1. Reduction part

Unbeneficiated Kiruna iron ore was used with 0.7% of P; see the chemical composition in **Table 9**; the particle sizes are summed up in **Table 10**. Applying such a high P material facilitates the detection in the subsequent SEM-EDX analysis. Two DRI samples were prepared to simulate a shaft furnace and a fluidized bed reactor.

Table 9: Chemical composition of Kiruna ore samples, before and after oxidation / wt.-%

	Fe_{tot}	Fe^{2+}	SiO_2	Al_2O_3	CaO	MgO	MnO	P
raw	59.5	15.3	7.05	1.13	3.03	2.00	0.17	0.70
oxidized	57.8	0.39	6.84	1.11	2.97	1.96	0.17	0.68

Table 10: particle sizes of the mixtures

sample	amount / %	size min / mm	size max / mm
lump	50	10.0	12.5
	50	12.5	16.0
fine	50	0.15	0.25
	50	0.25	0.50

- DRI 1 – Lump ore
 - Kiruna raw lump ore, magnetitic; composition, and particle sizes see **Tables 9** and **10**.
 - Reduction of 500.6 g in the VRF (see chapter 3.2) at 900°C with 25 NI/min H_2 .
 - **Figure 21** shows the test conditions and the progress of mass, RD, and MD.
 - The final reduction degree is 85.9%, and the final metallization degree is 80.0%, respectively (determined based on the mass balance).

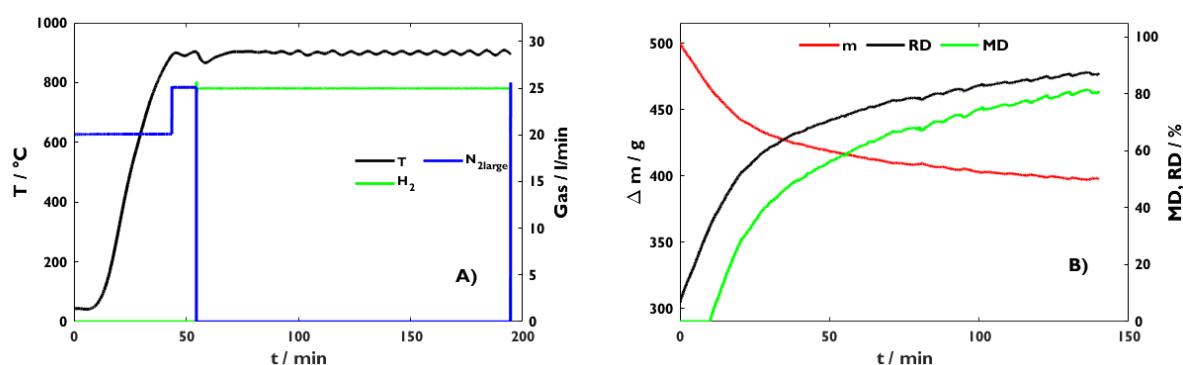


Figure 21: A) Conditions (T , N_2 , H_2) during reduction of DRI 1 – lump; B) m , RD, and MD during reduction of DRI 1 – lump

- DRI 2 – Fine ore
 - Grinded Kiruna lump ore, composition, and particle sizes see **Tables 9** and **10**.

- Preoxidation at 1000°C for 8 h (see chapter 3.2); composition of the oxidized material see **Table 9**. That is necessary to guarantee fluidizability. Another advantage is the improved reducibility of the hematite.
- Reduction in the 68 mm Fluidized bed reactor (see chapter 3.2) at 650°C with 12 NI/min N₂ and 16 NI/min H₂.
- **Figure 22** shows the test conditions and the progress of mass, RD, and MD. Unfortunately, the mass signal shows many fluctuations. Probably, the lower thermocouple touched the ground during the test; see the reactor in **Figure 19**. Due to the thermal expansion, a vertical force was generated, leading to an increased mass loss superimposed with fluctuations. Therefore, these curves cannot be used to evaluate the reduction progress. Another explanation for this effect could be a partial defluidization of the material.
- The final reduction degree is 93.0%, and the final metallization degree is 89.6%, respectively (determined based on the mass balance).

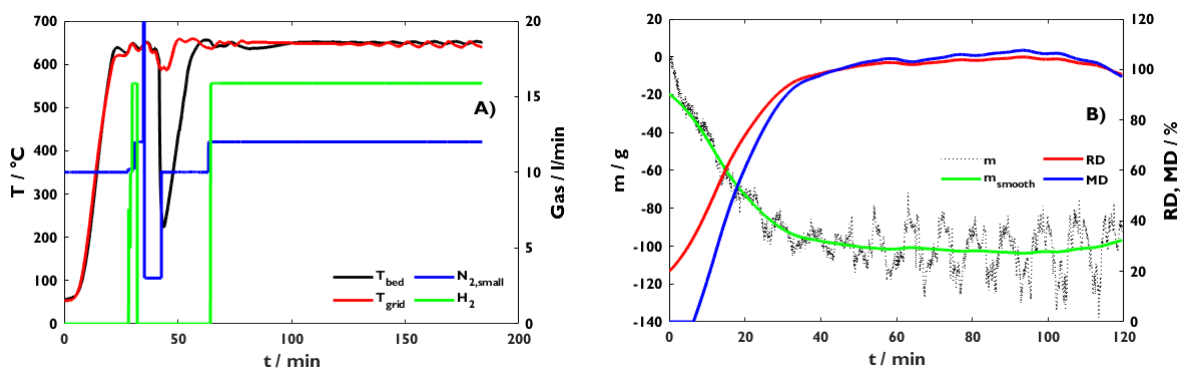


Figure 22: A) Conditions (T , N_2 , H_2) during reduction of DRI 2 – fine; B) m , RD, and MD during reduction of DRI 2 – fine

By using scanning electron microscopy (SEM) with energy dispersive x-ray (EDX) detection, the behavior of the apatite particles during reduction is studied. Therefore, random samples of raw-, oxidized-, and reduced fines, as well as raw- and reduced lump material, are embedded, ground, and polished. Then digital- and scanning electron microscopy are performed. All samples were sputtered with a carbon layer which enables accurate results.

3.4.2. Modeling part

Target of the modelling part is to extend the knowledge from the reduction to the behavior in the subsequent melting step. Therefore, equations 8 and 9 as well as thermodynamic calculations are applied to illustrate the partition of phosphorus between slag and metallic melt. **Table II** summarizes the boundary conditions for the calculated partitions. (MgO) and (Al₂O₃) are set as constant values; (FeO) according to the given range; no Fe³⁺ is considered. Since equation 8 depends on (%P₂O₅), a hypothetical value is calculated with 2 iterations, assuming an initial [%P]₀ content of 0.3%, representing high phosphorus hot metal.

Table II: Boundary conditions for the phosphorus partitions, shown in **Figures 74 to 77**

	EAF/BOF	Hismelt
B ₂ range	1.6-3.5	1-2
(%FeO) range / wt.-%	10-30	1-5
T / °C	1600	1600

(%Al ₂ O ₃) / wt.-%	5	5
(%MgO) / wt.-%	10	10

Both approaches are calculated because LP and LP* are not directly comparable.

Equations 15-17 solve Equation 6 concerning [%P].

$$[\%P]_0 = [\%P] + (\%P) \Leftrightarrow (\%P) = [\%P]_0 - [\%P] \quad 15$$

$$\Leftrightarrow L_P = \frac{[\%P]_0 - [\%P]}{[\%P]} \quad 16$$

$$\Leftrightarrow [\%P] = \frac{[\%P]_0}{1 + L_P} \quad 17$$

Equations 15, 18-20, and the quadratic equation solve Equation 7. M_P and M_{P₂O₅} represent the molar masses of P and P₂O₅.

$$L_P^* = \frac{(\%P) \cdot 2 \cdot M_P}{M_{P_2O_5} \cdot [\%P]^2} \quad 18$$

$$\Leftrightarrow L_P^* = \frac{2 \cdot M_P}{M_{P_2O_5}} \cdot \frac{[\%P]_0 - [\%P]}{[\%P]^2} \quad 19$$

$$\Leftrightarrow L_P^* \cdot [\%P]^2 + \frac{2 \cdot M_P}{M_{P_2O_5}} \cdot M_P - \frac{2 \cdot M_P}{M_{P_2O_5}} \cdot [\%P]_0 \quad 20$$

In order to relate this information to thermodynamic conditions, equilibrium is calculated using FactSage™ 8.2 software and FToxid and FactPS databases. **Figure 23** shows the corresponding input scheme for B₂=1 and (FeO) = 0.3 g. A system of 100 g of liquid metal in contact with 30 g slag was defined:

- 99.9 g Fe_{liq} with 0.1 g [P]
- 30 g slag with
 - 3 g MgO
 - 1.5 g Al₂O₃
 - 0.3 g < (FeO) < 9 g
 - 1 < B₂ < 3.5
- T = 1600°C

Quantity(g)	Species	Phase	T(C)	P(total)**	Stream#	Data
99.9	Fe				1	
* 0.1	P				1	
* 3	MgO				2	
* 1.5	Al2O3				2	
* 12.6	CaO				2	
* 12.6	SiO2				2	
* 0.3	FeO				2	

Figure 23: FactSage™ input scheme

After the calculations, the results are imported into Matlab R2020b and fitted with cubic-spline-surface fits. **Figure 24** compares the two-dimensional cubic-spline fit with the calculated values and a polynomial fit with degree 4. Although both approaches fit the points well, the cubic-spline algorithm is preferable since polynomial fits can be sensitive to oscillations.

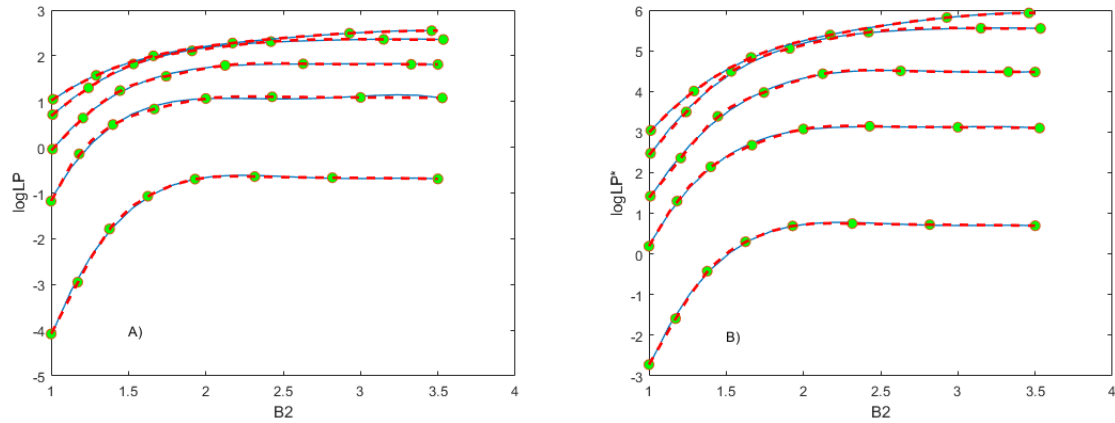


Figure 24: Goodness of polynomial fit; A) L_P ; B) L_P^* ; different lines represent different FeO-contents; circles: calculated values, solid blue lines: polynomial fit, degree 4; red dashed line: cubic-spline fit

3.5. Interaction between DRI and liquids (results see chapter 6)

Two test series were performed using a similar method. Series I was performed in the Vertical Tube Furnace Gero® HTR-V100-250/17, shown in **Figure 25**. It is equipped with an Alumina furnace chamber capable of reaching temperatures $>1700^\circ\text{C}$.



Figure 25: Gero® vertical tube furnace

[140] precisely describes the procedure for test series I; **Figure 26-A** shows the corresponding setup. An alumina tube connects the DRI sample with a pneumatic cylinder which dips the sample into the melt. Based on the results of series I, a second series was performed using the induction furnace, see chapter 3.3. The pellet was also fixed on an alumina tube. A graphite crucible was used instead of the alumina crucible, with the pellet dipped by hand. That decreased the handling time and allowed for more dipping tests. **Figure 26-B** shows the test setup; **Table 12** describes the corresponding components. While the goal of series I is to investigate the interaction between sponge iron and liquid phases in general, series II is more focused on the smelter. Looking at **Figure 10** and **Figure 11**, and considering that the DRI density is significantly lower than that of hot metal, the contact with low iron oxide-containing slag is expected to be decisive. Therefore, a dipping time variation in addition to series I was performed.

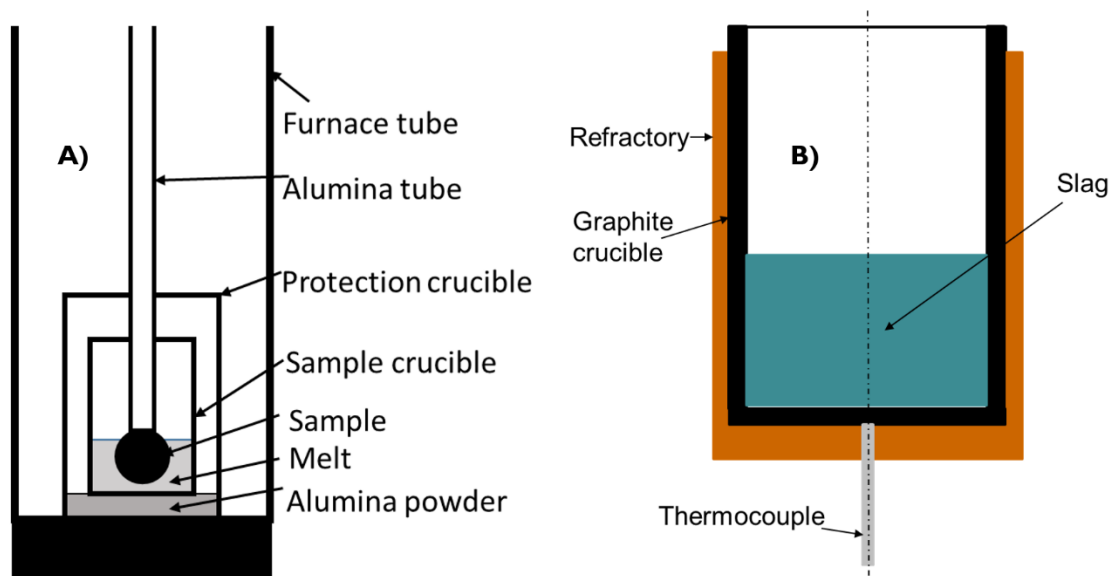


Figure 26: Test setup A) series I^[140]; B) series II

Table 12: Test setup components^[140]

Series	Component	Dimensions / mm	Material	Comment
I	Protection crucible	Ø117.6 x Ø108.6 x 180	Al ₂ O ₃	
I	MgO sample crucible	Ø48.5 x Ø36.0 x 105	MgO	for EAF slag test
I	Alumina sample crucible	Ø49.5 x Ø42.6 x 68.7	Al ₂ O ₃	for ULC, HM, and SAF slag tests
I & II	Wire	Ø1	Mo	
I & II	Screw	“Spax” 2.5 x 12	steel	
I	Furnace chamber	Ø180	Al ₂ O ₃	
II	Graphite crucible	Ø110 x Ø80 x 65	C	

After dipping, the samples were pulled out and quenched in liquid nitrogen. Most melt temperatures were separately measured using a Heraeus Type S thermocouple. Nevertheless, these measurements were impossible in the MgO crucibles due to their smaller inner diameter. Series II was done without temperature measurements. On the one hand, the location of the furnace thermocouple, see **Figure 26**, provides an accurate value. Furthermore, no exact measurement is possible since the induction furnace would influence the thermocouple. After the tests, the samples were analyzed optically and metallographically^[140].

Table 13 shows the raw pellet compositions; two similar BF-grade pellets are applied. **Table 14** gives the carburization temperatures and the sample compositions. The pellets are reduced at 900°C with 25 Nl/min H₂ in the VRF, described in chapter 3.2. Selected pellets are carburized in the VRF at 750 and 800°C using 4 Nl/min CH₄. **Figures 27-29** document the sample preparation processes. Unfortunately, the carburization data for sample II-C800.2 was lost, but since LECO analyses were performed, the final carbon content is precisely known.

Table 13: Pellet compositions applied in test series I and II / wt.-%

Series	Fe _{tot}	Fe ₂ O ₃	FeO	CaO	SiO ₂	Al ₂ O ₃	MgO
I	64.9	92.5	0.37	0.48	4.55	0.84	0.45
II	64.8	92,1	0.538	0.48	5.79	0.47	0.60

Table 14: DRI compositions; C... measured by LECO; Fe_{met}, Fe²⁺... measured by titration methods; Fe³⁺... determined by mass balance with Fe_{tot}; *based on mass balance; *xcarburization time lost

Series	Sample	T _{Carb} / °C	t _{Carb} / min	Fe _{met}	Fe ²⁺	Fe ³⁺	C	MD / %
I	0%C	-	-				0	88.4*
	C750	750	20	81.35	5.01	0.01	1.79	94.2
	C800	800	25	82.46	2.82	0.00	3.71	96.7
	HBI	-	-	84,6	4,1	2,3	2,00	93,0
II	0%C.2	-		78,24	8,50	0,15	0	90
	C800.2	800	-x	79,62	2,79	0,23	2,80	96,3

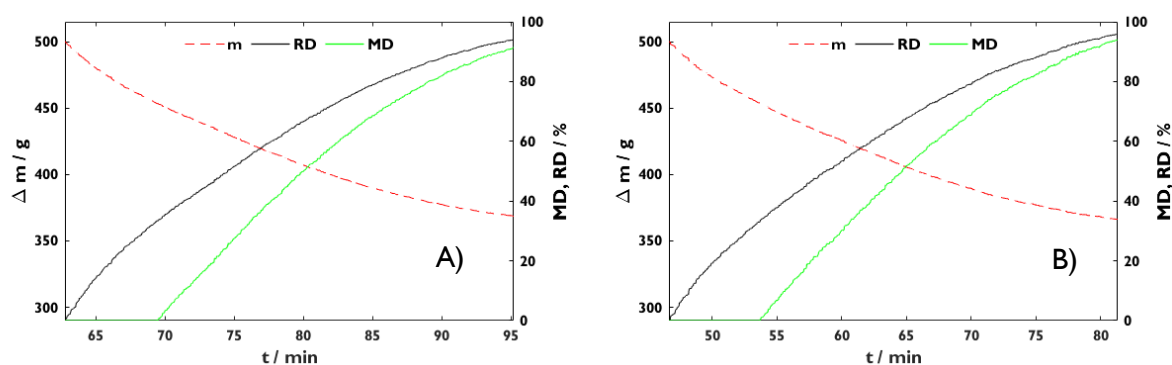


Figure 27: Prerduction of pellets A) I-0%C; B) Prerduction for I-C750 and I-C800; just reduction period shown => timescale does not start at 0

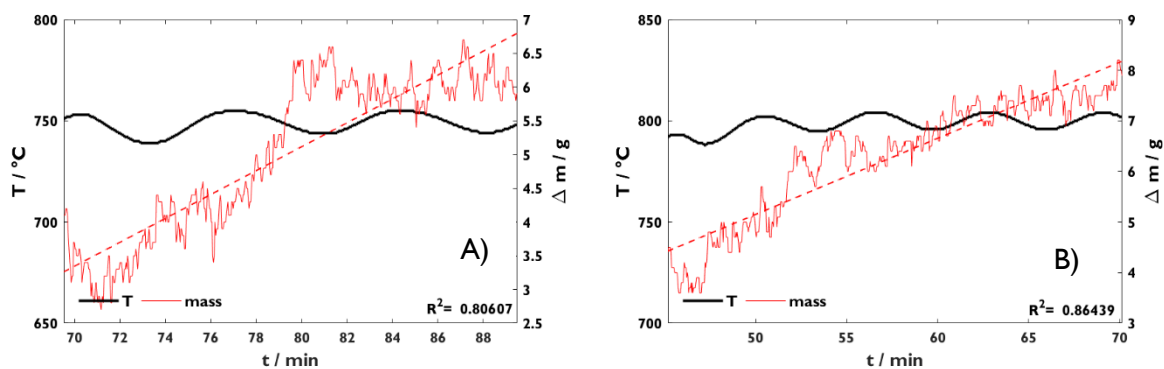


Figure 28: Carburizing of series I samples A) I-C750, and B) I-C800; just carburization period shown => timescale does not start at 0

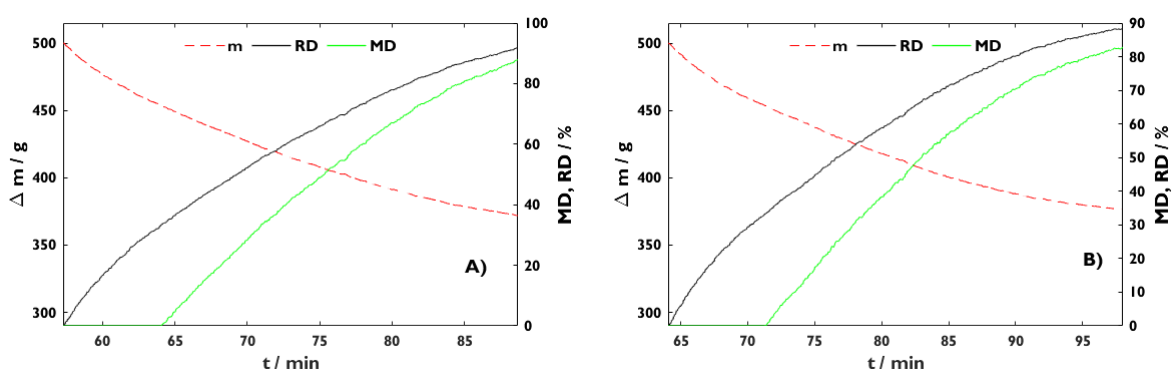


Figure 29: Prereduction of pellets for series II; A) II-0%C.2, and B) II-C800.2; just reduction period shown => timescale does not start at 0

The ULC steel, as well as the HM samples, were residuals from former projects. **Table 15** and **Table 16** list the respective compositions.

Table 15: ULC composition; determined by optical emission spectroscopy (OES)^[140]

C	Si	Mn	Al	Ti	S	P	Ni	Cu	Cr
0.007	<0.001	0.146	0.028	0.079	0.015	0.009	0.011	0.005	0.027

Table 16: HM composition; determined by OES^[140]

C	Si	Mn	S	P
4.6	0.4	0.6	0.004	0.07

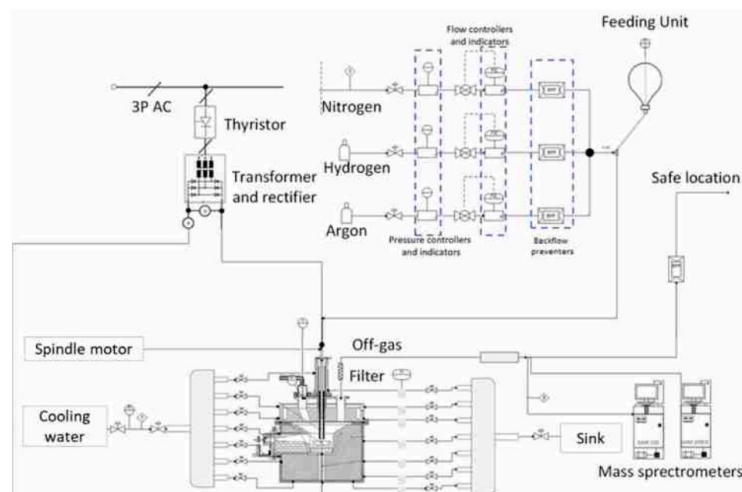
The slags were mixed from the oxides in **Table 8** and premelted according to the procedure in chapter 3.3 in MgO crucibles. **Table 17** lists the slag compositions before and after each test.

Table 17: Slag compositions determined by inductively coupled plasma optical emission spectroscopy (ICP-OES); *by SEM-EDS^[140]

	I-SAF		I-EAF		II-SAF	
	before test	after test	before test	after test	before test	after test*
CaO	40,1	39,4	27,2	18,8	43,9	43,3
SiO ₂	39,8	39,1	21,2	13,4	36,3	36,9
Al ₂ O ₃	11,3	12,9	8,20	9,73	10,8	10,8
MgO	8,02	7,80	9,88	31,2	7,8	8,4
Fe	0,62	0,62	26,1	20,9	0,71	0,47
B2	1,01	1,01	1,28	1,40	1,2	1,2

3.6. Arc melting behavior (results see chapter 7)

The arc melting tests were performed using the hydrogen plasma smelting reduction reactor (HPSR); see the flowsheet in **Figure 30**. This facility is usually applied for smelting reduction tests. However, operated under inert conditions, it can be considered a small-scale electric arc furnace. The tests were done with a hollow graphite electrode and a steel crucible, described in ^[141], as the bottom anode. The furnace has an Axis-Q1775 camera system from Axis Communication AB, Sweden, a GAM 200 mass spectrometer from Pfeiffer Vacuum Technologies, Vienna, and a HOBO UX120-006M 4-channel analog logger. During the test, these devices allow monitoring of the electrical data, offgas composition, and electric arc.

**Figure 30:** Flowsheet of the hydrogen plasma smelting reduction facility^[142, 143]

The first test is considered a pretest to check the possibility of continuous DRI feeding. Nevertheless, this feed material is stuck in the hollow graphite electrode. Therefore, the following tests were performed batch-wise, with approximately 100 g DRI, see **Figure 31**. The reactor was flushed with 2 Nl/min nitrogen. The Transformer current was set to 100 A at the beginning, and the stepwise

decreased, depending on the transformer temperature and Voltage, using a silicon-controlled rectifier (SCR) controller. The electrode distance was adjusted according to the meltdown of the charged material.



Figure 31: Batchwise pellet feed

One test was performed with the addition of slag-forming oxides. Technically pure CaO and MgO with 99% cleanliness were continuously fed in this case. The detailed masses can be found in the mass balances of the tests in chapter 7.

Iron ore of Canada (IOC) pellets and fines, as well as Poltavsker BF-pellets, are used for the arc melting tests. **Table 18** lists the chemical compositions and particle sizes, respectively.

Table 18: Composition of the iron ores; *determined by mass balance calculation, wt.-%

	Fe _{tot}	Fe ²⁺	SiO ₂	Al ₂ O ₃	CaO	MgO	MnO	TiO ₂	size / mm	Ore
DR-pellets	67.5	0.19	1.94	0.32	0.87	0.35	0.21	0.06	10-12.5	IOC
Fines-raw	66.8	6.19	-	-	-	-	-	-	D50 = 0.1	IOC
Fines-oxi*	66.4	1.87	-	-	-	-	-	-	D50 = 0.1	IOC
BF-pellets	64.8	0.42	5.79	0.47	0.48	0.60	0.06	0.04	12.5-16	Poltavsker

The samples are prepared as follows:

- 0%C-DRI-DR
 - Pellets acc. to **Table 18** “DR-pellets”
 - Reduction of 500.4 g in the VRF (see chapter 3.2) at 900°C with 25 NI/min H₂.
 - **Figure 32** shows the progress of mass, RD, and MD.
 - The final reduction degree is 92.8%, and the final metallization degree is 89.4%, respectively (based on the mass balance).

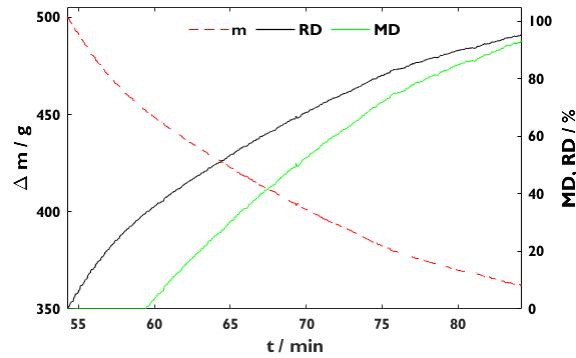


Figure 32: *m*, RD, and MD during reduction of 0%C-DRI-DR; just reduction period shown => timescale does not start at 0

- 0%C-DRI-BF
 - Pellets acc. to **Table 18** “BF-pellets”
 - Reduction analog to 0%C-DRI-DR
 - The final reduction degree is 93.2%, and the final metallization degree is 90.2%, respectively (based on titration analysis).
- C-DRI-DR
 - Pellets acc. to **Table 18**
 - Reduction of 500.6 g in the VRF (see chapter 3.2) at 900°C with 25 NI/min H₂.
 - Carburization of the material in the VRF at 800°C with 8 NI/min CH₄.
 - **Figure 33** shows the progress of mass, RD, and MD, as well as the mass evolution during the carburizing procedure
 - RD after reduction is 96.2%, and the metallization degree is 94.4%, respectively. The carbon content is ≈2.1% (based on the mass balance). The high initial RD was chosen to avoid extensive reduction during carburizing.

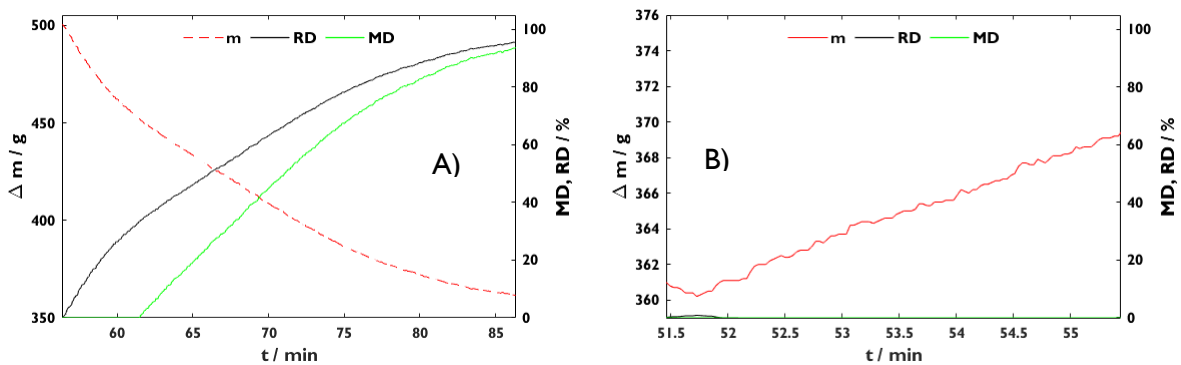


Figure 33: A) RD and MD during reduction of C-DRI-DR; B) mass evolution during carburizing; just reduction and carburization periods shown => timescale does not start at 0

- 0%C-DRI-Fine
 - IOC fine ore => composition see **Table 18**
 - Preoxidation at 700°C for one night; composition of the oxidized material see **Table 18**. A conventional heat treatment furnace is used for this procedure, described more precisely by Spreitzer^[7].

- Reduction in the 68 mm fluidized bed reactor (see chapter 3.2). $T=600^{\circ}\text{C}$; $\text{N}_2=6\text{ NI/min}$; $\text{H}_2=15\text{ NI/min}$
- **Figure 34** shows the progress of mass, RD, and MD.
- The final reduction degree is 92.8%, and the final metallization degree is 89.4%, respectively (based on the mass balance).

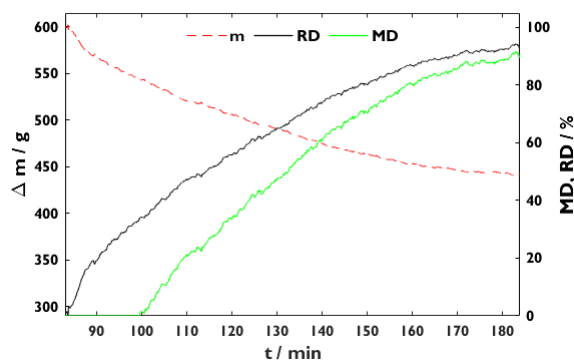


Figure 34: m , RD, and MD during reduction of 0%C-DRI-Fines; just reduction period shown => timescale does not start at 0

After the tests, photographs are made. Then they are filled with embedding mass, cut according to the scheme in **Figure 35** and prepared metallographically. 1% Nital etching for 5-20 s improves the contrast between crucible and molten sample for digital microscopy.

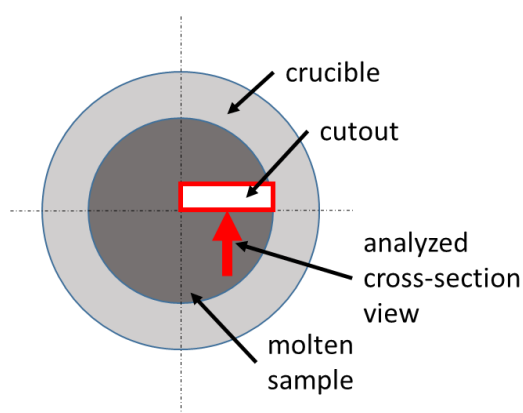


Figure 35: Location of the cutted cross-sections

3.7. Slag Foaming (results see chapter 8)

Slag foaming was investigated in two ways. First, a method to experimentally investigate slags was developed. Its methodology is described in the scope of this chapter. However, these experiments only provide snapshots of fixed slag compositions. Therefore, a sensitivity analysis was performed in a second step, based on published data on the slag foaming index concept, presented in chapter 2.3.2. While this observation provides an ideal possibility to compare the experiments from this thesis to published test results, it further enables the extrapolation from fixed slag compositions to slag paths with varying compositions, e.g., how does the foamability change with varying (FeO) content? As the derivation of the subparameters (density, surface tension, viscosity) can be considered a result themselves, these calculations are summed up in chapter 8.

The induction furnace from chapter 3.3 was used for the slag foaming tests. **Figure 36** shows the corresponding test setup. The experiments went as follows.

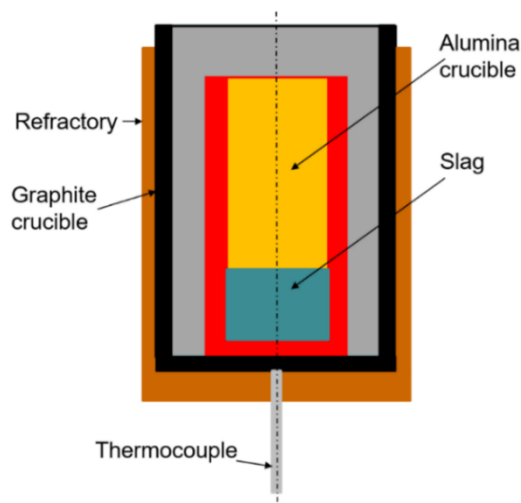


Figure 36: Test setup for slag foaming tests

- Slag mixtures without FeO are premelted in a graphite crucible according to the procedure from chapter 3.3. The composition of these two premelts can be found in **Table 19**.

Table 19: Composition of premelts for slag foaming tests in chapter 8, determined by SEM-EDX

	Premelt 1	Premelt 2
CaO	35.6	44.5
SiO₂	29.9	42.3
Al₂O₃	15.5	5.6
MgO	19.0	7.5

- Premixing of the premelt, oxides, and prereduced iron ore to reach the target slag composition; a piece of ULC steel was added to stabilize Fe²⁺ during the tests. The mixtures, normalized for 100 g, are listed in **Table 20**. EAF represents EAF-like, SAF (Submerged Arc Furnace) smelter-like slags.

Table 20: Slag mixtures for 100 g; Premelt no. according to **Table 19**

	SAF-1	SAF-2	EAF	EAF-sat
Premelt no.	2	2	2	1
Premelt mass / g	94.1	83.8	48.1	57.9
CaO-95 / g	0.3	0	13.1	11.1
SiO₂-99 / g	0	0	0	0
Al₂O₃-99 / g	0	6.8	3.3	0
MgO-99 / g	0	0	6.0	0
FeO-prered. / g	5.5	9.4	29.4	31.0

- Heat the mixture to 1600°C and hold for 15 min. The location of the thermocouple and the fact that the ULC sheets are not liquefied indicate that the crucible temperature is lower than 1600°C. It can be expected that the crucible temperature is approx. 50°C below the furnace temperature.
- Add carbon carrier (t_0) and mix for 10 s using a molybdenum wire. Calcined petrol coke, with $C_{\text{fix}}=99\%$ and a particle size between 0.5 and 1 mm, was applied. The amount was adjusted according to a total FeO-reduction to gain reproducible tests. The high C_{fix} source was selected to minimize the added total mass, making the addition easier and minimizing the influence of by-materials. Keeping the carbon carrier constant is essential, as it influences the foaming behavior due to varying reactivity and wetting^[144, 145].
- Wait for the predefined time. If the foam rises above the crucible, stop the test.
- Quench the crucible in liquid nitrogen. Applying fabric tape once the crucible gets cold enough avoids breakage.
- After the tests, the crucibles are filled with a low-viscosity two-component metallographic mass and cut into halves for further evaluation. For SEM-EDX analysis, smaller samples are necessary. Therefore, selected halves are cut into 40x40 mm² pieces, embedded again, and metallographically prepared. These samples are sputtered with a carbon layer to increase their conductivity.
- Digital microscopy is applied for making images and measuring the foaming height. SEM-EDX enables the possibility to determine the chemical composition and its distribution after foaming.

Echterhof and Pfeifer^[146] did a comparable test series. Their target was the investigation of different biomass-based carbon sources regarding their foaming properties. Two aspects of their work differ from these experiments: They premixed slag and carbon carrier before heating the crucibles, which may lead to low-temperature reactions such as carbon oxidation or reduction of iron oxide with either solid carbon or CO from the preoxidized carbon. Further, after the test, the authors measured the foaming height by the frozen slag layer, which is a good indicator. However, the author estimates the method in this thesis to be better for the following reasons: Quenching the sample superficially freezes the hot condition. As can be seen in chapter 8, **Figure 110**, the foam forms a meniscus. Therefore, the wetted crucible surface does not represent the maximum foaming height. Further, it is unclear which initial height Echterhof and Pfeifer considered. Although the method based on the calculated density described below may not be completely accurate, it provides good reproducibility. Last but not least, the cross-sections offer the possibility of metallographic analyses and an EDX-based distribution of the composition.

Table 21 lists the four target slag mixtures. While the SAF slags are liquid above approx. 1380°C, the slag EAF-sat is saturated with MgO and shows Magnesiowustite precipitations, as seen in **Figures 37** and **38**. Additionally, the slag-specific physical parameters are given in **Table 21**. It must be mentioned that the volume fraction ϵ was approximated with the mass fraction. Since the actual density of the precipitations is difficult to determine, this is considered a valid approximation.

Table 21: Target slag compositions for slag foaming tests; ρ , σ acc. to^[147]; η_1 , ϵ , T_{Liquidus} acc. to FactSage™ 8.2; η_2 acc. to Urbain model^[123, 129]; * Σ for bath smelting slags; * Σ for MgO_{sat} slags; ✓ for CaO based slags ... see **Table 6**; Mo acc. to equation 12

wt.-%	SAF-1	SAF-2	EAF-sat	EAF
CaO	43.9	41.9	31.6	35.0
SiO ₂	39.6	38.0	19.4	22.0

Al_2O_3	4.89	4.90	9.10	8.00
MgO	6.00	5.70	11.9	9.00
FeO^*	5.62	9.50	28.0	26.0
$\text{B2} / \text{l}$	1.1	1.1	1.6	1.6
$T_{\text{Liquidus}} / ^\circ\text{C}$	1399	1381	1681	1529
$\rho / (\text{kg}/\text{m}^3)$	2855	2925	3439	3361
$\epsilon / \text{wt.}\%$	0	0	3.11	0
$\sigma / (\text{N}/\text{m})$	0.496	0.502	0.568	0.560
$\eta_1 / (\text{Pa}\cdot\text{s})$	0.107	0.093	0.038	0.041
$\eta_{1, \text{eff}} / (\text{Pa}\cdot\text{s})$	0.107	0.093	0.045	0.041
$\eta_2 / (\text{Pa}\cdot\text{s})$	0.223	0.211	0.143	0.148
$\eta_{2, \text{eff}} / (\text{Pa}\cdot\text{s})$	0.223	0.211	0.168	0.148
Mo / l	$3.69 \cdot 10^{-6}$	$1.97 \cdot 10^{-6}$	$6.11 \cdot 10^{-8}$	$4.69 \cdot 10^{-8}$
Σ / s	0.327*	0.279*	1.01 \times	0.202 \checkmark

Some aspects can be noticed in **Figures 37** and **38**. The SAF diagram's right phase area (slag_{liq}) can be neglected. Fe_{met} balances the composition to 100%, and above $(\text{FeO}) \approx 0.096$, 100% is already reached. Further, this slag is totally liquid in a wide range, meaning an independency of the phases when changing the FeO content or the temperature in practically relevant ranges. In the EAF case, fluctuations in MgO can move the phases from totally liquid to magnesiowustite particles containing slag. Nevertheless, the slag is resilient against fluctuations in FeO, highlighted by the nearly horizontal phase border. This appearance corresponds to the exemplary isothermal solubility diagram shown in **Figure 14**.

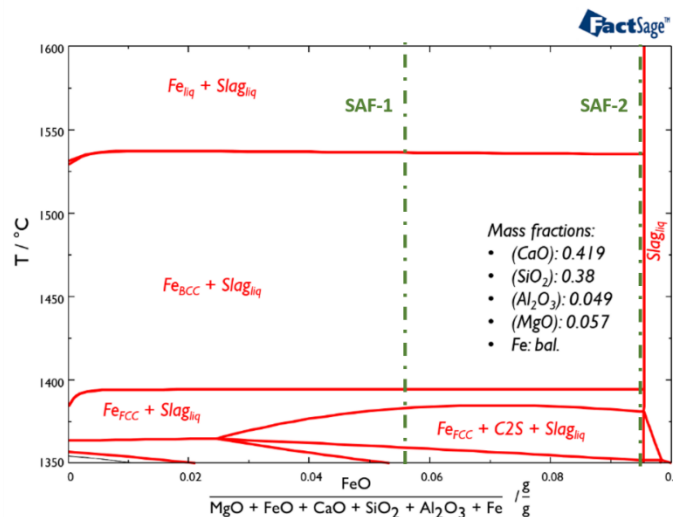


Figure 37: Phase diagram of SAF (smelter) slags, calculated by FactSage™ 8.2

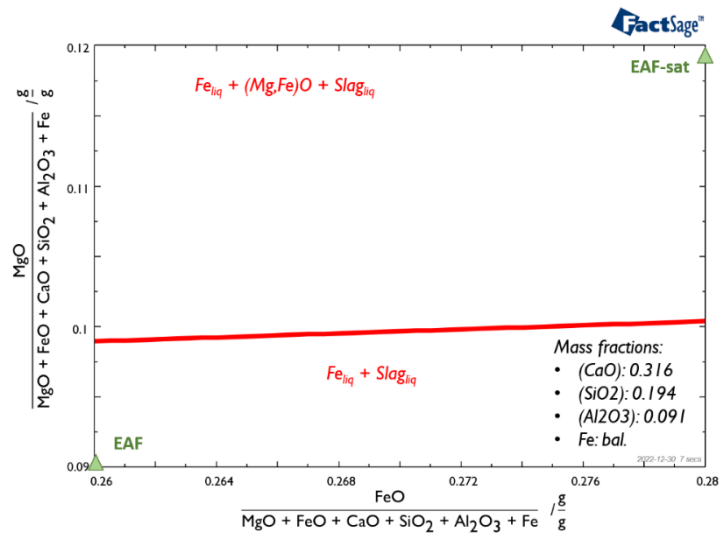


Figure 38: Phase diagram of EAF slags, calculated by FactSage™ 8.2; $T = 1600^{\circ}\text{C}$

The foaming volume^[146] is one characteristic to compare the foaming behavior. Therefore, digital microscope images were applied to measure the average foaming height, see **Figure 39**. Then the cylindrical volume after foaming was calculated. The increase based on the initial volume according to equation **21** was determined and evaluated.

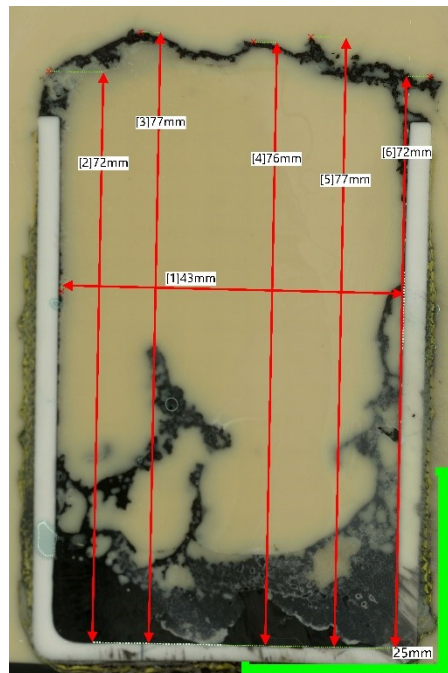


Figure 39: Foaming height measurement

$$\frac{\Delta V}{V_0} = \frac{V_1 - V_0}{V_0}$$

21

3.8. Sample Investigation Techniques

The evaluation of samples was performed using the following devices:

- Sony Alpha 6000, with Sigma Contemporary 30 mm lens – for making macroscopic sample images
- Keyence VHX 7000 digital microscope – for optical microscope evaluations
- SEM Jeol 7200F with an Oxford Instruments EDX detector for scanning electron microscopy (SEM) and energy dispersive x-ray analysis (EDX)

4. Definition and comparison of processing strategies

The first in chapter 1.3 defined targets is to find a steelmaking route that is lean in CO₂ emissions, capable of processing DRI from BF-grade iron ores, and producing a recyclable slag as a by-product. Based on this target, three exemplary routes are defined. **Figure 40** shows the associated flowsheet.

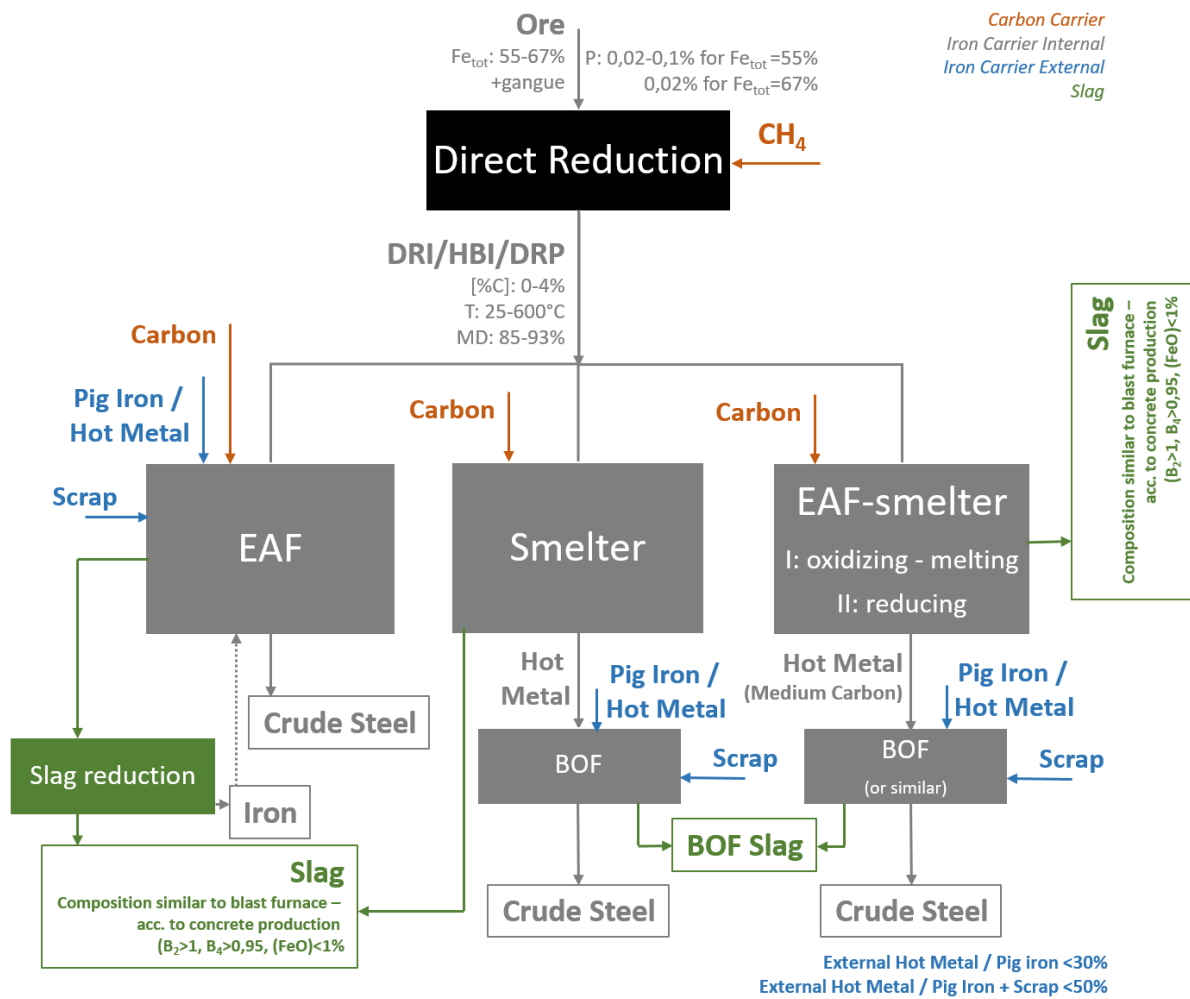


Figure 40: Flow sheet for the three defined melting strategies

In the following, the term “route” describes the processing sequence, either EAF, smelter-BOF, or EAF-smelter-BOF. The term “case” describes various raw material mixtures of DRI/DRP, scrap, and pig iron from a separate blast furnace. The DRI/DRP/HBI composition is defined based on a direct reduction shaft. The following variations were made:

- DRI/DRP carbon content from 0 to 4%

- b. Fe_{tot} in the iron ore from 55.6 to 67.2%; reduced to a metallization degree between 85 and 95%
- c. DRI/DRP charging temperature in the subsequent aggregate is either 25 or 600°C
- d. Phosphorus content of either 0.02 or 0.1%
- e. Mixtures with scrap and pig iron from a blast furnace

The first route is the electric arc furnace (EAF) which melts and refines the mixture to crude steel in one step. The Sankey diagram in **Figure 41** shows the material flows. The sponge iron is charged with scrap and pig iron, as well as dolomite and lime additives, carbon for slag foaming, and oxygen for refining. The products are crude steel, as well as slag and off-gas. The slag reduction step is not considered in the calculations. The calculation sequence is shown in **Figure 16**, and the additive, ore, and external iron carrier compositions are listed in **Tables 22 to 24**.

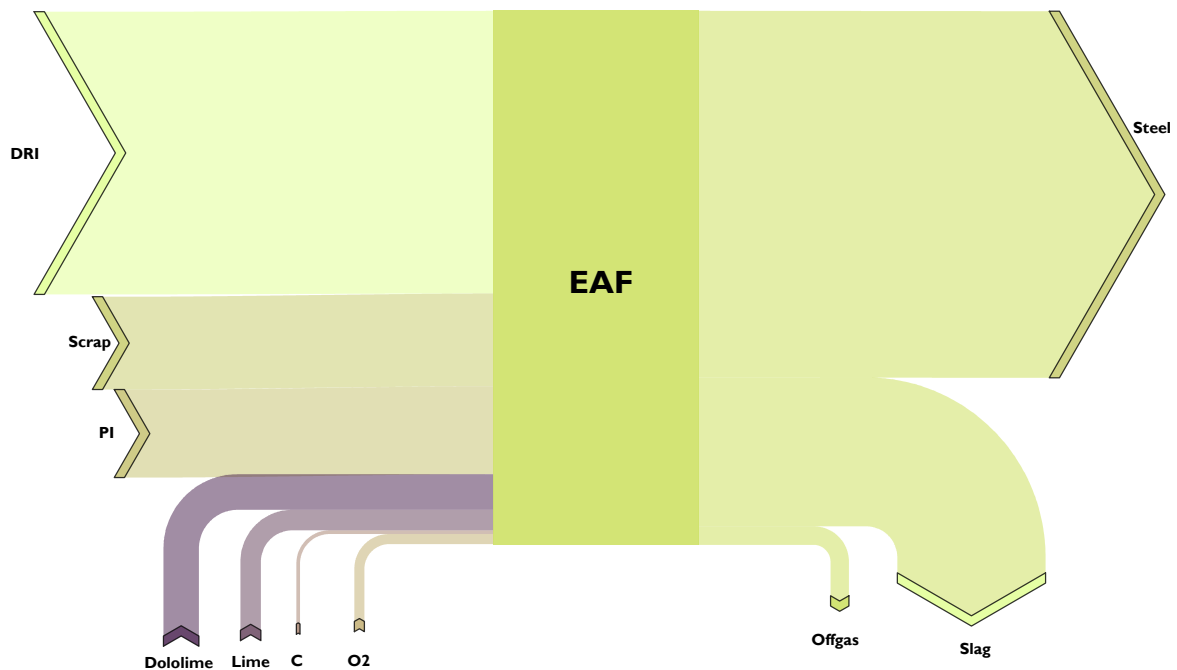


Figure 41: Sankey diagram of the mass flow for route 1

Table 22: Additive compositions

Additive	CaO	SiO ₂	Al ₂ O ₃	MgO	CO ₂	C	O ₂
Lime	95,2	1,5	2,3		1,0		
Dolomite	57,0	2,5	0,8	39	0,7		
Quartz		100					
Carbon						100	
O ₂							100

Table 23: External iron carrier compositions / wt.-%

Iron carrier	Fe	C	Mn	Si	Al	SiO ₂	Al ₂ O ₃	MgO	FeO	P
Scrap	94,9	0,35	0,6	0,5	0,02	0,8	0,9	0,2	0,6	0,1
Pig iron	93,5	4,5	0,8	0,25						0,1

Table 24: Ores considered for the calculations / wt.-%

Ores	Fe _{tot}	P	FeO	Fe ₂ O ₃	CaO	SiO ₂	Al ₂ O ₃	MgO	MnO
„DR-Pellet“	67,2	0.02	0,23	95,9	0,94	1,7	0,5	0,06	0,09
„BF-Pellet“	64,9	0.02 / 0.1	0,37	92,5	0,48	4,6	0,84	0,45	0,13
„Sinter“	55,6	0.1	9,6	68,8	7,89	6,33	1,80	2,40	1,00

Figure 42 gives the Sankey diagram for the two-step routes EAF-smelter – BOF and smelter – BOF. smelter and EAF-smelter act as melting, deslagging, and final reduction aggregates, producing a hot metal refined in the subsequent BOF. Additives from Table 22 are charged in all aggregates, external iron carriers pig iron, and scrap from Table 23 only in the BOF.

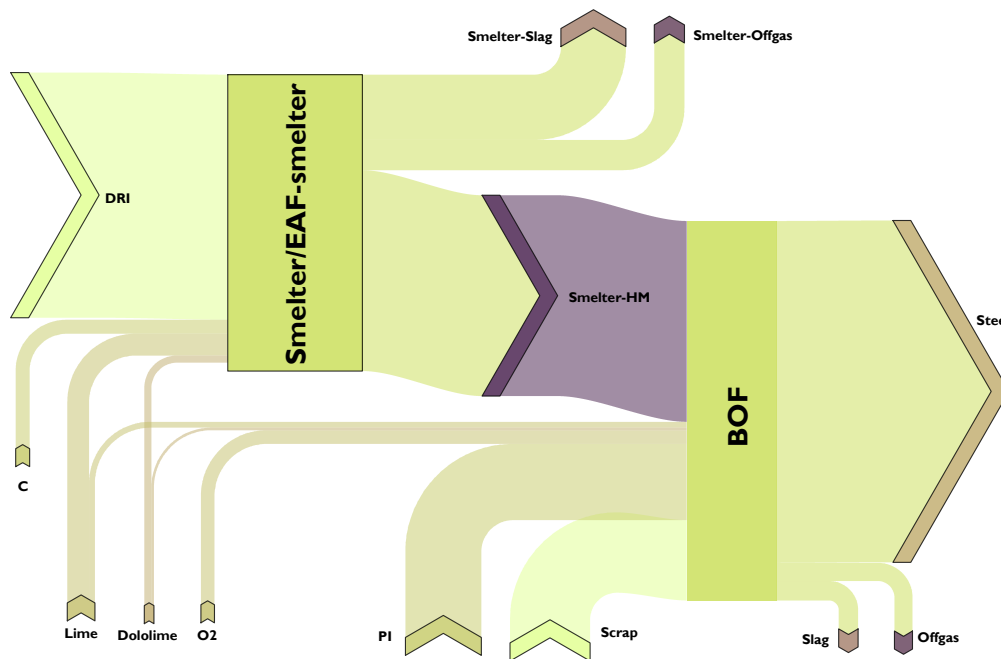

Figure 42: Sankey diagram of the mass flow for routes 2 and 3

Table 25 summarizes the boundary conditions for all four smelting and refining aggregates. While the EAF data was chosen according to state-of-the-art DR-EAF plants, the smelter conditions were defined according to published data from literature^[82, 93, 94], with the slag being similar to conventional BF-slag. Equation 22 defines the slag basicity B_4 . The EAF and the smelter are well-known technologies. However, the EAF-smelter should present a hypothetical new development combining the best of both worlds. It can be considered an EAF-like aggregate with reducing conditions. The thermal losses are

based on literature data. In the EAF case, an intermediate value was chosen; for the smelter, a significantly smaller value was assumed since the prereduction degrees in the literature were significantly lower. The thermal loss in the EAF-smelter was selected higher than in the EAF but lower than in the smelter.

$$B4 = \frac{(\text{wt.}\% \text{CaO}) + (\text{wt.}\% \text{MgO})}{(\text{wt.}\% \text{SiO}_2) + (\text{wt.}\% \text{Al}_2\text{O}_3)} \quad 22$$

Table 25: Boundary conditions for melting aggregates

	EAF	Smelter	EAF-smelter	BOF
Tapping Temperature / °C	1660	1450	1485	1660
B2	1.6	1.1	1.3	3.5
[%C]	<0.05	3.4	2	<0.05
(%MgO)	>10	-	-	7
B4	-	>0.95	-	-
(%FeO)	-	1	5	-
Thermal and electrical losses	100 kWh/t ^[148, 149]	200 kWh/t ^[94, 95, 105]	120 kWh/t	50°C

The BOF tapping temperature is of particular importance. Based on that and the hot metal configuration from smelter or EAF-smelter, the scrap rate is calculated iteratively for each case. Equation 23 defines this parameter itself.

$$\text{Scrap rate / \%} = \frac{m_{\text{scrap}}}{m_{\text{scrap}} + m_{\text{DRI}} + m_{\text{PI}}} \cdot 100 \quad 23$$

Table 26 lists the twelve calculated cases. They were chosen to evaluate the following factors:

- Comparison between DR-Pellet and BF-Pellet (cases 2 and 7)
- Influence of carbon in DRI (cases 1 and 2 as well as 3-5)
- Influence of phosphorus (cases 7 and 9)
- Influence of DRI charging temperature (cases 7 and 8)
- Influence of additional BF pig iron (cases 7 and 10 as well as 11-12)
- Behavior of low-grade sinter (cases 11-12)

Every case has been calculated for all three routes. Two scrap rates are considered to meet the different demands of the smelter and EAF-smelter routes.

Table 26: Calculated case studies

Case	Pellet			DRI			Pig iron / %
	Ore	Fe _{tot} / %	%P	MD	[%C]	T _{DRI} / °C	
1	DR-Pellet	67.2	0.02	93	2	600	0
2	DR-Pellet	67.2	0.02	93	0	600	0
3	BF-Pellet	62.6	0.02	95	4	600	0
4	BF-Pellet	62.6	0.02	95	2	600	0
5	BF-Pellet	62.6	0.02	95	0	600	0
6	BF-Pellet	62.6	0.02	93	0	600	0
7	BF-Pellet	62.6	0.02	85	0	600	0
8	BF-Pellet	62.6	0.02	85	0	25	0
9	BF-Pellet-high P	62.6	0.10	85	0	600	0
10	BF-Pellet	62.6	0.02	85	0	600	20
11	Sinter	55.6	0.10	85	0	600	0
12	Sinter	55.6	0.10	85	0	600	20

4.1. Check with Emirates Steel data

Whether the order of magnitude suits published data from Emirates Steel, a calculation inspired by the data from al Dhaerj^[105] is done. The raw material is the DR-grade pellet from **Table 24**, reduced to DRI with MD=95% and 2.1% carbon.

Table 27 summarizes the results and the published data. Most of the values are in good agreement. The unclear ore composition can explain the deviation in the slag amount. The significant difference in oxygen consumption may result from post-combustion. However, this comparison is only possible for the EAF route since there is insufficient published data for smelter and EAF-smelter.

Table 27: Comparison between published and calculated Emirates Steel data; *coal for 90% hot and 10% cold DRI

	Emirates ^[105]	Emirates calculated
T _{Tap} / °C	1640	1640
O ₂ / Nm ³ /h	34,8	25.4
Lime + Dolomite / kg/t		72.2
Electric. Energy / KWh/t	392	399
MD / %	94,9	95
[C] _{DRI} / wt.-%	2,1	2.1
HDRI/CDRI	HDRI	HDRI
(FeO) / wt.-%	28,3	29.0

(MgO) / wt.-%	10,8	10.6
B2	2,1	2.1
C / kg/t	12.9*	13
Slag / kg/t	145	184

4.2. Results

The scrap rates must be adjusted accordingly as the hot metals from the smelter and the EAF-smelter differ significantly in their carbon and silicon content. **Figure 43-A** shows the resulting scrap rates. The corresponding tapping temperatures, shown in B), are at the demanded 1660°C, with a tolerance of 5°C. The rates correlate with the BOF carbon input; compare the dashed lines and the pig iron rates in **Figure 44**. Further, the scrap rate depends on the iron carrier qualities. Since the value, as defined in equation 23, is based on the total input mass, including the gangue, lower-grade sponge iron input leads to a decreasing scrap addition.

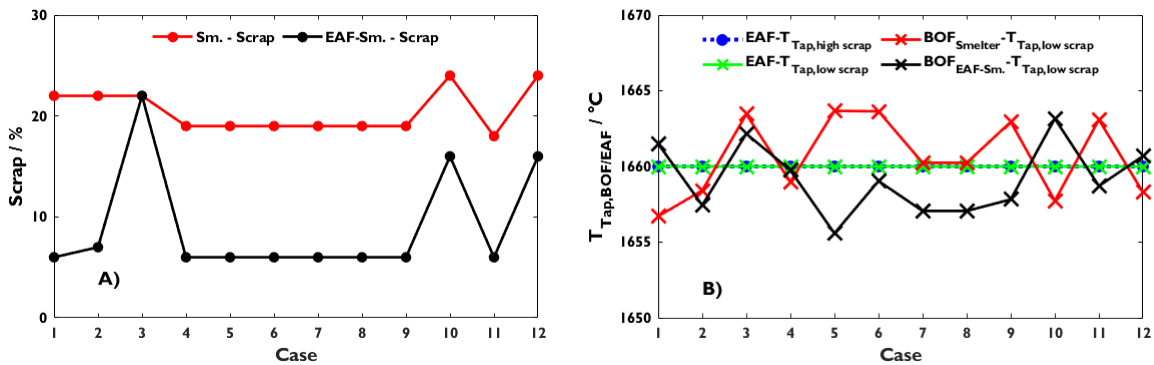


Figure 43: A) Scrap rates; B) EAF/BOF tapping temperatures for the calculated cases (assignment see **Table 26**)

Looking at **Figure 44**, a significant surplus of carbon in case 3 can be noticed, especially in the EAF-smelter case. The residual iron oxide reduction does not consume that surplus and increases the hot metal carbon. Therefore, in case 3, there is no significant difference between the smelter and the EAF-smelter from a mass balance perspective.

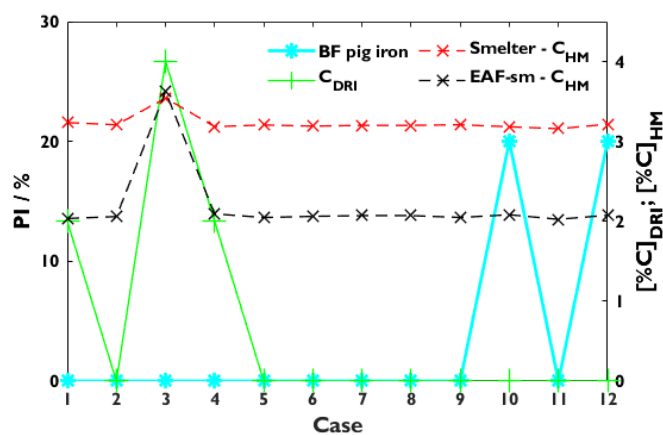


Figure 44: Pig iron rates and carbon contents for the calculated cases (assignment see **Table 26**)

The Mn content correlates with the raw materials; see **Figure 45**. That is particularly striking in cases 10-12, operated with sinter or pig iron. As described above, hot metal Si is artificially capped in smelter and EAF-smelter and not corrected in EAF and BOF. Consequently, the final content was unsurprisingly $\approx 0\%$ in all cases. The carbon levels in crude steels and FeO contents (Figure 46) in the slag are lower in BOF than in EAF.

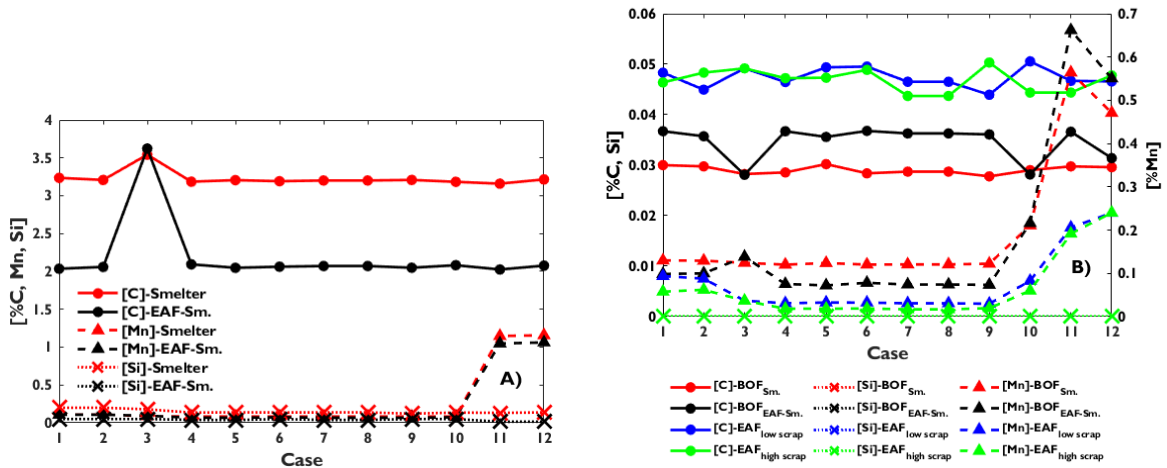


Figure 45: Composition of A) hot metal and B) crude steel (assignment see Table 26)

Figure 46 gives the crucial properties of the smelter and EAF-smelter slags. Considering variations in (MgO), all values reach the target values of the aggregates well. That also applies to the steelmaking slag properties in Figure 47. The only outlier is the BOF basicity of case 12 with EAF-smelter hot metal. Usually, such cases were recalculated with a lower lime addition. In that instant, it was ignored to study the basicity influence on the final phosphorus content, which is described below.

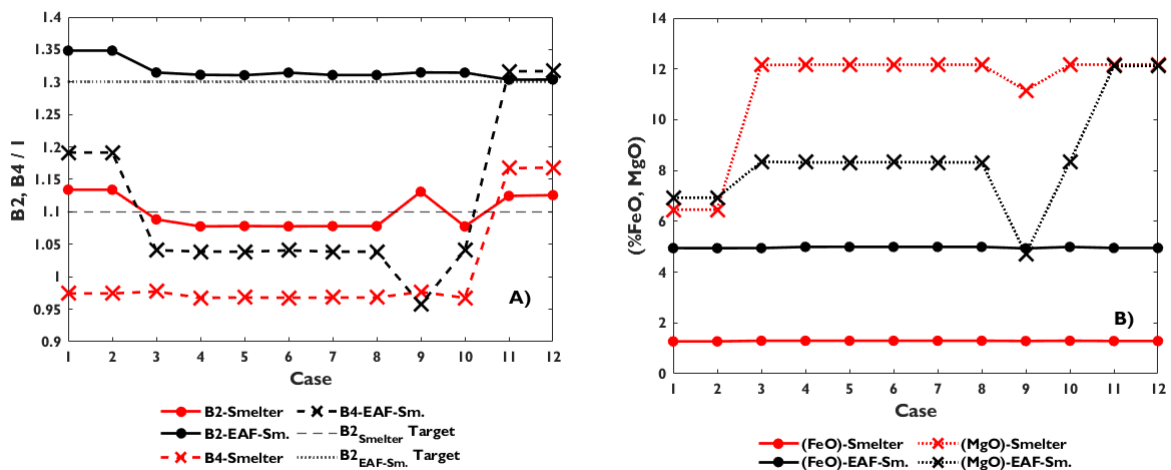


Figure 46: A) Basicities and B) (FeO), (MgO) in smelter slags (assignment see Table 26)

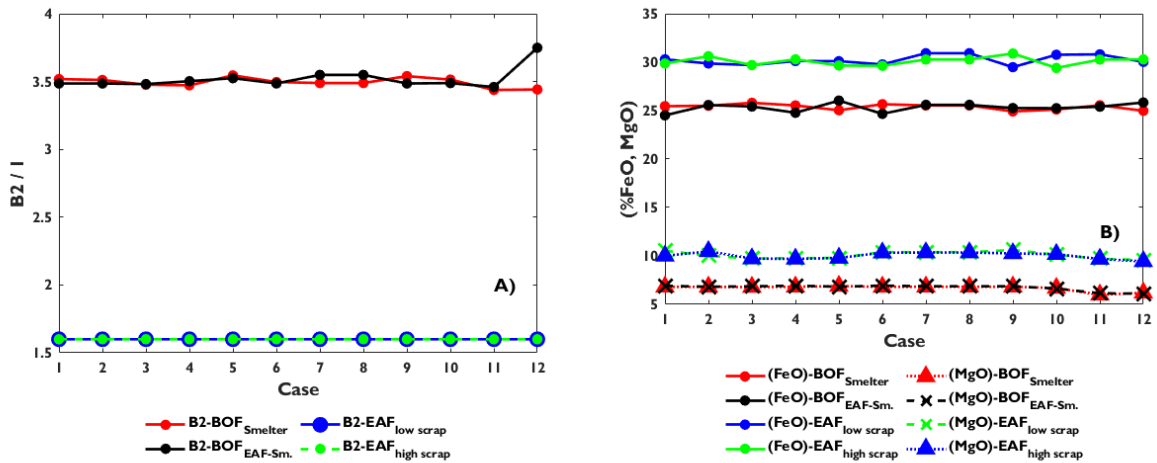


Figure 47: A) B2 and B) (FeO), (MgO) in EAF/BOF slags (assignment see Table 26)

Figure 48 highlights the electrical energy consumption based on hot metal and crude steel. The difference between the smelter and the EAF-smelter in A) has two reasons: On the one hand, higher thermal losses were assumed for the former. On the other hand, more residual iron oxide is reduced. However, this not only increases the energy demand but also increases the hot metal output. Therefore, these effects are partially balancing. B) is more informative since scrap and hot metal additions are also considered. The least electrical energy consumption can be noticed for cases with high chemical or thermal energy additions. That is the case for no. 3, with high-C-DRI, and cases 10 and 12, with pig iron; vice versa, cold DRI addition in case 8 results in the highest electricity demand. EAF steelmaking appears to be the most sensitive regarding raw material quality and charging temperature. While the EAF is the preferred aggregate for high-metallized materials, it is the worst for case 8 with low metallization, acidic gangue, and cold feeding. Nevertheless, these results must be considered approximate values since the thermal losses strongly influence them.

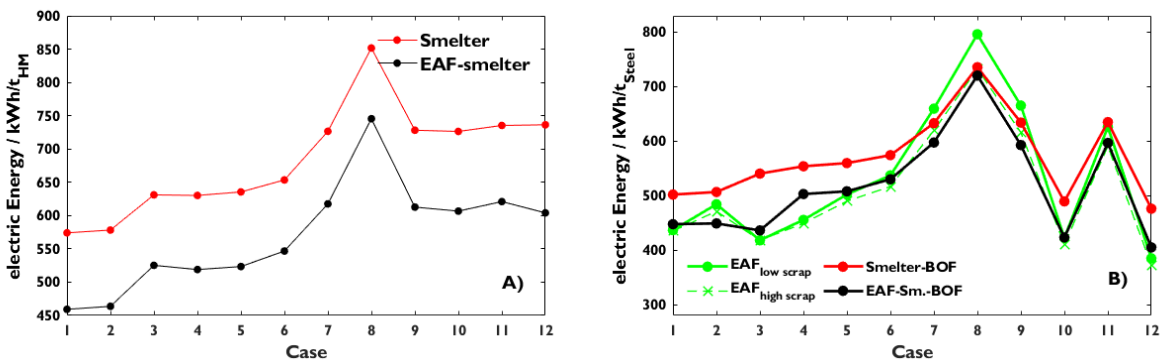


Figure 48: Electrical Energy consumption A) per t hot metal; B) per t crude steel for the calculated cases (assignment see Table 26)

The influence of the DRI carbon is shown in Figure 49. A significant effect can be seen in the EAF. In this case, this additional carbon means additional chemical energy. Since this is just a mass balance perspective, no significant difference is determined for the other aggregates if it does not result in excessive carbon in hot metal. Then, the scrap rate is unusually high, and the specific energy consumption decreases consequently; see case 5, EAF-smelter.

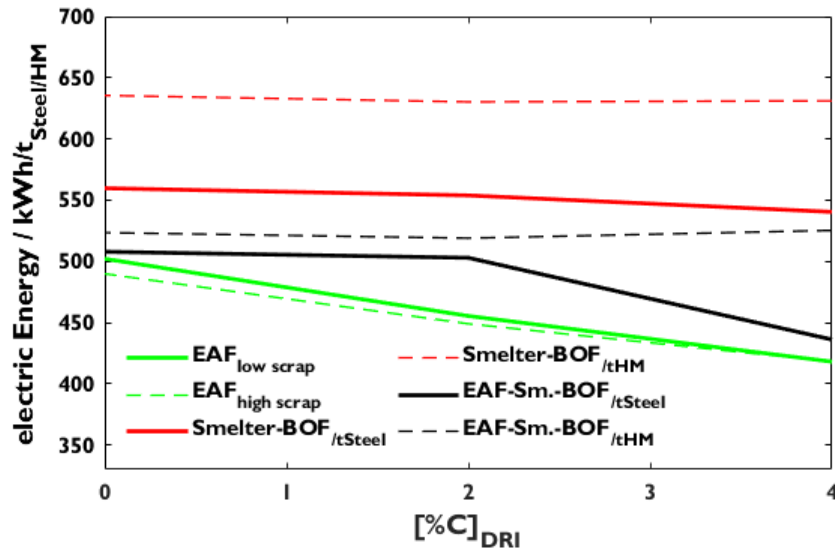


Figure 49: Electrical Energy consumption per t vs. the carbon content of the DRI (cases 3-5; assignment see Table 26)

Figure 50 highlights the impact of MD on electrical energy consumption. Since the iron oxide reduction is endothermal, compared to equation 3, as expected, the demand decreases with better prerduced material. Noteworthy is that this is the most significant for the EAF.

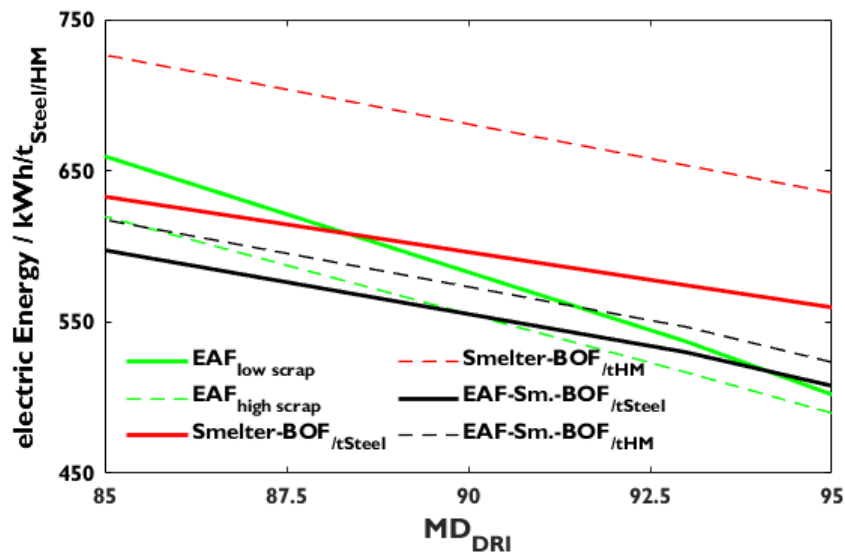


Figure 50: Electrical Energy consumption per t vs. MD (cases 5-7; assignment see Table 26)

The phosphorus contents in Figure 51 show a clear trend with the phosphorus input; see cases 9-12. Further, the two-step processes are beneficial, leading to low contents in crude steel.

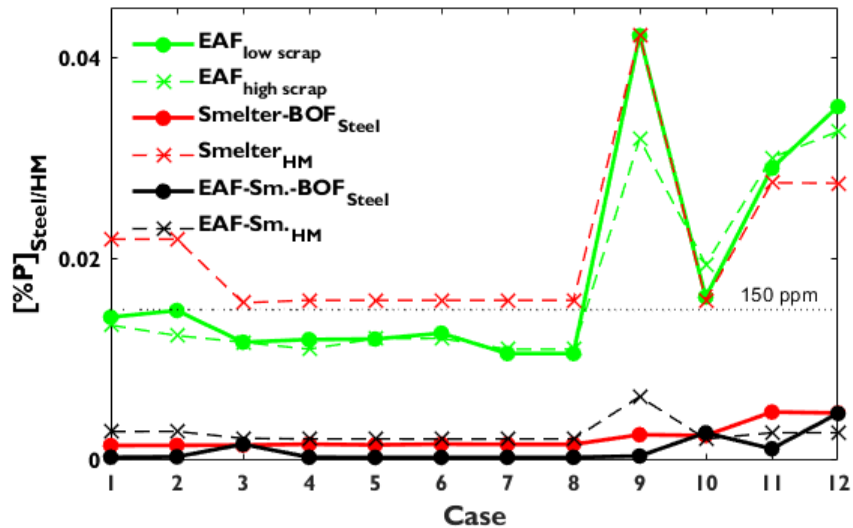


Figure 51: Phosphorus contents for crude steel and smelter hot metal for the calculated cases (assignment see Table 26)

The slag masses of all aggregates are shown in Figure 52. While the converter slag masses remain relatively constant at about 50 kg/t, the amount increases with poorer raw material quality in the melting aggregates. That is especially true in the EAF, where acidic gangue dramatically increases the total slag mass. Like the basicity, (MgO) and (FeO) are lower in the smelter and the EAF-smelter, compare Figure 46 and Figure 47. Therefore, this effect is less pronounced in these aggregates.

In line with the slag amounts, the yield decreases in EAF-steelmaking when poor raw materials are charged; see the yield and the iron losses in Figure 53. The converter slag also has a high iron oxide content; it is produced in much smaller quantities. Hence, the two-step strategies show much higher resilience when dealing with lower iron-containing raw materials.

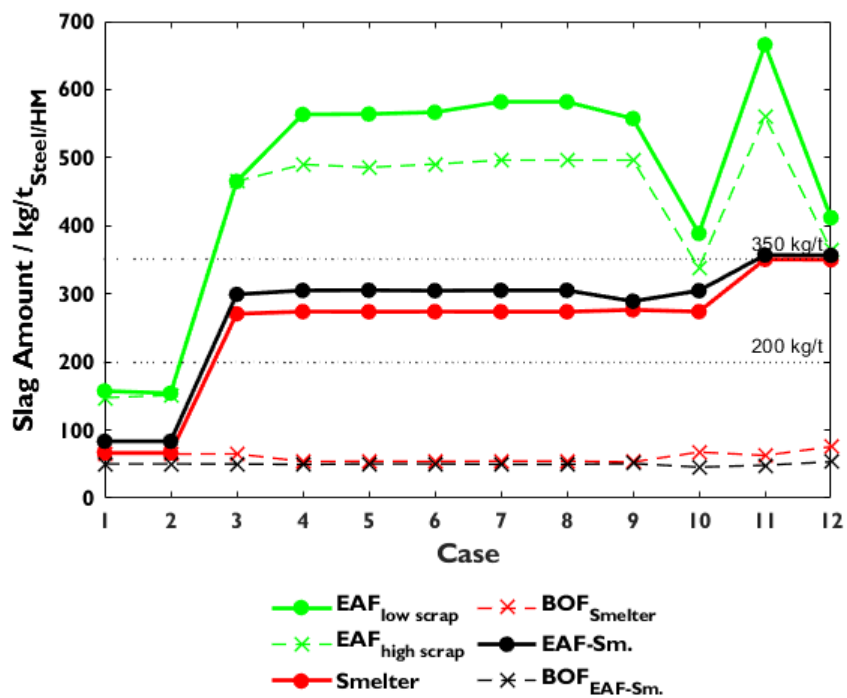


Figure 52: Slag amount in EAF, smelter, EAF-smelter, and BOF for the calculated cases (assignment see Table 26); 200 and 350 kg/t are considered as critical values in EAF and smelter/EAF-smelter

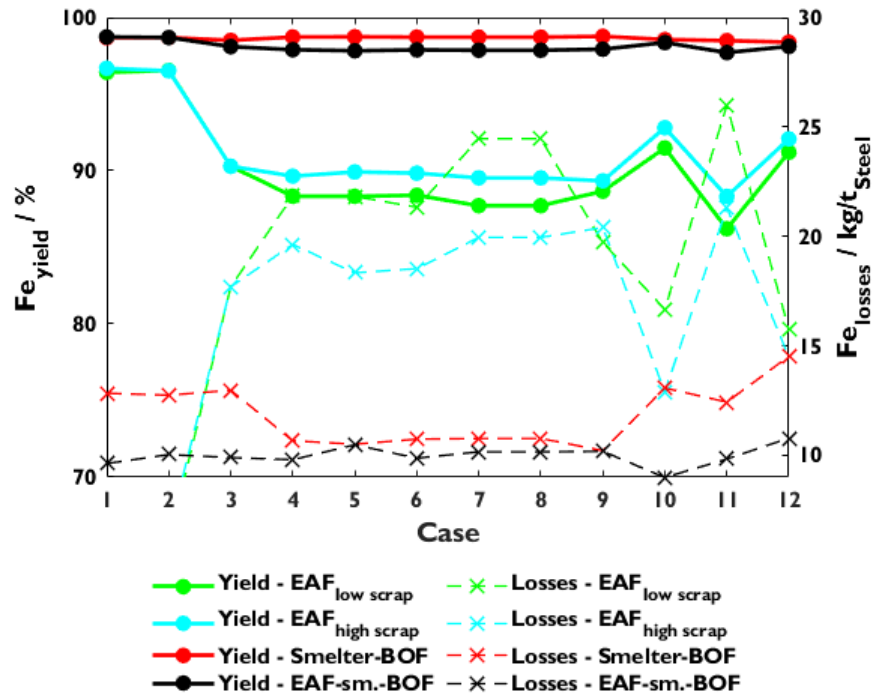


Figure 53: Fe-yield and Fe-losses for the calculated cases (assignment see Table 26)

The charged additives in Figure 54 correlate with the provided input materials. While the EAF consumes the most slag-forming oxides, the smelter route is much more economical. Since all slag concepts rely on MgO, dolomite is the central oxide. Noticeable are the additions of SiO₂ in the two-step procedures. Si in the Smelter- and EAF-smelter hot metals can be very low, so this additional silica addition was considered to avoid falling the BOF-slag mass significantly below 50 kg/t. In A), the dotted lines represent the masses of additional carbon. In the EAF, this amount remains relatively constant between 10 and 12 kg/t. In the reducing aggregates, the additional carbon also acts as carburizing material. Less C is added in the EAF-smelter, compared to the smelter, which is not plausible at first sight. Nevertheless, the scrap rate is much higher in the smelter, leading to a larger crude steel mass, which explains the lower specific carbon consumption.

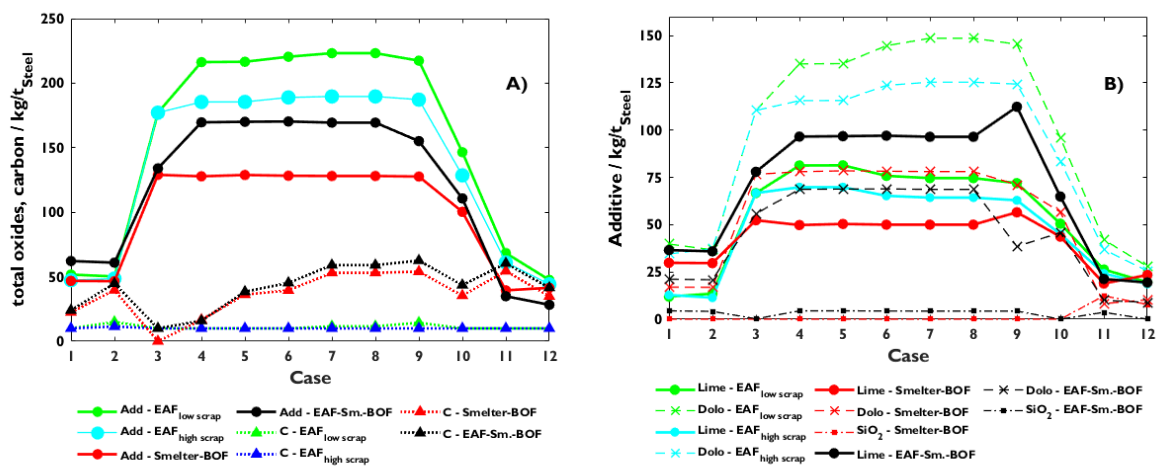


Figure 54: Additive consumption, A) total oxides and carbon; B) type-specific, for the calculated cases (assignment see Table 26)

Last but not least, the smelter sulfur input is approximated using conventional coke. The calculated case 8 needs 53 kg of carbon per t crude steel. Considering 825 kg of hot metal per ton of steel, 9.7 kg are added into the smelter. A typical sulfur content of 0.7% and fixed carbon of 90% in coke results in a S input of 0.5 kg S per t HM. Compared to the blast furnace with an input of 2.5-3 kg, sulfur should be less of a problem in the smelter^[100]. If biomass-based material replaces conventional carbon carriers, this input is reduced further due to its lower sulfur content^[150, 151].

4.3. Discussion

Cases 1 and 2 represent typical input materials applied in existing integrated DR-EAF routes. With such high-grade raw materials, the one-step melting strategy is beneficial. Because the slag amount stays low, at approximately 150 kg/t, the yield stays high, and the additive consumption remains moderate. Considering lower operational expenditures (OpEx) as one processing step can be saved, the conventional EAF is preferable. Further, the capital expenditures (CapEx) are lower as well. Hence, this strategy is further interesting for new greenfield projects.

If the gangue content increases, two-step methods look optimal. The Fe-yield can be kept high by adding a reduction and deslagging step. Since hot metal is the intermediate product, existing BOF-melt shops can be further used and remain a competitive advantage for existing brownfield plants, transforming the integrated BF-BOF route to CO₂ neutrality. The BOF further provides productivity and steel quality advantages, represented by lower tap-to-tap times and lower phosphorus contents. Most of the slag accrues during the smelting step, showing similar properties to BF-slag. Therefore, it can be optimally recycled.

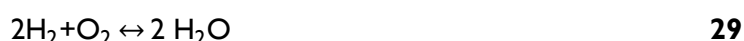
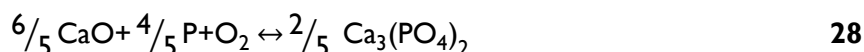
From the raw materials perspective, the DRI should be as rich in iron and as highly reduced as possible. Nevertheless, further sensitivity analyses must be performed, considering site-specific information. For example, the costs for additional carbon and CO₂ emissions in the smelter or EAF-smelter must be compared with hydrogen costs in the DR-shaft when optimizing the final reduction degree of the sponge iron. These model cases represent exemplary calculations. Other concepts may also be possible depending on the supply of different raw materials. For instance, if high-quality scrap or pig iron is available, the operation of an EAF with lower grade DRI in a minor share or the combination of a smelter with refining in an EAF may be thinkable.

5. Phosphorus

When it comes to new iron and steelmaking technologies, the final product quality is an essential topic. In this case, trace elements play an important role. Phosphorus is one of the most prominent trace elements and is mainly considered harmful for steel properties. P accompanies iron ores, so its behavior is especially relevant in ore-based steelmaking strategies. Therefore, this chapter investigates P in two aspects. Firstly, its behavior during direct reduction is experimentally studied, which defines the DRI properties relevant for the subsequent processing steps. Secondly, data from thermodynamic calculations and published literature are applied to characterize the DRI processing aggregates, EAF, and smelter, about their capability of melting and refining sponge iron with different phosphorus contents. These two examinations provide information to evaluate the dephosphorization capacities in DR-EAF or DR-smelter-BOF steelmaking and classify it compared to the BF-BOF route.

5.1. Phosphorus behavior in direct reduction conditions

In hot metal, phosphorus occurs in reduced condition^[9]. Nevertheless, DR plants' conditions are entirely different from blast furnaces. Therefore, whether P in DRI is charged in a reduced or oxidic state into the melting aggregate is unclear. **Figure 55** shows the oxygen potential of reactions **24-29**. The fact that the oxygen potential of the iron–wustite equilibrium is lower than that of the phosphorus oxidation, indicates a higher oxygen affinity of metallic iron and further a reduction of phosphorus oxide in the DR-plant. Nevertheless, the oxide is much more stable if P is bound in $\text{Ca}_3(\text{PO}_4)_2$. On the one hand, the given chart considers thermodynamics without kinetics. On the other hand, the calculated oxides are just an approximation since phosphorus can occur as apatite in iron ore^[152–154]. Apatite is a mixed oxide with the chemical formula $\text{Ca}_5[(\text{F},\text{Cl},\text{OH})](\text{PO}_4)_3$. Therefore, whether the thermodynamic conditions can be transferred to the actual reduction process is unclear. The two hydrogen lines represent different reduction gases. The blue one is highly reducing, similar to this test series, and the magenta one is comparable to an industrial-scale reactor. A test series was performed and described in the following chapter to study phosphorus behavior during the reduction step.



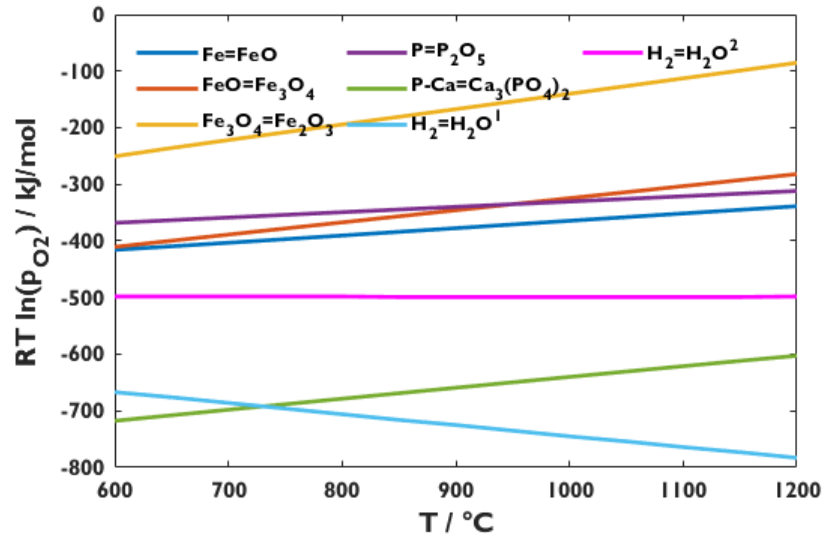


Figure 55: Oxygen potential vs. Temperature (Richardson-Jeffes diagram) for iron- and phosphorus oxides; standard conditions; data from FactSage™ 8.2, reaction and equilib modes, FactPS database; $^1p_{H_2}/p_{H_2O}=10^8$; $^2p_{H_2}/p_{H_2O}=10^2$

Figures 56-60 illustrate the digital microscope images of the materials in raw, oxidized, and reduced conditions. Since most of the gangue is dark in color, it is not easy to differentiate between the different nonmetallic phases. Nevertheless, chalcopyrite ($CuFeS_2$)^[155] can be seen in some domains. One such particle is highlighted in **Figure 58**. Further, the optical images provide an outstanding possibility to analyze the evolution of the iron phases during the treatment steps. In the raw samples, **Figure 56** and **Figure 58**, the iron particles appear magnetic. After preoxidation of the fines, most of the magnetite is oxidized to hematite. That can be examined with the lighter gray level in **Figure 59**. Further, some residual magnetite strips can be observed in the marked area. The impression of a deep preoxidation corresponds to the chemical analysis in **Table 9**. The magnetic lump material's reduction behavior differs from the preoxidized fines' behavior. The former is inhomogeneously reduced; compare the two images in **Figure 57**. While in some areas, the structure is metallic and porous; others show particles of wustite framed by a dense layer of metallic iron. The metallization progress can be seen in the right-hand picture as a porous metallic area growing into the dense residual wustite. Contrary to this, the reduced fines in **Figure 60** are much more homogeneous and occur mostly metalized.

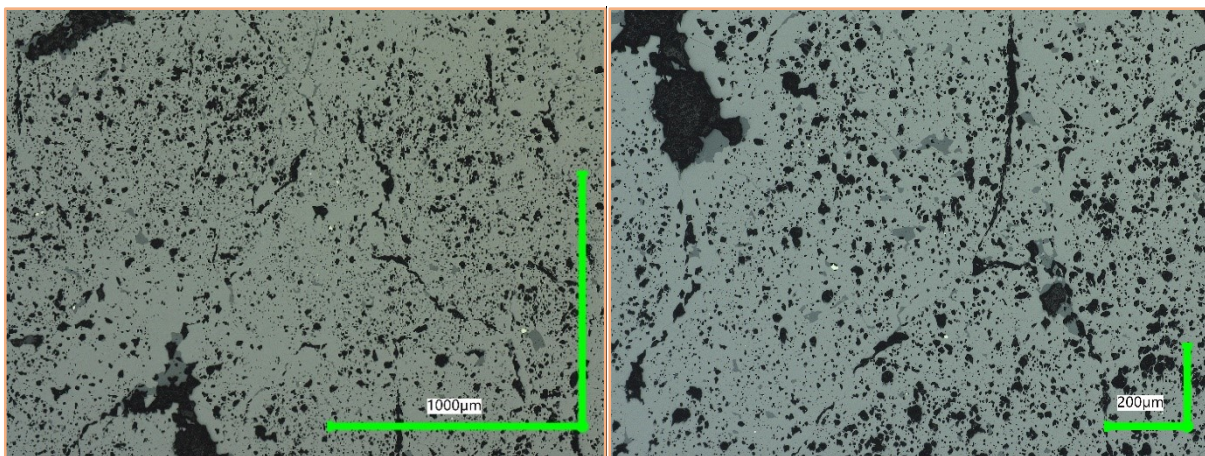


Figure 56: Digital microscope images of raw Kiruna lump samples

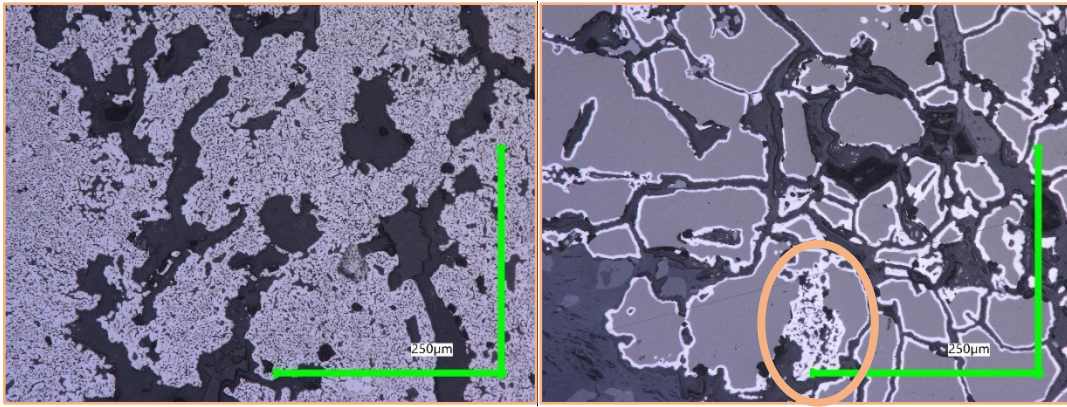


Figure 57: Digital microscope images of reduced Kiruna lump samples; marked spot: porous metallic iron phase, growing into dense magnetite

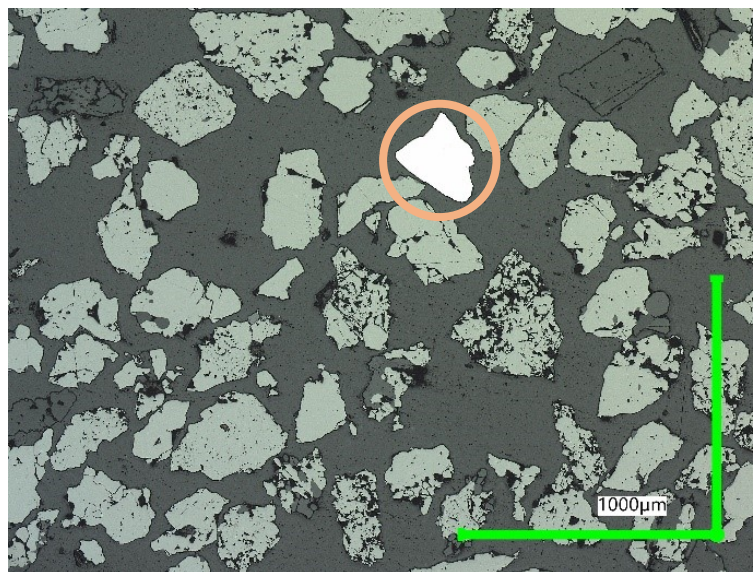


Figure 58: Digital microscope images of raw Kiruna fine ore; 250-500 µm; marked particle: chalcopyrite (CuFeS_2)

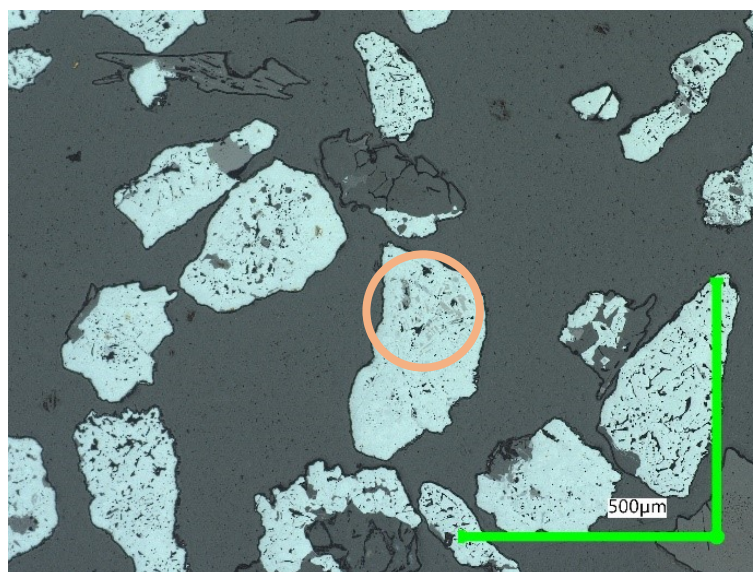


Figure 59: Digital microscope images of oxidized Kiruna fine ore; 250-500 µm; marked spot: residual magnetite bars

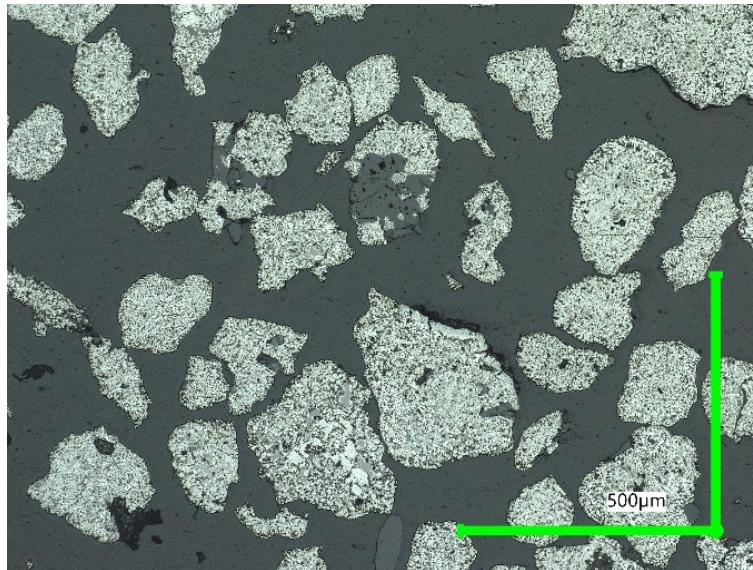


Figure 60: Digital microscope images of reduced Kiruna fine ore; 125-500 μm

Figures 61-70 show the SEM images and the EDX distribution mappings. All images contain phosphorus-bearing spots, as the target was to investigate its behavior. The following aspects can be noticed when looking at these figures:

- All observed P-spots contain oxygen and Ca as well. On the other hand, Mg, Al, and Si appear to be separated from them. This observation aligns with the idea of apatite as the phosphorus carrier in the Kiruna iron ore.
- Other particles are enriched in Ti, Mg, or Si. While titanium seems to be a pure oxide, Mg, Al, and Si partly occur as mixed oxides; see **Figures 62, 64, 66, and 70**. It must be considered that these relative observations can be pretty misleading. Because the matrix is rich in Fe, the Fe content in the other areas appears very low. Therefore, e.g., the Ti-rich parts may also be ilmenite, FeTiO_3 ^[156].
- Especially in **Figure 69**, the oxidic phases seem to be separated by a gap from the metallics.

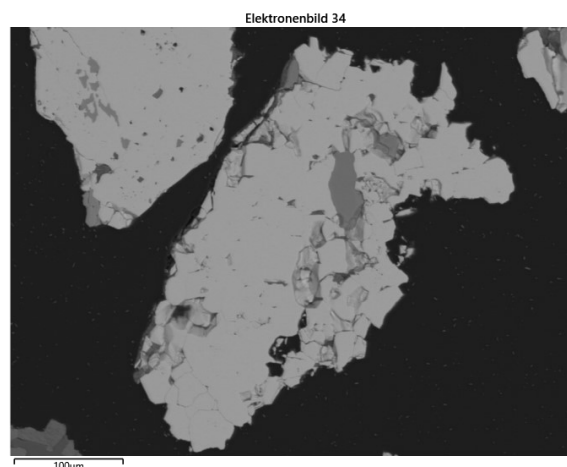


Figure 61: SEM image of an apatite-containing particle; Kiruna fines 250-500 μm , raw

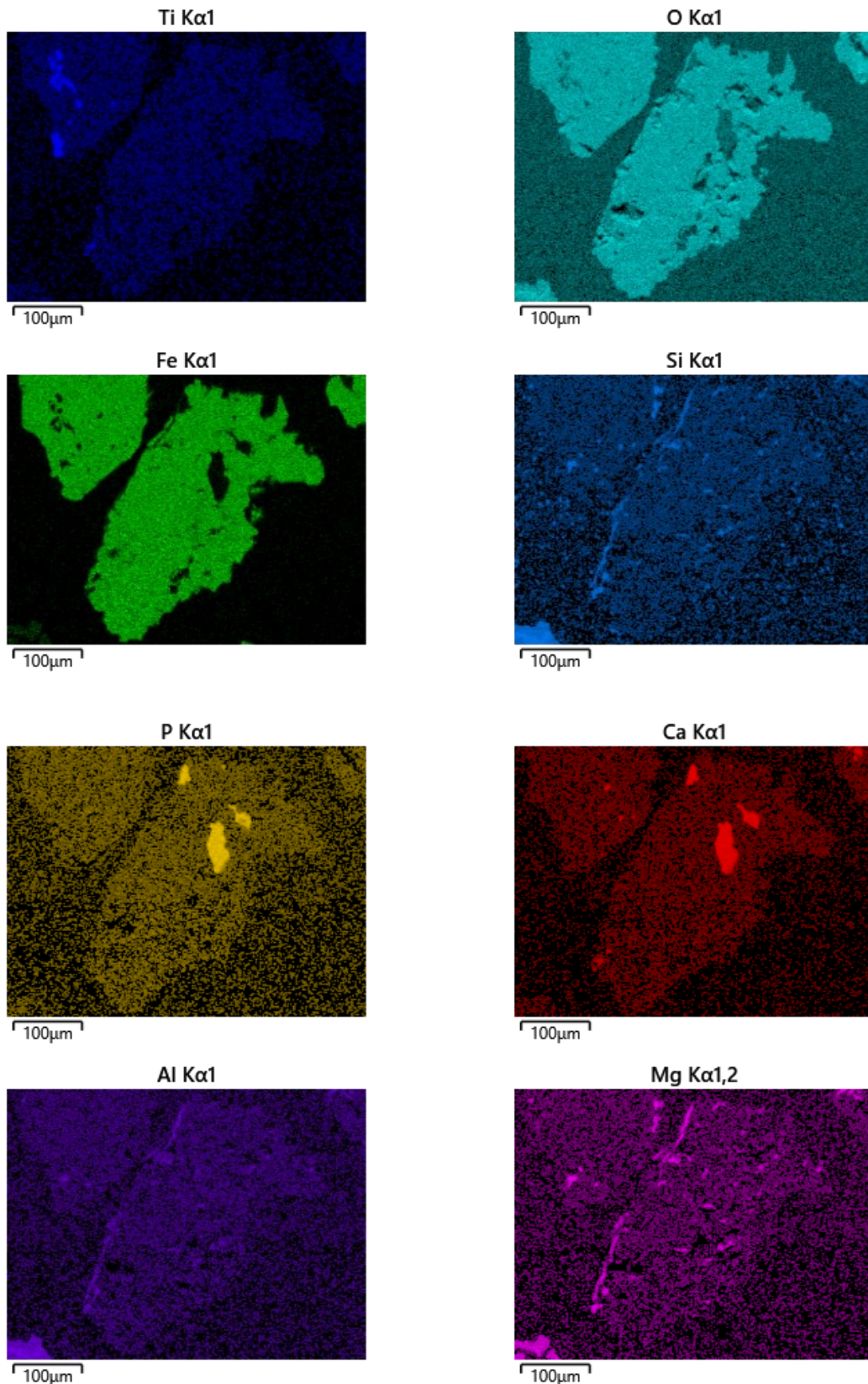


Figure 62: EDX-mapping of an apatite-containing particle; Kiruna fines 250-500 μm, raw; corresponding SEM image see **Figure 61**

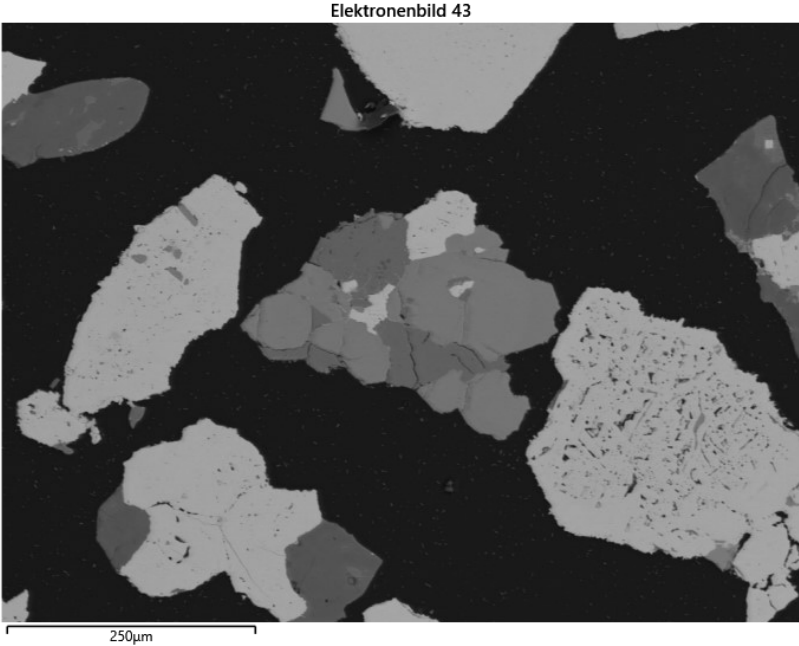
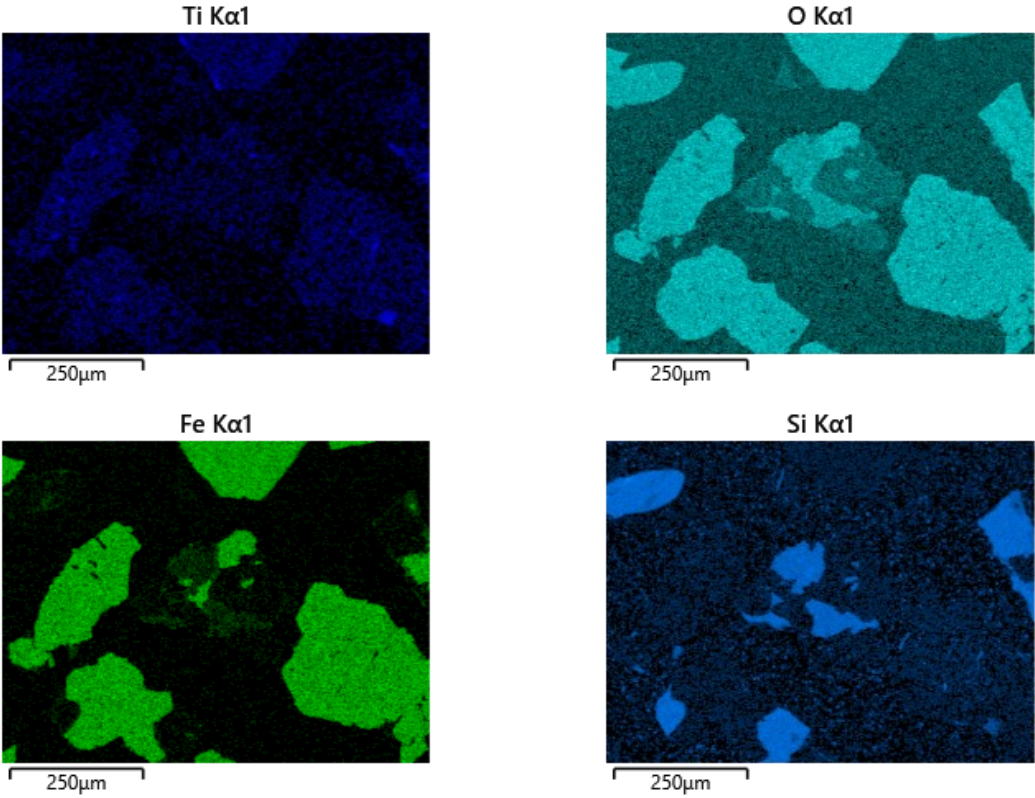


Figure 63: SEM image of an apatite-containing particle; Kiruna fines 250-500 μm, oxidized



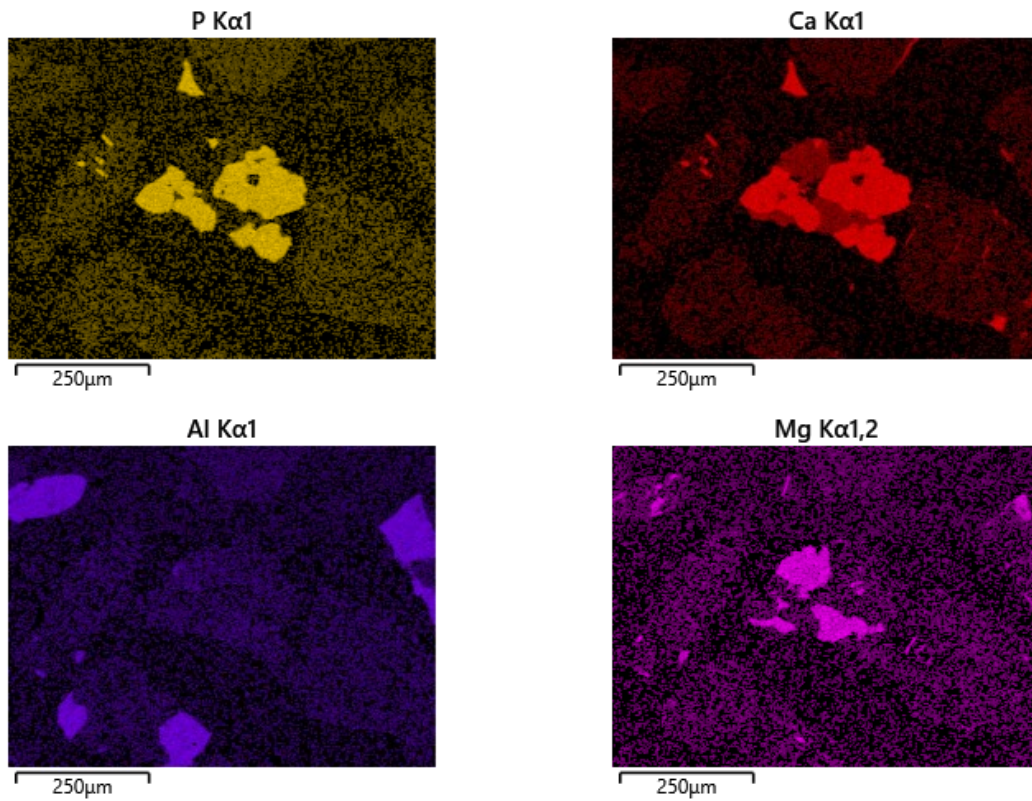


Figure 64: EDX-mapping of an apatite-containing particle; Kiruna fines 250-500 μm, oxidized; corresponding SEM image see **Figure 63**

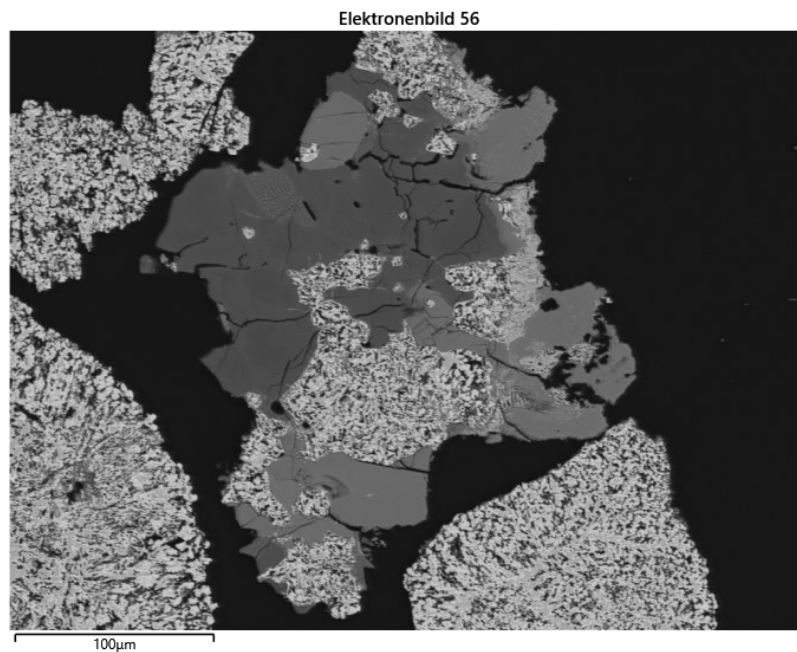


Figure 65: SEM image of an apatite-containing particle; Kiruna fines 250-500 μm, reduced

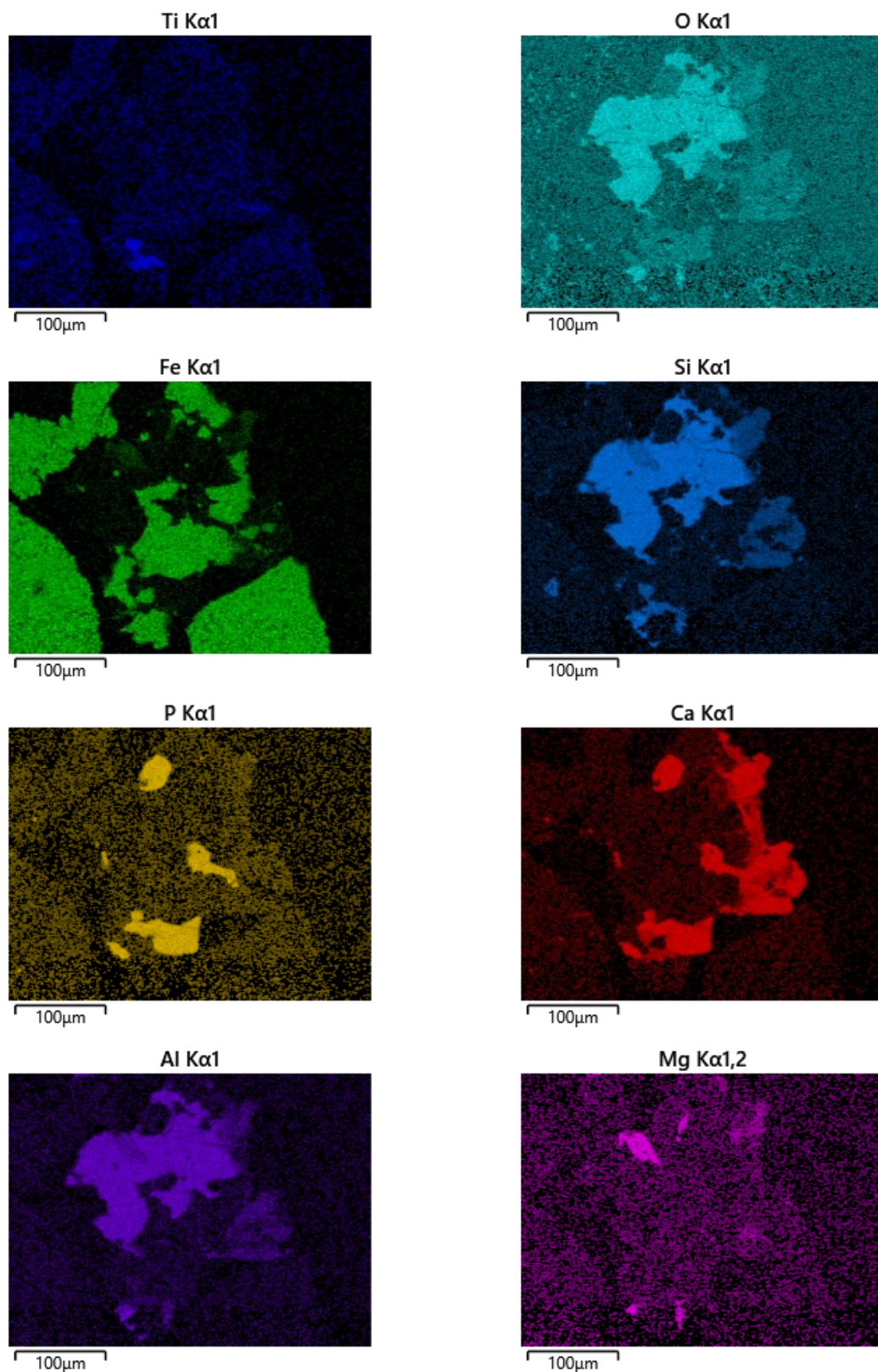


Figure 66: EDX-mapping of an apatite-containing particle; Kiruna fines 125-500 µm, reduced; corresponding SEM image see **Figure 65**

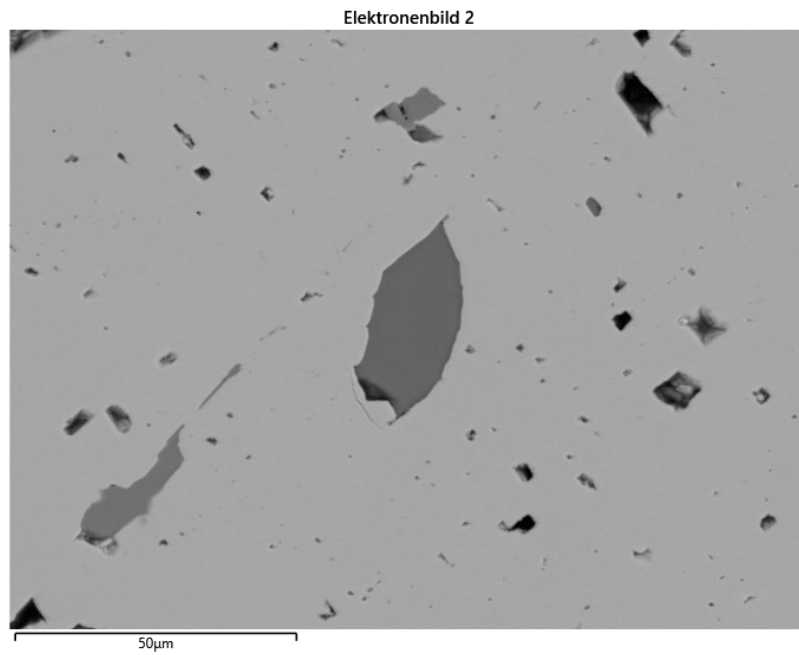
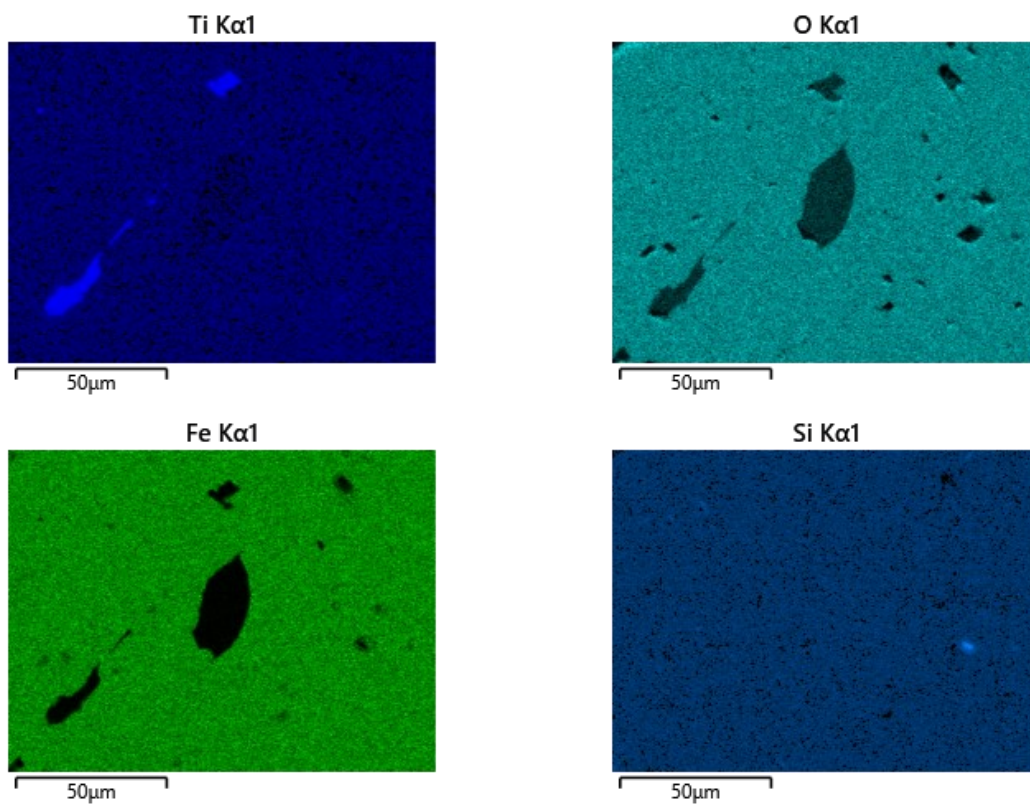


Figure 67: SEM image of an apatite-containing particle; Kiruna lump, raw



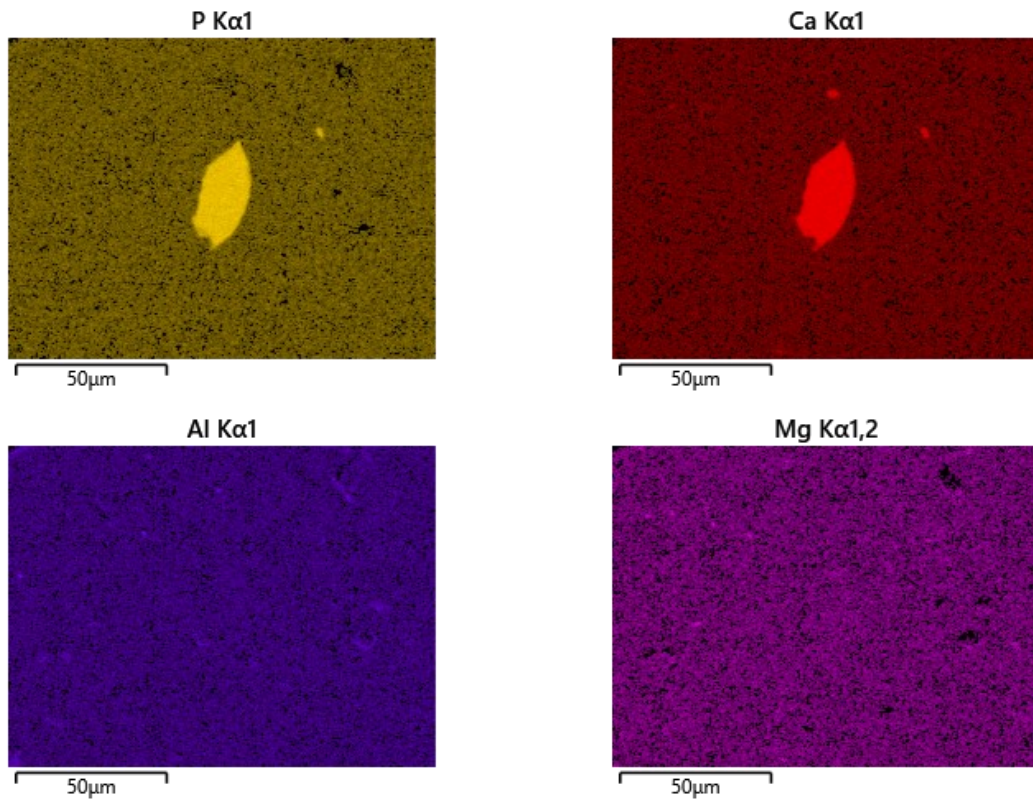


Figure 68: EDX-mapping of an apatite-containing particle; Kiruna lump, raw; corresponding SEM image see **Figure 67**

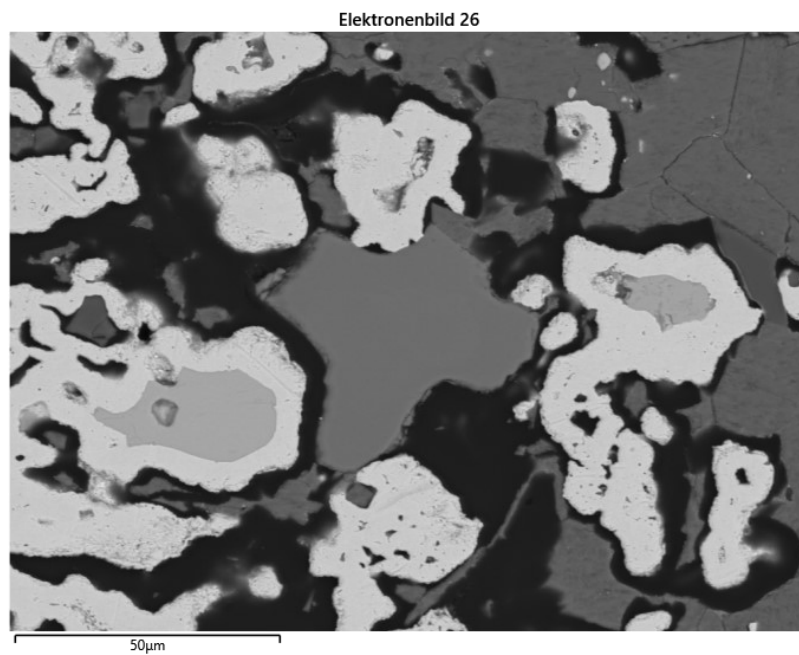


Figure 69: SEM image of an apatite-containing particle; Kiruna lump, reduced

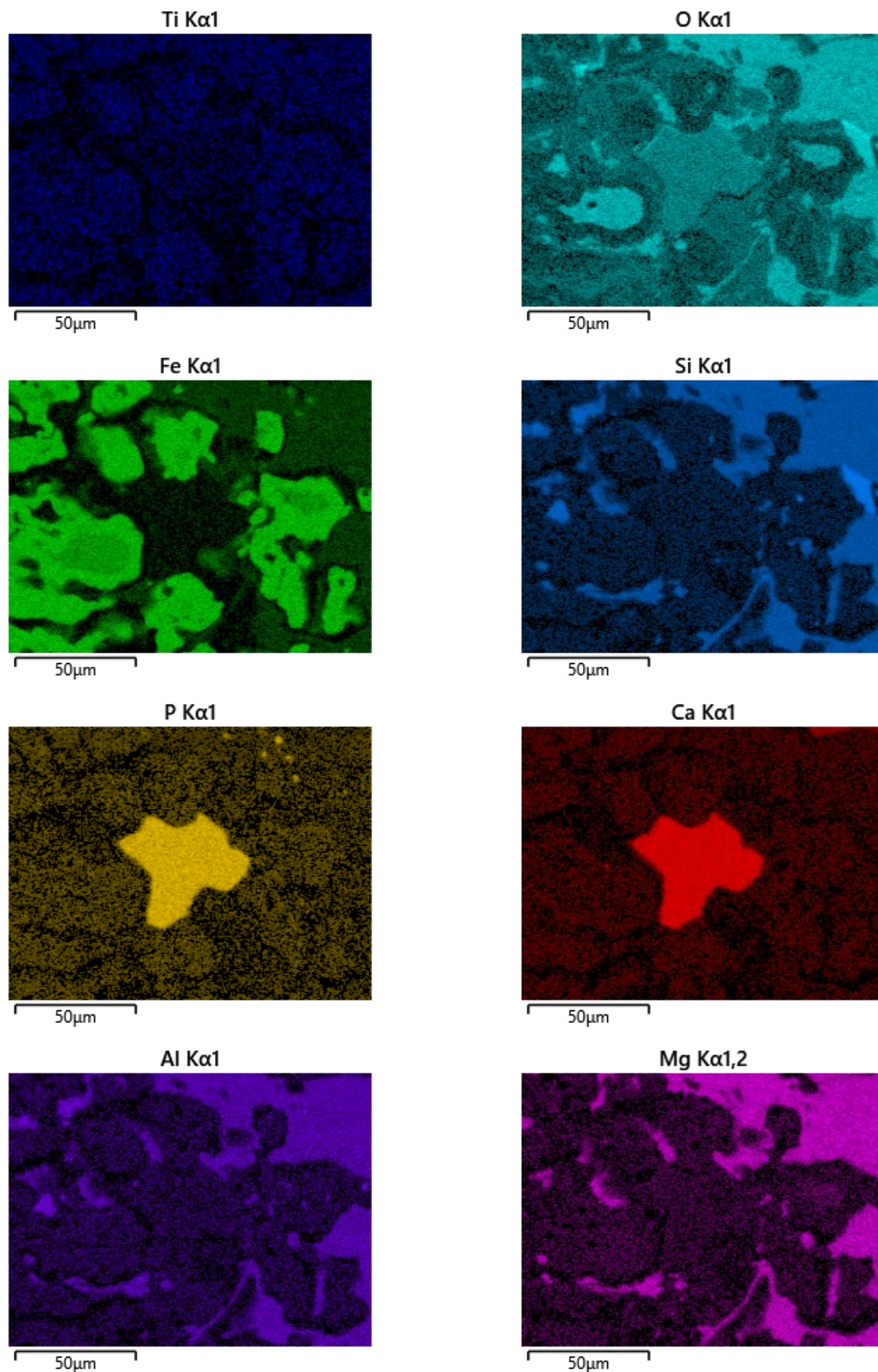


Figure 70: EDX-mapping of an apatite-containing particle; Kiruna lump, reduced; corresponding SEM image see **Figure 69**

A so-called line-scan analysis was performed to examine the apatite particles and quantify their composition closely. The following **Figures 71-73** show the line courses through a particle and the

composition along the line, measured at 20 evenly distributed points. The following aspects can be observed when having a closer look at the diagrams:

- All particles are enriched with phosphorus, as well as calcium and oxygen, indicating to be apatite. That confirms the assumptions made from the qualitative mappings above.
- The particles are depleted in Fe. Further, no P increase in the metallic phase can be observed in the reduced condition compared to the raw or oxidized states. That is consistent with the thermodynamic evaluation in **Figure 55** that phosphorus remains in the oxidic apatite phase during the reduction step.
- Fluorapatite ($\text{Ca}_5[\text{F}(\text{PO}_4)_3]$) consists of approximately 39.6 wt.-% Ca, 18.5 wt.-% P and 38.1 wt.-% O. The measured results in the line scans match the theoretical values from the order of size.

A gap between the metallic matrix and the apatite particles can be seen when comparing the reduced state with the unreduced. That is analog to the previous images and may result from shrinkage of the former due to the removal of oxygen atoms.

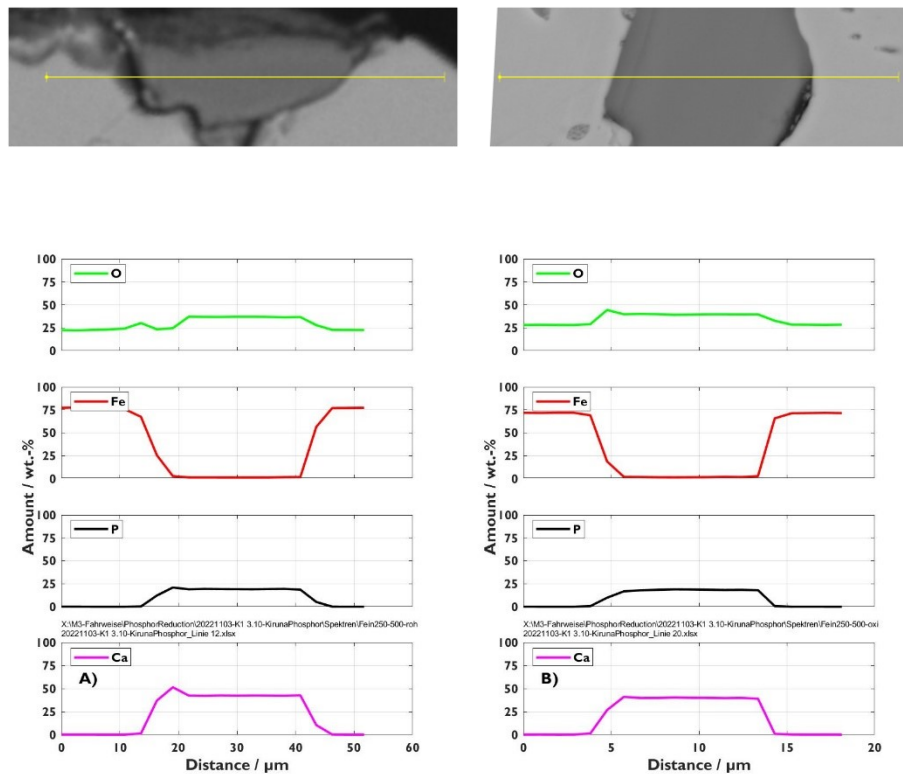


Figure 71: Apatite EDX-line scan; A) Kiruna fines 250-500 μm , raw; B) Kiruna fines 250-500 μm , oxidized

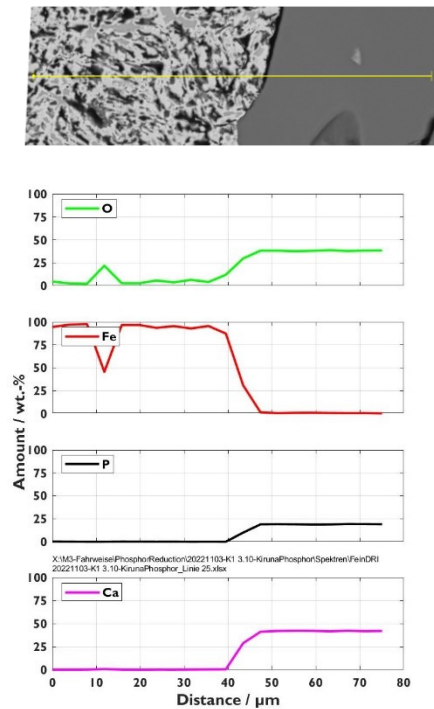


Figure 72: Apatite EDX-line scan; Kiruna fines reduced, 150-500 µm

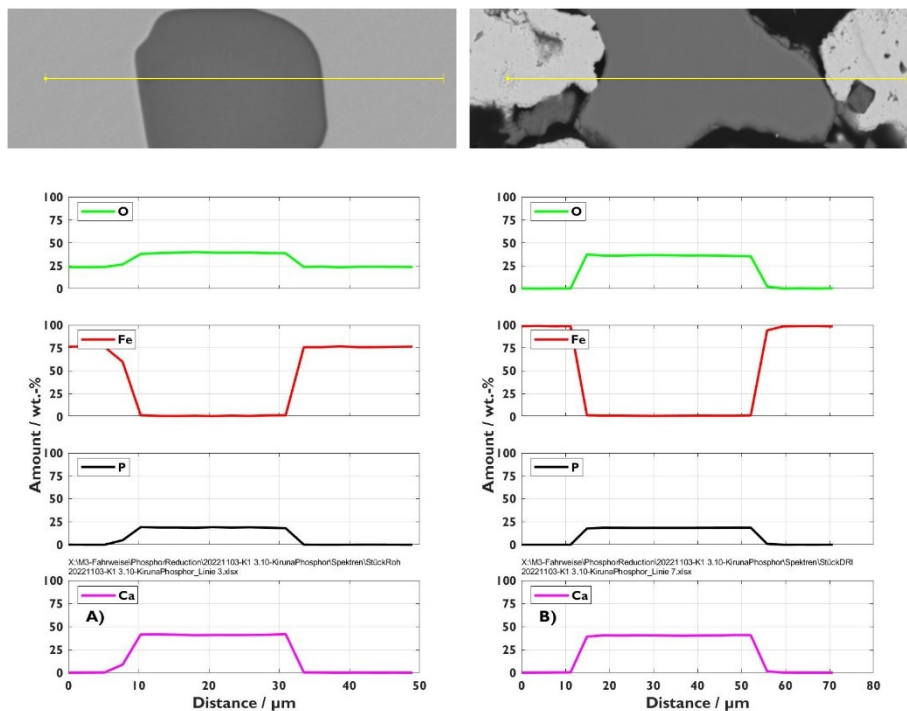


Figure 73: Apatite EDX-line scan; Kiruna lump; A) raw; B) reduced

5.2. Phosphorus distribution

The observations in 5.1 describe the occurrence of phosphorus in DRI, which is the raw material for the subsequent melting step. Chapter 5.2 presents two phosphorus partition models to evaluate its behavior in these melting aggregates. The derivation is given in chapter 3.4.2. To get an idea about the

behavior depending on basicity and (%FeO), **Figure 74-A** and **Figure 75-A** show the phosphorus partitions from equations **8** and **9** in the form of a surface and a contour plot. The latter represents horizontal sections. The following aspects can be identified when looking at the charts:

- The (%FeO) content is the primary driving force promoting dephosphorization.
- Higher basicity is beneficial as well. Nevertheless, the effect is not so pronounced in this case and seems to reverse for high basicities and high (%FeO) contents, see **Figure 74-A**.
- For the converter case, above a basicity of approximately 2, the behavior becomes more independent of (%FeO).

The diagrams in B) show the same data but iteratively recalculated to the hot metal or steel phosphorus amount. The first iteration starts with [%P]=0.3%.

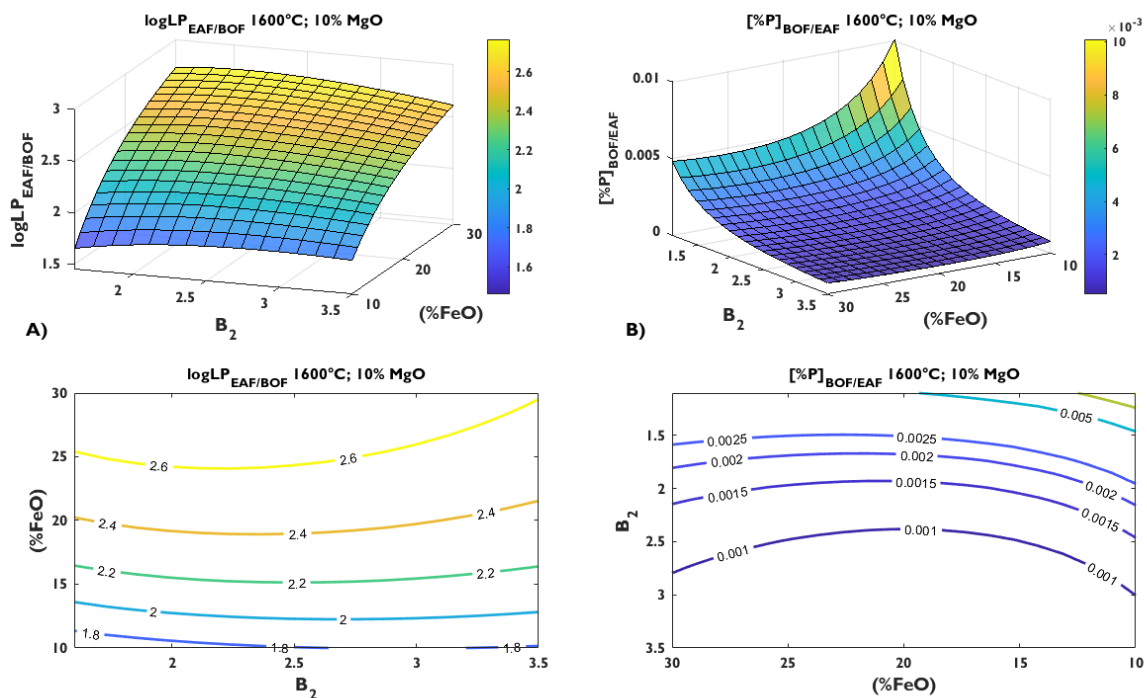


Figure 74: Surface- and contour chart of phosphorus partition in EAF/BOF; A) Partition according to equation **8**; B) Phosphorus content in the melt, based on equation **8**, with an initial [%P] content of 0.3%

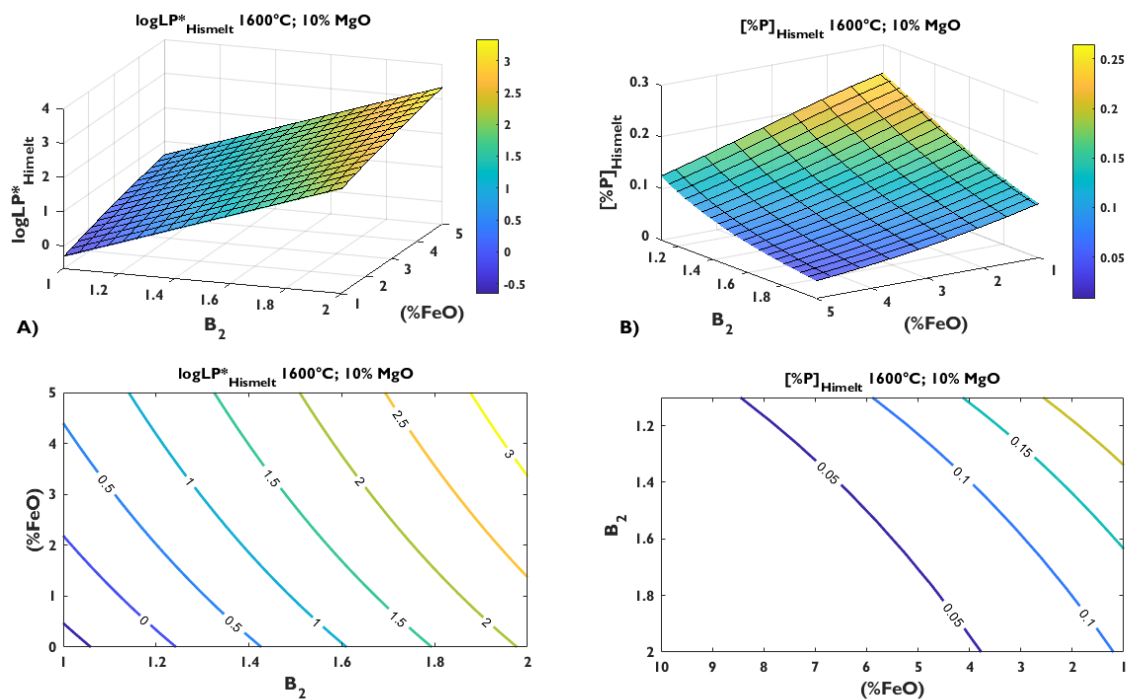


Figure 75: Surface- and contour chart of phosphorus partition in the smelter (based on HISMELT); A) Partition according to equation 9; B) Phosphorus content in the melt, based on equation 9, with an initial [%P] content of 0.3%

In the isothermal diagrams above, the temperature influence is neglected. As equations 8 and 9 and the exothermic reaction indicate, inverse proportionality of the partition coefficient with the temperature exists. Mathematically described: $L_P/L_{P^*} \approx f(1/T)$. **Figure 76** gives the distributions at higher temperatures. Although the surfaces are shifted slightly downwards, the influence of the temperature is small compared to basicity and (%FeO).

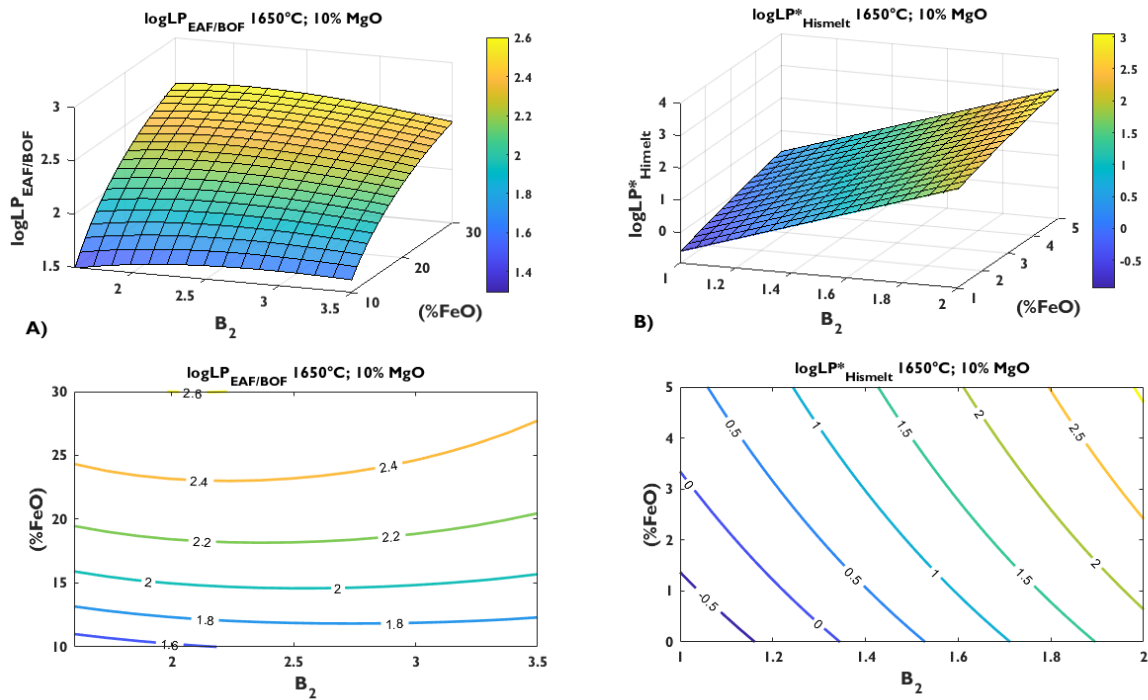


Figure 76: Surface- and contour chart of phosphorus partition in BOF/EAF and smelter at an increased temperature of 1650°C

Figure 77 illustrates the equilibrium surface- and contour charts, shown as L_P as well as L_P^* , in ranges suitable to the diagrams above. The difference is minimal when comparing the surface with the EAF- and the BOF case highlighted as red- and blue dots in A). That is plausible considering the long holding times performed by the authors^[110, 111]. The Hismelt distribution; see the blue dot in B) and a published reference value in the green dot are significantly above the equilibrium surface, indicative of a higher amount of phosphorus in the slag. Since the smelting reduction technology charges phosphorus with the iron ore in oxidic condition, this result is plausible. Due to a kinetic delay, not all phosphorus may be reduced.

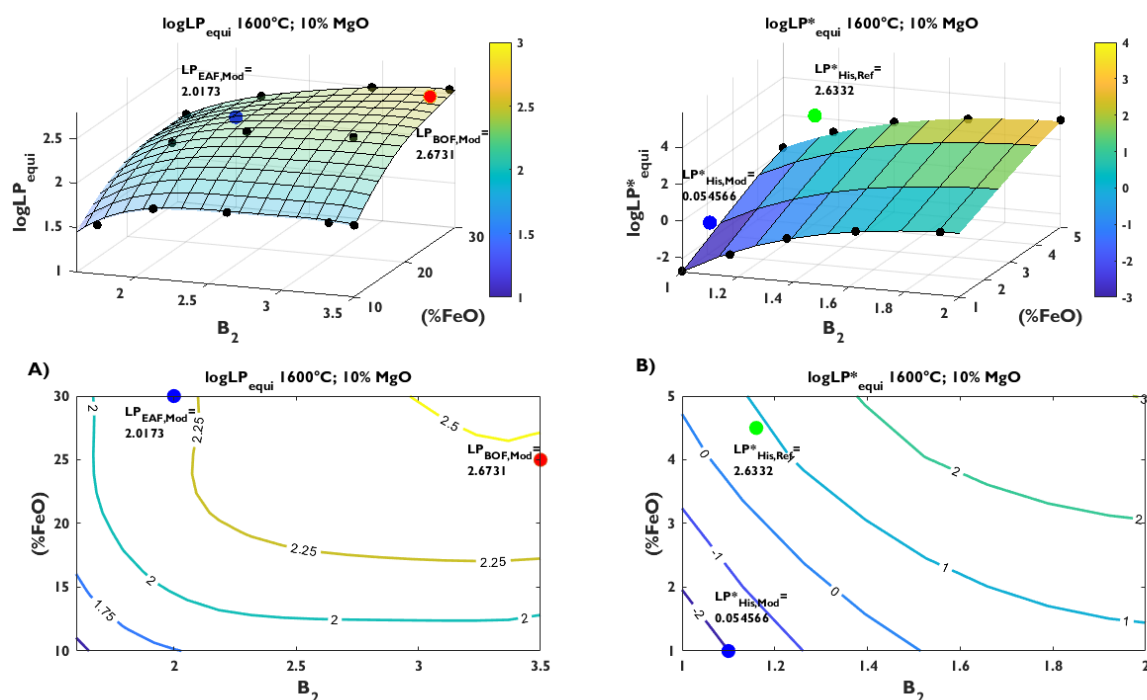


Figure 77: Surface- and contour chart of phosphorus equilibrium partition; dots represent the calculated values; A) L_P ; $L_{P,EAF,Mod}$, $L_{P,BOF,Mod}$... acc. to equation 8 ; B) L_P^* ; $L_{P,His,Mod}$ acc. to equation 9, $L_{P,His,Ref}$ acc. to ^[19]

5.3. Discussion

Two reduction tests were performed to study the phosphorus behavior. Unbeneficiated Kiruna iron ore was chosen because it is high in phosphorus, simplifying the P detection. To simulate different reduction strategies, magnetitic lump and preoxidized fines are considered. The EDX results align with the literature^[153], suggesting that P is bound as apatite. When looking at the thermodynamics, the Richardson-Jeffes diagram lines show that calcium phosphate is much more stable than pure phosphorus oxide. Since the EDX distributions and the line scans show that P still occurs as a mixed oxide, the conditions during gas-solid reduction are not sufficient to reduce it. Comparing this result to hot metal, in which P is dissolved in the iron melt, the oxidic form may act as a kinetic obstacle, indicating it to be preferable in case of the phosphorus distribution in the iron- or steelmaking aggregate. Huss et al.^[157] observes a rapid dissolution of apatite in the slag phase as soon as the DRI is in contact with a liquid slag. That is further evidence that carbon addition is decisive for industrial processes. While, at high carbon DRI, C may be directly dissolved into the metal pool, carbon injection into the slag could locally make the conditions more reducing, indicating an increased phosphorus reduction in the melting aggregate. Putting these findings in the context of the distributions in **Figures 73-76** as well as the aggregate specific peculiarities, see **Figures 7,8,12, and 13**, the thermodynamic equilibrium can be seen as a minimum value for L_P and L_P^* , beneficial for the production of low phosphorus crude steel.

6. Interaction between DRI and liquids

Chapter 4 presents and compares different DRI processing strategies. Next to such balance data, sponge iron's behavior during the melting step is also of great interest. To deepen the previously published and in chapter 2.1 summarized knowledge, tests were performed to compare various DRI grades when in contact with metallic melts and slags. The first test series was published in [140]. **Table 28** lists all according to the procedure from chapter 3.5 performed tests, including the immersion times and furnace and melt temperatures. The applied materials are described in method chapter 3.5. The sample number is defined as follows: “test series”-“DRI sample”-“liquid medium”-“sequential number”. E.g., I-C750-ULC-1 was part of series I, a carburized sample was dipped into liquid ULC steel, and it was the first test with this configuration.

Table 28: List of DRI dipping tests; *pretests, which were cooled in flushed nitrogen and not further examined^[140]

Series	Sample number	Liq. medium	t _{Immersion} / s	T _{furnace} / °C	T _{melt} / °C
I	I-C750-ULC-1*	ULC	4	1625	-
	I-C750-ULC-2		3		1544
	I-C750-ULC-3		4		1555
	I-C800-ULC-1*		4		-
	I-C800-ULC-2*		3		-
	I-C800-ULC-3		3		1555
	I-C800-ULC-4		4		1555
	I-0%C-ULC-1		4		1544
	I-0%C-ULC-2		3		1544
	I-0%C-ULC-3-10s		10		1558
	I-HBI-ULC-1		3		1558
	I-HBI-ULC-2		3		1558
	I		I-0%C-HM-1		HM
I-0%C-HM-2		3			
I-HBI-HM-1		3			
I	I-0%C-SAF-1	I-SAF slag	3	1550	1479
	I-0%C-SAF-2		3		
	I-C800-SAF-1		3		
I	I-0%C-EAF-1	I-EAF slag	3	1600	-
	I-0%C-EAF-2		3		

	I-C800-EAF-3		3		
	II-0%C.2-SAF-1		3		
II	II-0%C.2-SAF-2	II-SAF slag	6	1600	-
	II-0%C.2-SAF-3		9		
	II-0%C.2-SAF-4		21		
	II-C800.2-SAF-1		3		
II	II-C800.2-SAF-2	II-SAF slag	6	1600	-
	II-C800.2-SAF-3		10		
	II-C800.2-SAF-4		14		

6.1. Results

Figures 78-84 show the photographs of selected samples. Duplicated test samples are not shown as the results are qualitatively reproducible. Smooth surfaces characterize the 0%C samples, indicating the absence of any chemical reactions between pellet and melt. If the immersion time in ULC extends, the surface appears matte instead of shiny; compare **Figure 79** with **Figure 78-A**.

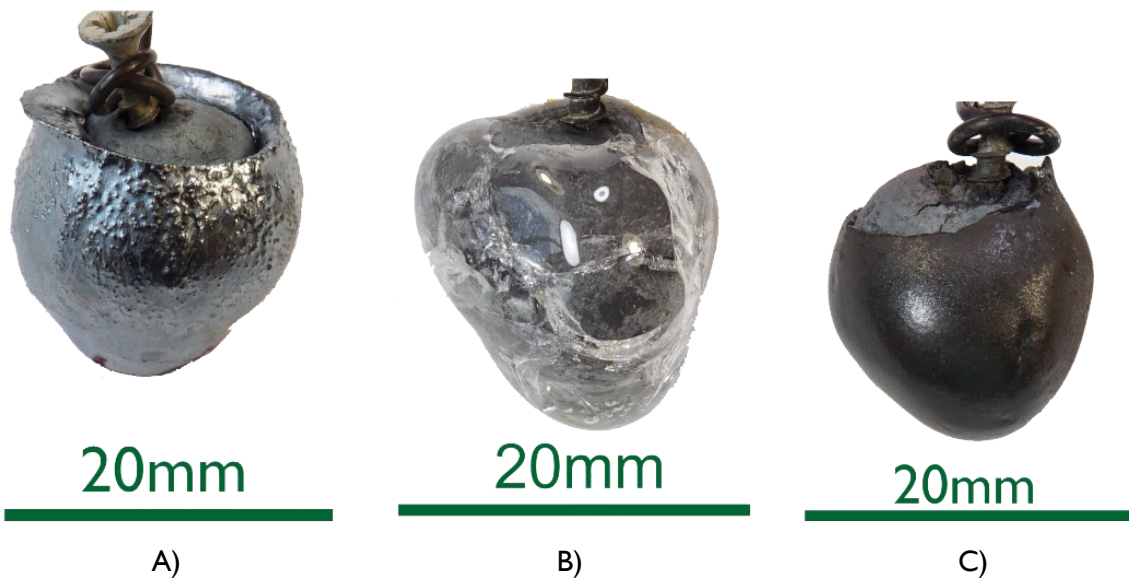


Figure 78: Macroscopic photographs of selected series I 0%C samples A) I-0%C-ULC-1; B) I-0%C-SAF-1; C) I-0%C-EAF-2^[140]



20mm

Figure 79: Macroscopic photograph of sample I-0%C-ULC-3-10s^[140]

If the sample contains carbon, reduction reactions with residual iron oxide seem to happen. The formation of superficial bubbles, shown in **Figure 80** and **Figure 81-A**, reflects the occurrence of reactions in the form of a gas formation. The number of fissures correlates with the carbon content since the rough surface is more pronounced at I-C800-ULC than at the medium carbon I-C750-ULC sample. Further, a difference in the shell shape can be noticed. While the carbon-free samples dipped in ULC look droplet-shaped, the bottom of the carbon-containing samples appear to be “cut-off” or drained. The digital microscope images in **Figure 85** and **Figure 87** further highlight this effect. An explanation for this behavior is the carbon diffusion to the surface near liquid, decreasing its viscosity^[140, 158].



20mm

Figure 80: Macroscopic photograph of sample I-C750-ULC-3^[140]

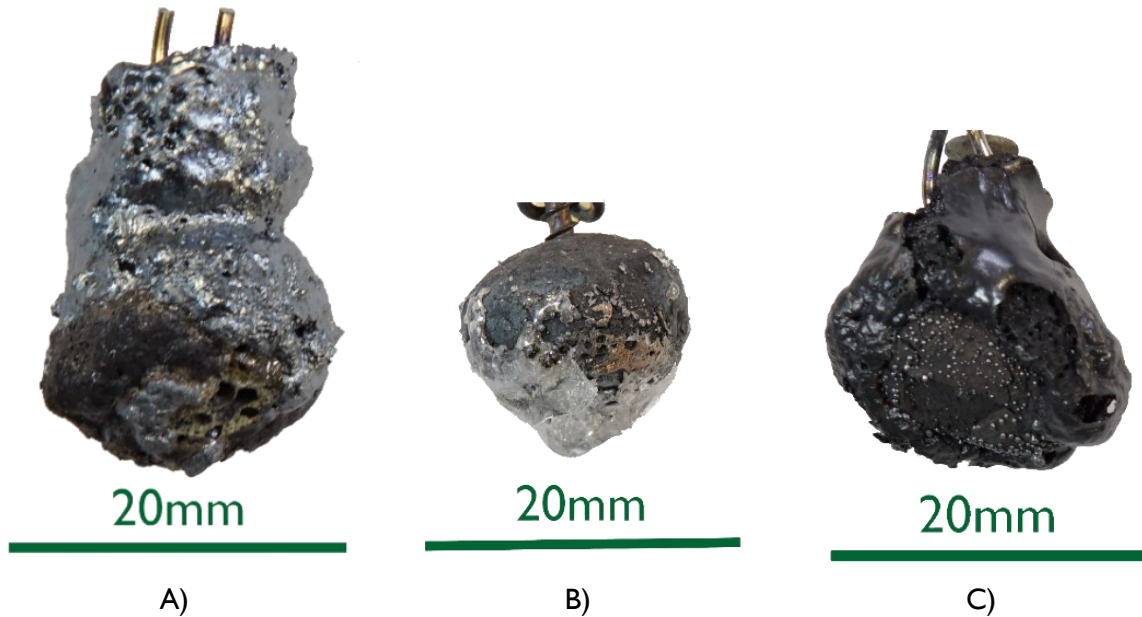


Figure 81: Macroscopic photographs of selected series I C800 samples A) I-C800-ULC-4; B) I-C800-SAF-1; C) I-C800-EAF-1^[140]

While no reactions occur in contact with the iron oxide free I-SAF slag, the sample appears to react with the FeO-rich EAF slag; compare **Figure 81-B** and C. Comparing the nonreactive slag samples, the carbonaceous one looks significantly less wetted with slag than the carbon-free. That correlates with the behavior of carbon-containing refractory material^[140, 159]. Although the HBI sample contains $\approx 2\%$ carbon, its surface is smooth, indicating the sample density to be a significant lever in case of the melting behavior.



Figure 82: Macroscopic photograph of sample I-HBI-ULC-2^[140]

Figure 83 and **Figure 84** show the series II samples in chronologically ascending order. Excluding II-C800.2-SAF-3, shown in **Figure 84-C**, all DRI pellets look unmelted and covered with a slag layer. The one outlier happened most likely due to intensive contact with the graphite crucible leading to carburization and strong induction of furnace power. Since the series I samples, dipped into ULC steel, are superficially liquefied much earlier, heat transfer through the slag seems to be significantly poorer.

The samples dipped into hot metal were totally melted after the immersion. As the actuator for controlling the pneumatic cylinder was at its limit, no further time reduction was manageable. Therefore, no evaluation of these specimens was possible.

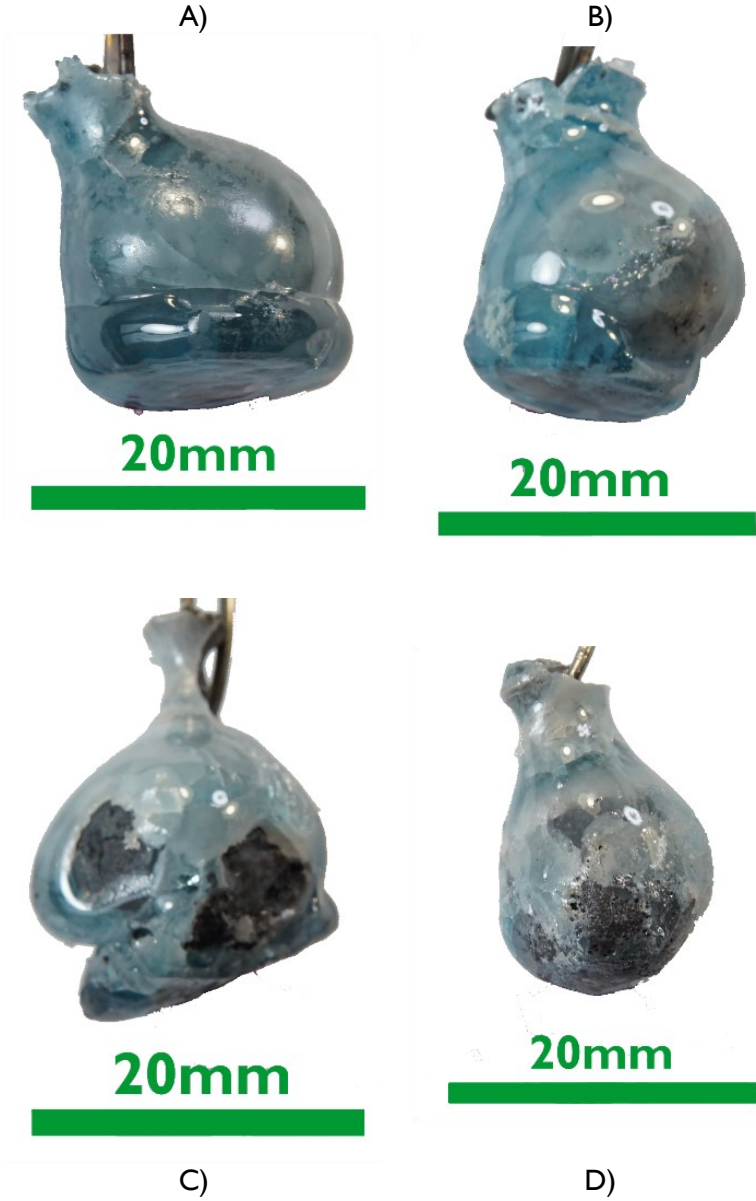


Figure 83: Macroscopic photograph of series II 0%C.2 samples A) 3 s; B) 6 s; C) 9 s; D) 21 s

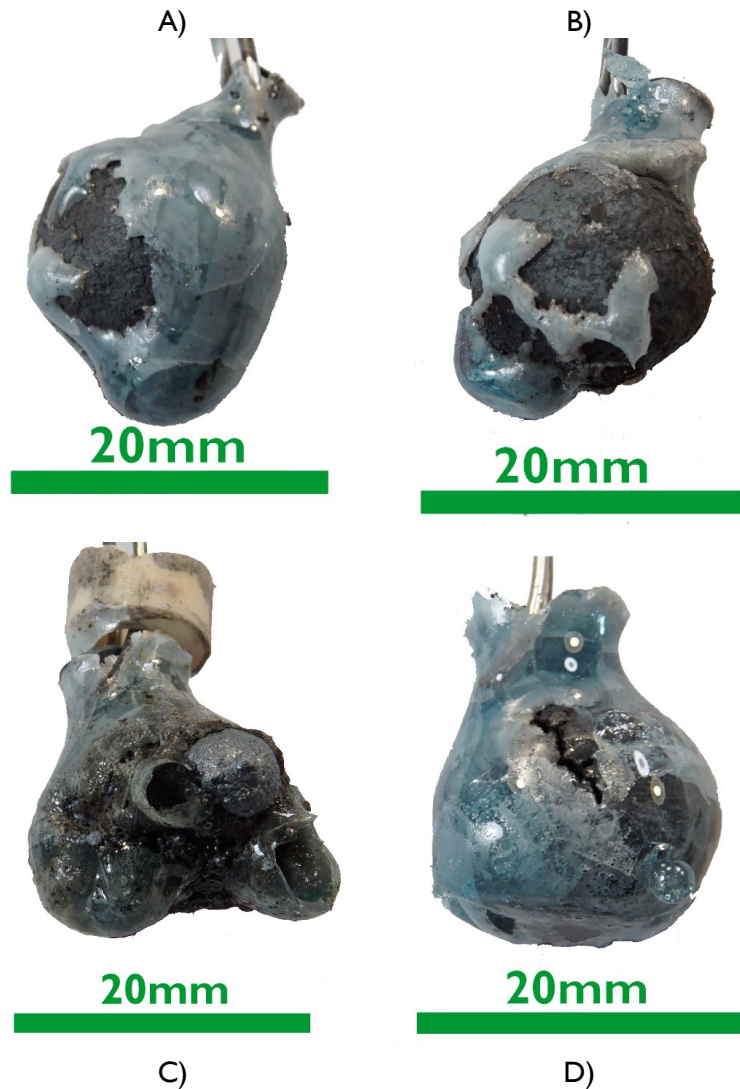


Figure 84: Macroscopic photograph of series II C800.2 samples A) 3 s; B) 6 s; C) 9 s; D) 14 s

Figures 85-91 show the digital microscope images. Different exposure types are applied to ULC- and slag samples to improve visibility. The series I carbon-free samples remain unmelted after 3-4 s immersion. The sharp borders between the shell and the porous DRI structure in **Figures 85-A and 86** highlight that observation. After 10 s in liquid steel, shown in **Figure 85-B**, the spongelike structure appears superficially liquefied. The liquid shell runs off and forms a droplet in the lower part. All covers seem dense and unporous. That indicates no reactions occur during contact with 0%C DRI and agrees with observations that were made when viewing the photographs above^[140].

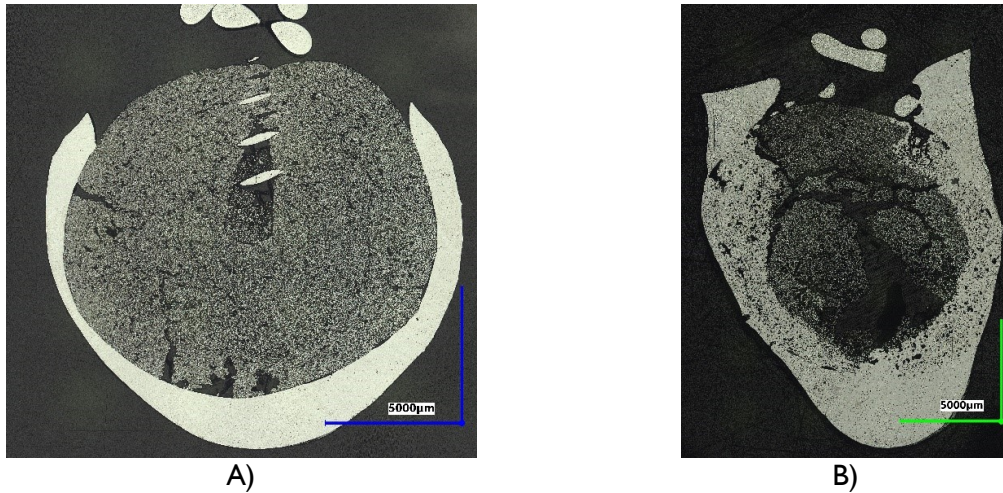


Figure 85: Digital microscope images of A) I-0%C-ULC-1; B) I-0%C-ULC-10s-3; dipped into liquid ULC steel^[140]

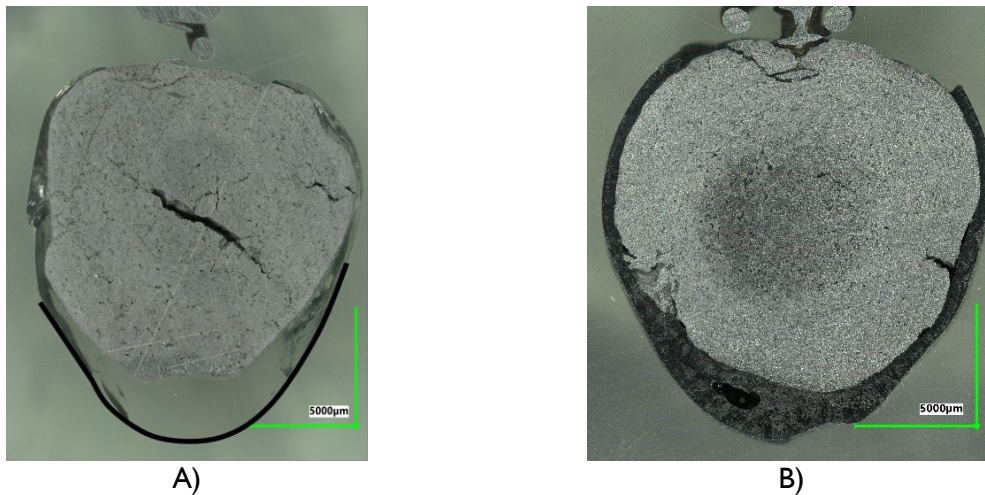


Figure 86: Digital microscope images of A) I-0%C-SAF-2; B) I-0%C-EAF-2; dipped into EAF/SAF slag^[140]

Contrary to 0%C-DRI, the carbon-containing samples I-C750 and I-C800 appear liquefied in most cases, except for contact with FeO-free slag; see the images in **Figures 87** and **88**. In contact with steel, a matte DRI structure can no longer be seen in the highly carburized sample I-C800. In contrast, samples dipped into slags remain mostly solid and melt superficially.

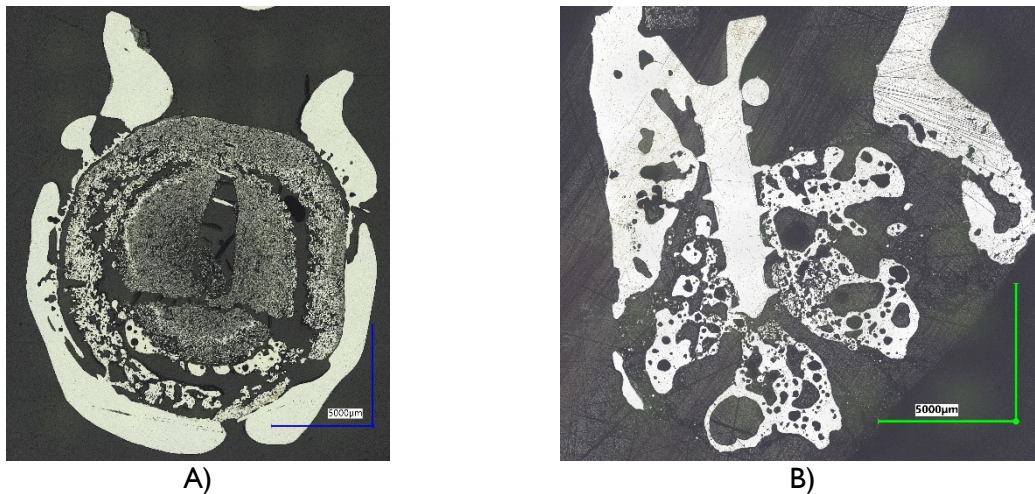


Figure 87: Digital microscope images of A) I-C750-ULC-2; B) I-C800-ULC-4; both dipped into liquid ULC steel^[140]

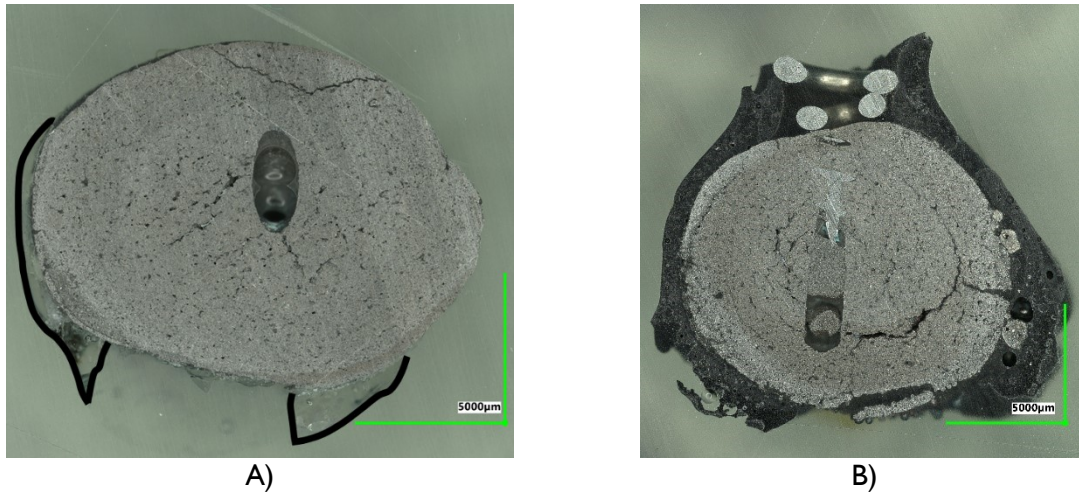


Figure 88: Digital microscope images of A) I-C800-SAF-1; B) I-C800-EAF-1; dipped into slag^[140]

The HBI image in **Figure 89** confirms the impression from the macroscopic photograph in **Figure 82** that a steel layer merely covers the core without any melting. Consequently, HBI behaves similarly to carbon-free DRI, and the density seems to influence the melting behavior more than the carbon content.



Figure 89: Digital microscope image of the I-HBI-ULC-1 sample, dipped into ULC^[140]

Figures 90 and **91** show the digital microscope images of series II tests. Apart from the outlier II-C800.2-3, all DRI samples remain unmelted. A circular zone can be seen in places that are heat-affected in the near-surface region. Although less striking than in the photos above, the slag layers adhere better to carbon-free material and drain and thin out with longer dipping times.

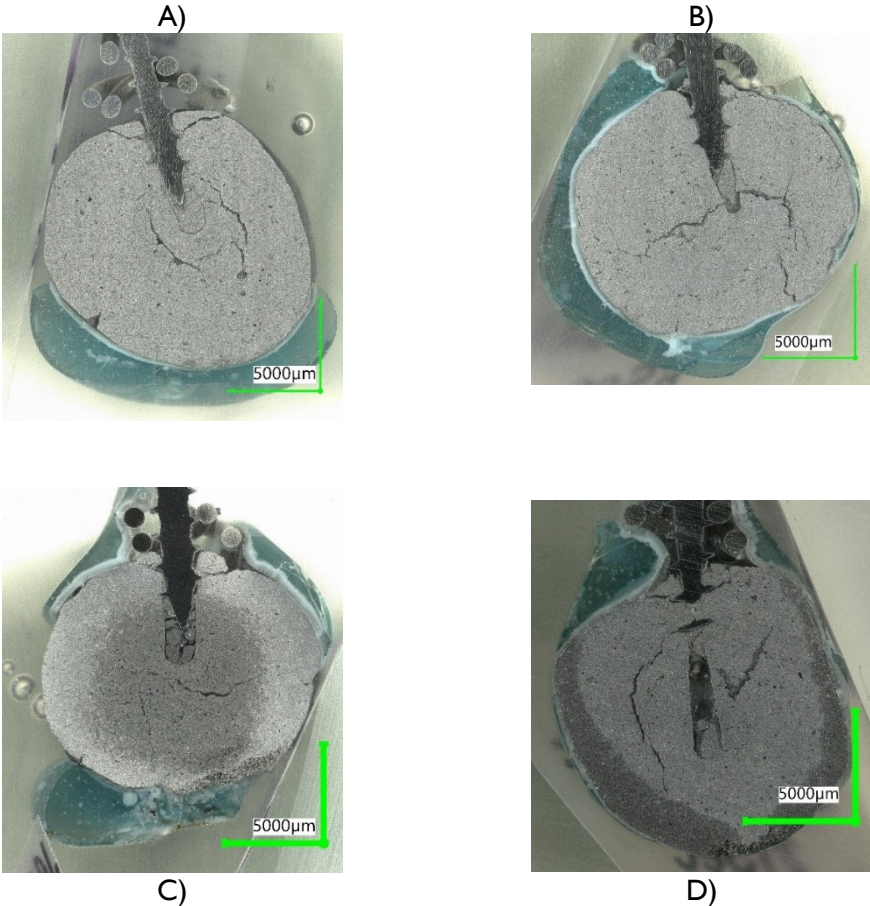


Figure 90: Digital microscope images of series II 0%C.2 samples A) 3 s; B) 6 s; C) 9 s; D) 21 s

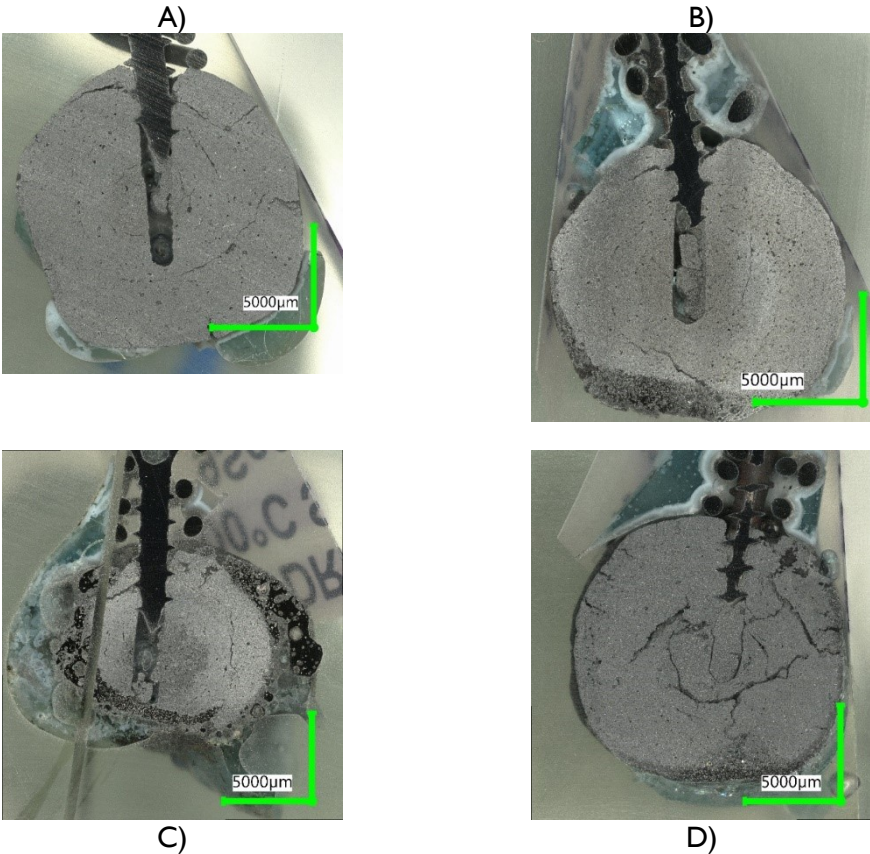


Figure 91: Digital microscope images of series II C800.2 samples A) 3 s; B) 6 s; C) 9 s; D) 14 s

The different results between slag and steel are worth a closer look. The liquidus temperature of I-C800 with 3.79% C is approx. 1213°C, calculated by FactSage™ 8.0 using FSSStel database. This results in an overheating of 266°C for the I-SAF slag case. Nevertheless, the core remains unmelted, even after longer dipping times in series II, while the same sample rapidly liquefies in the steel bath. That indicates different heat transfer conditions. The Prandtl numbers, see equation 30, are approximately calculated to classify them. Pr is the ratio between the kinematic viscosity ν /(m²/s) and the thermal diffusivity a /(m²/s). Transformed, it is a function of the dynamic viscosity η /(Pas), the fluid heat capacity c_p /(J/Kmol), and thermal conductivity λ_{FI} . Compared to the Nusselt^[160] number, Pr is exclusively dependent on fluid-specific parameters. Therefore, the complicated determination of the heat transfer coefficient, which depends on temperatures and flow conditions, can be avoided^[140].

$$\text{Pr} = \frac{\nu}{a} = \frac{\eta \cdot c_p}{\lambda_{FI}} \quad 30^{[161, 162]}$$

Table 29 summarizes the applied parameters and Pr for DRI in contact with slag and liquid Fe. For slag, Pr is smaller by a factor of ≈ 1500 . Their different thermal conductivities can explain the difference since the heat capacities are similar in magnitude. That is consistent with the experiments and poor melting of DRI in slags.

Table 29: Calculated dimensionless Prandtl numbers, incl. literature data for the parameters^[163]

Parameter	Value	Comment	Source
$c_{p,Fe,liq}$	820 J/(kgK)		[60]
$\lambda_{Fe,liq}$	37,65 W/(mK)		[60]
$\eta_{Fe,liq}$	5.08 mPas	at 1550°C	[164]
$c_{p,slag}$	696-1171 J/(kgK)	696 used for calculation	[60, 158]
λ_{slag}	1.1715-1.3589 W/(mK)	1.2625 used for calculation	[60]
η_{slag}	0.320 Pas	calculated with Factsage™ for 1479°C	
Pr_{Fe-DRI}	0.111		
$\text{Pr}_{Slag-DRI}$	176		

6.2. Discussion

- *ULC experiments:* 0%C samples indicate the formation of a solid surface layer. DRI starts to soften as the heat transfer progresses. These observations agree in principle with the calculated results from González et al. and Ramirez-Argaez et al.^[58, 59], visualized in **Figure 5**. The higher the carbon content, the faster this process occurs; compare **Figure 85** with **Figure 87**. Carbon lowers the liquidus temperature of iron dramatically. Consequently, the temperature gradient gets steeper, and the softening point is reached more quickly. Furthermore, the carbon reacts with residual iron oxide, which is accompanied by the formation of bubbles and fissured sample surfaces.
- *Hot metal experiments:* DRI and HBI melt entirely after 3-4 s when immersed into hot metal. The liquidus temperature of pure iron (1538°C, according to FactSage™ 8.0 and FactPS database) is higher than the hot metal temperature. The results differ significantly from the ULC tests and suggest a different melting mechanism. Penz et al.^[165-167] investigated the dissolution of scrap in hot metal and described the following mechanisms:

- An initial solid layer forms and liquefies again after heat transfer progresses, increasing the temperature above T_{liq} .
- Carbon is transported from hot metal to solid steel.
- As the carbon content increases, the liquidus temperature decreases. The sample melts if the carbon level rises and enough heat is delivered through heat transport.
- *Slag experiments:* The SAF-slugs are unreactive due to their low FeO content. Nevertheless, the high carbon samples are striking in multiple aspects. First, the slag layers adhere loosely to the sample, indicating less wetting than the carbon-free samples. That agrees with knowledge from carbon-bearing refractories^[59]. Secondly, the samples remain unmelted, even after long immersion times of up to 21 s. Contrary, in contact with liquid steel, melting progresses much faster. A good explanation can be found in the different heat transfer conditions, showing that Pr is 1500 times higher for steel than for slag. In other words, slag forms a thin temperature boundary layer compared to the velocity boundary layer indicating a weak thermal diffusion. This observation is qualitatively consistent with the literature^[58, 60], reporting significantly longer melting times for the slag case. Furthermore, in contact with FeO-rich EAF slag, the carbon-containing DRI is very reactive. Although the fissured surface indicates higher turbulence in the near-surface region, the core of the sample remains unmelted, confirming the argument of a poor heat transfer between slag and sponge iron.

The following conclusions can be made by transforming these results to full-size EAF and smelters conditions. Highly carburized DRI melts faster than carbon-free material, which is advantageous to avoid iceberg formation in the EAF. Furthermore, its reactivity is high, beneficial for the reaction with the FeO-rich slag. The formation of gas bubbles may induce bath turbulence and improve slag foaming behavior and denitrification. Nevertheless, this is valid in electric arc furnaces, where DRI is charged in the arc hot spot. The temperature is extremely high, and the mixing is pronounced, leading to contact between DRI and the steel melt. Contrary to that, **Figure 11** indicates that the brush arc in the smelter induces a lower stirring effect. Due to the high porosity of sponge iron, the material tends to swim in the slag layer without touching the hot metal below. Because of the poor heat transport in contact with slag, it must be expected that melting DRI in such smelters is challenging.

7. Arc melting behavior

The hydrogen plasma smelting reduction reactor (HPSR) at the Chair of Ferrous Metallurgy was applied for lab-scale melting tests to study the behavior of direct reduced iron in an electric arc. This chapter describes the results of these experiments.

Table 30 lists the performed tests. Test 1 is a pretest to check the possibility of continuous DRI fines feeding. This test was unsuccessful since the fines remained in the graphite electrode. As the material transport works in cold condition, the magnetic field in the hollow electrode is the most likely reason for the material blockage. Therefore, tests 2-4 were done batch-wise, and test 5 with precharged DRI pellets and continuous addition of slag-forming oxides through the hollow graphite electrode. The furnace chamber was flushed with 2 NI/min N₂ to minimize atmospheric influences. Steel crucibles with a centric pin were applied for the tests. After melting, the electrical data, the off-gas composition, the camera images, and the metallographic samples are observed.

Table 30: List of arc melting tests

Test no.	Gas	Material	Comment
1	N ₂ purging before the test; no gas addition during the test	0%C-DRI DR-Pellets + Fine addition	Pretest; Batch + continuous feed of DRI fines
2	2 NI/min N ₂	0%C-DRI DR-Pellets	batch
3	2 NI/min N ₂	C-DRI DR-Pellets	batch
4	2 NI/min N ₂	H ₂ -DRI Fines	batch
5	2 NI/min N ₂	0%C-DRI BF-Pellets + Slag forming oxides	Batch + continuous feeding of slag-forming oxides

Test 5 stands out since slag-forming oxides were added. In this case, BF-grade material was applied to increase the slag amount. To gain a slag similar to EAF-slag, 14.0 g CaO, and 3.1 g MgO were added. Based on the gangue composition and the residual FeO, a final slag with 10% MgO, 29% FeO, and B₂=1.8 can be expected.

7.1. Results

The following **Tables 31-35** list the tests' mass balances. Noticeably, the mass balances of all tests are negative, meaning a material loss. Since a reduction of residual iron oxide is minor compared to the noticed losses, dust and vaporization in the furnace chamber are the most likely reasons. This behavior aligns with the extreme values: While test 5, with a slag cover, shows just 2.8 g loss, the C-DRI in test 3 leads to a deviation of 27 g.

Table 31: Mass balance of arc melting test 1

	Before test	After test
$m_{\text{crucible}} / \text{g}$	1591.9	1611.8
$m_{\text{DRI}} / \text{g}$	49.7 (0%-DRI-DR) + 50 (DRI-Fines)	-
$m_{\text{filter}} / \text{g}$	1670	1670
$m_{\text{refr.ring}} / \text{g}$	596.0	600.8
$m_{\text{electrode}} / \text{g}$	55.7	55.0
Balance / g		-24.9
$l_{\text{electrode}} / \text{mm}$	110	102

Table 32: Mass balance of arc melting test 2

	Before test	After test
$m_{\text{crucible}} / \text{g}$	1593.7	1680.1
$m_{\text{DRI}} / \text{g}$	101.6	-
$m_{\text{filter}} / \text{g}$	1670.1	1676.3
$m_{\text{refr.ring}} / \text{g}$	489.1	491.0
$m_{\text{electrode}} / \text{g}$	57.8	57.6 + 2 g metal droplet
Balance / g		-11.3
$l_{\text{electrode}} / \text{mm}$	95	90

Table 33: Mass balance of arc melting test 3

	Before test	After test
$m_{\text{crucible}} / \text{g}$	1593.0	1671.4
$m_{\text{DRI}} / \text{g}$	101.7	-
$m_{\text{filter}} / \text{g}$	1670.5	1671.4
$m_{\text{refr.ring}} / \text{g}$	460.7	472.0
$m_{\text{electrode}} / \text{g}$	107.9	108.8
Balance / g		-27.0
$l_{\text{electrode}} / \text{mm}$	170	168

Table 34: Mass balance of arc melting test 4

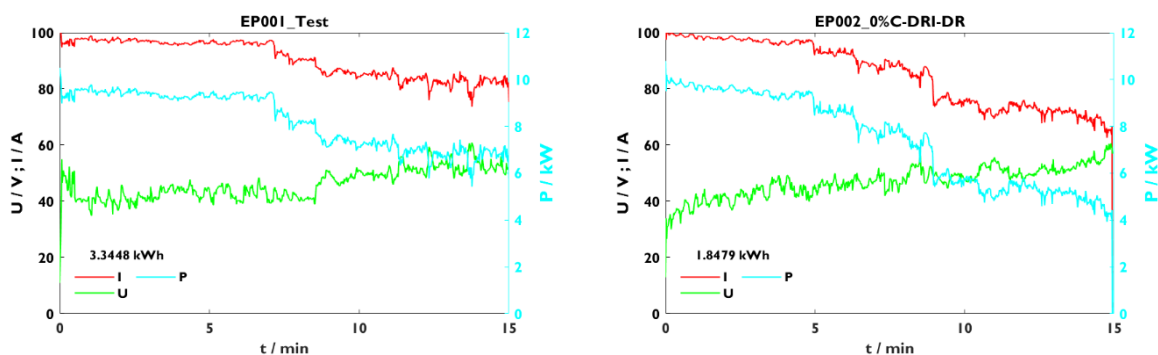
	Before test	After test
$m_{\text{crucible}} / \text{g}$	1593.6	1676.6
$m_{\text{DRI}} / \text{g}$	100.1	-
$m_{\text{filter}} / \text{g}$	1670.7	1671.4
$m_{\text{refr.ring}} / \text{g}$	470.5	472.3
$m_{\text{electrode}} / \text{g}$	107.5	107.2
Balance / g		-14.9
$l_{\text{electrode}} / \text{mm}$	107.5	107.2

Table 35: Mass balance of arc melting test 5

	Before test	After test
$m_{\text{crucible}} / \text{g}$	1591.7	1707.2
$m_{\text{DRI}} / \text{g}$	100.4 (0%-DRI-BF) + 14.0 (CaO) + 3.1 (MgO)	-
$m_{\text{filter}} / \text{g}$	1679.9	1679.9
$m_{\text{refr.ring}} / \text{g}$	-	-
$m_{\text{electrode}} / \text{g}$	63.3	62.5
Balance / g		-2.8
$l_{\text{electrode}} / \text{mm}$	102	99

Figure 92 shows voltage (U), current (I), and power (P) as a function of the time for all tests. The transformer current was set to 100 A at the beginning and then stepwise decreased, depending on the transformer temperature and the Voltage, using a silicon-controlled rectifier (SCR) controller. At test 5, the current was increased again during the last three minutes to study the stirring effect due to the electric arc.

In the beginning, all signals were relatively stable. The increasing voltage indicates the electrode burn-off. Nevertheless, significant fluctuations can be observed in the last five minutes, especially at test 4. Comparing this with the U vs. I plot in **Figure 93**, the samples with the highest fluctuations, C-DRI-DR (Test 3) and 0%C-DRI-Fines (Test 4), are located in the upper section of the diagram, indicating a higher voltage drop. On the other hand, test 5, with the slag-forming oxides, shows a very stable signal, indicating that the slag layer stabilizes the electric arc.



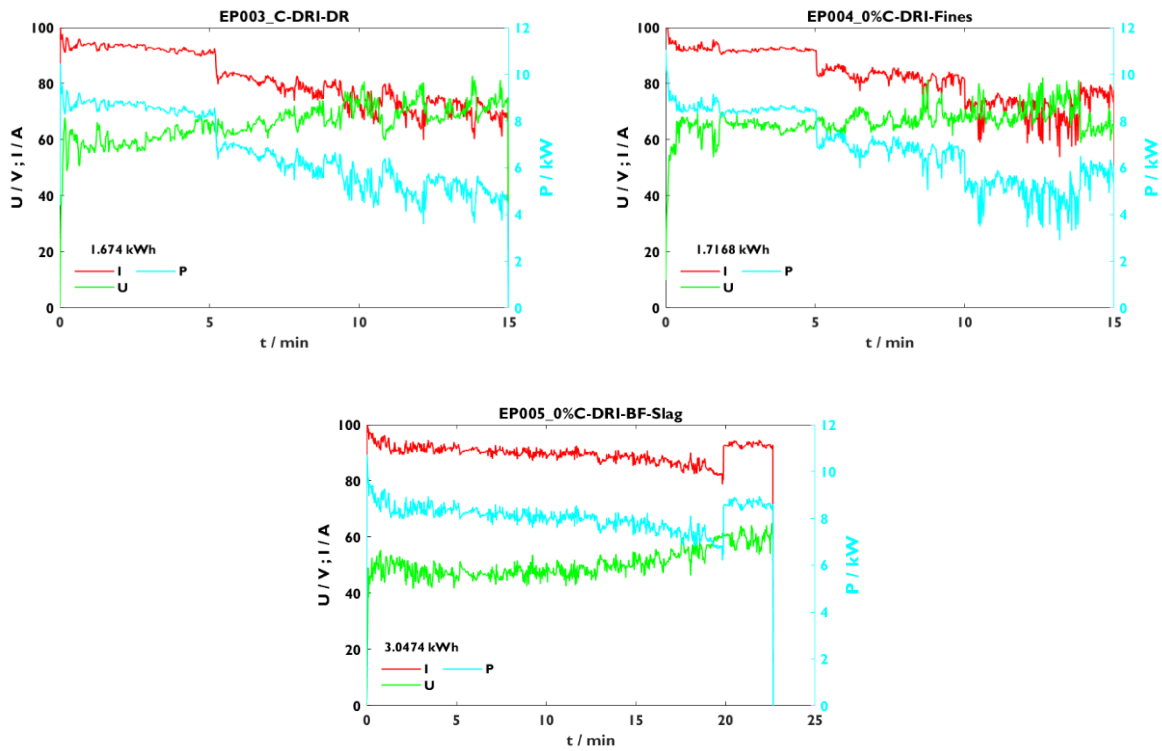


Figure 92: U, I, P vs. time for all arc melting tests

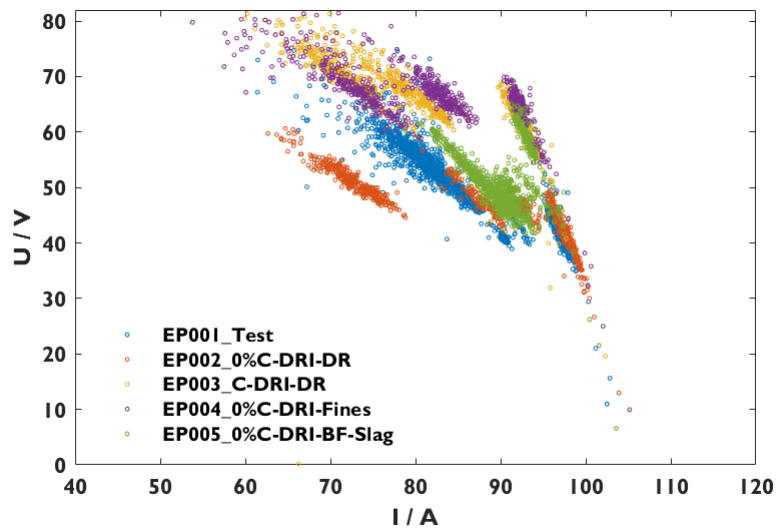


Figure 93: Voltage as a function of current as a cloud of points for all arc melting tests

Figures 94-98 show screenshots from the camera, with consecutive time from A) to D). No particular highlights for tests 1 (pretest) and 2 (0%C-DRI-DR) in Figure 94 and Figure 95 can be observed. The arc starts melting the sample at a specific spot and continues moving circularly. Due to the intensively cooled system and the steel crucible with its high thermal conductivity, the liquid pool is relatively small.

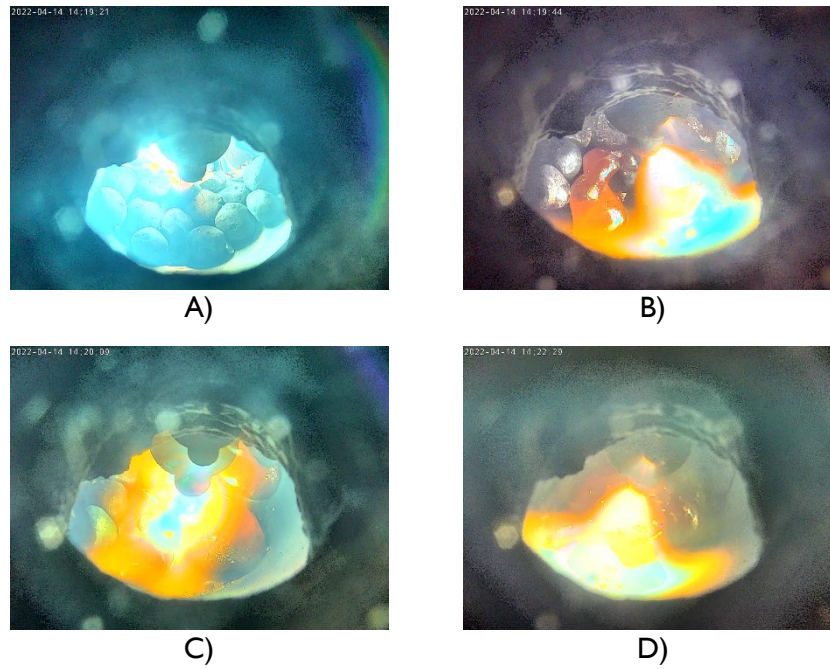


Figure 94: Screenshots from the thermal camera during the 0%-C-DRI-Test (Test 1 - pretest); time progressing from A) to D)

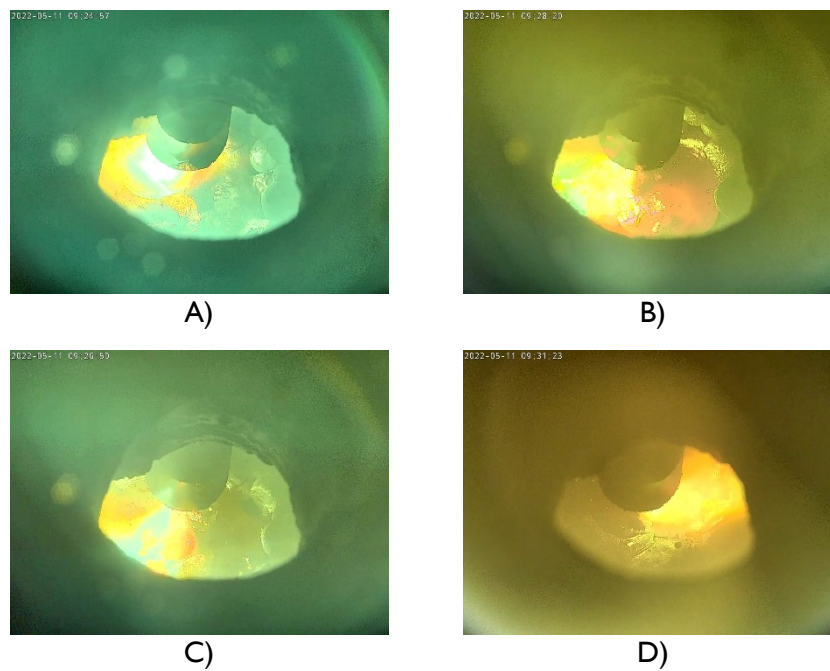


Figure 95: Screenshots from the thermal camera during the 0%-C-DRI-DR (Test 2); time progressing from A) to D)

While melting the carbon-bearing sample C-DRI-DR in **Figure 96**, tiny bubbles are noticed, visible in B). That indicates a reaction between residual iron oxide and carbon. Compared to the other tests, the overall impression looks opaque, indicative of CO gas.

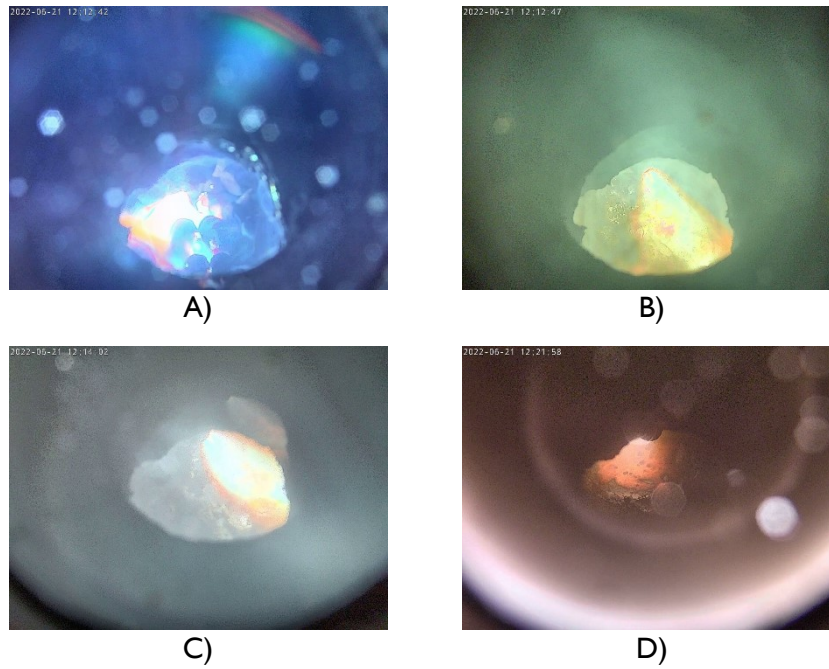


Figure 96: Screenshots from the thermal camera during the C-DRI-DR (Test 3); time progressing from A) to D)

As expected, the 0%-C-DRI-Fines images in **Figure 97** show similar behavior as the carbon-free pellets. However, it is more difficult to study the melting progress as the contrast of the pellets is missing.

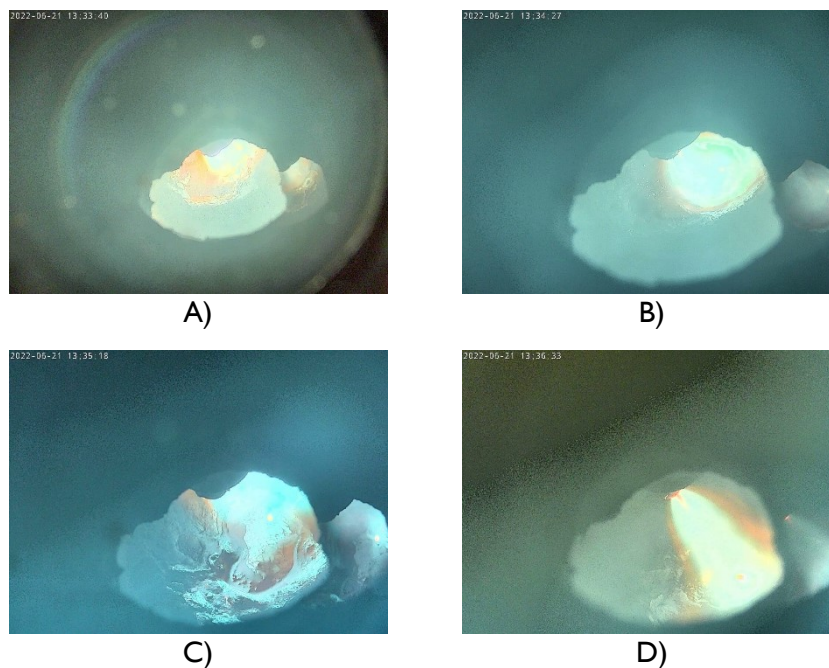


Figure 97: Screenshots from the thermal camera during the 0%-C-DRI-Fines (Test 4); time progressing from A) to D)

Figure 98 shows Test 5, with the additional slag forming oxides. Due to the small liquid spots, the dissolution can be observed well. In B), the white powder from charging is visible. Once the powder enters the liquid pool, it dissolves, showing small blisters (C). Compared to the other tests, the limited thermal conductivity of the slag layer seems to insulate the bath. Therefore, the whole sample occurs orange glowing in this case.

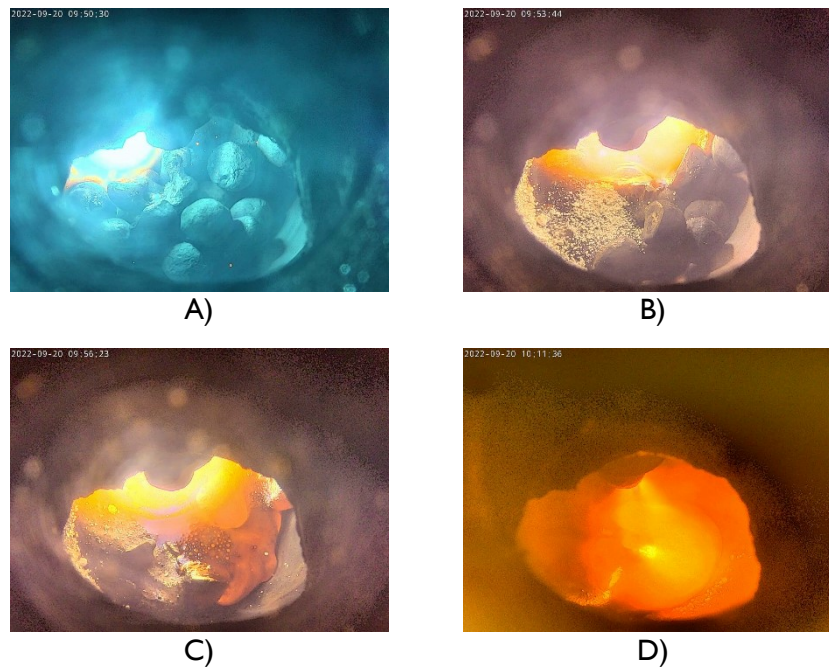


Figure 98: Screenshots from the thermal camera during the 0%-C-DRI-BF-slag (Test 5); time progressing from A) to D)

During the tests, a GAM mass spectrometer analyzed the off-gas composition. Unfortunately, the result files from tests 1 and 2 were lost due to an issue during the saving process. **Figures 99 to 101** give compositions from tests 3-5 with two different y-scales.

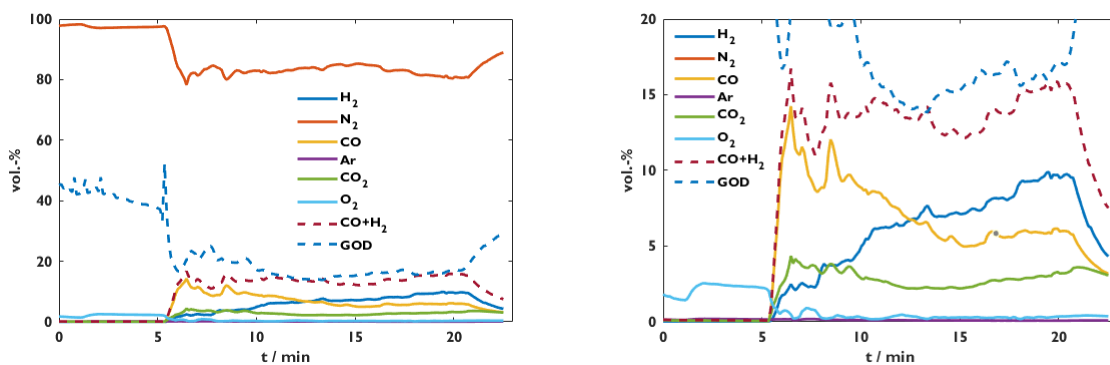


Figure 99: off-gas analyses of C-DRI-DR (Test 3) with two different y-scales; measurement started already before igniting the arc

The carbon-containing sample C-DRI-DR in **Figure 99** is characterized by its significant CO and CO₂ content from the reduction of residual FeO. Unexpectedly, also H₂ is measured. The most likely explanation for that is water in the furnace refractory. The higher the furnace temperature gets, the more is released. Due to the heterogeneous shift reaction hydrogen is formed. Therefore, the H₂ trend is upward with increasing experiment time.

Carbon-free tests 4 and 5 in **Figures 100** and **101** show similar behavior. Next to the increasing H₂ trend, small amounts of CO and CO₂ are measured, resulting from electrode burnup. The oxygen peak at the beginning of Test 4 could result from a time delay as the measurement takes place in the off-gas region.

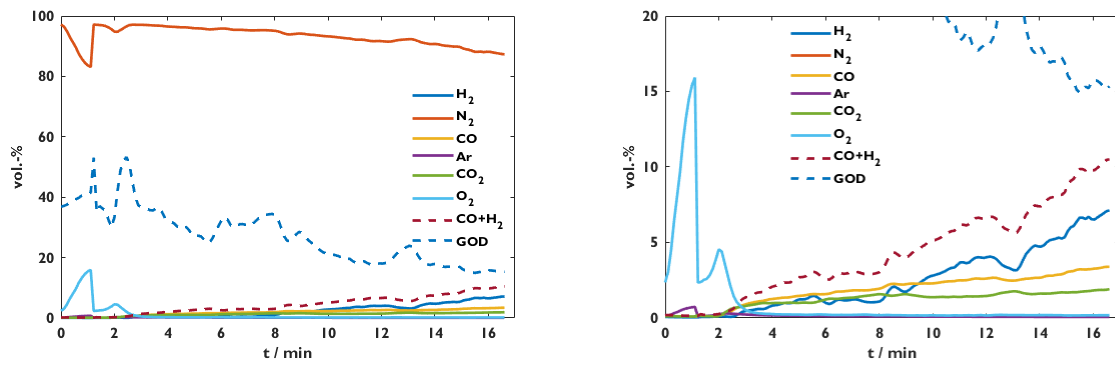


Figure 100: off-gas analyses of 0%-C-DRI-Fines (Test 4) with two different y-scales; measurement started already before igniting the arc

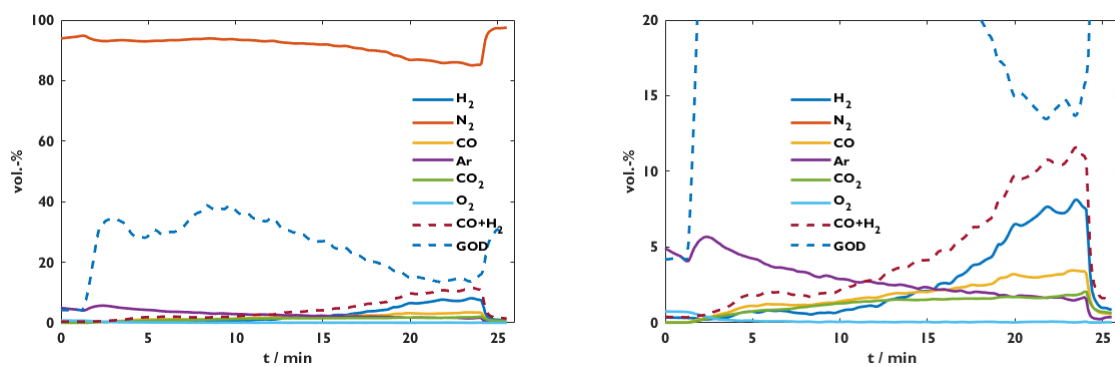


Figure 101: off-gas analyses of 0%-C-DRI-BF-slag (Test 5) with two different y-scales; measurement started already before igniting the arc

Figures 102 to 106 give the metallographic images of the cross-sections, as well as photographs from the top. The green line in the images defines this transition zone. After the experiments, all samples showed a red dust layer. The most likely explanation is dust, which reacts with the water vapor from the refractory to iron oxide or hydroxide.



Figure 102: Digital microscope image of the 0%-C-DRI-Test (Test 1 - pretest) cross-section

All slag-free samples merged with the crucible. Striking are the blisters in the carbon-free samples 1, 2, and 4, being the most pronounced for the fine DRI in **Figure 105**. The absence of blisters in the carbon-bearing sample correlates with the bubble formation during the test. The CO blisters remove nitrogen from the pool.

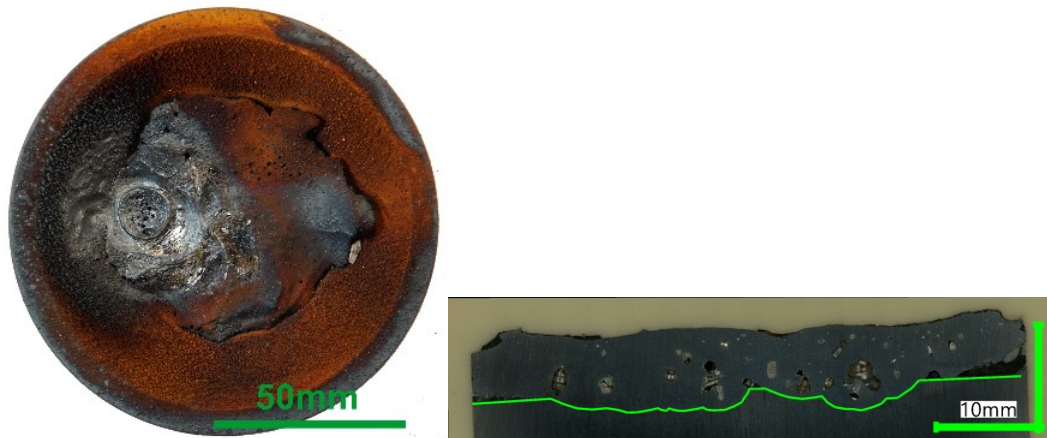


Figure 103: Photograph from the top and digital microscope image of the 0%-C-DRI-DR (Test 2) cross-section

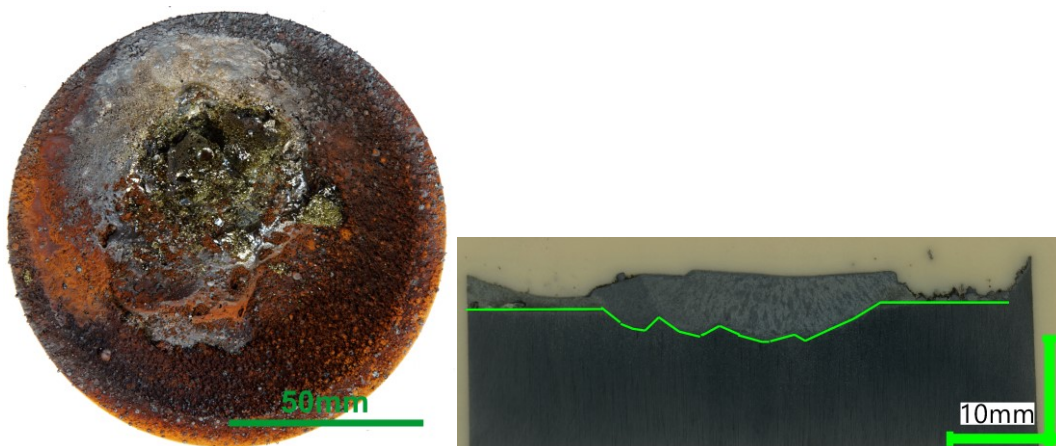


Figure 104: Photograph from the top and digital microscope image of the C-DRI-DR (Test 3) cross-section

Sample C-DRI-DR is characterized by forming a slightly yellow-colored top layer. This layer is described in detail below.

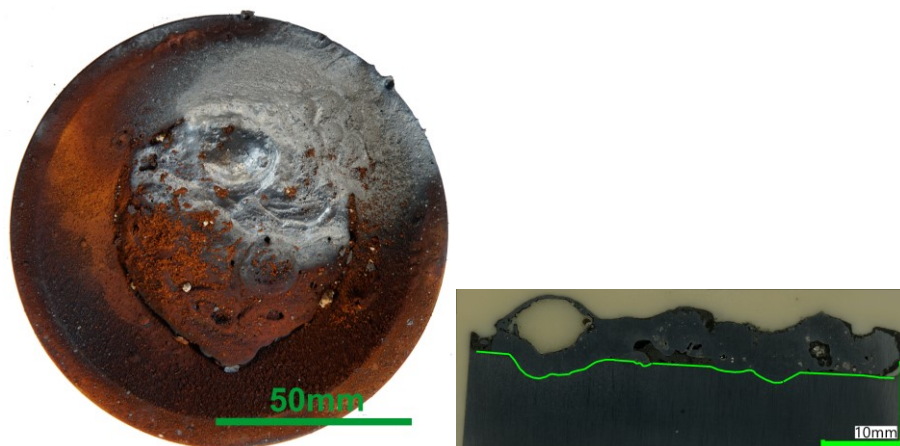


Figure 105: Photograph from the top and digital microscope image of the 0%-C-DRI-Fines (Test 4) cross-section

As seen in **Figure 106**, the addition of slag-forming oxides leads to a different behavior. On the one hand, the specimen is covered with a brittle slag layer. As seen in the cross-section, this slag layer is not just superficial; it frames the metallic part. The straight separation line between the sample and crucible indicates that the latter remains unmelted. This fact highlights the stirring effect of the electric arc since the slag density is lower than that of iron.

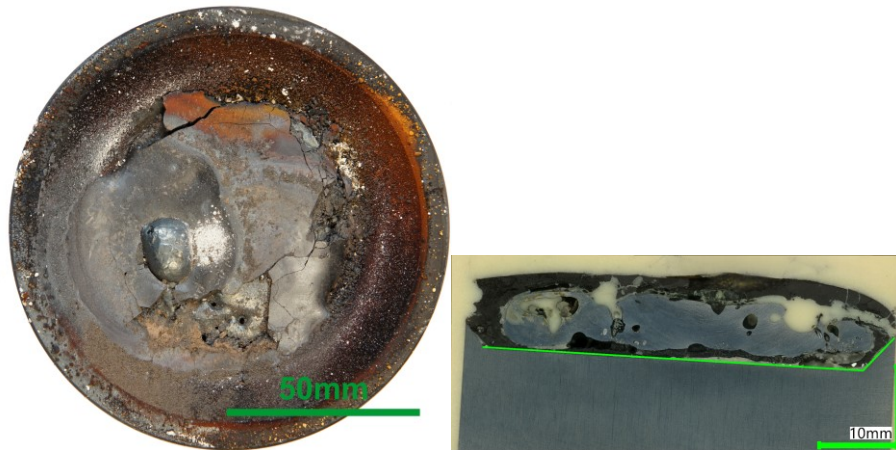


Figure 106: Photograph from the top and digital microscope image of the 0%-C-DRI-BF-slag (Test 5) cross-section

As mentioned above, the carbon-bearing sample forms a cover layer. Detailed digital microscope images are shown two-dimensionally in **Figure 107** and as a surface profile in **Figure 108**. While one side is spongelike and yellow, the other is smooth and grey with many blisters.

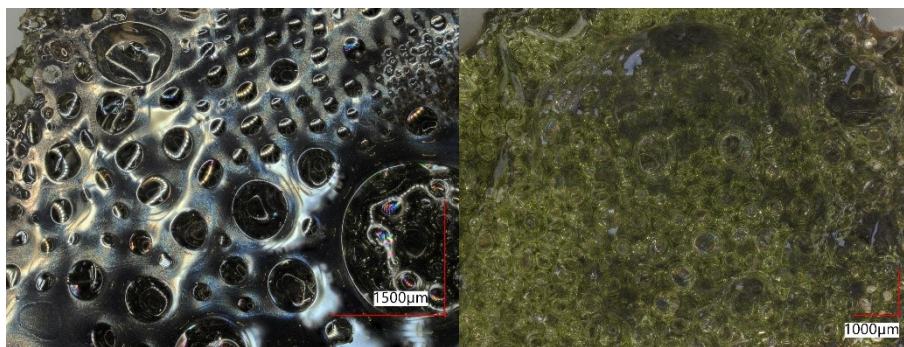


Figure 107: Cover layer of sample C-DRI-DR from both sides after melting

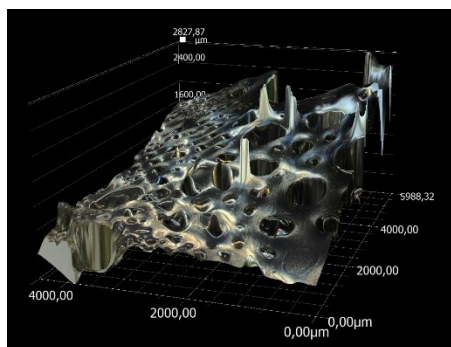


Figure 108: Surface profile of the C-DRI-DR cover layer

The chemical composition was determined by SEM-EDX from both sides and is summarized in **Table 36**. The phase is rich in SiO₂ and MnO with a basicity in the order of magnitude of the raw pellet, which indicates that the gangue oxides are locally collected. This behavior is likely the result of a stirring effect from CO bubbles.

Table 36: Chemical composition based on the element distribution, determined by SEM-EDX, wt.-%

	FeO	MnO	SiO ₂	Al ₂ O ₃	CaO	MgO	TiO ₂
grey, smooth	16.9	9.33	36.3	7.40	19.0	9.57	1.55
yellow, spongy	14.3	9.19	38.3	7.77	19.7	9.16	1.58

7.2. Discussion

Small scale melting tests were done using a laboratory hydrogen plasma smelting reduction (HPSR) facility. All samples behave well during melting batch-wise. Nevertheless, continuous DRI addition through the hollow electrode is not possible, likely due to the ferromagnetic properties of DRI.

All mass balances are negative, indicating losses because of dusting and evaporation. This loss is the most significant in test 3 with fine material. Applying carbon-containing DRI leads to the formation of CO bubbles. These bubbles can be observed visually with the camera and indirectly at the off-gas analysis. As a result, fewer blisters remain in the sample, indicating a lower nitrogen content. This observation correlates with industrial work from ArcelorMittal Lázaro Cardenas, done by Lule et al.^[168]. The authors report a negative correlation between the carbon in DRI and nitrogen in crude steel. Moreover, gangue oxides accumulate, while in carbon-free samples, gangue agglomerates remain distributed at some spots. Therefore, the latter is riskier regarding slag entrainment and accumulations of nonmetallic inclusions.

Last but not least, the operation with slag was tested via the addition of MgO and CaO. Two significant observations can be made. The electric arc leads to an intensive stirring of the melt. The slag layer is not localized as a top of the melt but instead frames the melt. This observation partly aligns with carbon-free material, that slag does not float up automatically, although its density is below that of iron. Secondly, the infrared image occurs orange glowing all over the sample, indicating a heat-insulating effect.

8. Slag foaming

In the electric arc furnace, the slag foaming behavior is a decisive factor for an efficient process. Chapters 3.7 and 8.1 presents a method for characterizing different slag concepts (acidic vs. basic and FeO-rich vs. FeO-poor) in case of their foamability as well as the results of a test series with EAF and smelter slags. In subchapter 8.2, the slag foaming index concept from 2.3.2 is used to perform a sensitivity analysis of iron and steelmaking slags concerning their foamability. Finally, these calculations are discussed critically and compared with the experiments.

8.1. Experimental slag foaming investigation

Based on the method described in 3.7, a series of slag foaming tests was performed with EAF and smelter-like slags. SAF (Submerged Arc Furnace) abbreviates the smelter slags in this chapter. **Table 37** lists all slag foaming tests with the respective major parameters. Foaming times were set between 0 s, for reference test no. 4, to 5 min for SAF test no. 10. Two types of Al₂O₃ crucibles were applied, Ø70 and Ø50 mm. The reason for that is the low thermal conductivity of refractory material. With this measure, the crucible's core could be quenched faster. It must be mentioned that longer times were planned for test 7. However, as seen in **Figure 112-B**, the slag foam surpassed the top of the crucible. This test is aborted to avoid a complete pass-over of the crucible and difficulties with the removal.

Table 37: List of slag foaming tests; m_{PC} ... mass petrol coke; m_{slag} ... mass of slag mixture; t ... foaming time (from PC addition to quenching); *Outer diameter x Inner diameter x Outer height

Test no.	Slag	m_{PC} / g	t / min	m_{slag} / g	Crucible*/mm
1	EAF-sat	7.2	1	153	Ø70xØ52x101
2	SAF	1.3	2	150	Ø70xØ52x101
3	EAF	6.6	2	149	Ø70xØ52x101
4	EAF-sat-reference	0	-	152	Ø70xØ52x101
5	EAF-sat	3.5	2	76.7	Ø50xØ44x70
6	EAF	3.3	1	77.1	Ø50xØ44x70
7	EAF-sat	3.5	1.5	76.4	Ø50xØ44x70
8	EAF	3.4	2.5	76.9	Ø50xØ44x70
9	EAF	3.4	3.5	76.6	Ø50xØ44x70
10	SAF	1.3	5	75.4	Ø50xØ44x70

After adding the carbon carrier, the EAF- and EAF-sat slags foamed immediately. Contrary to that, SAF slag in test 2 did not foam. To exclude a poor gas formation resulting from a low FeO-content and -activity, test 10 was done with nearly 10% iron oxide and an increased reaction time. Nevertheless, the result was the same. In test one, the undissolved particles being agglomerated and

not homogeneously distributed. Therefore, reference test 4 was done. The target of this reference was to get information about the location of solid precipitations in supersaturated slags.

8.1.1. Optical microscope evaluation

Figures 109-113 show the cross-sections. SAF-tests in **Figure 109** confirm that these samples do not foam. The only difference between them is the missing blowholes in sample 10. This absence may result from different cooling conditions due to the smaller crucible. As expected, the EAF-sat reference test in **Figure 112-A** looks similar to the SAF experiments.

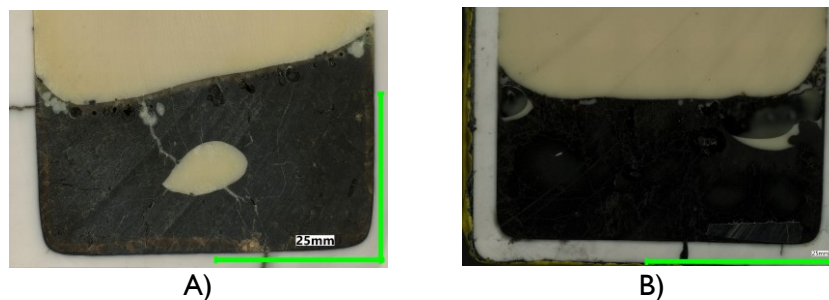


Figure 109: Digital microscope images of slag foaming A) Test 2; B) Test 10; see **Table 37**

All cores are mostly empty. It is not entirely clear if this is also the case during the experiments or a result of the low thermal conductivity of the crucible. The EAF-sat sample of test 1, reaction time = 1 min, in **Figure 110-A**, shows a horizontal layer accompanied by bubbles ≈ 1 mm in diameter. Comparing it with the corresponding EAF sample in B), only two larger bubbles can be observed. While no thin layer is present, the structure looks more sponge-like, with a network of very fine blisters.

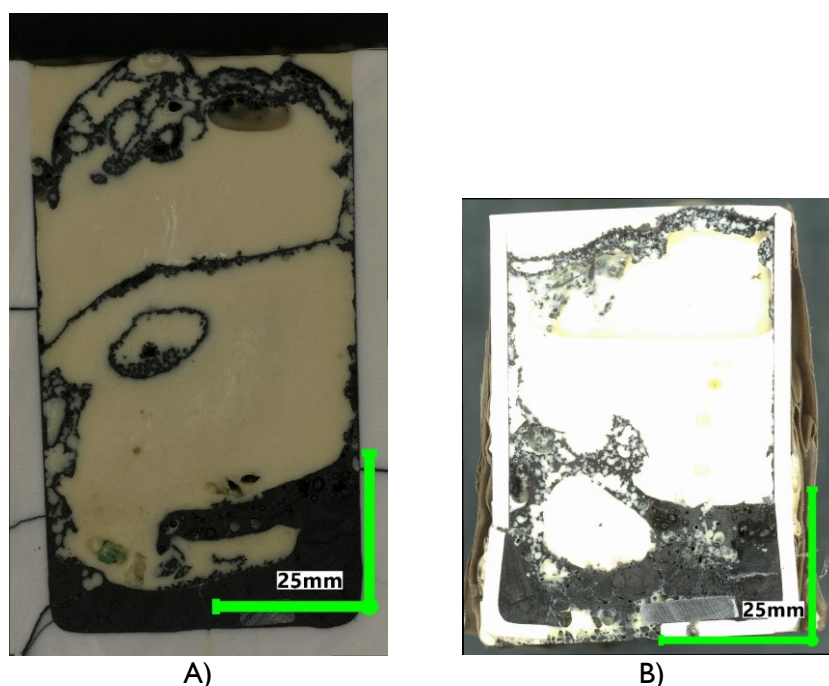


Figure 110: Digital microscope images of A) Test 1; B) Test 6; see **Table 37**

The same can be said about the 2 min foaming tests in **Figure 111**. Although foam in test 5 collapsed due to intensive stirring, visible by the central depression, structures look like the 1 min samples.

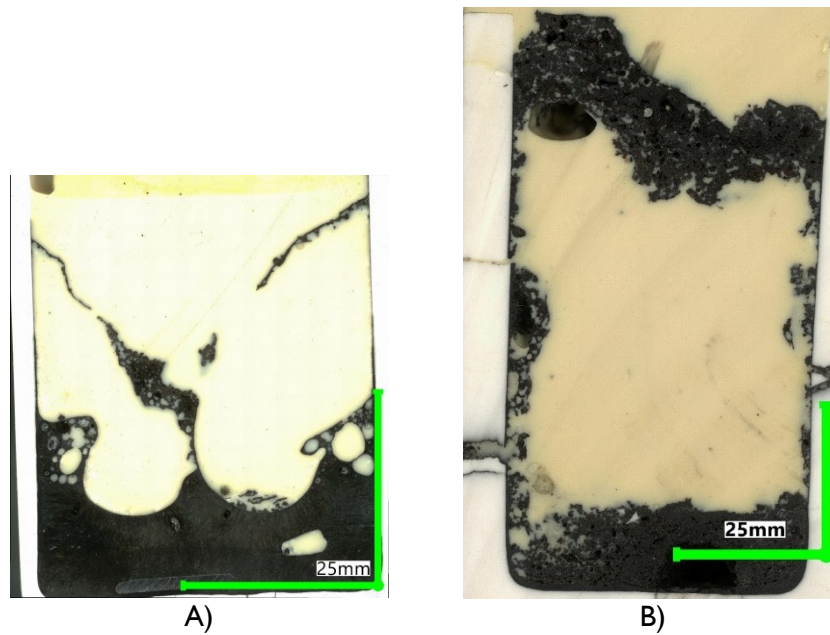


Figure 111: Digital microscope images of slag foaming A) Test 5; B) Test 3; see **Table 37**

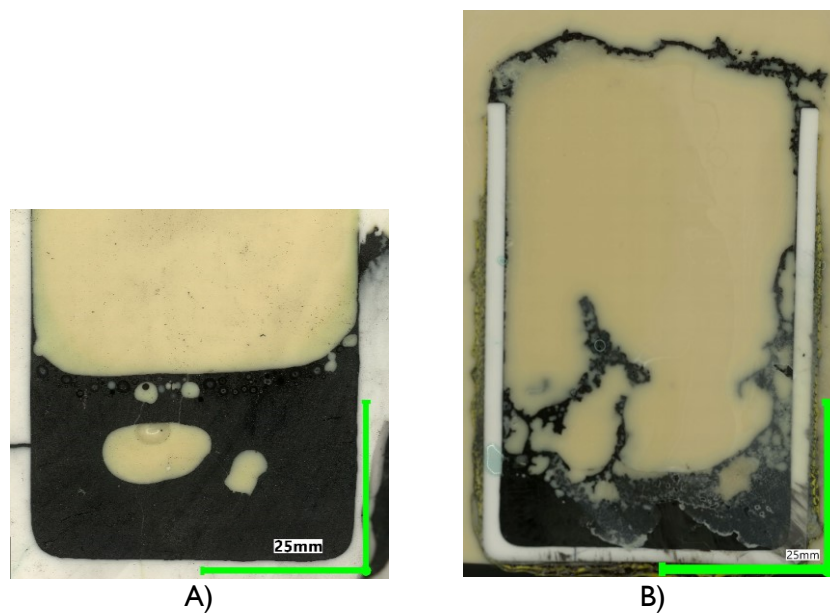


Figure 112: Digital microscope images of slag foaming A) Test 4; B) Test 7; see **Table 37**

The 1.5 min EAF-sat test no. 7 in **Figure 112-B** correlates to this observation. Nevertheless, the EAF samples with 2.5 and 3.5 min reaction times in **Figure 113** do not confirm the trend of a sponge-like structure in unsaturated EAF-slag. However, the broad layer in **Figure 113-A** and the thin layer in B) indicate that a fine blister network is initially formed in unsaturated slag. This network agglomerates and forms bigger bubbles.

While the unsaturated slags slightly overshoot the small crucible in the center after 2.5 and 3.5 min, the saturated slag in the small crucible overshoot it significantly faster. Having a closer look at the meniscus shapes, samples in **Figure 113** show depressions in the crucible near regions. Contrary, test 7 in **Figure 112-B** forms a nearly circular shape. This behavior indicates the saturated slags to be stiffer. Unfortunately, test 5 was stirred too intensively during the foaming leading to a collapsing foam layer. Therefore, it breaks out of this trend.

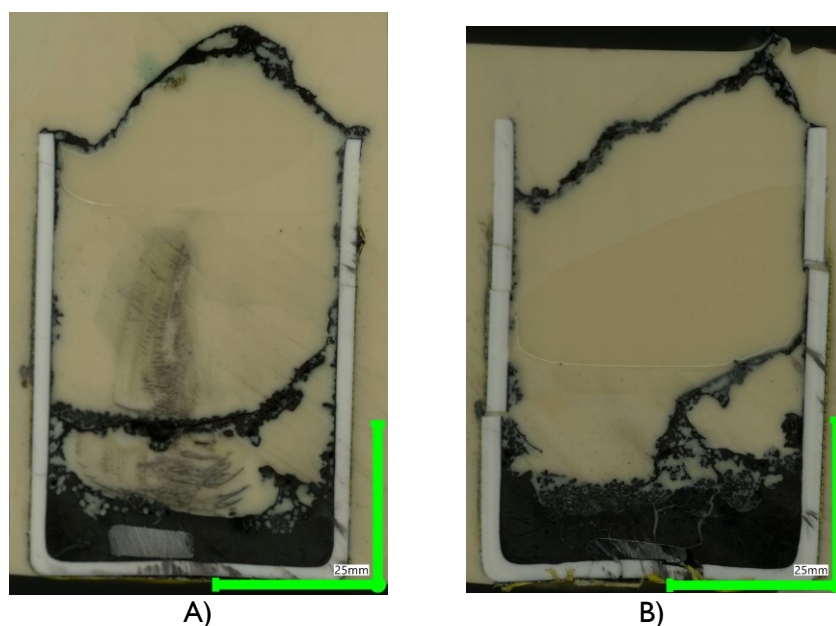


Figure 113: Digital microscope images of slag foaming A) Test 8; B) Test 9; see **Table 37**

Figure 114 shows the normalized volume increase from equation 21. The reference test and the SAF tests show a slight volume increase. That, on the one hand, results from blowholes and may, on the other hand, result from deviations between the calculated density and the actual density. The EAF slags show a volume increase between 2 and 3.5, with the lower being an outlier due to a collapsing foam. Between the EAF and EAF-sat slags, no significant difference can be noticed.

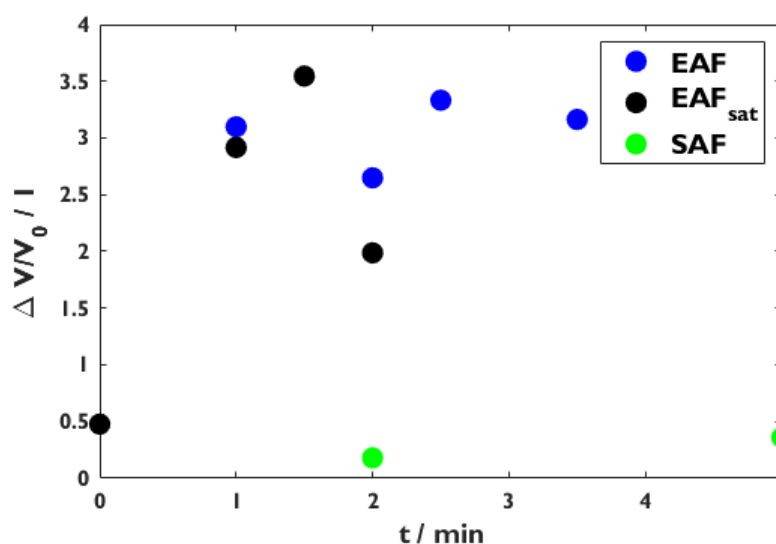


Figure 114: Normalized increase in volume

8.1.2. SEM-EDX distribution mappings and chemical analyses

Selected samples, no. 1, 4, 6, 7, 8, 9, and 10, are analyzed using SEM-EDX analysis. The target of this was to answer the following questions:

- Can metallic iron be found? Does it remain in the foam or sink to the bottom?
- Are the samples homogeneous, or can one notice segregation?

Residual petrol coke particles are ignored. Measuring light elements like C is difficult with this method; further, the embedding mass and the sputtering layer also contain carbon. **Figures 115-120** show images of sample 1, EAF-sat. Three locations are analyzed and visualized as SEM images, as well as distribution mappings. This chapter contains the central images to highlight the findings. The appendix contains the other SEM images, EDX mappings, and line scans for further information. Characteristic spots are analyzed in detail, with markers in the SEM images and the corresponding compositions in

Table 38. In the foam in **Figures 115** and **116**, metallic iron droplets can be seen. Looking at the Matrix, regions, poor in Al and rich in Ca and Si, occur, indicating a network of Calciumsilicates. Although Mg is relatively homogeneously distributed, some regions seem enriched together with Fe. In the SEM image, these regions appear lighter than the matrix but darker than metallic iron. This appearance is an indication of magnesiowustite since Al is depleted. One of the Fe droplets is surrounded by an Mg layer, while the other is not. A possible explanation is the reaction of carbon with FeO in the melt and iron oxides in the (Mg,Fe)O particles.

Elektronenbild 24

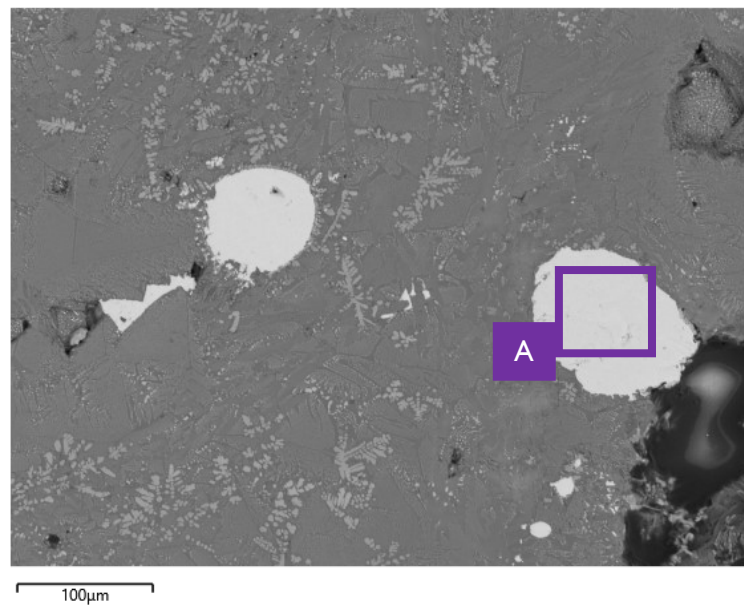
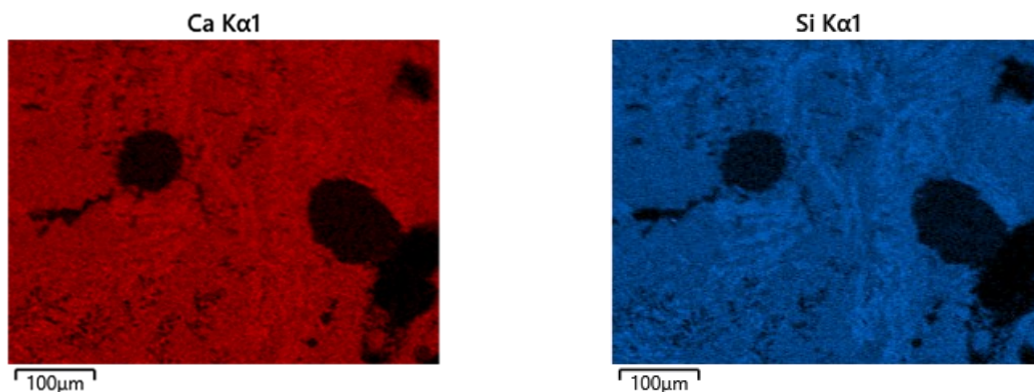


Figure 115: SEM image of foaming sample 1 EAF-sat, upper part of the crucible; A) see **Table 38**



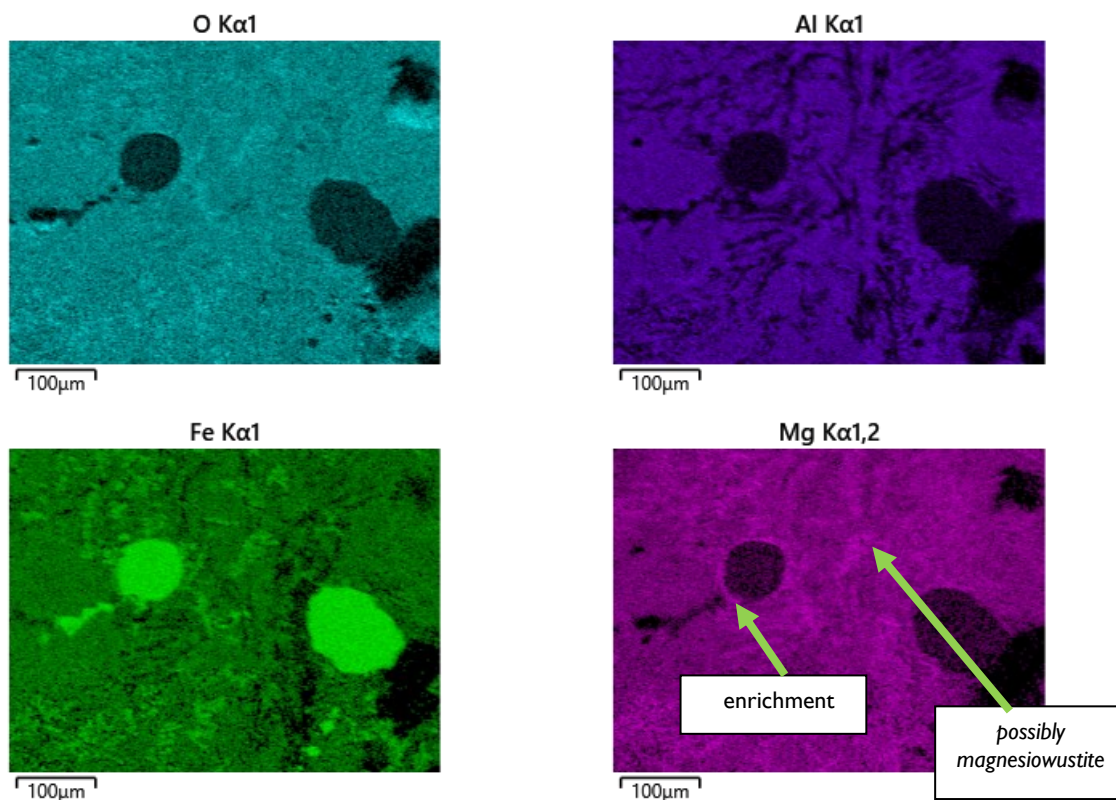


Figure 116: EDX-mapping of foaming sample I EAF-sat, upper part of the crucible; corresponding SEM image see **Figure 115**

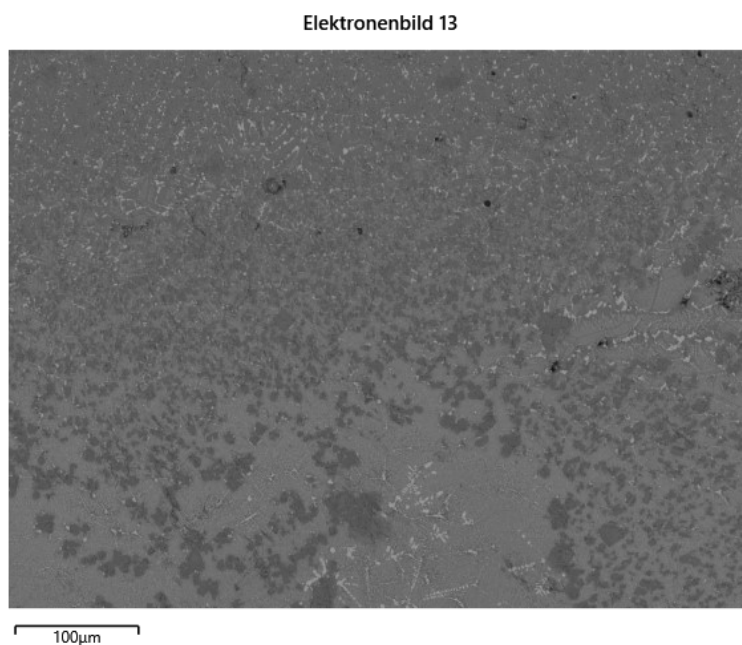


Figure 117: SEM image of foaming sample I EAF-sat, lower and outer part of the crucible

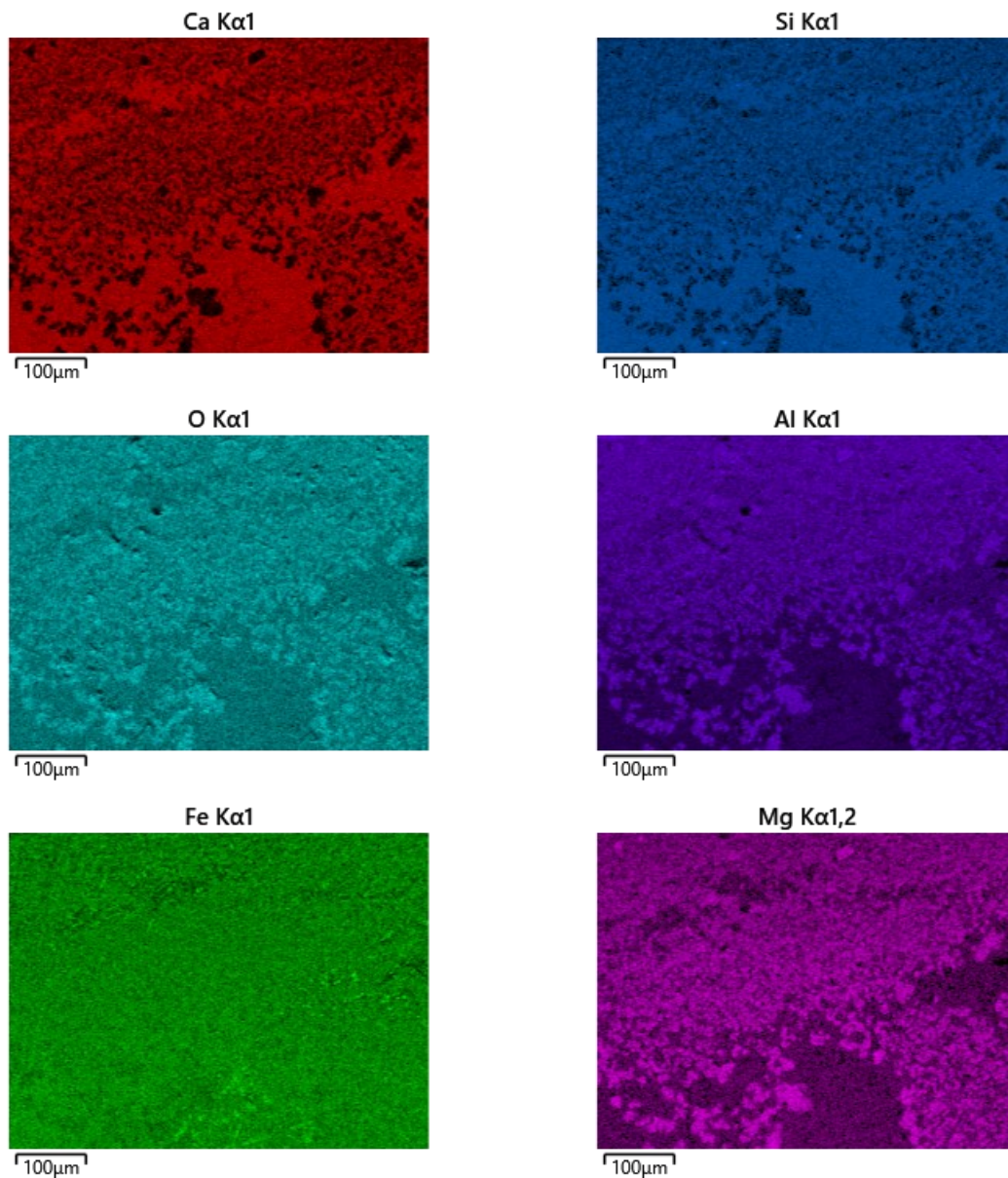
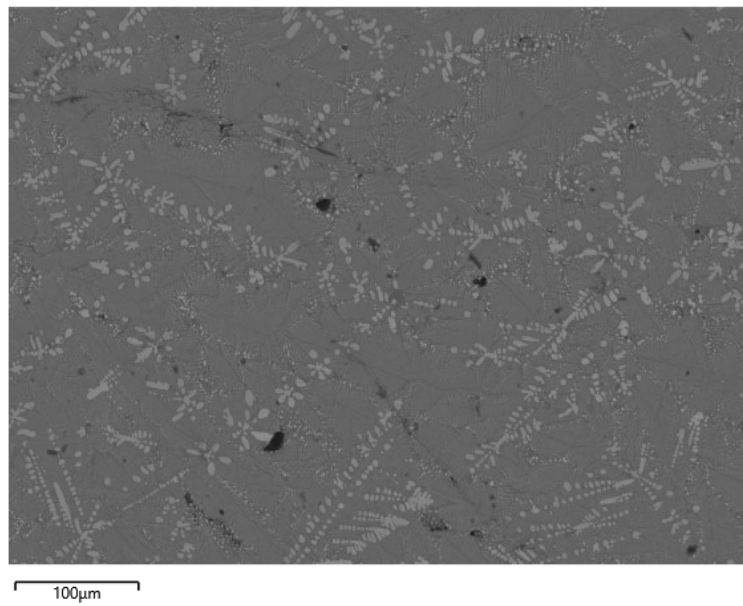
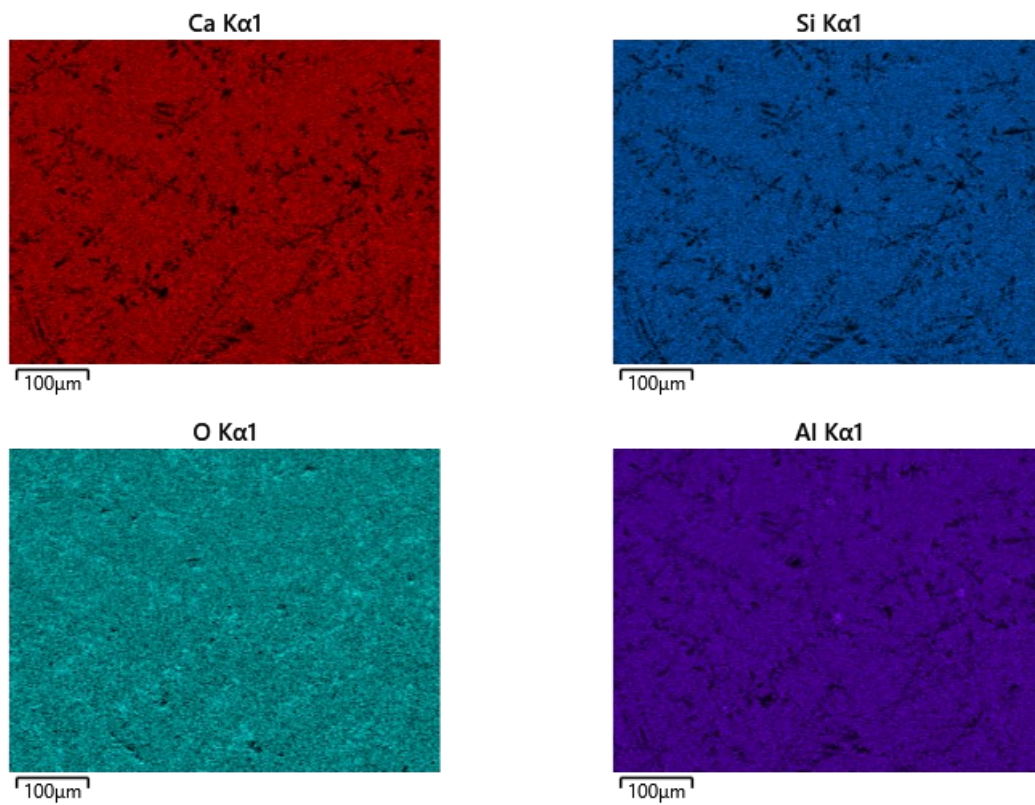


Figure 118: EDX-mapping of foaming sample 1 EAF-sat, lower and outer part of the crucible; corresponding SEM image see **Figure 117**

Looking closely at the surface-near region in **Figures 117** and **118**, the Mg- and Al-rich particles are eye-catching. The most promising explanation is the formation of Magnesium-Alumina-Spinel (MA). Although this is of little importance for the test results, it is a significant factor regarding the method. This layer prevents the crucible from dissolution.

Elektronenbild 17

**Figure 119:** SEM image of foaming sample I EAF-sat, lower and central part of the crucible

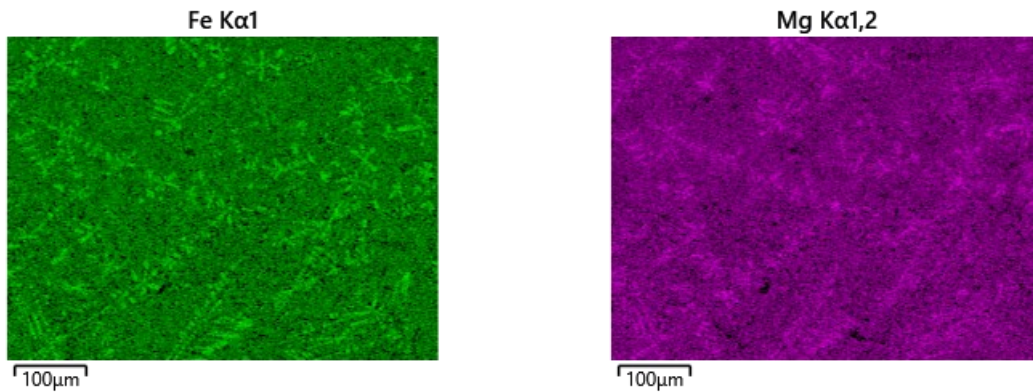


Figure 120: EDX-mapping of foaming sample 1 EAF-sat, lower and central part of the crucible; corresponding SEM image see **Figure 119**

The center in **Figures 119** and **120** contains a Si, Ca, and Al matrix and Fe and Mg-enriched dendrites. These dendrites indicate magnesiowustite (MW) but also highlight the limited cooling rate in the crucible center. Since the thermal conductivity of slag and refractory are poor, the heat is removed moderately.

Figures 121 to **124** give the images of sample 4, EAF-sat reference, without foaming. The upper part in **Figures 121** and **122** is striking in two ways. Next to the Mg- and Fe-enriched dendrites, the sample shows a layerwise structure. These ledges appear to be calcium silicates.

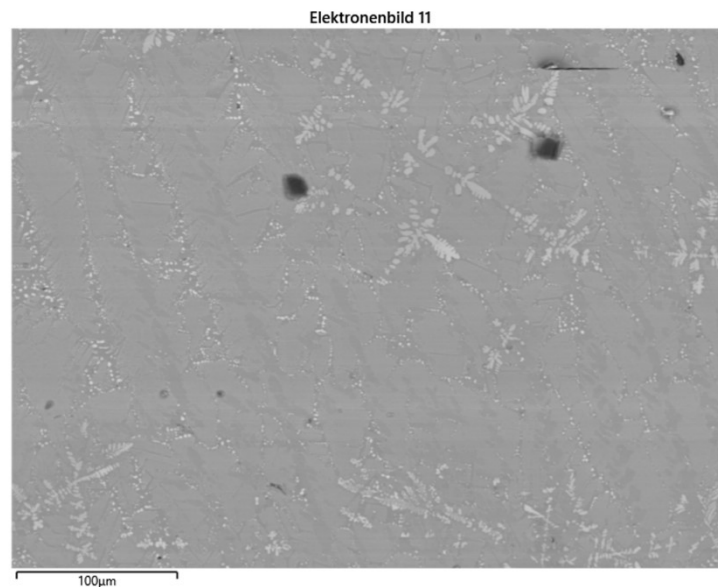


Figure 121: SEM image of foaming sample 4 EAF-sat-reference, upper and central part of the crucible

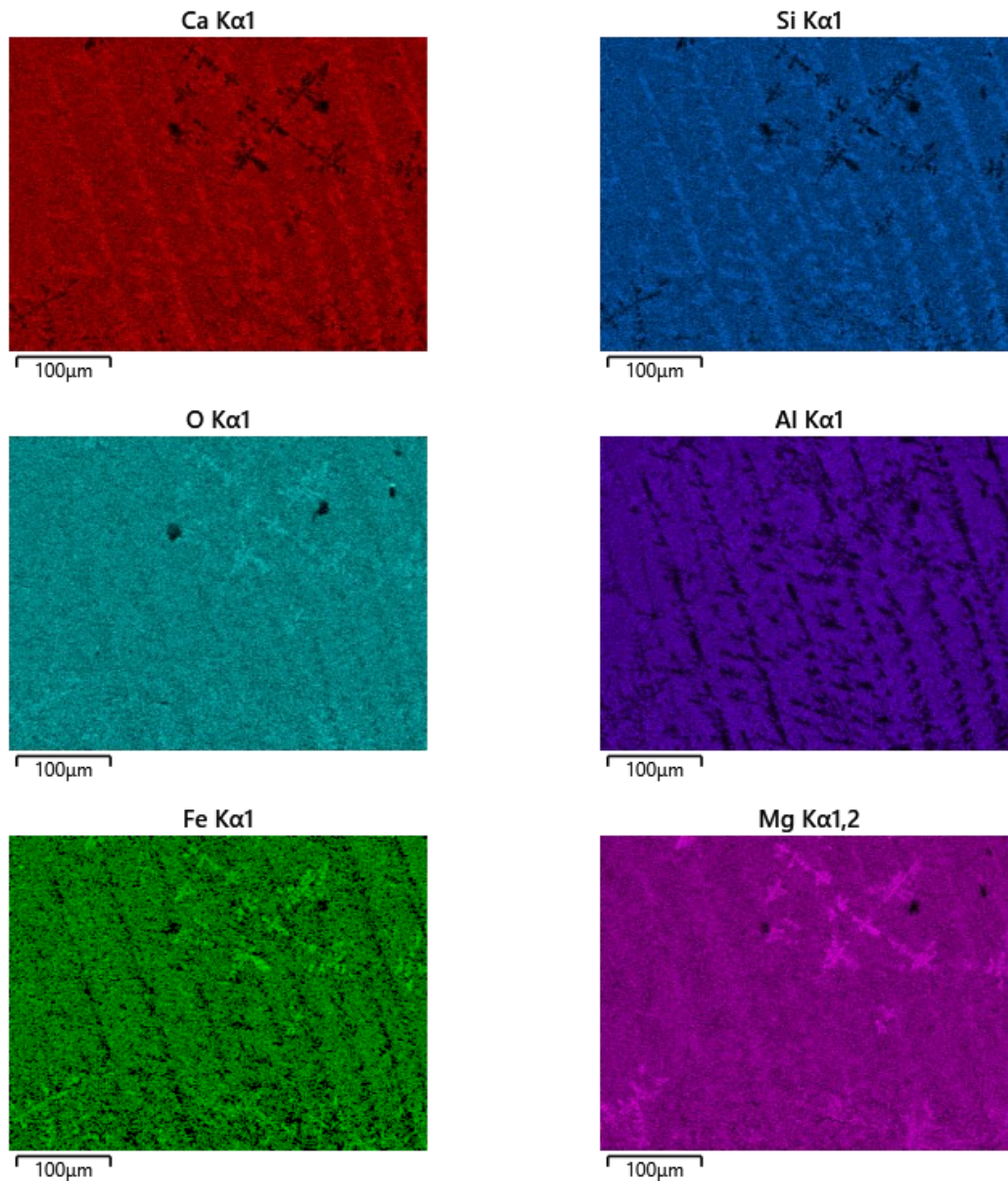


Figure 122: EDX-mapping of foaming sample 4 EAF-sat-reference, upper and central part of the crucible; corresponding SEM image see **Figure 121**

The lower part of the crucible in **Figures 123** and **124** again shows a Ca-, Si- and Al-rich matrix. Further, MA can be seen, as well as Fe-enriched dendrites. Contrary to the samples above, these dendrites do not appear rich in Mg. Due to extensive Al_2O_3 dissolution from the crucible, the slag forms MA and depletes the dendrites from MgO.

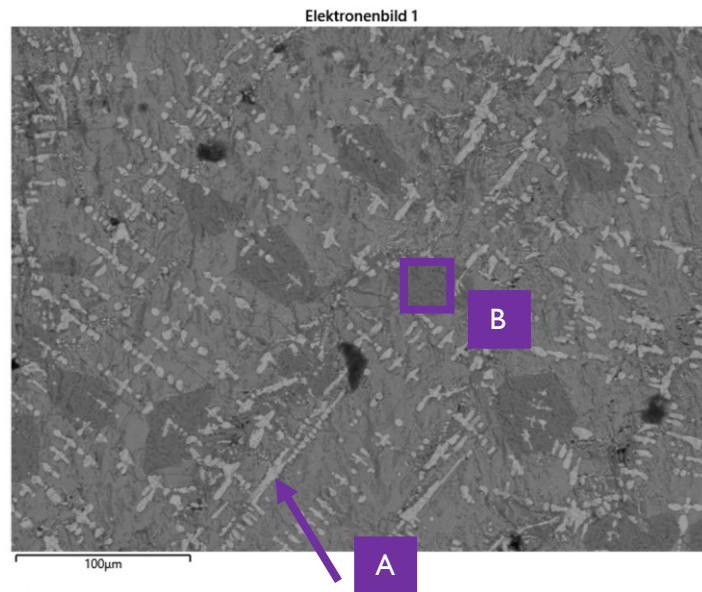
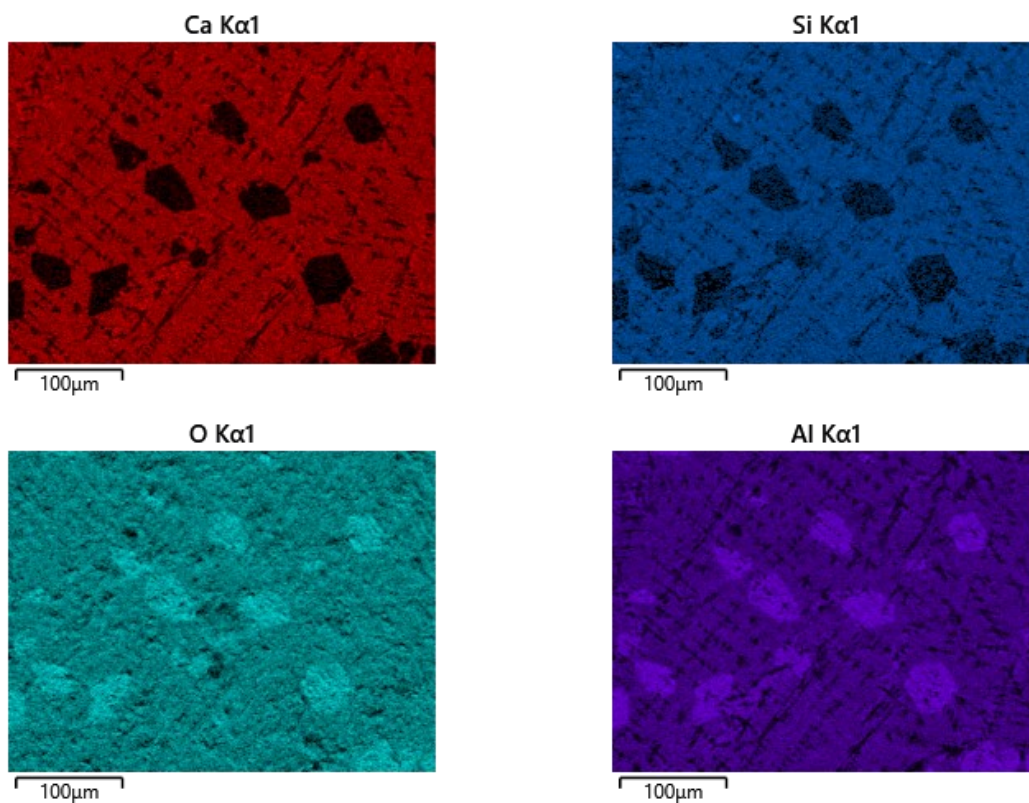


Figure 123: SEM image of foaming sample 4 EAF-sat-reference, lower and central part of the crucible; A) and B) see **Table 38**



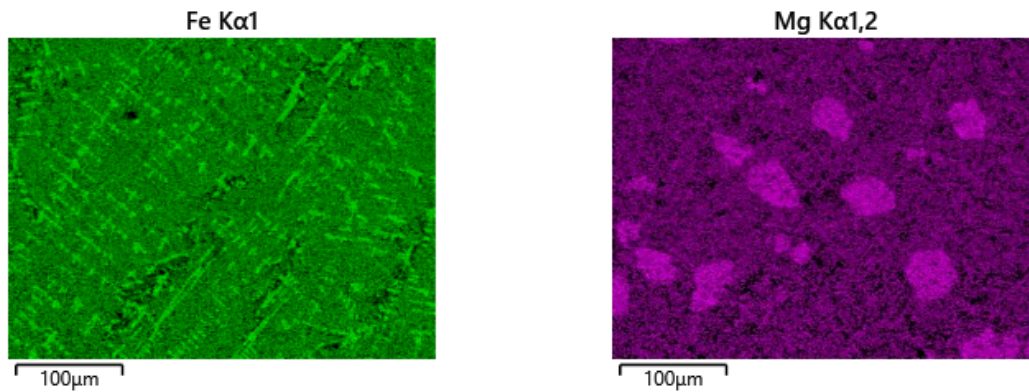


Figure 124: EDX-mapping of foaming sample 4 EAF-sat-reference, lower and central part of the crucible; corresponding SEM image see **Figure 123**

The mappings of the unsaturated EAF-slag test no. 6 are shown in **Figures 125 to 128**. Similar to above, the foam in **Figures 125 and 126** contains metallic iron surrounded by an Mg-rich layer. Further, it is noticeable that lots of Calcium silicates appear in the foam, and Al is primarily located in the matrix. The details confirm that since B) appears depleted from FeO, compare **Table 38**.

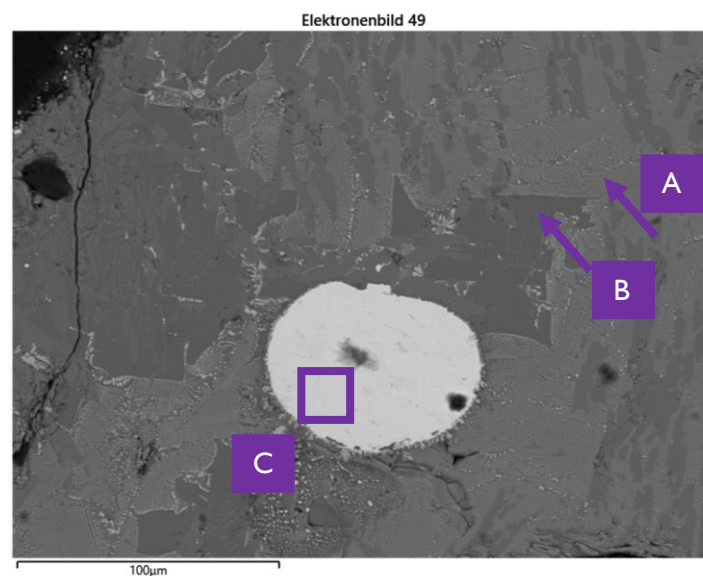
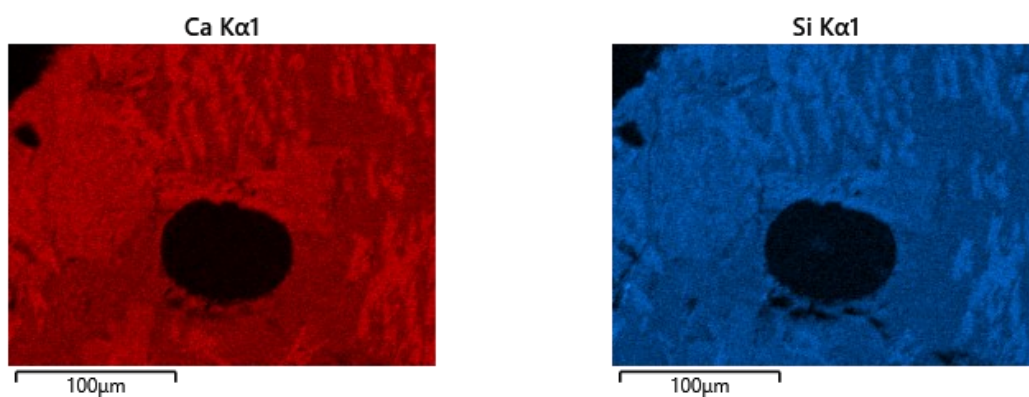


Figure 125: SEM image of foaming sample 6 EAF, part of the foam; A), B), and C) see **Table 38**



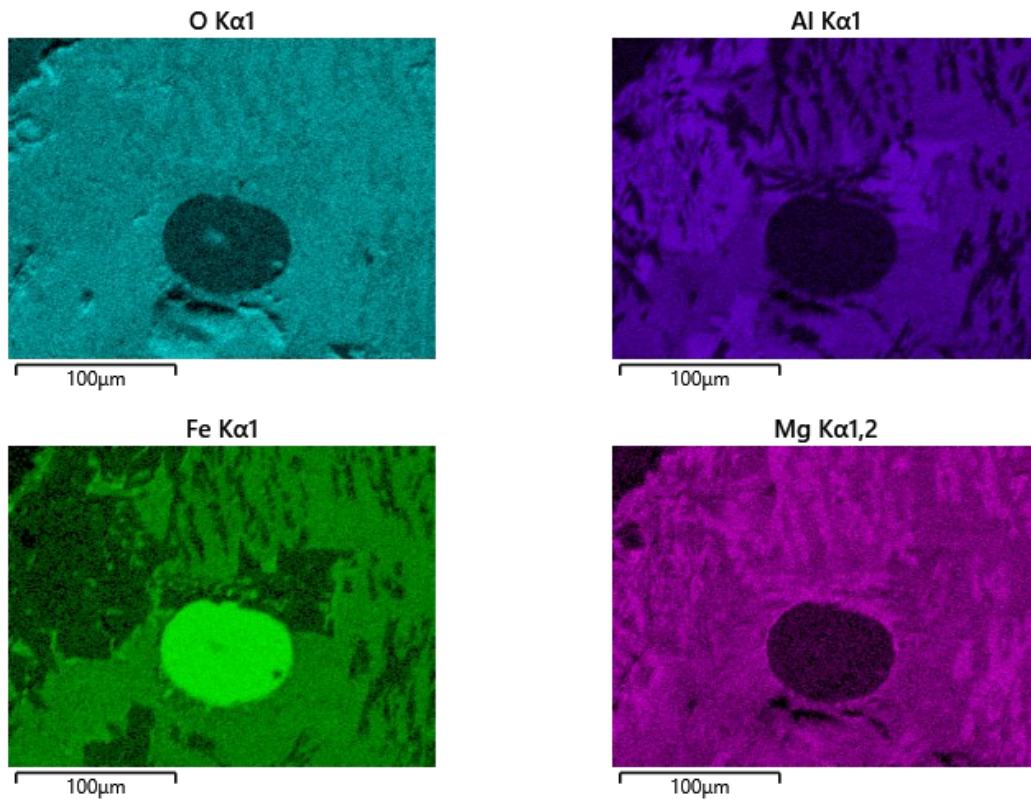


Figure 126: EDX-mapping of foaming sample 6 EAF, part of the foam; corresponding SEM image see **Figure 125**

Unexpectedly, also in this sample, Mg- and Fe-enriched particles can be noticed, indicating MW precipitations, as seen in **Figures 127** and **128**. However, the details in **Table 39** do not confirm this observation. The differing Ca and Fe distribution indicate inaccurate measurement results.

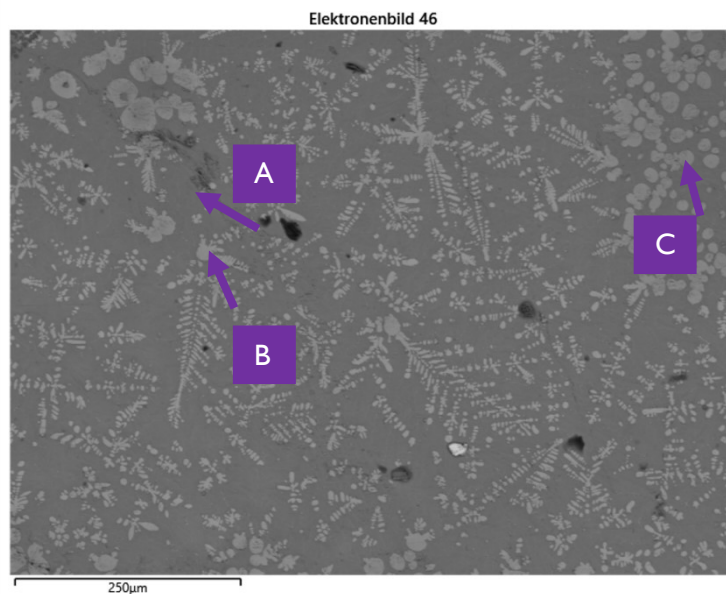


Figure 127: SEM image of foaming sample 6 EAF, lower and central part of the crucible

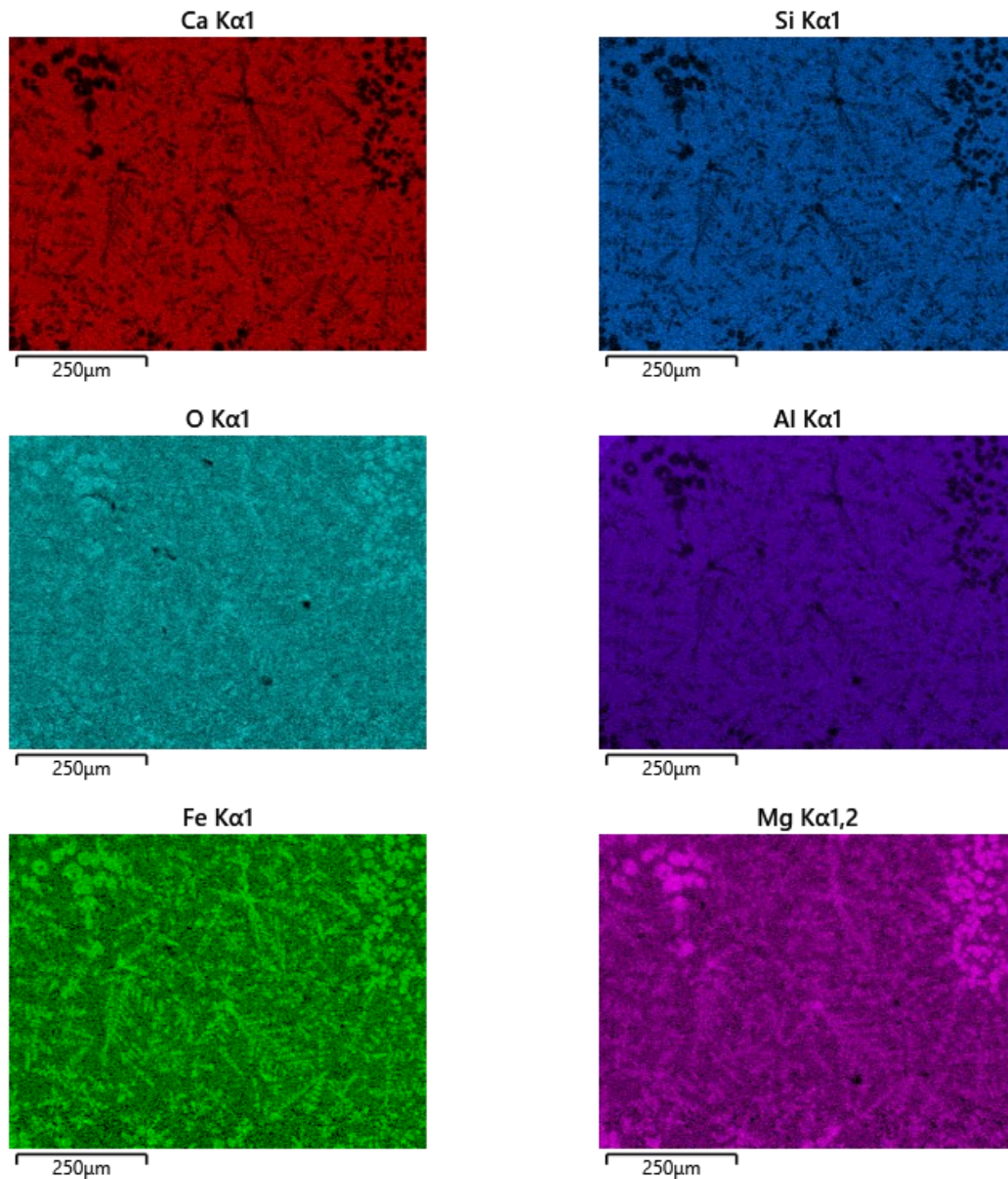


Figure 128: EDX-mapping of foaming sample 6 EAF, lower and central part of the crucible; corresponding SEM image see **Figure 127**

Figures 129 and 130 show the surface-near region of the SAF-test no. 10. This surface-near layer is similar to the EAF samples. Unlike the other samples, see detail A), FeO-enriched acidic ledges can be observed. Detail B) shows a small spot of metallic iron.

Elektronenbild 30

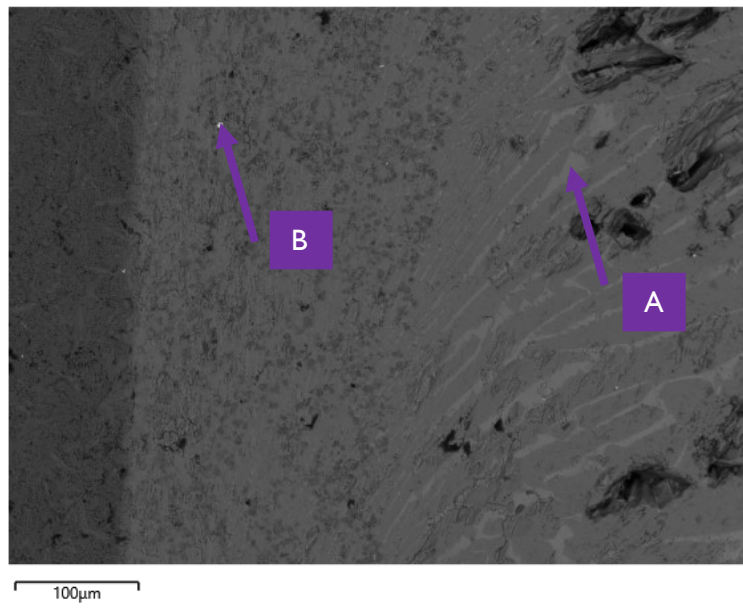
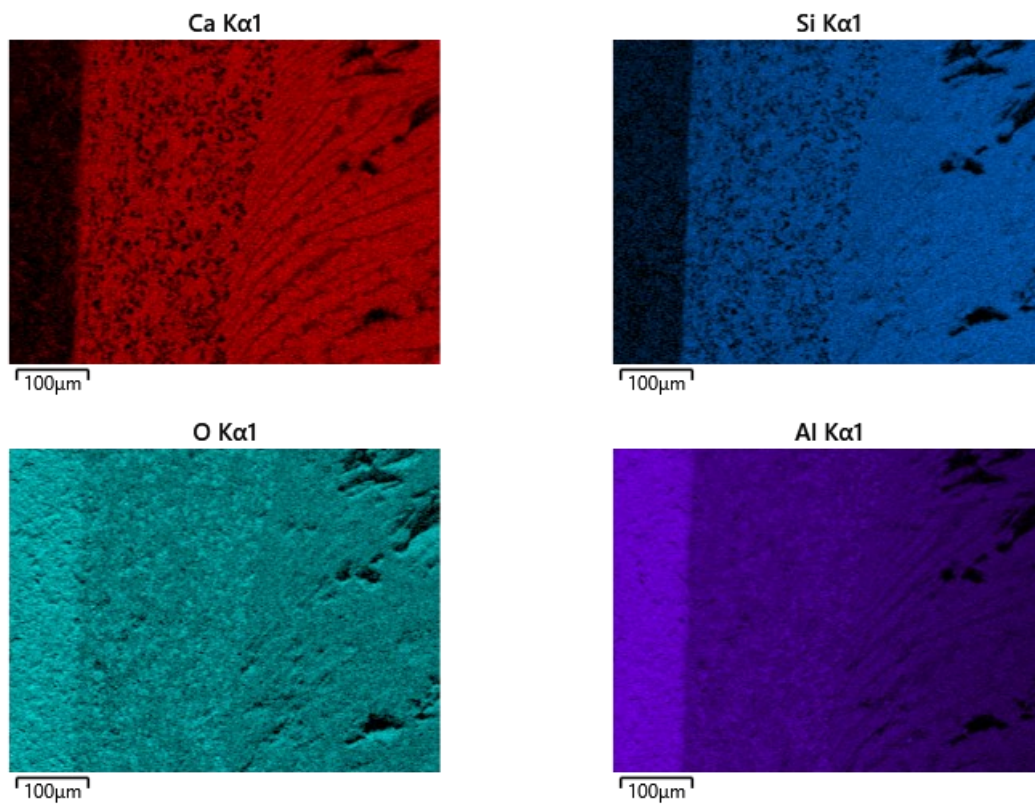


Figure 129: SEM image of foaming sample 10 SAF, lower and outer part of the crucible



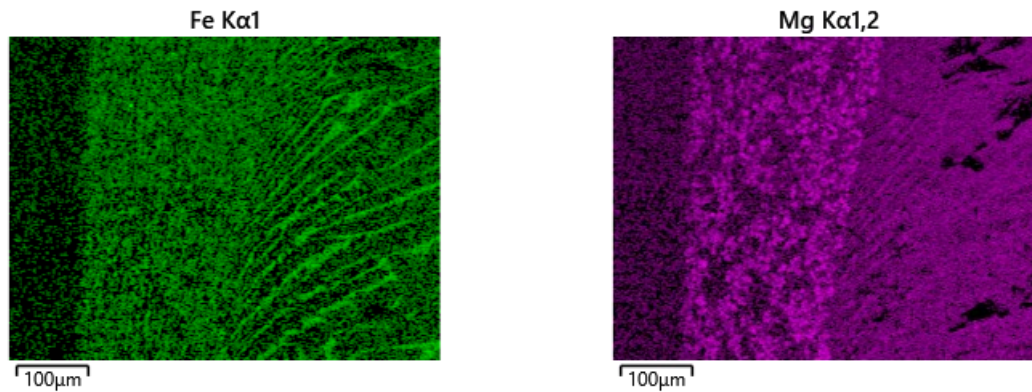


Figure 130: EDX-mapping of foaming sample 10 SAF, lower and outer part of the crucible; corresponding SEM image see **Figure 129**

Table 38: Analyses of the Figures' detailed spots; * If not metallic, Fe was assumed to be 100% FeO.; * Balanced by traces of oxides, possibly resulting from margin blur.

Figure	Region	CaO	SiO ₂	Al ₂ O ₃	MgO	FeO*	B2	Fe _{met}
Figure 115	A	-	-	-	-	-	-	100
Figure 123	A	1.9	0.0	0.7	6.6	90.8	-	-
	B	0.4	0.4	56	9.9	33	1.0	-
Figure 125	A	31	22	15	5.8	26	1.4	-
	B	41	26	27	2.7	2.8	1.6	-
	C	-	-	-	-	-	-	100
Figure 127	A	35	23	20	3.6	18	1.5	-
	B	15	11	11	15	48	1.4	-
	C	36	24	19	5.3	17	1.5	-
Figure 129	A	15	34	16	6.6	29	0.4	-
	B ^x	-	-	-	-	-	-	96.6

Lastly, macroscopic compositions are determined. Therefore, the samples are subdivided into sections, as shown in **Figure 131**. Besides the superficial outer part, core, and transition, the foams in samples 1, 6, 7, 8, and 9 are analyzed.

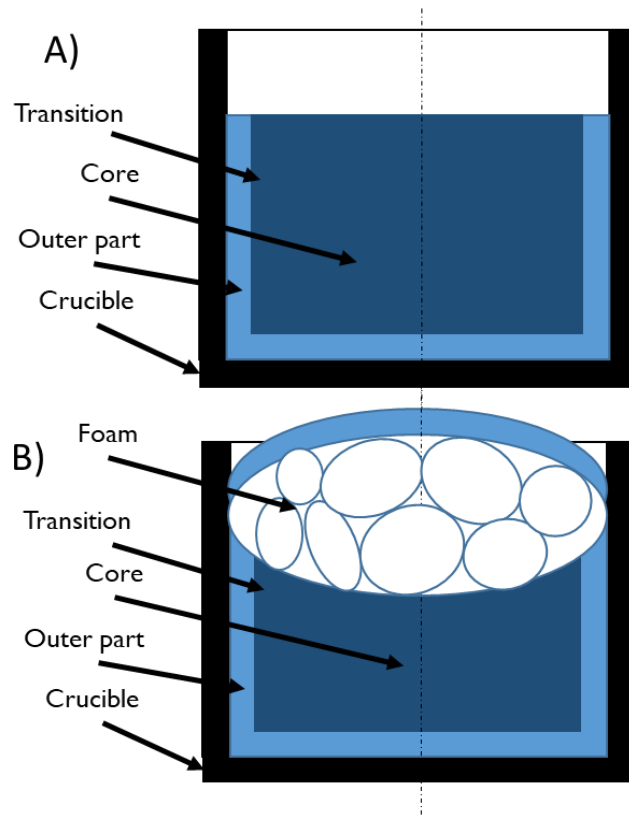


Figure 131: Schematic description of the different slag foaming crucible zones; A) non-foaming samples 4,10; B) foaming samples 1,3,5,6,7,8,9

Table 39 sums up these average results. The following aspects can be observed:

- In all foams, FeO is depleted; CaO and SiO₂ are enriched compared to other locations. That is consistent with the calcium silicate networks observed above.
- While Al₂O₃ is significantly higher than in the initial mixture, it is even more enriched in the superficial regions, indicating the significant dissolution of refractory material.
- The EAF reference test no. 4 is separated into an upper part, directly at the surface, and a lower part. Some aspects can be highlighted in this case. On the one hand, FeO seems to move to the lower part. On the other hand, MgO is enriched in the upper section, as well as the basicity is increased.
- Sample 8 seems to be an outlier. In the surface near region, the basicity increases unexpectedly. Although different areas were measured, this appears to be a local depletion of SiO₂.

Although all samples are stirred, the slags tend to segregate. Influencing effects could be the density, gravity, and dissolution of refractory material.

Table 39: Chemical analyses of selected foaming samples, determined by SEM-EDX; *Fe assumed to be 100% FeO

Sample	Region	CaO	SiO ₂	Al ₂ O ₃	MgO	FeO*	B2
1	foam	32.7	23.0	14.2	7.37	22.6	1.4
	core	28.3	19.9	14.1	7.10	30.3	1.4
	transition	29.3	14.8	20.8	1.57	33.6	2.0
	outer part	17.6	7.57	41.9	5.32	27.7	2.4
6	foam	35.8	25.8	12.8	6.27	19.4	1.4
	core	31.0	20.9	13.7	7.44	27.0	1.5
	transition	31.8	17.9	19.3	6.43	24.6	1.8
	outer part	17.4	9.71	40.3	11.4	21.3	1.8
7	foam	34.0	23.6	16.9	8.50	17.1	1.4
	core	32.1	21.4	16.4	8.44	21.8	1.50
	transition	24.1	10.5	24.4	4.89	36.2	2.3
	outer part	19.0	7.01	37.0	6.52	30.5	2.7
8	foam	34.0	21.5	17.5	6.97	20.1	1.6
	core	32.1	19.7	15.9	6.94	25.4	1.6
	transition	19.0	4.1	37.0	6.50	33.4	5.0
	outer part	20.3	1.85	46.5	3.38	27.9	11
9	foam	32.1	23.9	14.4	8.65	21.03	1.3
	core	28.3	16.5	16.6	10.9	27.8	1.7
	transition	30.5	21.9	14.3	9.82	23.6	1.4
	outer part	16.4	9.61	35.7	12.0	26.3	1.7
4 lower- part	core	23.9	13.3	21.8	3.95	37.0	1.9
	transition	23.5	10.3	21.3	1.45	43.2	2.2
	outer part	11.8	4.62	45.9	5.21	32.5	2.6
4 upper- part	core	28.3	19.9	14.1	7.10	30.6	1.4
	transition	29.1	23.4	25.5	10.2	11.6	1.2
	outer part	19.1	17.5	41.3	13.8	8.27	1.1
10	core	35.7	30.6	15.8	4.36	13.6	1.2
	transition	31.8	27.7	21.3	4.18	15.0	1.1
	outer part	29.2	20.6	38.6	4.2	7.3	1.4

8.2. Slag foaming index – sensitivity analysis

The test series above provides specific information about the investigated slags. However, they can be considered as snapshots since the slag composition does not stay constant during iron and steelmaking. It rather follows a path. As mentioned in 2.3.2, the so-called slag foaming index Σ describes foamability as a viscosity, density, and surface tension function. That enables a sensitivity analysis of the slag foamability as a function of their composition. Such a sensitivity analysis, which means Σ vs. FeO and B2, is described in this chapter. Three equations from **Table 6** are considered: for MgO_{sat} slags, CaO-based slags, and bath smelting slags. To achieve this objective, surface tension σ , density ρ , and viscosity η must be calculated. While the MgO_{sat} equation already considers solid particles, the others do not. Therefore, η is corrected using equation **14**. Further, the Morton number Mo is calculated. On the one hand, this visualization allows the study of foamability over a slag path; on the other hand, the experiments can be compared to these calculated values. The following boundary conditions are assumed:

- $T = 1600^\circ\text{C}$
- $(\%\text{MgO}) = 10$
- $(\%\text{Al}_2\text{O}_3) = 5$
- $1.1 < \text{B2} < 3$
- $1 < (\%\text{FeO}) < 30$

The Σ equations indicate the viscosity η to be the primary parameter. Therefore, two methods are applied to calculate η , the FactSage™ viscosity module and the Urbain^[123] model with parameters from^[129].

To get viscosity values from FactSage™, a slag matrix in the demanded range is created. For the compositions in this matrix, the viscosities are calculated. These values are fitted using a polynomial surface fit in Matlab®. Since the Urbain equations are an empirical approach as a function of the composition and constants, no fitting is necessary. Therefore, the given boundary range is subdivided into a discrete mesh to draw a surface plot.

Figure 132 shows the corresponding surface plots with horizontal sections, visualized as a view along the z-axis. In A), the surface is shown with the calculated values, given as blue dots. This illustration provides the possibility to check the goodness of fit. Only minor oscillations can be observed. The charts are striking in two aspects: On the one hand, the Urbain values are higher by a factor of ≈ 2 . On the other hand, the FactSage™ viscosity is more sensitive to a changing (FeO) content. This sensitivity can be recognized by the lower diagrams' steeper angle of the contours. For further calculations, the FactSage™ calculations are used since the data should be more up to date. A slag composition from Emirates steel^[105] was added to classify the data. The Emirates furnace is a DRI-based EAF and representative for this task.

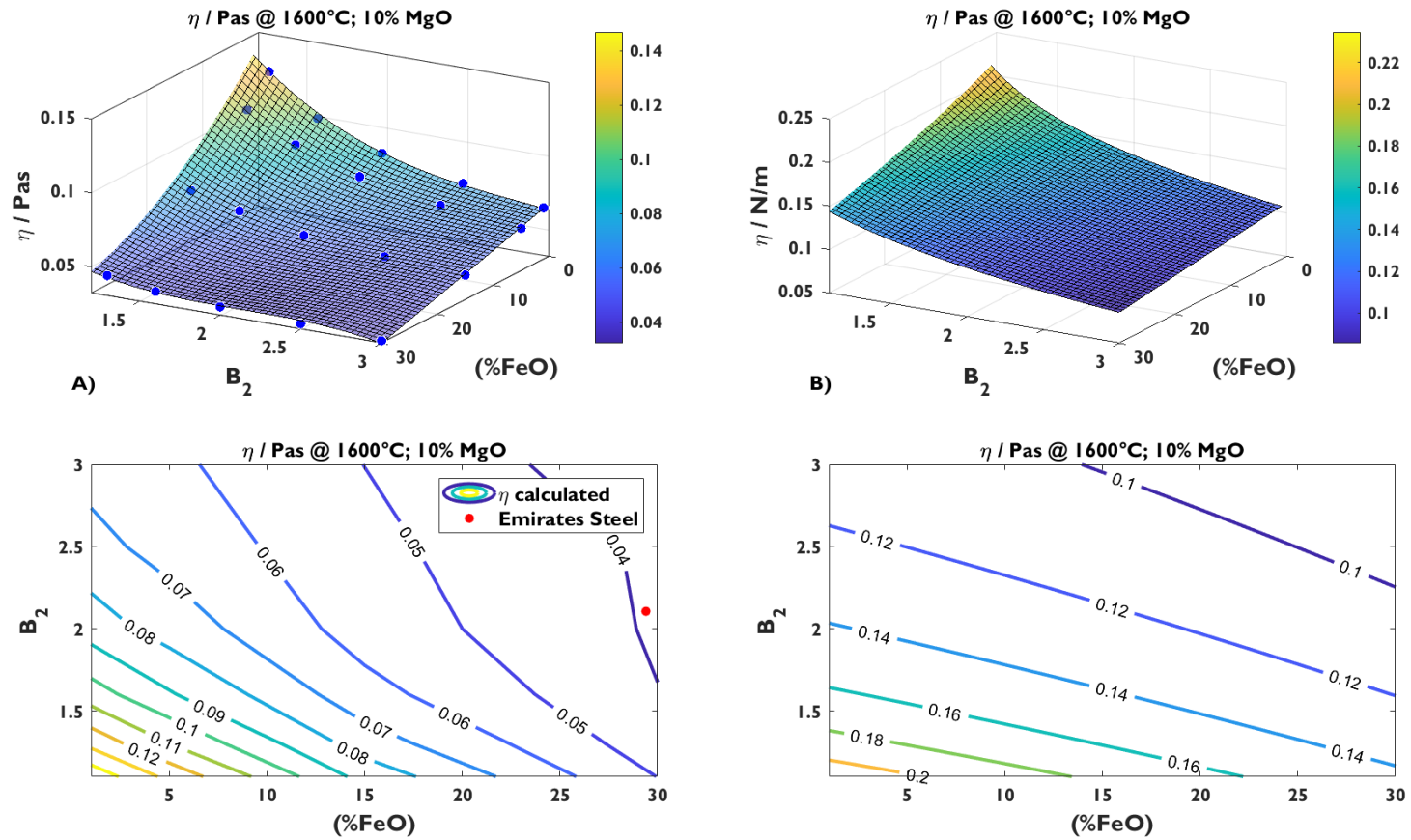


Figure 132: Surface plot and horizontal sections of viscosity η , neglecting solid particles; A) based on fitted FactSage™ data; B) acc. to Urbain^[123] model with parameters from^[129]; Emirates steel data from^[105]

The data in **Figure 132** must be corrected for the solid particles. Therefore, a FactSage™ 8.0 calculation is performed using FactPS and FToxide databases. The resulting Slag-liq mass is extracted into an Excel spreadsheet. The mass of solids is calculated by subtracting it from the initial mass of 100 g. As can be seen in **Figure 133**, the surface is again overlaid with the calculated values, represented by blue dots. The red-dotted Emirates steel slag contains more than 5 wt.-% of magnesiowustite particles.

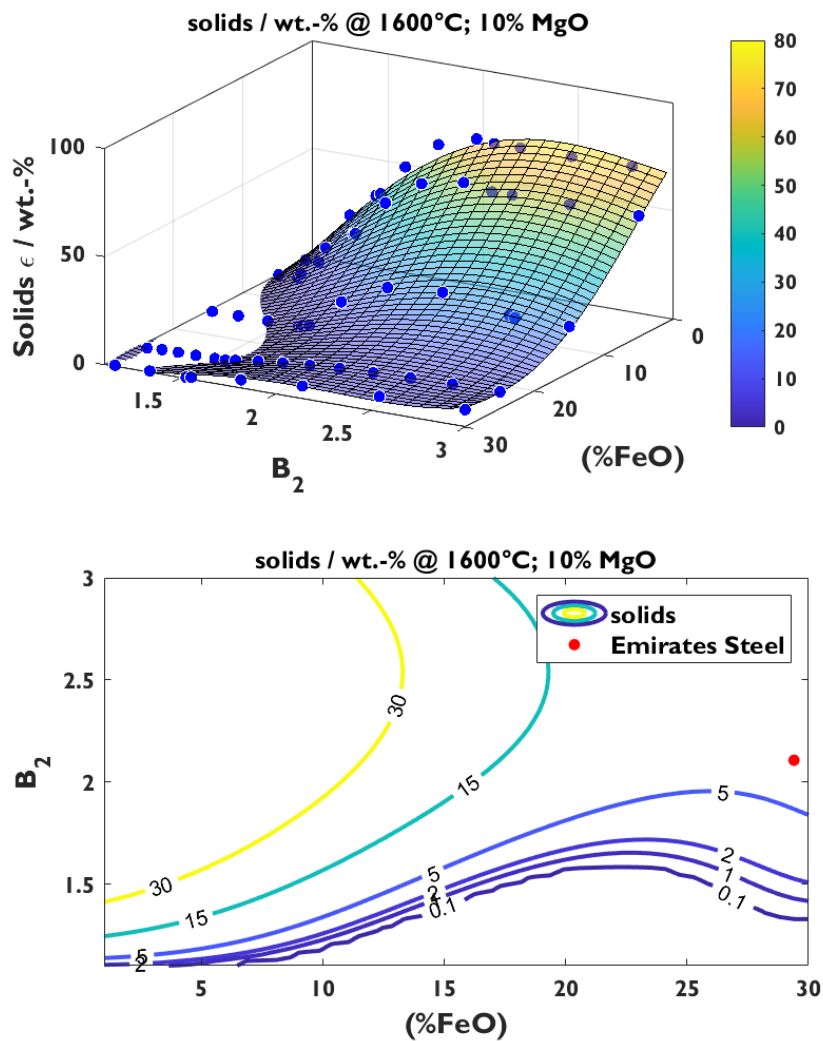


Figure 133: Surface plot and horizontal sections of the solid fraction ϵ in wt.-% based on fitted FactSage™ data; Emirates steel data from^[105]

The effective viscosity is calculated using the modified Einstein equations in **13**^[95] and **14**^[124]. Areas with a solid fraction >25% are neglected since these lead to unrealistic values. Further, the solid fractions are equated with the volume fractions. While the density of liquid slag and magnesiowustite particles is difficult to calculate, this is considered a valid approximation. **Figure 134** gives the corresponding charts for both equations, showing only minor differences. The diagrams reproduce the fitting oscillations from the solids above. Equation **13**^[95] is applied for further calculations.

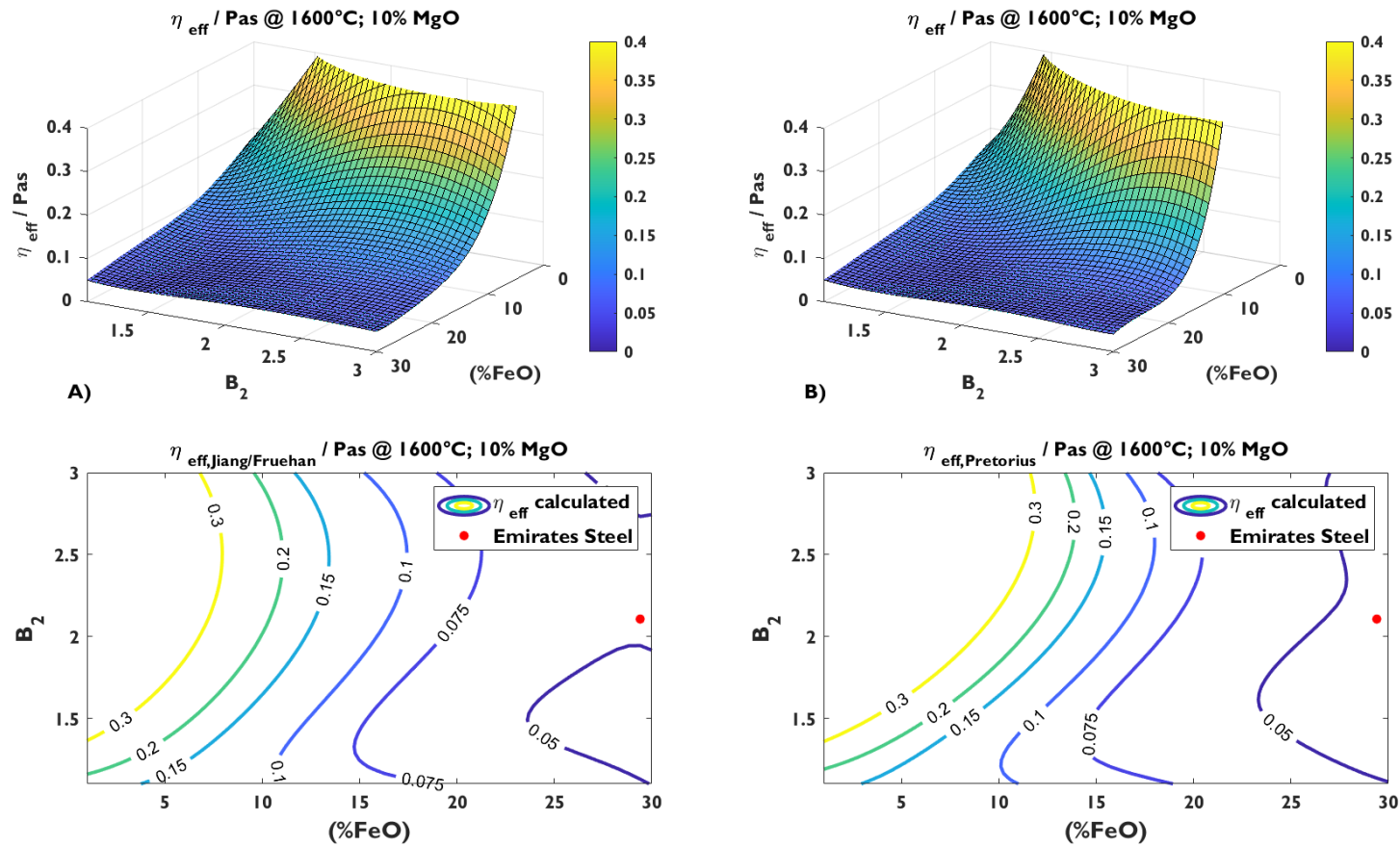


Figure 134: Surface plot and horizontal sections of effective viscosity η_{eff} , A) based on equation 13^[95]; B) based on equation 14^[124]; Emirates steel data from^[105]

Approaches for surface tension σ and density ρ were taken from Heo et al.^[147]. **Figures 135** and **136** give the corresponding plots. While the former is dependent on (FeO) as well as B₂, iron oxide is the determining factor of the density.

The following conclusion can be made by comparing the effective viscosity η_{eff} in **Figure 134**, surface tension σ in **Figure 135**, and density ρ in **Figure 136**. The viscosity is the determining parameter of the slag foaming index in two ways. On the one hand, over the given range, η_{eff} increases from ≈ 0.05 to ≈ 0.4 , a factor of 8. Contrary to that, surface tension increases by a factor of ≈ 1.2 and density by ≈ 1.3 . On the other hand, looking at the approaches in **Table 6**, $\Sigma \sim \eta / \sqrt{\sigma \cdot \rho}$. As ρ and σ are under the root, they are less relevant for the index.

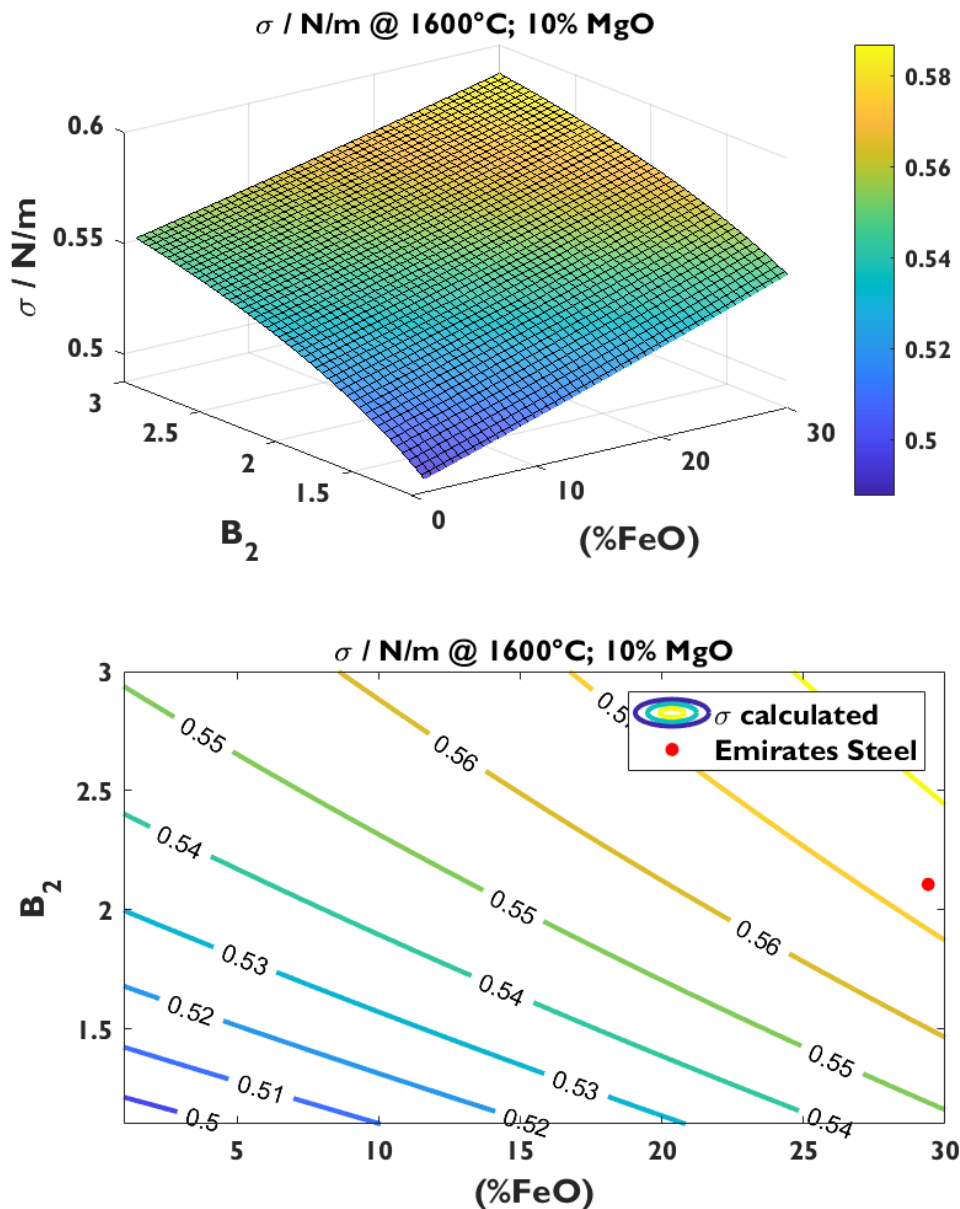


Figure 135: Surface plot and horizontal sections of the surface tension σ based on^[147]; Emirates steel data from^[105]

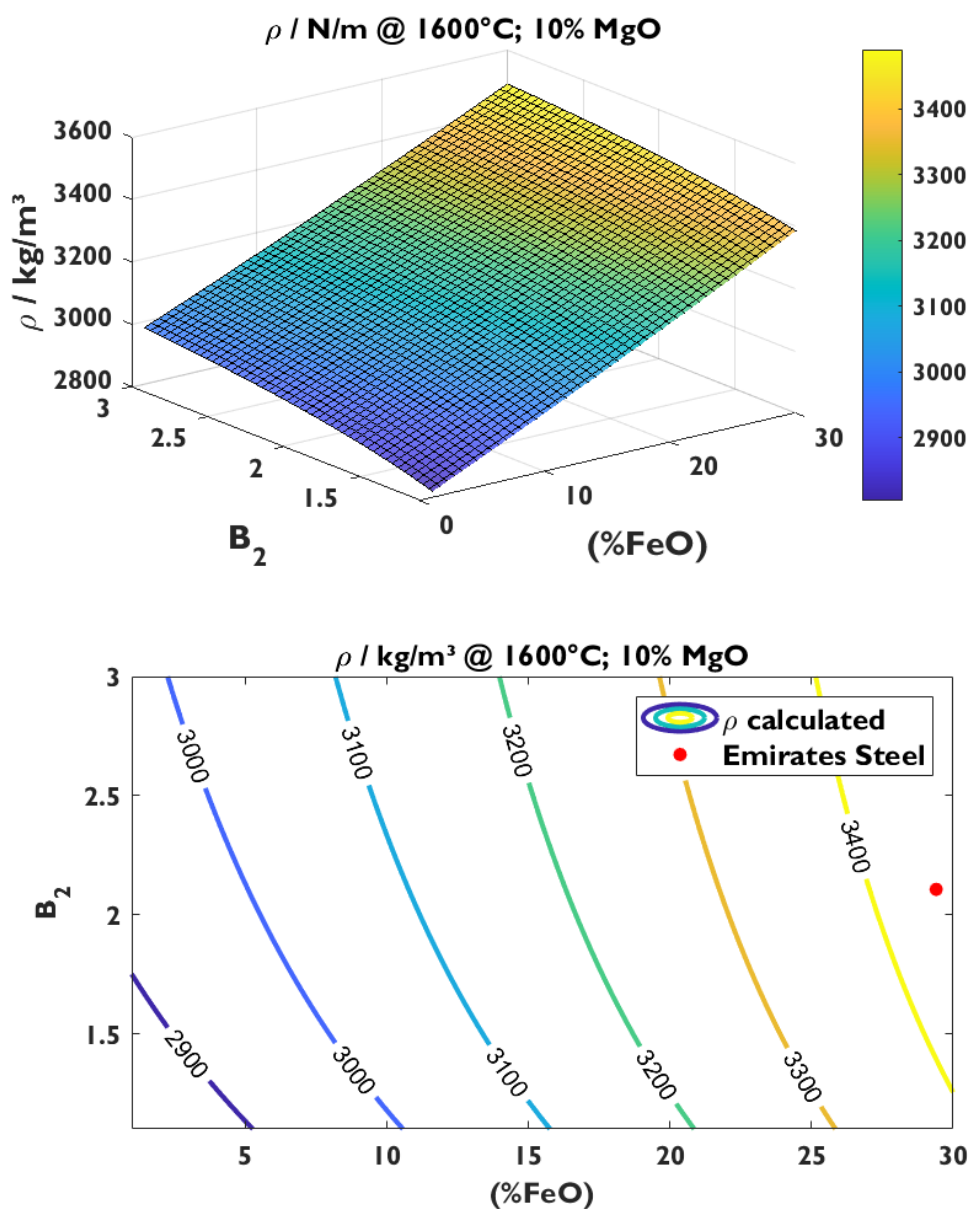


Figure 136: Surface plot and horizontal sections of the density ρ based on^[147]; Emirates steel data from^[105]

Figure 137 shows the resulting slag-foaming indices. A) and C) look similar as they use the same viscosity calculation. In B), in the MgO_{sat} case, the conventional liquid viscosity is applied. There is a significant difference between the lowest, A) bath smelting slags, and the highest, C) MgO_{sat} slags. This deviation indicates that checking if the approach is valid for the given slag composition is essential.

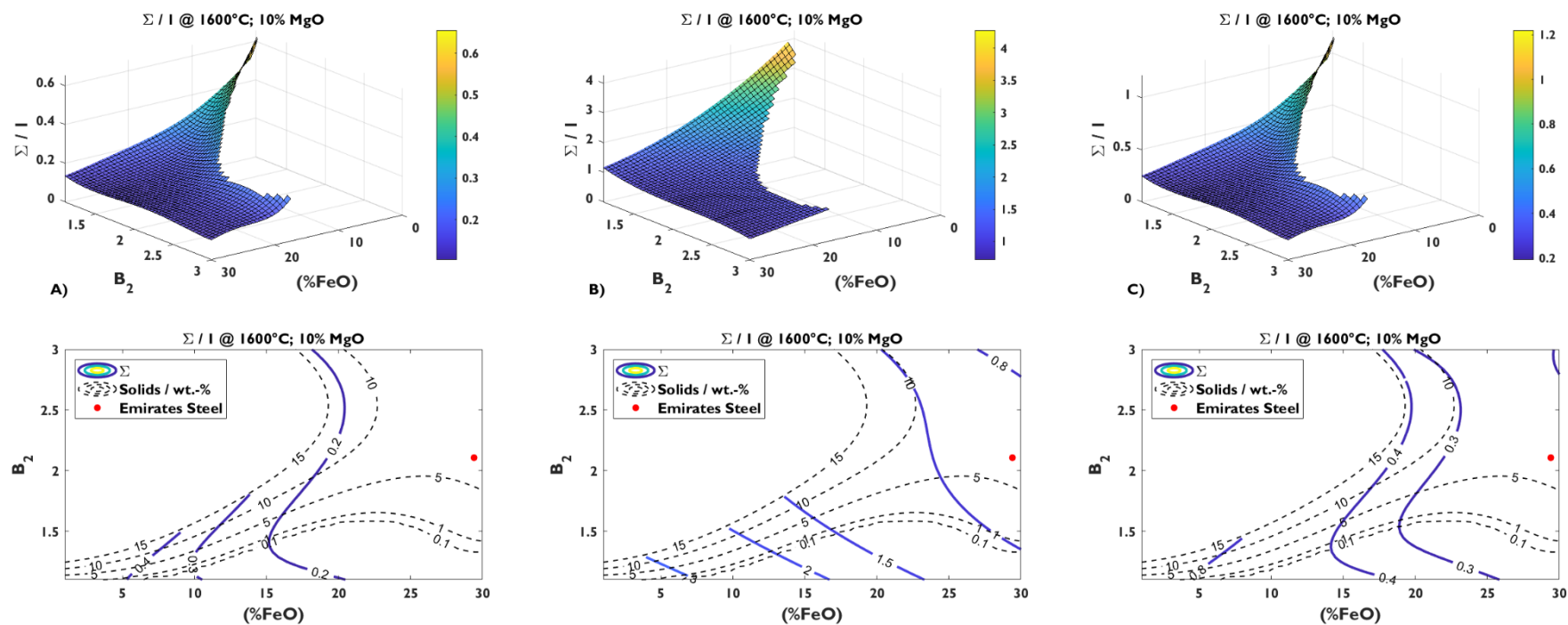


Figure 137: Surface plot and horizontal sections of Slag foaming index Σ ; A) for bath smelting slags; B) for MgO_{sat} slags; C) for CaO-based slags; Emirates steel data from^[105]

The Morton number in **Figure 138** is also calculated using the effective viscosity. This equation is even more sensitive regarding viscosity changes. The qualitative form of the logarithmic surface aligns with Σ above. Looking at the shape of the curve at (%FeO) = 30%, the Mo number is high at low basicities. Further, it shows a minimum with increasing basicity and a second maximum with increasing solids.

The corresponding diagrams for 10% MgO and 1500°C, as well as 5% MgO and 1600°C, are added in the appendix.

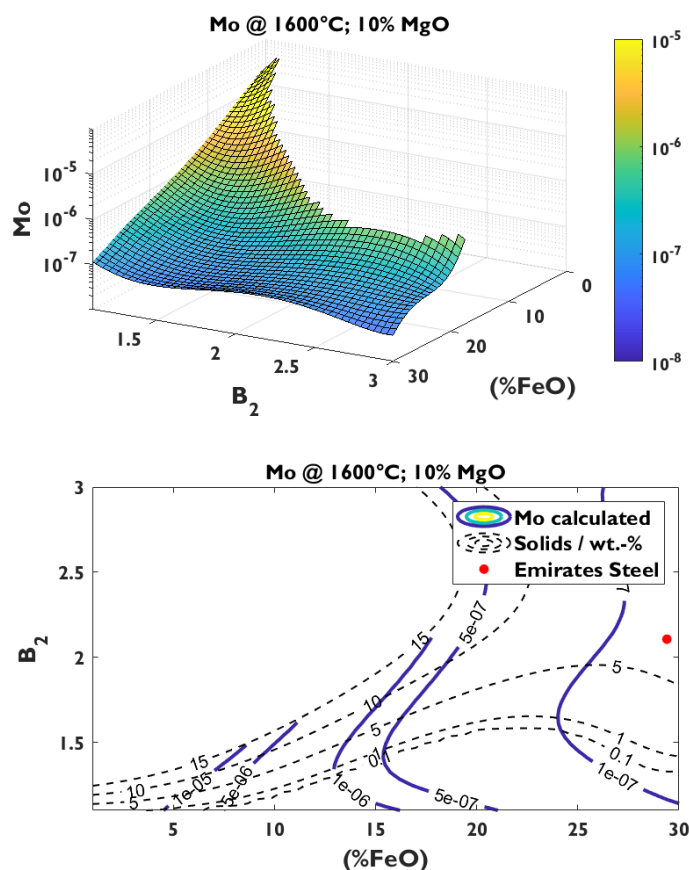


Figure 138: Surface plot and horizontal sections of the Morton number Mo ; Emirates steel data from^[105]

8.3. Discussion

In the scope of this thesis, a method for slag foaming tests was developed. The target is to evaluate slags for EAF- and smelter regarding their foaming behavior. While the EAF slags foam pretty well, the acidic smelter slags do not show any foam. The influence of poor gas formation is excluded by increasing the FeO content and the respective carbon carrier addition from 5 to 10%.

The literature describes the influence of solid particles extensively. Oversaturated and undersaturated slags show slightly different foam structures. However, they exhibit no significant difference in their foaming height or the respective volume increase.

As a second part, a sensitivity analysis of the slag foaming index Σ vs. (FeO) and B2 was performed. In this case, a low basicity and a low FeO content seem preferable since that increases viscosity. If the basicity reaches a certain level, solid particles are precipitated, and the effective viscosity increases in

line with the resulting slag foaming index. Although the density and surface tension influence the index, they play a minor role in the applied models.

No correlation can be observed when comparing the tests with the calculated indices in **Table 21**. While the SAF slags with $\Sigma \approx 0.3$ does not show any foam, the unsaturated EAF slag with $\Sigma \approx 0.2$ foams quite well. Further, the saturated EAF slag with $\Sigma \approx 1.0$ shows a behavior similar to the unsaturated one, although the index is increased by factor 5. This observation corresponds to the industrial tests by de Vos^[138] in the BOF. Further, the broad variety of approaches, partly summarized in **Table 6** and **Table 7**, points in a similar direction.

One explanation for this discrepancy is segregation effects. In all samples, segregations can be observed, showing calcium silicate networks and MA-spinel. Nevertheless, the latter is a result of the dissolution of refractory material. Although these solid particles are mathematically considered, these models do not simulate reality since they assume a homogeneous distribution. However, the SEM-EDX images and the macroscopic composition distribution of reference test no. 4 clearly show this is untrue. Wetting and interaction with the crucible can also be an influencing factor. Most index determination methods work with inert gas. In industrial conditions and the presented lab tests, foaming is induced by chemical reactions. Reduction reactions can decrease local temperature and change local viscosity and phase composition.

The developed method shows two weaknesses. On the one hand, the crucible critically influences the slag; on the other hand, the cooling rate in the center is limited. To avoid the former, high-density MgO crucibles may be applied. When applying MgO-saturated slags, this interaction should be minimized. The latter is more complicated to solve. Reducing the crucible diameter and decreasing the heat transport distance worsen the influence of the refractory. One possibility would be the application of a metallic crucible. In this case, pure iron at a lower temperature or refractory metals, either in an inert atmosphere or covered by a protection layer, can provide a remedy.

9. Conclusion and outlook

This thesis aims to provide basic knowledge about various aspects of DRI processing, focusing on lower grades. The following conclusions can be drawn from it. Firstly, the calculations in chapter 4 clearly define the preferred strategy for a specific raw material mixture. The route DR - EAF is selected if the amount of metallic iron in the raw material is high. This criterion can be achieved in different ways. Next to the application of DR-grade pellets with $Fe_{tot} > 67\%$ as the raw material, a mixture of quality scrap with pig iron and lower-grade DRI is also conceivable. Nevertheless, due to the limited dephosphorization capacity, tramp element enrichment and the phosphorus input must be considered. The lower the iron carriers' quality, the more the advantages of the two-stage variants EAF-smelter – BOF and smelter – BOF become apparent. Further, these strategies provide advantages regarding dephosphorization and total Fe yield. The former is mainly due to BOF's outstanding dephosphorization capacity. The latter results from lower beneficiation losses from the raw material and lower iron oxide losses in slags. Whether EAF-smelter or smelter prevails, cannot be decided from this work. However, the industry prefers a smelter in the form of SAF or OSBF^[82, 83]. From an economic perspective, the combination of DR and EAF may be preferable for green field plants as one saved operation step saves CapEx and the development of know-how for this step. Existing integrated BF – BOF facilities may pick the DR – smelter – BOF combination. In addition to the continued use of the current raw material mixt, the steelmaking and refining need only marginal changes. Therefore, the know-how remains a competitive advantage without too many adjustments.

The behavior of phosphorus in the DRI was studied with two reduction tests. As thermodynamics indicates, the apatite remains stable during direct reduction conditions in fixed and fluidized beds. Also, preoxidation does not influence this behavior. Consequently, this oxidic state seems preferable for further steelmaking compared to hot metal, in which phosphorus occurs in reduced and dissolved condition. However, the behavior during melting must be checked further. Although there is some published work on this topic^[109] available, the influence of slag basicity and iron oxide content are relevant variables worth studying.

A wide range of results occurred with the DRI dipping tests. Carbon-free DRI shows poor melting in slags, as well as steel. In carbon-rich hot metal, however, melting happens rapidly. The carburized sponge iron samples highlight the driving force of carbon in this case. Depending on the carbon content, these samples soften up to the whole cross sections in ≈ 3 s immersion in steel. The lower thermal conductivity of slags leads to different behavior. As the Prantl numbers indicate, a broader solid layer forms, blocking heat transfer into the DRI pellet. Hence, melting takes place very slowly in this case. In a nutshell, in line with the turbulence and the high temperature of the electric arc in the EAF, the reactive slag provides optimal conditions for sponge iron melting. Further, the slower softening of denser HBI correlates with the charging rates presented by Abel^[76]. The optimum conditions in the smelter need a closer examination in the future. According to the knowledge from this work, highly carburized DRI, charged into the brush-arc hotspot, can be seen as the best case.

Laboratory-scale arc melting tests confirm the decisive role of carbon during melting. While hydrogen-based DRI without C leads to many blisters, the carburized material shows the opposite. Reactions with residual iron oxide stir the bath via CO blisters. The locally decreased N_2 partial pressure denitrifies the melt. This effect further improves the separation between the gangue and the metallic phase. The last test with slag-forming oxides exhibits an outstanding result. While all the other melts merge with the crucible, the slag surrounds the melt in this case. The metallic crucible remains

unchanged. Interestingly, this happens on the top, bottom, outside, and inside. This behavior indicates a significant influence of electromagnetic forces from the arc.

This thesis presents a new method for slag foaming tests. Compared to most literature, it induces the bubbles, inspired by EAF, using a carbon carrier and iron oxide in the slag. The tests confirm the problematic transferability of the slag foaming index concept to actual processes, which corresponds to the literature^[138]. Driving parameters are endothermic reactions, interactions with refractory material, and inhomogeneities in the crucible. The smelter slag shows no foamability, independent of the FeO content. A particular slag path would be necessary to transform this observation into the EAF-smelter concept from chapter 4. Slag foaming may be possible during the first part if the sequence starts with high basicity and MgO content. The more DRI is continuously fed, the less lime and dolomite should be added, decreasing the basicity and approaching blast furnace slag at tapping. This pathway combines the advantages of a foamy slag with the reusability of BF slag. Lastly, EAF slag shows good foamability independent of the saturation degree in this test.

In a nutshell, the findings can be summarized with the following striking points:

- DR-grade based DRI is optimally processed via the electric arc furnace. The higher the gangue and phosphorus contents, the better the use case for a two-step strategy.
- Phosphorus remains bounded as apatite in hydrogen-based direct reduction conditions. This state indicates advantages compared to phosphorus in hot metal during the melting step.
- Concerning melting, the optimal condition would be a) a highly carburized DRI in b) a carbon-containing hot metal. Contact with slag should be avoided due to the poor heat conductivity, highlighting the importance of charging DRI in the hot spot of the electric arc.
- For product quality, arc melting tests further highlight the importance of carbon. On the one hand, the reduction reactions remove gases from the melt. Further, the stirring effect separates gangue and crude steel, indicative of advantages regarding nonmetallic inclusions.
- Last but not least, the foaming tests highlight the poor foamability of BF-like slag. However, looking at the SEM-EDX images, the tests confirm the problematic reproduction of this phenomenon on a laboratory scale.

This work provides basic knowledge regarding the processing behavior of DRI. While there is already much information about DRI in the EAF, the smelter operation is a new topic, demanding a closer look. From this thesis' findings, some critical questions arise. First, the results from chapters 6 and 7 must be combined in the scope of upscaled test conditions. Different arc operations, resistance heating, brush arc, and long arc can be compared, and the optimal DRI charging spot can be found. Secondly, the behavior of apatite during melting and the occurrence of other residual elements like sulfur, zinc, and alkalis in such a smelter needs further evaluation. Last but not least, the optimal process strategy, considering raw materials, carbon carriers, off-gas composition, and slag properties, has to be developed.

10. References

1. worldsteel.org: World Steel in Figures (21.09.2022), <https://worldsteel.org/steel-topics/statistics/world-steel-in-figures/>. Accessed 23 September 2022
2. Wikipedia: Stahl (2022), <https://de.wikipedia.org/w/index.php?title=Stahl&oldid=226371282>. Accessed 23 September 2022
3. EU Science Hub: EU climate targets: how to decarbonise the steel industry (15.06.2022), https://joint-research-centre.ec.europa.eu/jrc-news/eu-climate-targets-how-decarbonise-steel-industry-2022-06-15_en#_ftn1. Accessed 27 September 2022
4. EUROFER: Low Carbon Roadmap: Pathways to a CO₂-neutral European steel industry (01.04.2021), <https://www.eurofer.eu/publications/reports-or-studies/low-carbon-roadmap-pathways-to-a-co2-neutral-european-steel-industry/>. Accessed 1 April 2021
5. EUROFER: Map of key low-CO₂ emissions projects in the EU steel industry (27.09.2022), <https://www.eurofer.eu/issues/climate-and-energy/maps-of-key-low-carbon-steel-projects/>. Accessed 27 September 2022
6. Andreas Voß: *thyssenkrupp*, 2021.
7. Daniel Spreitzer: *Development of characterization methods for the evaluation of the kinetic behavior and the fluidization of iron ore fines during hydrogen-induced fluidized bed reduction*. PhD Thesis, 2021.
8. H. B. Lungen: *CO₂ emissions and their mitigation in the steel industry*, Webinar, 2020.
9. R. J. Fruehan, ed.: *The Making, Shaping and Treating of Steel: Ironmaking Volume*, 1999.
10. Kohlenstoffbasierte Stahlerzeugung - Stahlinstitut VDEh (27.09.2022), <https://vdeh.de/stahlherstellung/kohlenstoffbasierte-stahlerzeugung/>. Accessed 27 September 2022
11. S. Dworak and J. Fellner: *Resources, Conservation and Recycling*, 2021, vol. 173, p. 105692.
12. S. Dworak, H. Rechberger, and J. Fellner: *Resources, Conservation and Recycling*, 2021, p. 106072.
13. Wikipedia: Corex Process (2022), https://en.wikipedia.org/w/index.php?title=Corex_Process&oldid=1107088587. Accessed 28 September 2022
14. Primetals Technologies: COREX® – SCHMELZREDUKTIONSVORFAHREN | Primetals Technologies (28.09.2022), <https://www.primetals.com/de/portfolio/ironmaking/corexr>. Accessed 28 September 2022
15. Primetals Technologies: FINEX® — ENVIRONMENTALLY SAFE IRONMAKING | Primetals Technologies (28.09.2022), <https://www.primetals.com/portfolio/ironmaking/finexr>. Accessed 28 September 2022
16. Wikipedia: FINEX (steelmaking process) (2019), [https://en.wikipedia.org/w/index.php?title=FINEX_\(steelmaking_process\)&oldid=930271989](https://en.wikipedia.org/w/index.php?title=FINEX_(steelmaking_process)&oldid=930271989). Accessed 28 September 2022
17. K. Meijer, C. Guenther, and R. J. Dry, eds.: *Hlsarna pilot plant project*, 2011.
18. F. N.H. Schrama, E. M. Beunder, J. W.K. van Boggelen, R. Boom, and Y. Yang: *Science and Technology of Ironmaking and Steelmaking*, 2017, pp. 419–22.
19. KU Leuven, ed.: *Proceedings of the 6th international slag valorisation symposium*, Belgium, 2019.
20. TATA Steel: HISARNA (2020), <https://www.tatasteeleurope.com/sites/default/files/tata-steel-europe-factsheet-hisarna.pdf>. Accessed 28 September 2022
21. L. Youling, L. Huibin, W. Hua, Q. Shan, H. Jianhang, H. Yali, L. Hu, and L. Liangqing: *2011 International Conference on Computer Distributed Control and Intelligent Environmental Monitoring*, IEEE, 2011 - 2011, pp. 1283–86.

22. M. Atsushi, H. Uemura, and T. Sakaguchi: *Kobelco Technology Review*, 2010, vol. 29, pp. 50–57.
23. A. Elliot and G. Walker: *Direct from Midrex*, 2021, 1/2021, pp. 8–10.
24. X. Jiang, L. Wang, and F. M. Shen: *AMR*, 2013, 805-806, pp. 654–59.
25. D. Spreitzer and J. Schenk: *steel research int.*, 2019, vol. 90, p. 1900108.
26. M. Dorndorf: *Hydrogen-based reduction with HyL/Energiron*, Webinar, 2020.
27. Primetals Technologies: Current News of Primetals Technologies | Primetals Technologies (28.09.2022), <https://www.primetals.com/press-media/news/hydrogen-based-ironmaking-mhi-australia-and-primetals-technologies-join-heavy-industry-low-carbon-transition-cooperative-research-centre>. Accessed 28 September 2022
28. S. A. Elmquist, P. Weber, and H. Eichberger: *Stahl und Eisen*, 2002, vol. 122, pp. 59–64.
29. T. Stefan: *Hydrogen-based reduction with Circored*, Webinar, 2020.
30. A. Reindl: Zero-Carbon HYFOR Direct-Reduction Pilot Plant Starts Operation (24.06.2021), <https://magazine.primetals.com/2021/06/24/zero-carbon-hyfor-direct-reduction-pilot-plant-commences-operation-in-donawitz-austria/>. Accessed 28 September 2022
31. Primetals Technologies: Current News of Primetals Technologies | Primetals Technologies (28.09.2022), <https://www.primetals.com/press-media/news/hyfor-pilot-plant-under-operation-the-next-step-for-carbon-free-hydrogen-based-direct-reduction-is-done>. Accessed 28 September 2022
32. R. J. Fruehan, ed.: *The Making, Shaping and Treating of Steel: Steelmaking and Refining Volume*, 1998.
33. Midrex Technologies, Inc.: World DRI production reaches 119.2 Mt in 2021 Midrex Publishes World Direct Reduction Statistics - Midrex Technologies, Inc (02.09.2022), <https://www.midrex.com/company-news/world-dri-production-reaches-119-2-mt-in-2021-midrex-publishes-world-direct-reduction-statistics/>. Accessed 28 September 2022
34. A. Griesser and T. Buerger: *Berg Huettenmaenn Monatsh*, 2019, vol. 164, pp. 267–73.
35. thyssenkrupp is accelerating the green transformation: Decision taken on the construction of Germany's largest direct reduction plant for low-CO₂ steel (23.03.2023), <https://www.thyssenkrupp.com/en/newsroom/press-releases/pressdetailpage/thyssenkrupp-is-accelerating-the-green-transformation--decision-taken-on-the-construction-of-germanys-largest-direct-reduction-plant-for-low-co2-steel-146809>. Accessed 23 March 2023
36. R. Chaigneau: *Types and chemical compositions of iron ores*, Online, 2021.
37. R. Jonckbloedt: *Pelletizing of iron ores*, Online, 2021.
38. R. Chaigneau: *Iron ores for direct reduction and for hydrogen-based reduction*, Online, 2021.
39. J. Linklater: *Direct from Midrex*, 2021, 1/2021, pp. 3–7.
40. R. Lin: *Sintering of iron ores*, Online, 2021.
41. C. Barrington: *Outlook for DR-grade iron ore: issues and challenges for the industry*, Online, 2021.
42. Statista: Durchschnittlicher Eisenerzpreis weltweit bis 2021 | Statista (03.10.2022), <https://de.statista.com/statistik/daten/studie/432865/umfrage/durchschnittlicher-preis-fuer-eisenerz-weltweit/>. Accessed 3 October 2022
43. voestalpine Geschäftsbericht 2020/21: Kennzahlen Überblick - voestalpine Geschäftsbericht 2020/21 (27.06.2022), <https://reports.voestalpine.com/2021/gb/services/kennzahlen-ueberblick.html>. Accessed 3 October 2022
44. SSAB EBITDA Margin 2017-2022 | SSAAY (03.10.2022). Accessed 3 October 2022
45. Salzgitter AG.
46. ArcelorMittal EBITDA Margin 2010-2022 | MT (03.10.2022). Accessed 3 October 2022
47. ThyssenKrupp AG EBITDA Margin 2012-2022 | TYEKF (03.10.2022). Accessed 3 October 2022
48. Tradingeconomics: HRC Steel, <https://tradingeconomics.com/commodity/hrc-steel>. Accessed 3 October 2022
49. M. Kern: *Investigation of the Melting Behavior of Direct Reduced Iron*. Master Thesis, Leoben, 2021.
50. International Iron Metallics Association: Direct Reduced Iron (DRI) (05.07.2021), <https://www.metallics.org/dri.html>. Accessed 5 July 2021
51. D. Spreitzer and J. Schenk: *Metall and Materi Trans B*, 2019, vol. 50, pp. 2471–84.

52. International Iron Metallics Association: Hot Briquetted Iron (HBI) (05.07.2021), <https://www.metallics.org/hbi.html>. Accessed 5 July 2021
53. Wikipedia: Iron (2022), <https://en.wikipedia.org/w/index.php?title=Iron&oldid=1113800681>. Accessed 3 October 2022
54. G. Kim, Y. Kacar, and P. C. Pistorius: *Metall and Materi Trans B*, 2019, vol. 50, pp. 2508–16.
55. F. Memoli: *Proceedings of the Association for Iron and Steel Technology Conference Proceedings*, 2015.
56. E. Sharifi and M. Barati: *Metall and Materi Trans B*, 2010, vol. 41, pp. 1018–24.
57. O. J. P. Gonzalez, M. A. Ramírez-Argáez, and A. N. Conejo: *ISIJ Int.*, 2010, vol. 50, pp. 1–8.
58. O. J. P. González, M. A. Ramírez-Argáez, and A. N. Conejo: *ISIJ Int.*, 2010, vol. 50, pp. 9–16.
59. M. A. Ramirez-Argaez, A. N. Conejo, and M. S. López-Cornejo: *ISIJ Int.*, 2015, vol. 55, pp. 117–25.
60. E. Pineda-Martínez, C. A. Hernández-Bocanegra, A. N. Conejo, and M. A. Ramirez-Argaez: *ISIJ Int.*, 2015, vol. 55, pp. 1906–15.
61. K. Sadrnezhaad: *Melting of DR materials in steelmaking slags*, 1979.
62. SALCOS®: Unser Programm SALCOS® (12.10.2022), <https://salcos.salzgitter-ag.com/de/salcos.html#c141490>. Accessed 12 October 2022
63. HYBRIT. Eine neue, bahnbrechende Stahlerzeugungstechnologie (12.10.2022), <https://www.ssab.com/de-de/fossil-free-steel/hybrit-a-new-revolutionary-steelmaking-technology>. Accessed 12 October 2022
64. Tata Steel in Europe: Tata Steel invests 65 million euro in next phase hydrogen route (12.10.2022), <https://www.tatasteeleurope.com/corporate/news/Tata-Steel-invests-65-million-euroin-next-phase-hydrogen-route>. Accessed 12 October 2022
65. thyssenkrupp: Klimaneutraler Stahl - Unsere Strategie | thyssenkrupp Steel (12.10.2022), <https://www.thyssenkrupp-steel.com/de/unternehmen/nachhaltigkeit/klimastrategie/>. Accessed 12 October 2022
66. Hybridkonzept - greentec steel (12.10.2022), <https://www.voestalpine.com/greentecsteel/de/innovatives-hybridkonzept/>. Accessed 12 October 2022
67. Y. N. Toulouevski: *Electric Arc Furnace with Flat Bath: Achievements and Prospects*, SPRINGER, Cham, 2015.
68. P. Cavaliere and J. Madias, eds.: *Ironmaking and Steelmaking Processes: Chapter 16 - Electric Arc Furnace*, Springer International Publishing, Cham, 2016.
69. P. Cavaliere: *Clean ironmaking and steelmaking processes: Efficient technologies for greenhouse emissions abatement*, SPRINGER, Cham, 2019.
70. Primetals Technologies: EAF Ultimate, 2020.
71. YouTube: Consteel® EAF melt shop in Arvedi (Cremona, Italy) (24.01.2023), <https://www.youtube.com/watch?v=HEbjGmsz80k>. Accessed 24 January 2023
72. J. Lückhoff, A. Müller, J. Apfel, and H. Beile.
73. Primetals Technologies: EAF Quantum: Innovation in Steelmaking Frunace Technology of the Future, 2016.
74. [Der Titel "Hot_Transport_-_HOTLINK" kann nicht dargestellt werden. Die Vorlage "Literaturverzeichnis - Zeitschriftenaufsatz - (Standardvorlage)" beinhaltet nur Felder, welche bei diesem Titel leer sind.]
75. DRI Technology at Emirates Steel | Tenova (24.01.2023), <https://tenova.com/newsroom/latest-tenova/dri-technology-emirates-steel>. Accessed 24 January 2023
76. M. Abel: *Einschmelzen von DRI und HBI im Elektrolichtbogenofen*, Online, 2021.
77. T. Echterhof: *Energiebilanzen von Elektrolichtbogenöfen*, Online, 2021.
78. M. Abel and M. Hein, vol. 2008.
79. S. Lupi: *Fundamentals of Electroheat: Electrical Technologies for Process Heating*, Springer International Publishing, Cham, 2017.
80. E. T. Turkdogan: *Fundamentals of Steelmaking*, The institute of materials, London, 1996.

81. M. M. Elkoumy, A. M. Fathy, G. M. Megahed, I. El-Mahallawi, H. Ahmed, and M. El-Anwar: *steel research int.*, 2019, vol. 90, p. 1900208.
82. P. Cavaliere, A. Perrone, A. Silvello, P. Stagnoli, and P. Duarte: *Metals*, 2022, vol. 12, p. 203.
83. G. J. Lötter, A. A. van Niekerk, and G. E. Farmer: *INFACON XVI*, Ed. by SINTEF, NTNU, FFF, 2021.
84. N. K. Batra: *Ironmaking & Steelmaking*, 2003, vol. 30, pp. 399–404.
85. J. Björkvall, S. Angström, and L. Kallin: *7th International conference on Molten slag fluxes and salts, Johannesburg*, pp. 663–70.
86. J. Kunze and R. Degel: *Proceedings: Tenth International Ferrous Congress*, p. 4.
87. T. Coetsee: *Mineral Processing and Extractive Metallurgy Review*, 2020, vol. 41, pp. 255–78.
88. H. J. Oterdoom and J. H. Zietsman, vol. 2019.
89. J. Pais, W. Brown, and M. W. Saab: *INFACON VIII, The Eighth International Ferrous Congress*, pp. 237–42.
90. D. Pienaar: *Ironmaking Pre-reduction Strategy at EVRAZ Highveld*, 2011.
91. D. Sager, D. Grant, R. Stadler, and T. Schreiter: *Journal of the Southern African Institute of Mining and Metallurgy*, 2010, vol. 110, pp. 717–24.
92. The Ironmaking Process | New Zealand Steel (28.10.2020), <https://www.nzsteel.co.nz/new-zealand-steel/the-story-of-steel/the-science-of-steel/the-ironmaking-process/>. Accessed 28 October 2020
93. W. S. Steinberg, W. Geyser, and J. Nell: *Journal of the Southern African Institute of Mining and Metallurgy*, 2011, vol. 111, pp. 705–10.
94. W. S. Steinberg and P. C. Pistorius: *Ironmaking & Steelmaking*, 2009, vol. 36, pp. 500–04.
95. W. S. Steinberg and P. C. Pistorius: *Development of a control strategy for the open slag bath furnaces at Highveld Steel and Vanadium Corporation Ltd.* Dissertation, Pretoria, 2008.
96. G. Wimmer: Kindly provided by Primetals Technologies Austria GmbH.: Primetals Technologies Austria GmbH., Linz, 2022.
97. K. Huitu, M. Helle, H. Helle, M. Kekkonen, and H. Saxén: *steel research int.*, 2015, vol. 86, pp. 456–65.
98. C. Yilmaz and T. Turek: *Journal of Cleaner Production*, 2017, vol. 164, pp. 1519–30.
99. P. Chris Pistorius: *International Smelting Technology Symposium*, John Wiley & Sons, Ltd, 2012, pp. 141–46.
100. M. Geerdes, H. Toxopeus, and C. van der Vliet: *Modern Blast Furnace Ironmaking: an introduction*, 2nd ed., IOS Press BV, Amsterdam, 2009.
101. P. Kaushik and R. J. Fruehan: *Metall and Materi Trans B*, 2006, vol. 37, pp. 715–25.
102. P. Kaushik and R. J. Fruehan: *Ironmaking & Steelmaking*, 2006, vol. 33, pp. 507–19.
103. P. Kaushik and R. J. Fruehan: *Metall and Materi Trans B*, 2006, vol. 37, pp. 727–32.
104. S. D. Kumar, G. Prasad, P. K. Ghorui, and M. Ranjan: *Ironmaking & Steelmaking*, 2008, vol. 35, pp. 539–44.
105. A. Al Dhaeri, P. Razza, and D. Patrizio: *MPT International*, 2010, pp. 34–40.
106. thyssenkrupp Steel Europe AG: Pricidur® I ISMn30, https://www.thyssenkrupp-steel.com/media/content_1/publikationen/precision_steel/produktinformationen_1/automatenstahl/thyssenkrupp_1ismn30_produkthinformation_precision_steel_de.pdf. Accessed 24 January 2023
107. thyssenkrupp Steel Europe AG: patinax® - Produktinformation für wetterfesten Baustahl (Warmbreitband, Bandblech und Quattoblech), https://www.thyssenkrupp-steel.com/media/content_1/publikationen/produktinformationen/patinax_2/thyssenkrupp_patinax_produkthinformation_steel_de.pdf. Accessed 24 January 2023
108. R. Kiessling: *Metal Science*, 1980, vol. 14, pp. 161–72.
109. C. P. Manning and R. J. Fruehan: *Metall and Materi Trans B*, 2013, vol. 44, pp. 37–44.
110. A. N. Assis, M. A. Tayeb, S. Sridhar, and R. J. Fruehan: *Metall and Materi Trans B*, 2015, vol. 46, pp. 2255–63.

-
111. A. N Assis, M. A Tayeb, S. Sridhar, and R. J Fruehan: *Metals*, 2019, vol. 9, p. 116.
112. B. Li, L. Li, H. Guo, J. Guo, S. Duan, and W. Sun: *Ironmaking & Steelmaking*, 2020, vol. 47, pp. 771–80.
113. S. Basu, A. K. Lahiri, and S. Seetharaman: *Metall and Materi Trans B*, 2007, vol. 38, pp. 623–30.
114. S. Basu, A. K. Lahiri, and S. Seetharaman: *Metall and Materi Trans B*, 2007, vol. 38, pp. 357–66.
115. S.-M. Jung and Y.-J. Do: *Steel research international*, 2006, vol. 77, pp. 312–16.
116. S.-M. Jung, Y.-J. Do, and J.-H. Choi: *Steel research international*, 2006, vol. 77, pp. 305–11.
117. M. Abel: *Elektrische Auslegung von AC Lichtbogenöfen*, Online, 2021.
118. Matti Liukkonen, Karri Penttilä, and Pertti Sakari Koukkari, 2012.
119. E. B. Pretorius and R. C. Carlisle: *Iron and Steelmaker(USA)*, 1999, vol. 26, pp. 79–88.
120. K. Ito and R. J. Fruehan: *Metall and Materi Trans B*, 1989, vol. 20, pp. 509–14.
121. K. Ito and R. J. Fruehan: *Metall and Materi Trans B*, 1989, vol. 20, pp. 515–21.
122. J. H. Heo and J. H. Park: *Metall and Materi Trans B*, 2019, vol. 50, pp. 2959–68.
123. G. Urbain: *Steel Research*, 1987, vol. 58, pp. 111–16.
124. R. Jiang and R. J. Fruehan: *Metall and Materi Trans B*, 1991, vol. 22, pp. 481–89.
125. Y. Zhang and R. J. Fruehan: *Metall and Materi Trans B*, 1995, vol. 26, pp. 803–12.
126. S.A.C. Stadler, J. J. Eksteen, and C. Aldrich: *Minerals Engineering*, 2007, vol. 20, pp. 1121–28.
127. H. S. Kim, D. J. Min, and J. H. Park: *ISIJ International*, 2001, vol. 41, pp. 317–24.
128. B. Ozturk and R. J. Fruehan: *Metall and Materi Trans B*, 1995, vol. 26, pp. 1086–88.
129. S.-M. Jung and R. J. Fruehan: *ISIJ International*, 2000, vol. 40, pp. 348–55.
130. S. S. Ghag, P. C. Hayes, and H.-G. Lee: *ISIJ International*, 1998, vol. 38, pp. 1201–07.
131. G. Qiu, C. Shan, X. Zhang, and X. Lv: *Ironmaking & Steelmaking*, 2017, vol. 44, pp. 246–54.
132. L. S. Wu, G. J. Albertsson, and Du Sichen: *Ironmaking & Steelmaking*, 2010, vol. 37, pp. 612–19.
133. J. Heenatimulla, G. A. Brooks, M. Dunn, D. Sly, R. Snashall, and W. Leung: *Metals*, 2022, vol. 12, p. 1142.
134. R. Wang, B. Zhang, C. Hu, C. Liu, and M. Jiang: *Metall and Materi Trans B*, 2021, vol. 52, pp. 1805–17.
135. S. S. Ghag, P. C. Hayes, and H.-G. Lee: *ISIJ International*, 1998, vol. 38, pp. 1208–15.
136. S. S. Ghag, P. C. Hayes, and H.-G. Lee: *ISIJ International*, 1998, vol. 38, pp. 1216–24.
137. Morton-Zahl – Wikipedia (27.12.2022), <https://de.wikipedia.org/wiki/Morton-Zahl>. Accessed 10 January 2023
138. L. de Vos, V. Cnockaert, I. Bellemans, C. Vercruyssen, and K. Verbeken: *steel research int.*, 2021, vol. 92, p. 2000282.
139. M. Hanel: *Characterization of Ferrous Burden Material for Use in Ironmaking Technologies*. PhD Thesis, Leoben, 2014.
140. A. Pfeiffer, G. Wimmer, and J. Schenk: *Materials (Basel, Switzerland)*, 2022, vol. 15.
141. D. Ernst, U. Manzoor, I. R. Souza Filho, M. A. Zarl, and J. Schenk: *Metals*, 2023, vol. 13, p. 558.
142. D. Ernst, M. A. Zarl, J. Cejka, and J. Schenk: *Materials (Basel, Switzerland)*, 2022, vol. 15.
143. M. A. Zarl, D. Ernst, J. Cejka, and J. Schenk: *Materials (Basel, Switzerland)*, 2022, vol. 15.
144. Y. Zhang and R. J. Fruehan: *Metall and Materi Trans B*, 1995, vol. 26, pp. 813–19.
145. X.-A. Huang, K. W. Ng, L. Giroux, and M. Duchesne: *Metall and Materi Trans B*, 2019, vol. 50, pp. 1387–98.
146. T. Echterhof and H. Pfeifer: *Potential of biomass usage in electric steelmaking*, 2011.
147. J. H. Heo and J. H. Park: *Metall and Materi Trans B*, 2018, vol. 49, pp. 3381–89.
148. J. G.G. Cárdenas, an Conejo, and G. G. Gnechi: *Metal 2007*, 2007.
149. F. Bayer, J. Strasser, and H. Trenkler: *Steel Times*, 2000, vol. 228, p. 364.
150. O. Bazaluk, L. Kieush, A. Koveria, J. Schenk, A. Pfeiffer, H. Zheng, and V. Lozynskyi: *Materials (Basel, Switzerland)*, 2022, vol. 15, p. 1147.
151. L. Kieush, J. Schenk, A. Pfeiffer, A. Koveria, G. Rantitsch, and H. Hopfinger: *Fuel*, 2022, vol. 309, p. 122151.
-

152. Y.-s. Jin, T. Jiang, Y.-b. Yang, Q. Li, G.-h. Li, and Y.-f. Guo: *J Cent. South Univ. Technol.*, 2006, vol. 13, pp. 673–77.
153. T. Parak: *Economic Geology*, 1985, vol. 80, pp. 646–65.
154. H. Baïoumy, M. Omran, and T. Fabritius: *Ore Geology Reviews*, 2017, vol. 80, pp. 185–99.
155. Wikipedia: Chalcopyrite - Wikipedia (30.11.2022), <https://en.wikipedia.org/wiki/Chalcopyrite>. Accessed 1 December 2022
156. Wikipedia: Ilmenit (2022), <https://de.wikipedia.org/w/index.php?title=Ilmenit&oldid=226100248>. Accessed 1 December 2022
157. J. Huss, J. Fogelström, N. Kojola, and Du Sichen: *8th international congress on the science and technology of steelmaking*, Ed. by AIST, Montreal, 2022.
158. H. Zheng, Y. Ding, S. Zhou, Q. Wen, X. Jiang, Q. Gao, and F. Shen: *steel research int.*, 2021, vol. 92, p. 1900635.
159. Z. Liu, J. Yu, X. Yang, E. Jin, and L. Yuan: *Materials (Basel, Switzerland)*, 2018, vol. 11, p. 883.
160. Tec-science: Nusselt-Zahl zur Beschreibung konvektiver Wärmeübergänge - tec-science (2020). Accessed 1 July 2022
161. VDI-Gesellschaft Verfahrenstechnik und Chemieingenieurwesen: *VDI-Wärmeatlas: Mit 320 Tabellen*, 11th ed., Springer Vieweg, Berlin, Heidelberg, 2013.
162. Tec-science: Prandtl-Zahl - tec-science (2020), <https://www.tec-science.com/de/thermodynamik-waermelehre/waerme/prandtl-zahl/>. Accessed 1 July 2022
163. A. Pfeiffer, J. Schenk, G. Wimmer, and J. Wurm: *9th EOSC & 6th Clean Tech*, Ed. by Steel institute VDEh, 2022.
164. G. Feng, K. Jiao, J. Zhang, and S. Gao: *Journal of Molecular Liquids*, 2021, vol. 330, p. 115603.
165. F. Penz, J. Schenk, R. Ammer, G. Klösch, and K. Pastucha: *Metals*, 2018, vol. 8, p. 1078.
166. F. M. Penz and J. Schenk: *steel research int.*, 2019, vol. 90, p. 1900124.
167. F. M. Penz, J. Schenk, R. Ammer, G. Klösch, K. Pastucha, and M. Reischl: *Materials (Basel, Switzerland)*, 2019, vol. 12.
168. R. Lule, F. Lopez, J. Espinoza, R. Torres, and G.R.D. Morales: *Direct from Midrex*, 2009, 3-4 /2009, pp. 3–8.

Appendix

a) Publications related to this thesis

Andreas Pfeiffer, Gerald Wimmer, and Johannes Schenk. "Investigations on the Interaction Behavior between Direct Reduced Iron and Various Melts." *Materials* 15.16 (2022): 5691.

Andreas Pfeiffer, Gerald Wimmer, Johannes Schenk, Heng Zheng, and Daniel Ernst; "The Behavior of Direct Reduced Iron in the Electric Arc Furnace Hotspot"; *Metals* (2023), 13, 978.

Currently, as of May 2023, being reviewed

Andreas Pfeiffer, Gerald Wimmer, Johannes Schenk, Heinrich Mali, Heng Zheng, and Kathrin Thiele; "The Behavior of Phosphorus in the Hydrogen-based Direct Reduction – Smelter Ironmaking Route "; Steel Research International

b) Conference contributions

Andreas Pfeiffer, Gerald Wimmer, Johann Wurm and Johannes Schenk. "Processing low-grade Direct Reduced Iron – Definition and comparison of melting strategies" 9th EOSC & 6th CTSI, Aachen, 2022

Under Review by April, 2023

Andreas Pfeiffer, Gerald Wimmer, Johannes Schenk, and Kathrin Thiele; "Laboratory Scale Evaluation of the Slag Foaming Behavior"; EASES Oulu

c) Other publications

Bazaluk, Oleg, et al. "Metallurgical coke production with biomass additives: Study of biocoke properties for blast furnace and submerged arc furnace purposes." *Materials* 15.3 (2022): 1147.

Kieush, Lina, et al. "Investigation on the influence of wood pellets on the reactivity of coke with CO₂ and its microstructure properties." *Fuel* 309 (2022): 122151.

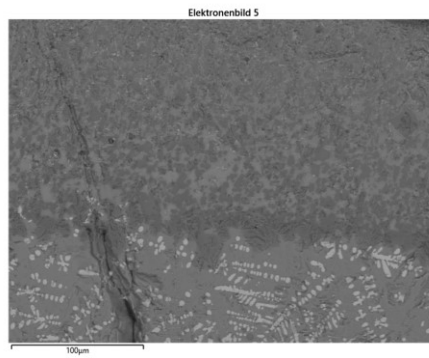


Figure A- I: SEM image of foaming sample 4 EAF-sat reference, lower and outer part of the crucible

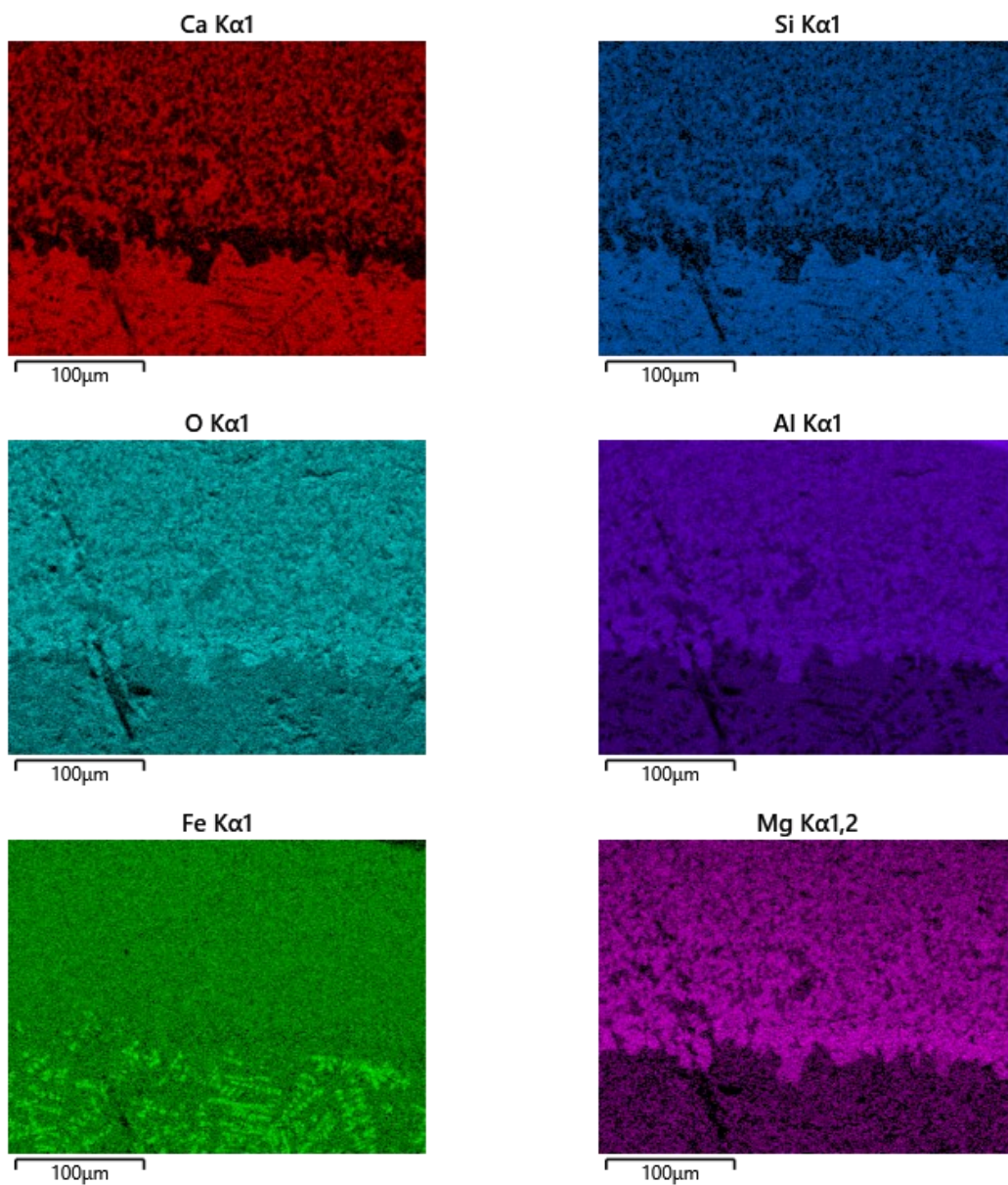


Figure A- II: EDX-mapping of foaming sample 4 EAF-sat reference, lower and outer part of the crucible; corresponding SEM image see Figure A- I

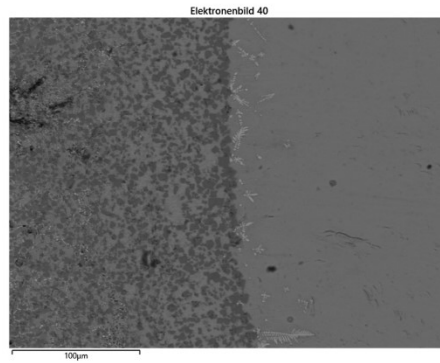


Figure A- III: SEM image of foaming sample 6 EAF, lower and outer part of the crucible

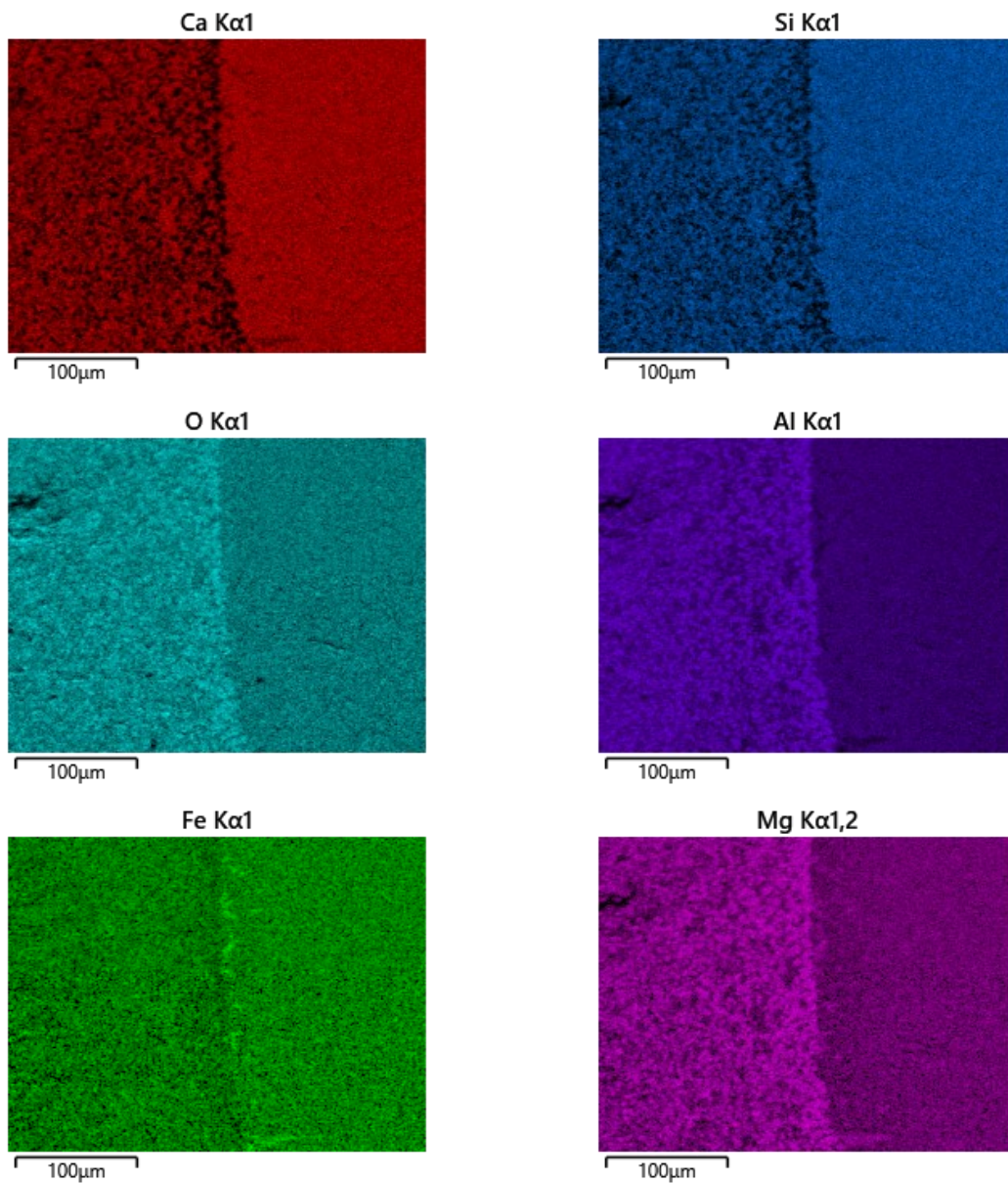


Figure A- IV: EDX-mapping of foaming sample 6 EAF, lower and outer part of the crucible; corresponding SEM image see Figure A- III

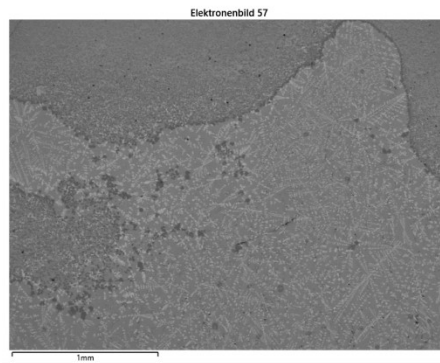


Figure A- V: SEM image of foaming sample 7 EAF-sat, lower and outer part of the crucible

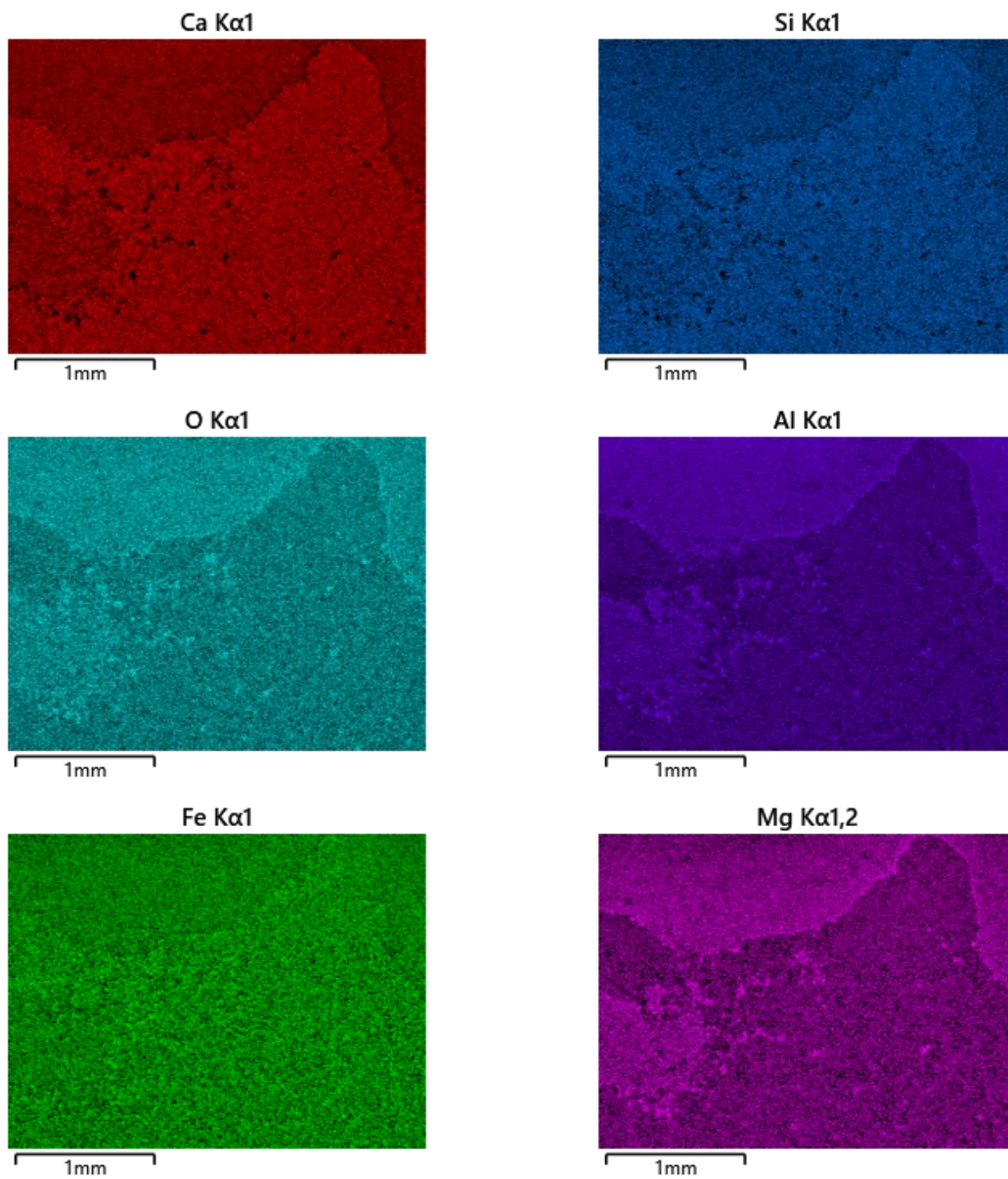


Figure A- VI: EDX-mapping of foaming sample 7 EAF-sat, lower and outer part of the crucible; corresponding SEM image see **Figure A- V**

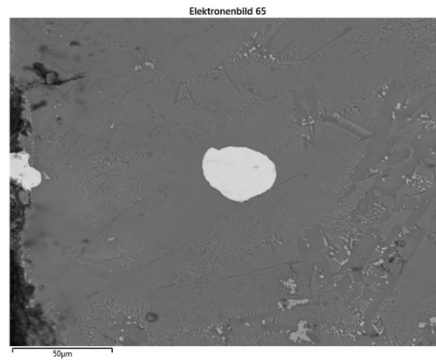


Figure A- VII: SEM image of foaming sample 7 EAF-sat, part of the foam

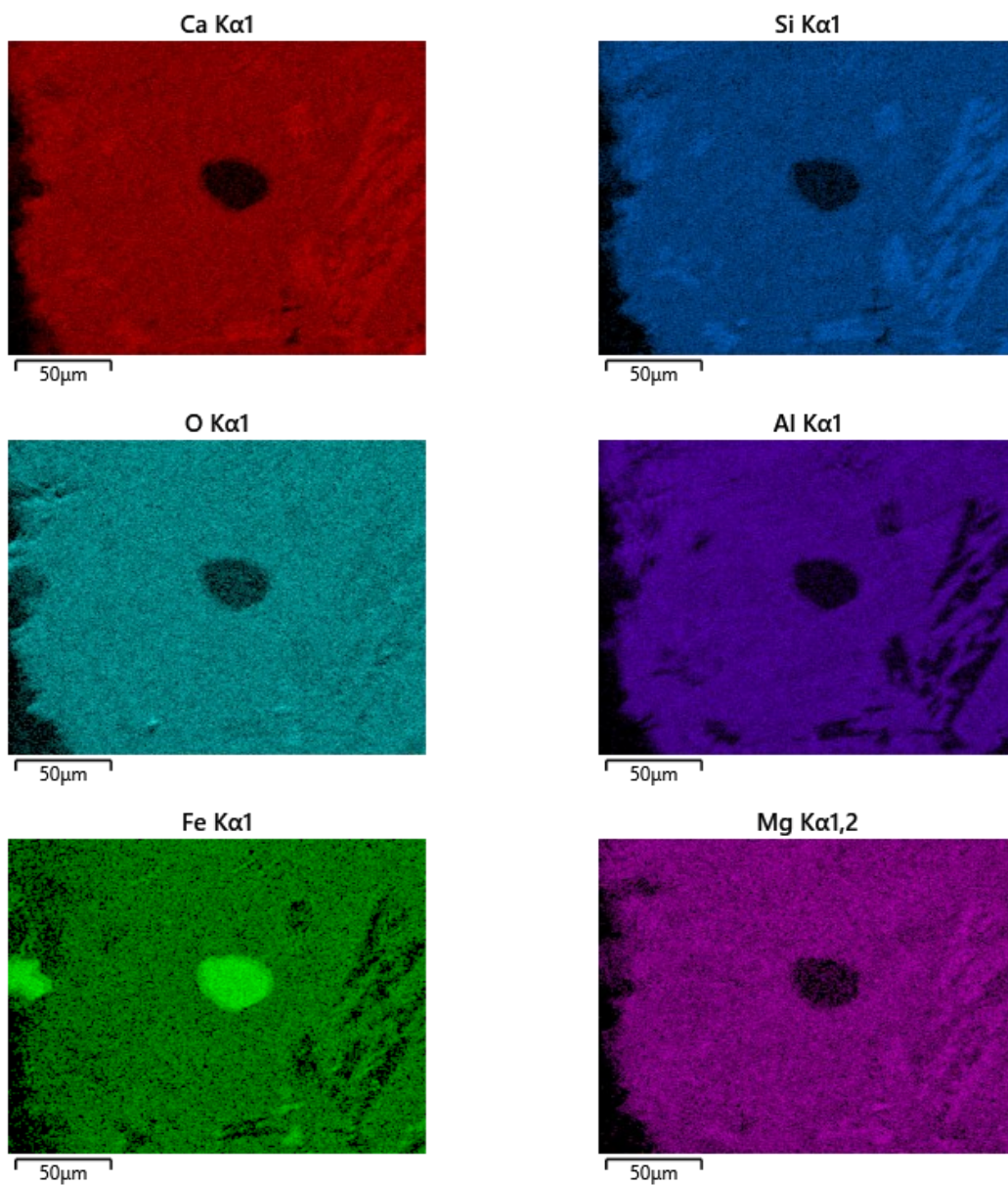


Figure A- VIII: EDX-mapping of foaming sample 7 EAF-sat, part of the foam; corresponding SEM image see **Figure A- VIII**

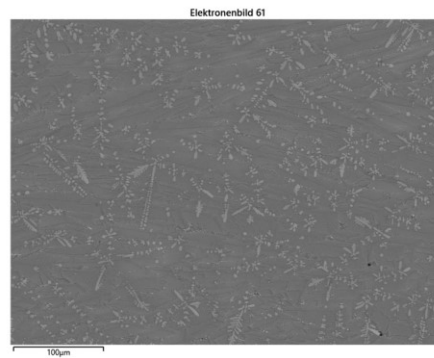


Figure A- IX: SEM image of foaming sample 7 EAF-sat, lower and central part of the crucible

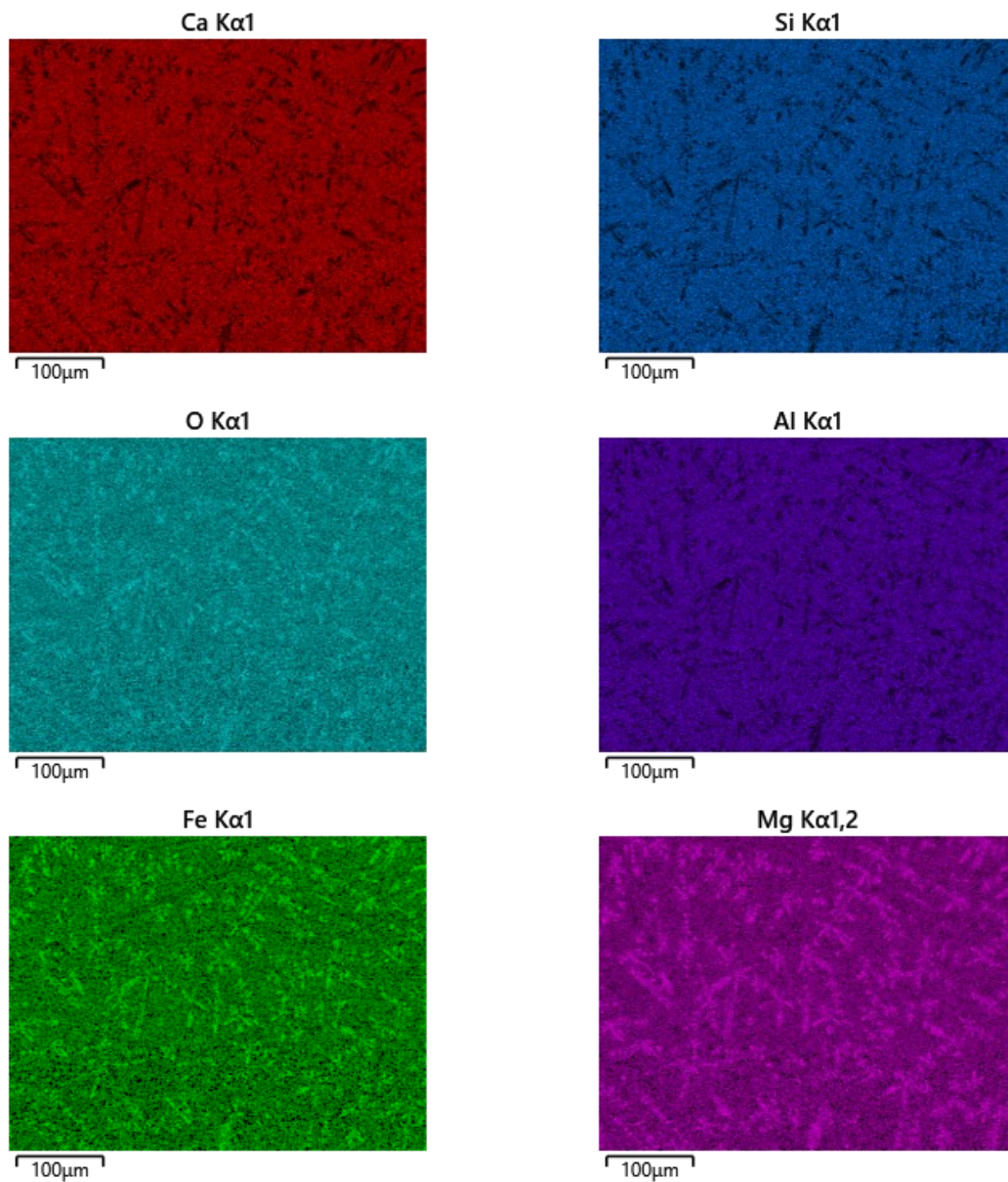


Figure A- X: EDX-mapping of foaming sample 7 EAF-sat, lower and central part of the crucible; corresponding SEM image see **Figure A- IX**

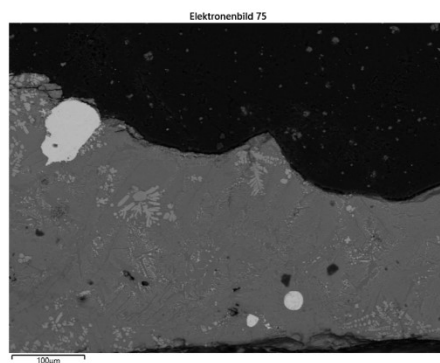


Figure A- XI: SEM image of foaming sample 8 EAF, part of the foam

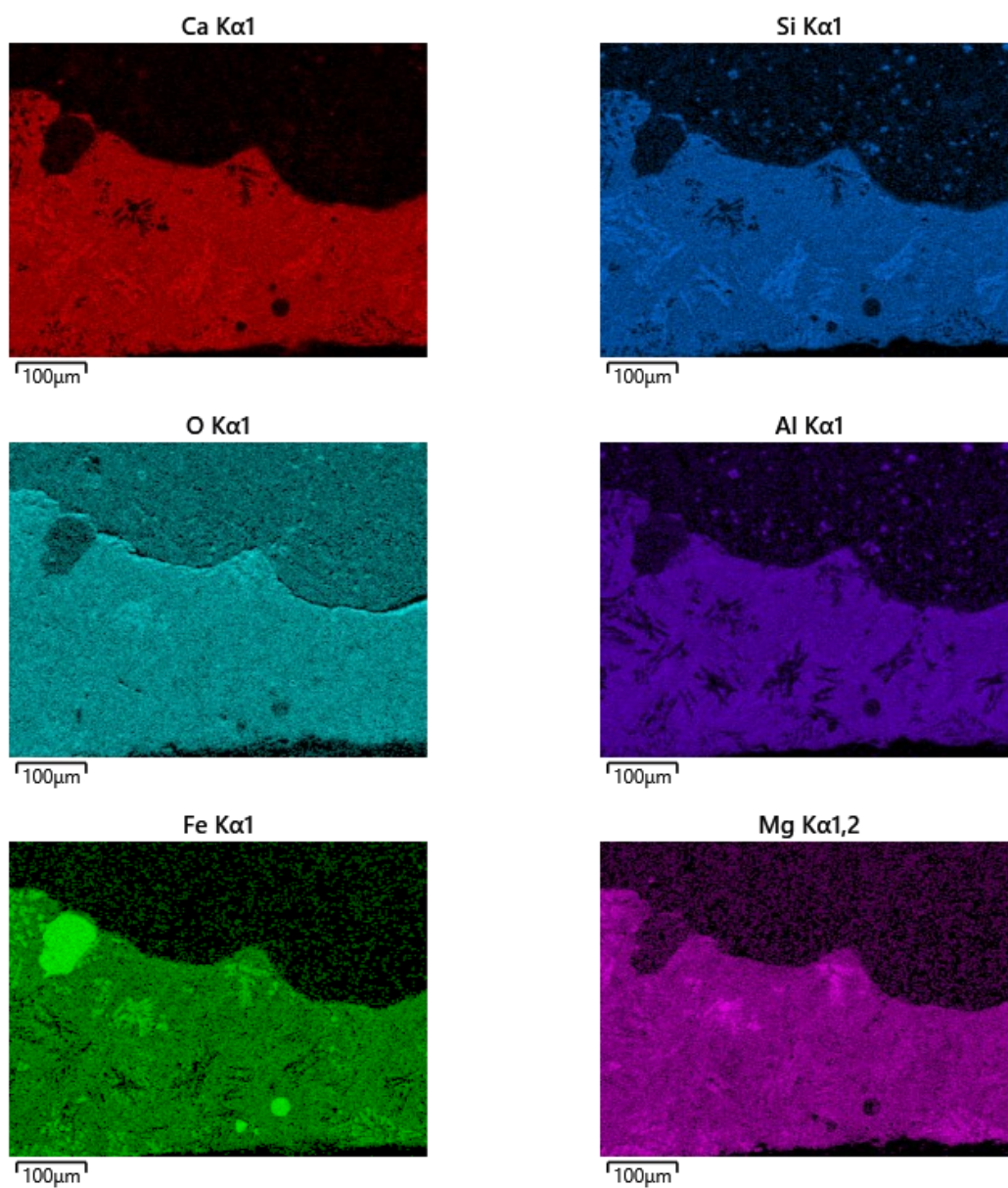


Figure A- XII: EDX-mapping of foaming sample 8 EAF, part of the foam; corresponding SEM image see **Figure A- XI**

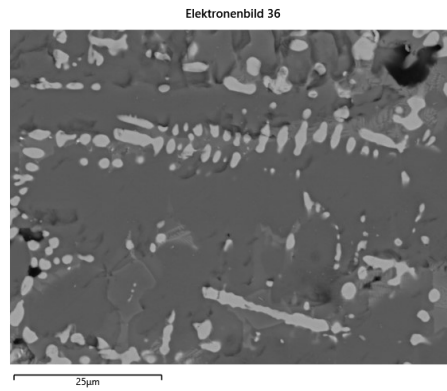


Figure A- XIII: SEM image of foaming sample 10 SAF, lower and central part of the crucible

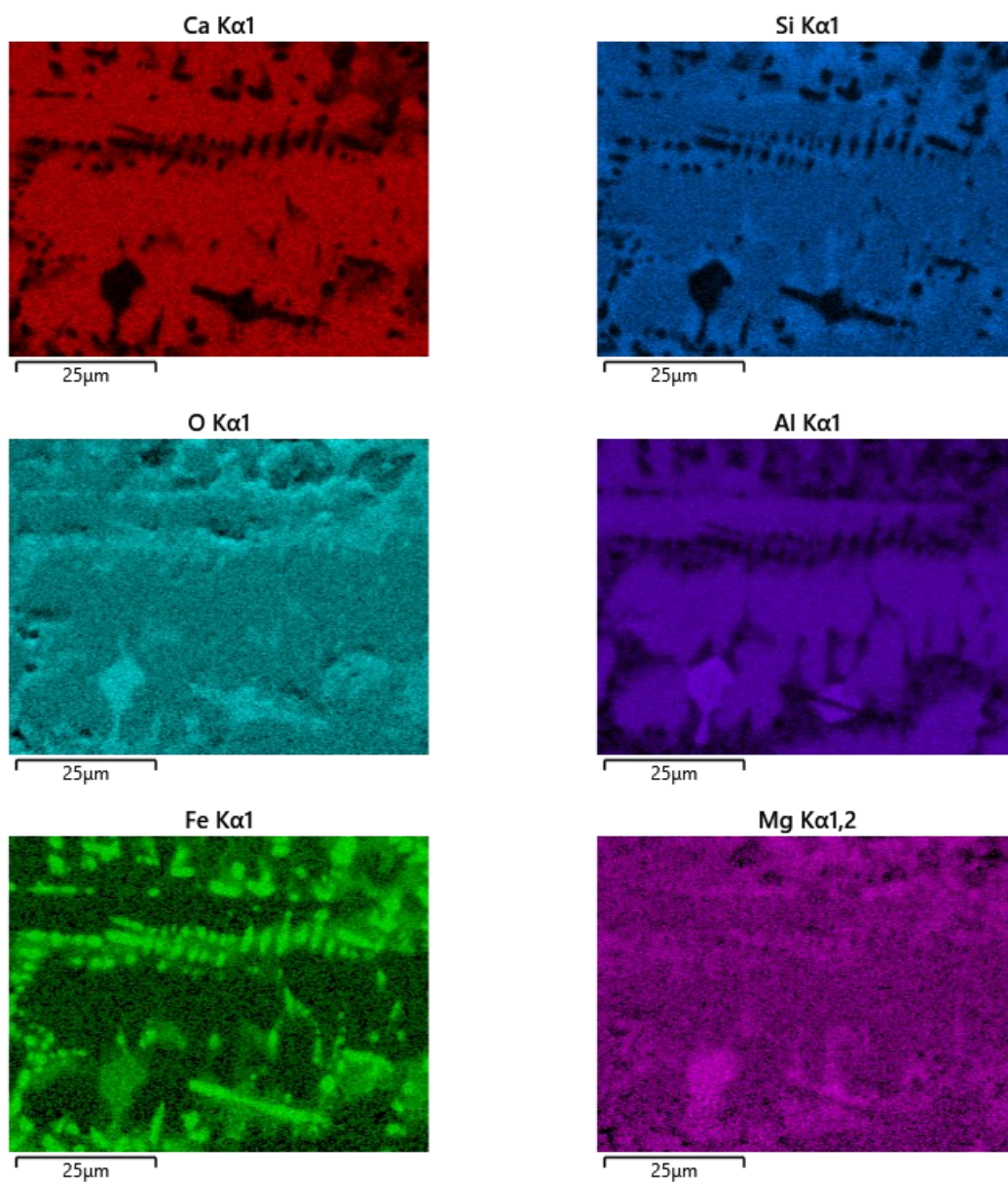


Figure A- XIV: EDX-mapping of foaming sample 10 SAF, lower and central part of the crucible; corresponding SEM image see **Figure A- XIII**

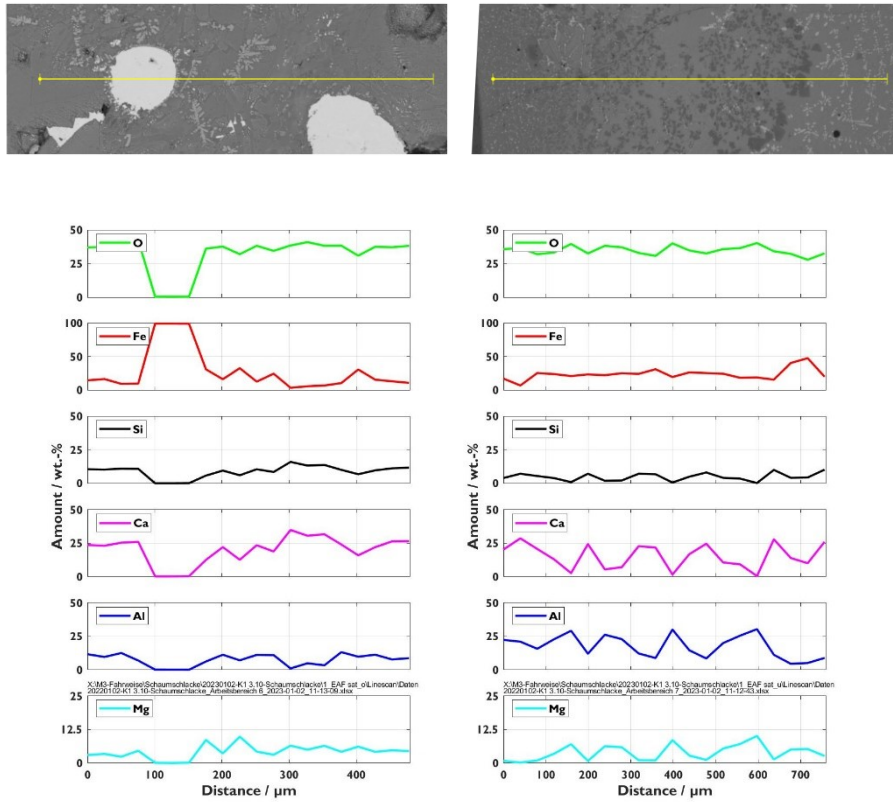


Figure A- XV: Linescans of sample no. 1 EAF-sat

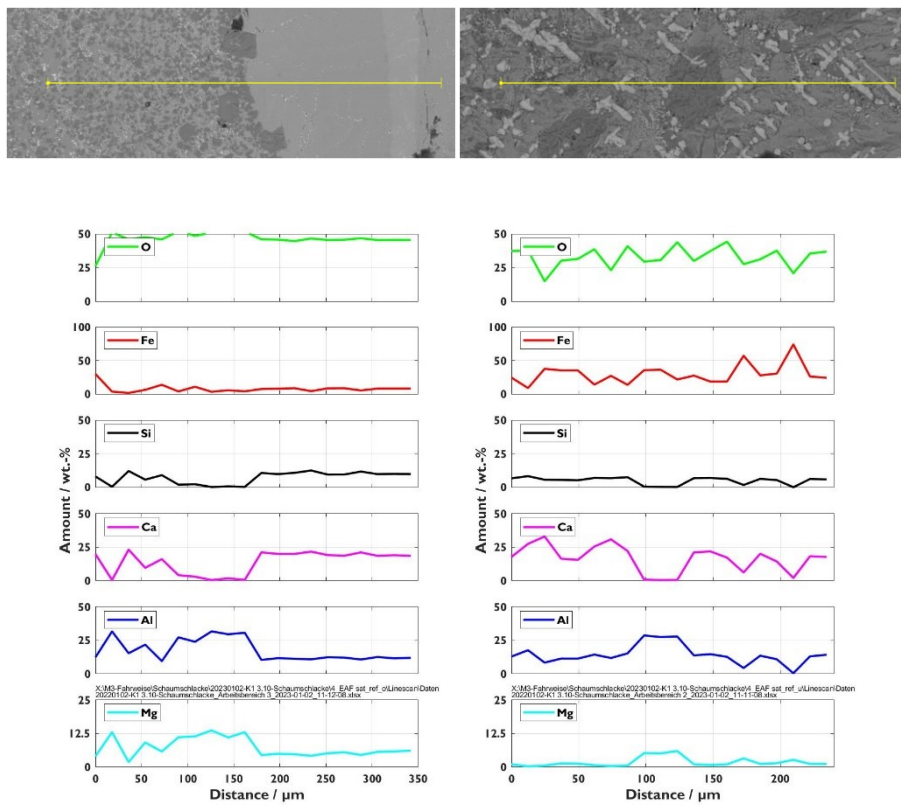


Figure A- XVI: Linescans of sample no. 4 EAF-sat ref

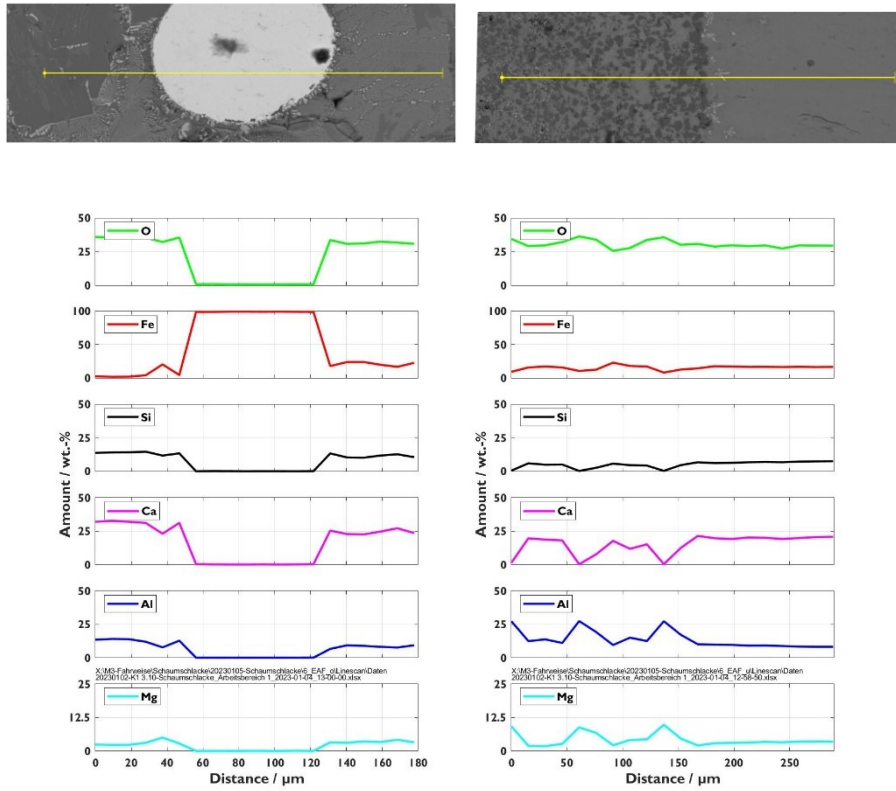


Figure A- XVII: Linescans of sample no. 6 EAF

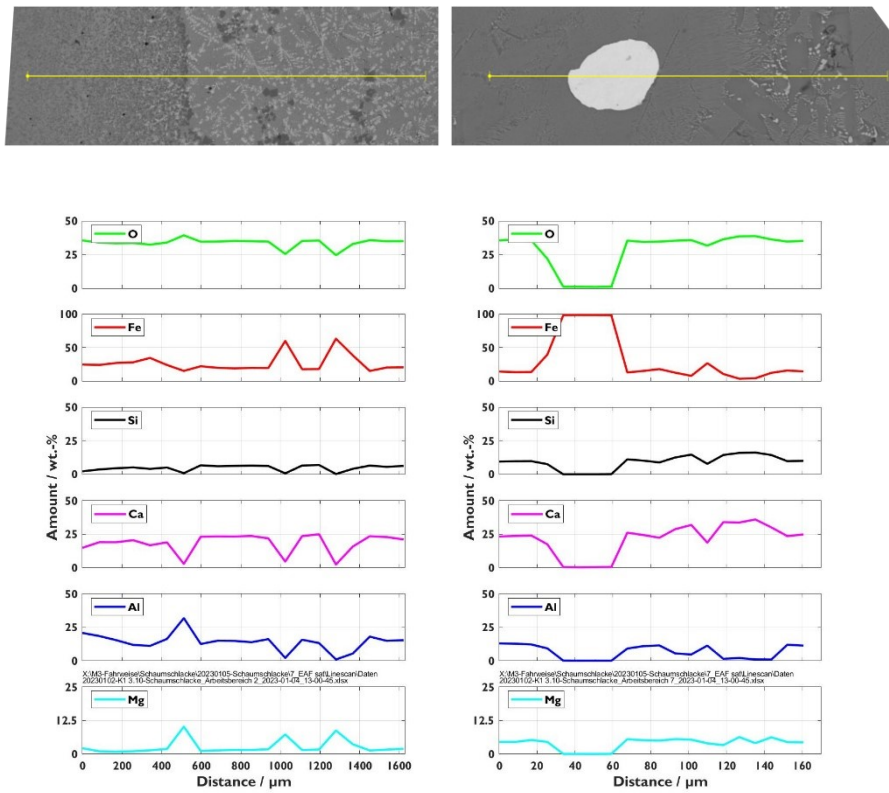


Figure A- XVIII: Linescans of sample no. 7 EAF-sat

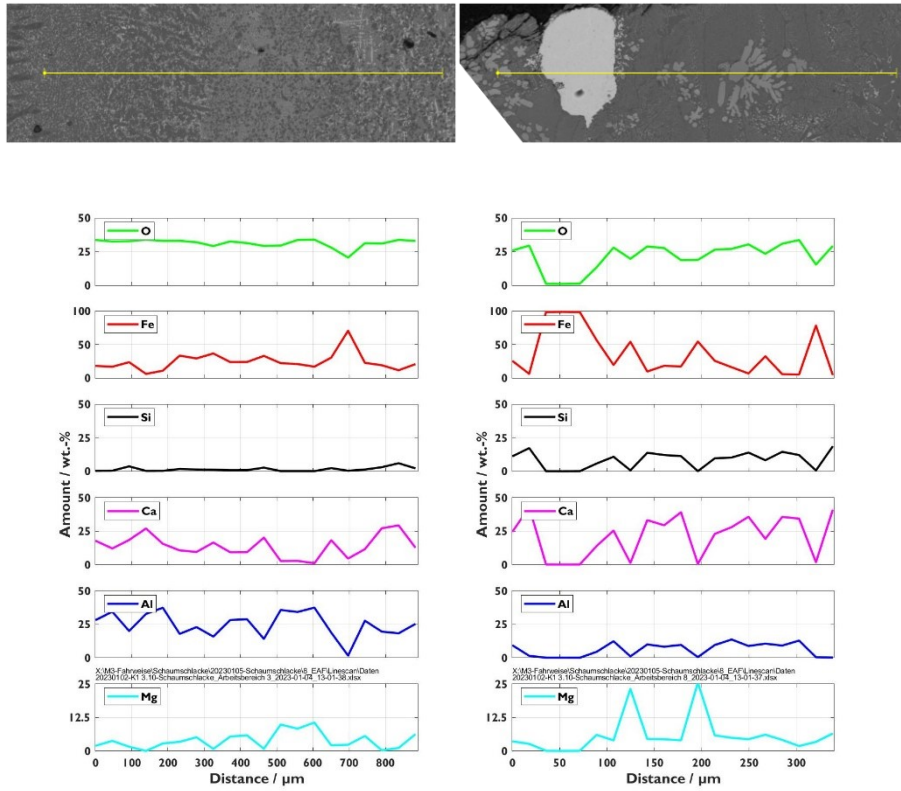


Figure A- XIX: Line scans of sample no. 8 EAF

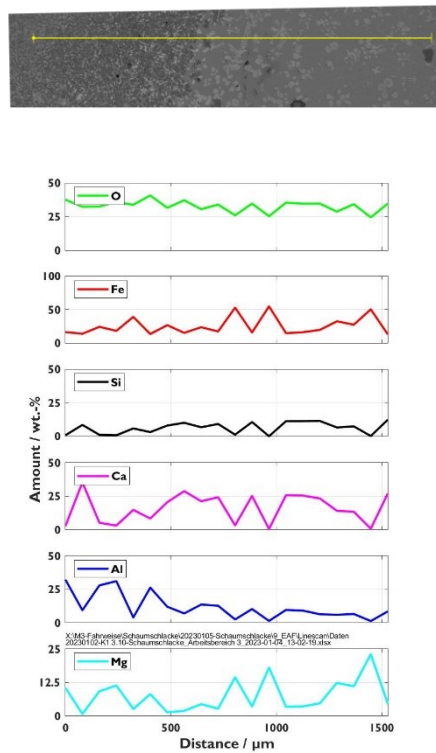


Figure A- XX: Line scans of sample no. 9 EAF

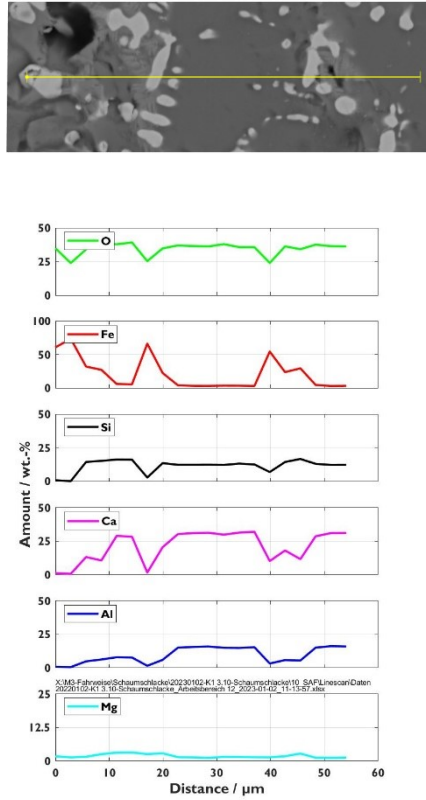


Figure A- XXI: Linescans of sample no. 10 SAF

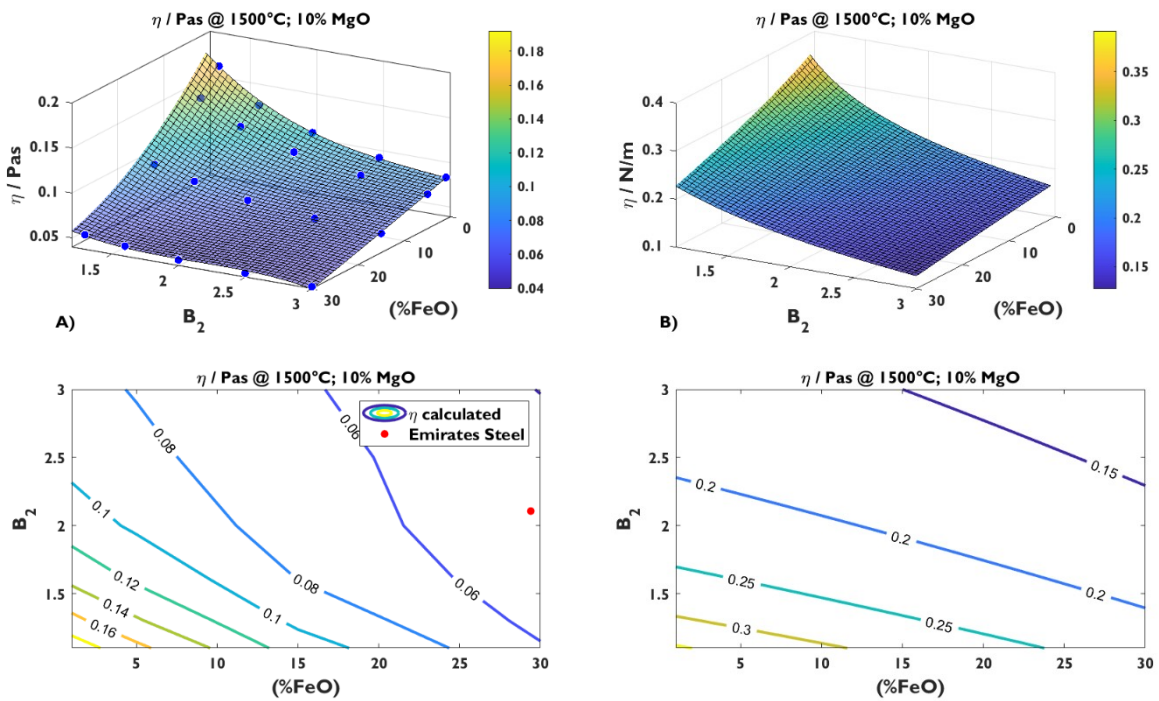


Figure A- XXII: Surface plot and horizontal sections of viscosity η , neglecting solid particles; 10% MgO, 1500°C; A) based on fitted FactSage™ data; B) acc. to Urbain^[123] model with parameters from^[129]; Emirates steel data from^[105]

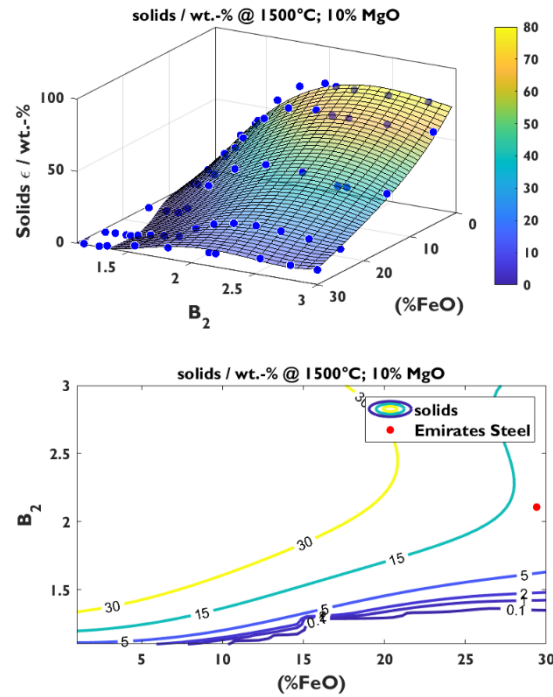


Figure A- XXIII: Surface plot and horizontal sections of the solid fraction ϵ in wt.-% based on fitted FactSage™ data; 10% MgO, 1500°C; Emirates steel data from^[105]

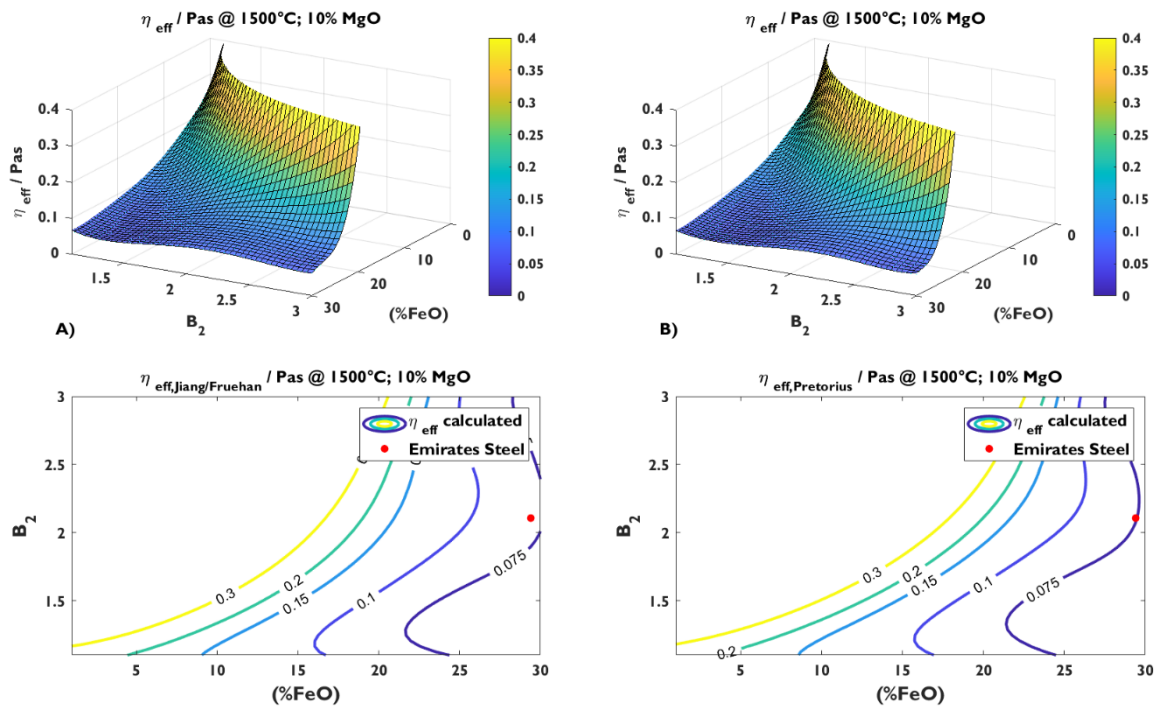


Figure A- XXIV: Surface plot and horizontal sections of effective viscosity η_{eff} , 10% MgO, 1500°C; A) based on equation 13^[95]; B) based on equation 14^[24]; Emirates steel data from^[105]

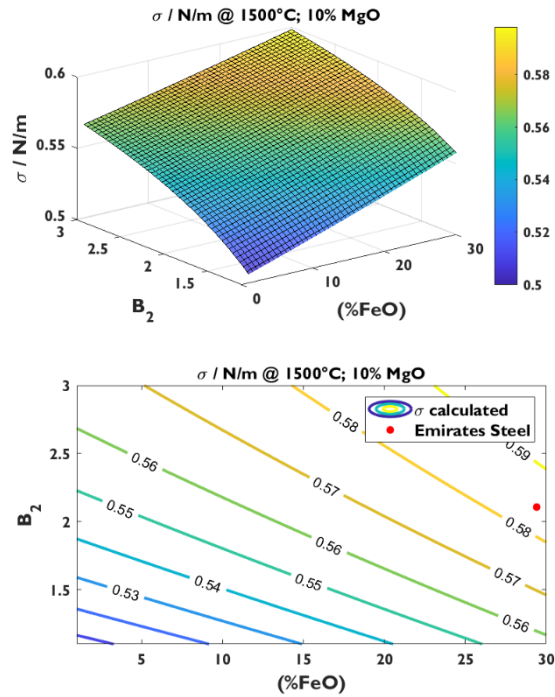


Figure A- XXV: Surface plot and horizontal sections of the surface tension σ based on^[147]; 10% MgO, 1500°C; Emirates steel data from^[105]

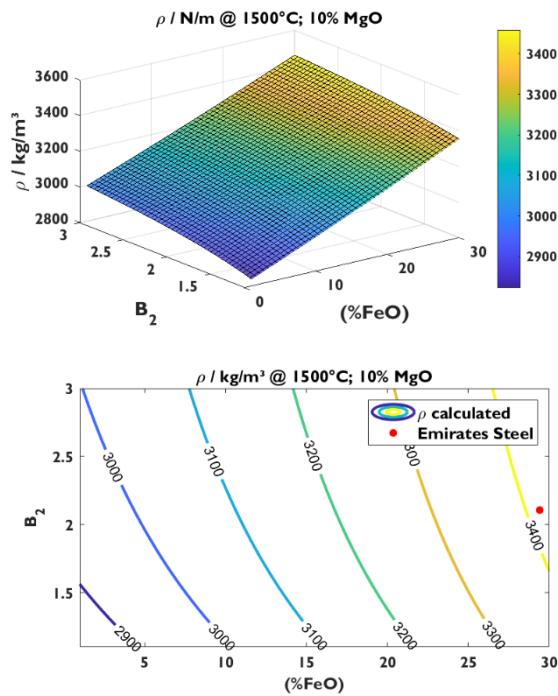


Figure A- XXVI: Surface plot and horizontal sections of the density ρ based on^[147]; 10% MgO, 1500°C; Emirates steel data from^[105]

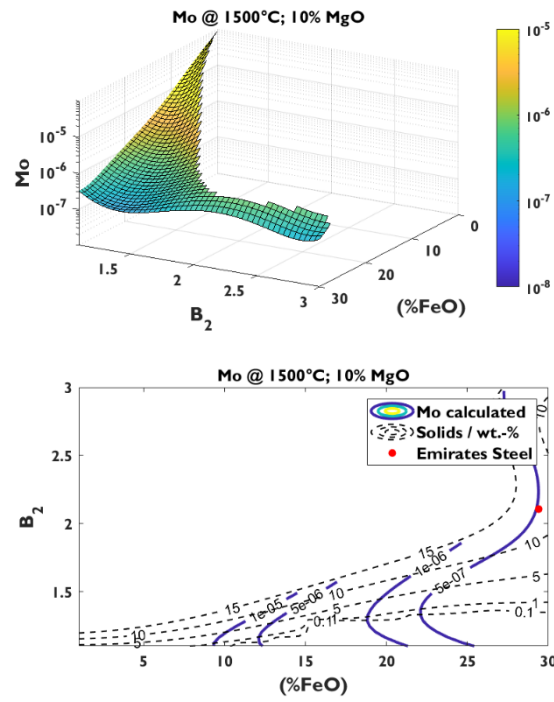


Figure A- XXVII: Surface plot and horizontal sections of the Morton number Mo ; $10\% \text{MgO}$, 1500°C ; Emirates steel data from^[105]

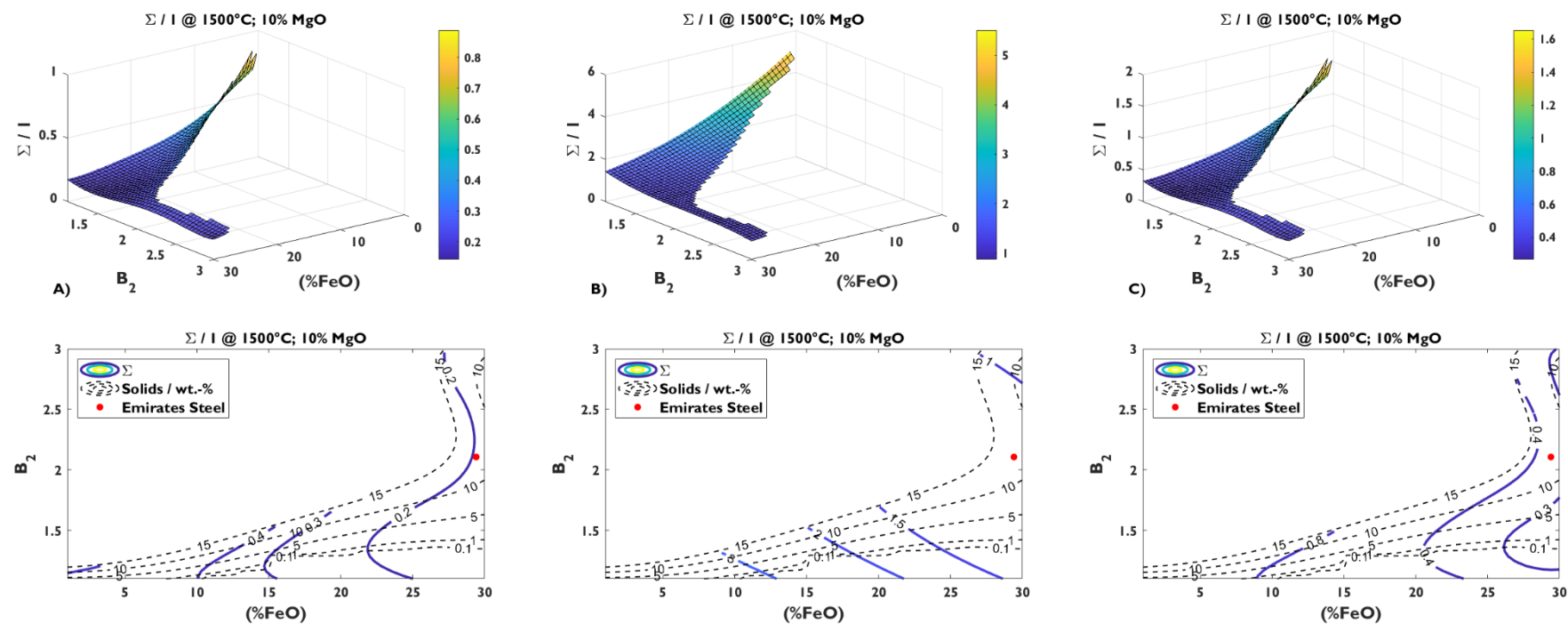


Figure A- XXVIII: Surface plot and horizontal sections of Slag foaming index Σ ; 10% MgO, 1500°C; A) for bath smelting slags; B) for MgO_{sat} slags; C) for CaO-based slags; Emirates steel data from^[105]

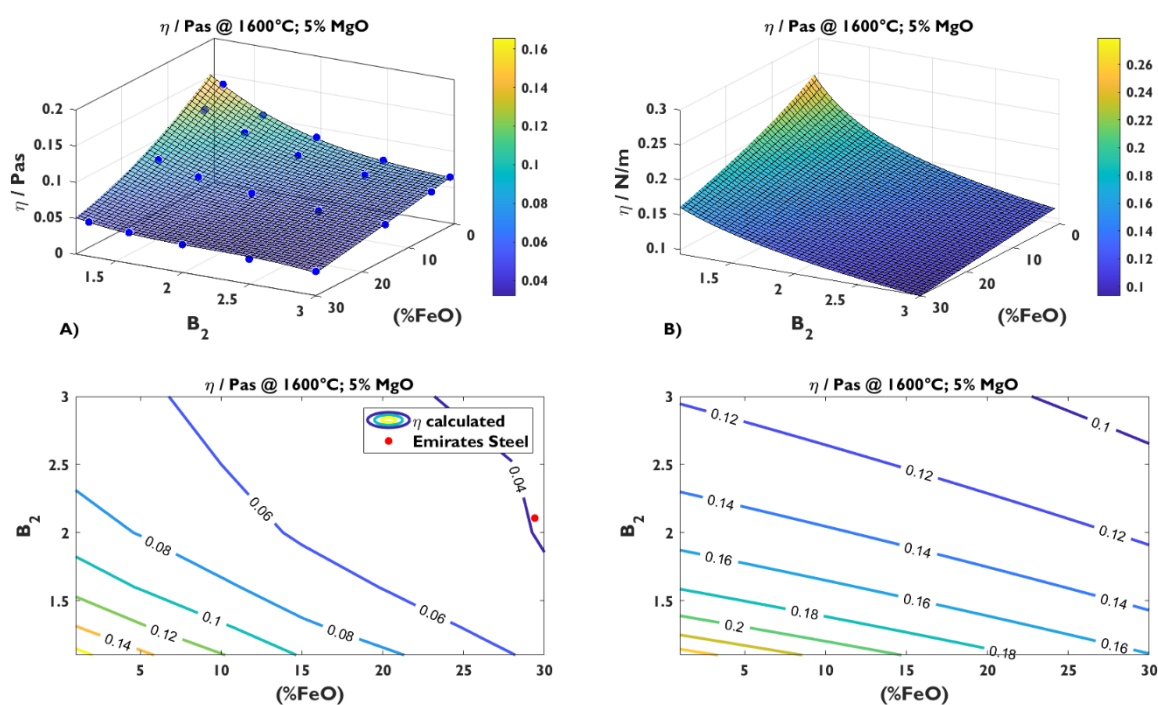


Figure A- XXIX: Surface plot and horizontal sections of viscosity η , neglecting solid particles; 5% MgO, 1600°C; A) based on fitted FactSage™ data; B) acc. to Urbain^[123] model with parameters from^[129]; Emirates steel data from^[105]

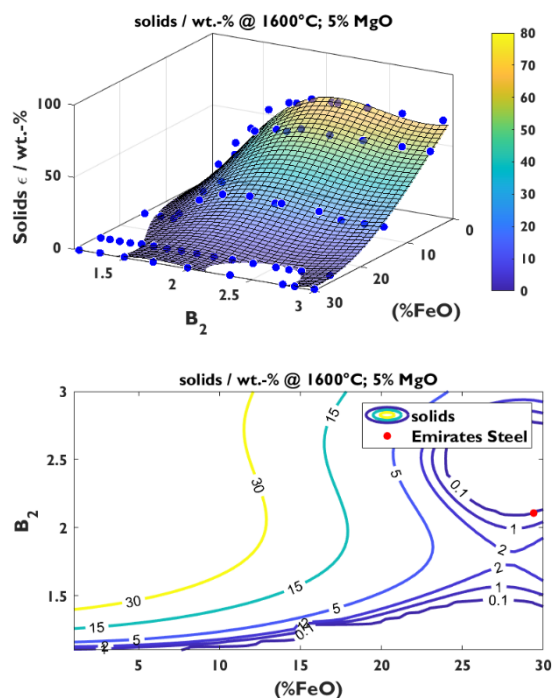


Figure A- XXX: Surface plot and horizontal sections of the solid fraction ϵ in wt.-% based on fitted FactSage™ data; 5% MgO, 1600°C; Emirates steel data from^[105]

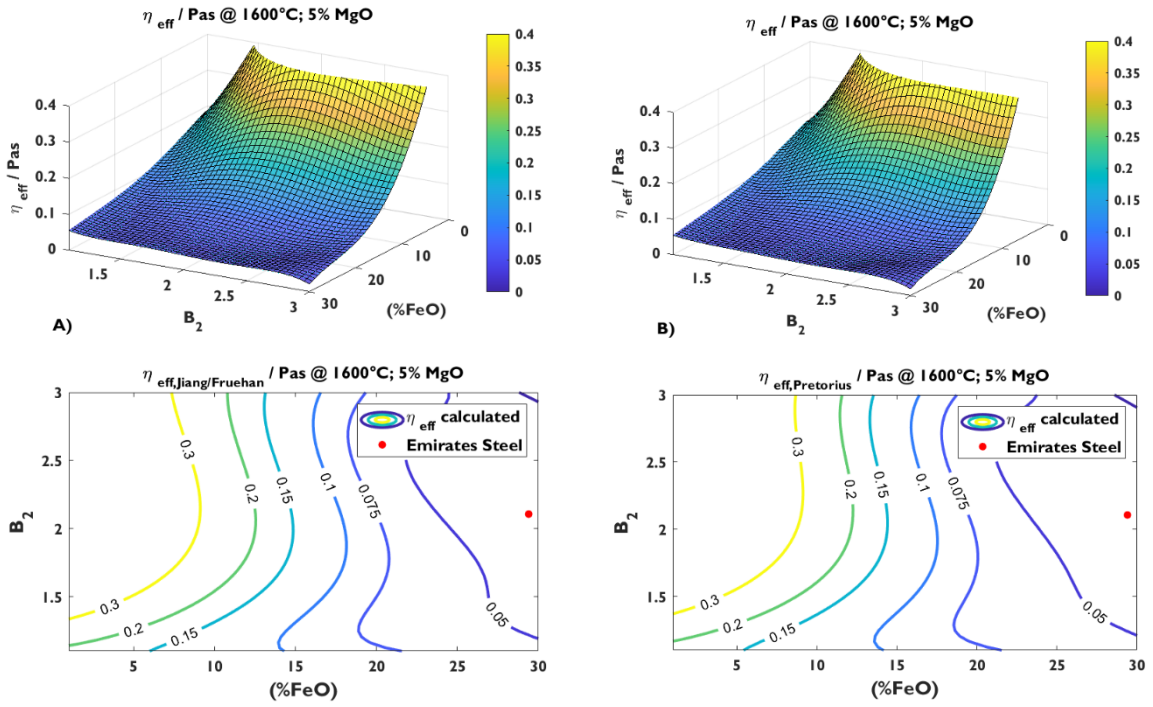


Figure A- XXXI: Surface plot and horizontal sections of effective viscosity η_{eff} , 5% MgO, 1600°C; A) based on equation 13^[95]; B) based on equation 14^[124]; Emirates steel data from^[105]

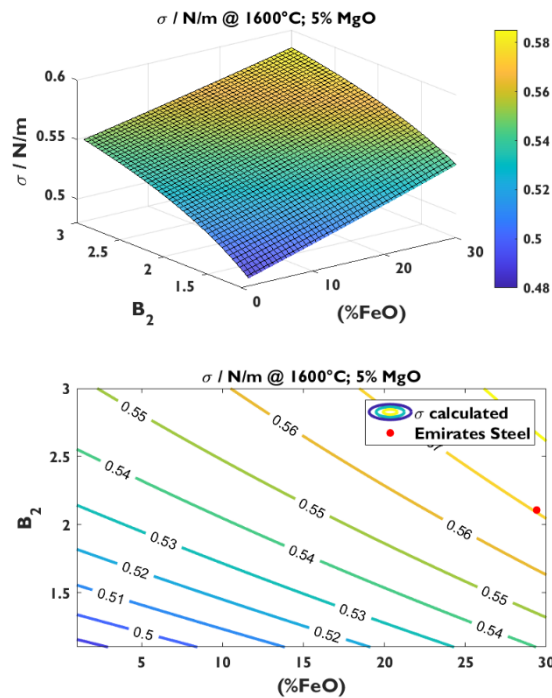


Figure A- XXXII: Surface plot and horizontal sections of the surface tension σ based on^[147]; 5% MgO, 1600°C; Emirates steel data from^[105]

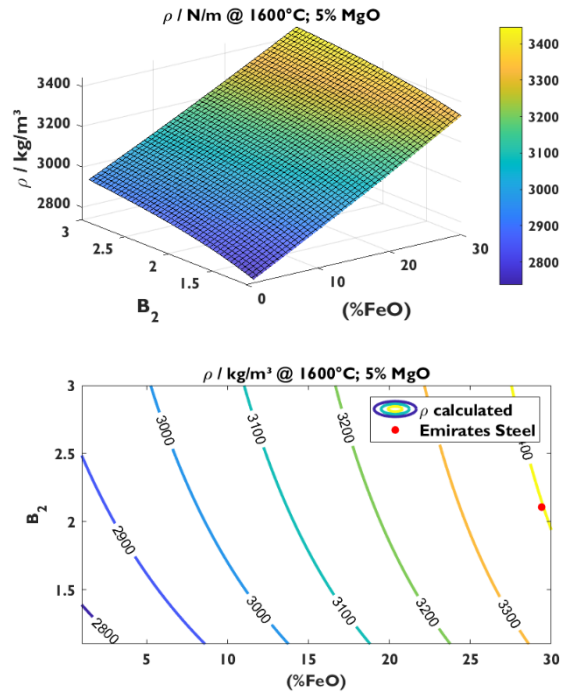


Figure A- XXXIII: Surface plot and horizontal sections of the density ρ based on^[147]; 5% MgO, 1600°C: Emirates steel data from^[105]

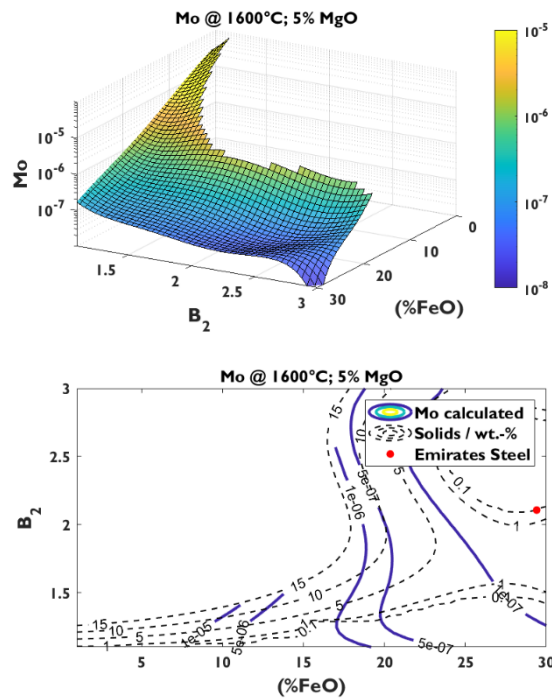


Figure A- XXXIV: Surface plot and horizontal sections of the Morton number Mo ; 5% MgO, 1600°C: Emirates steel data from^[105]

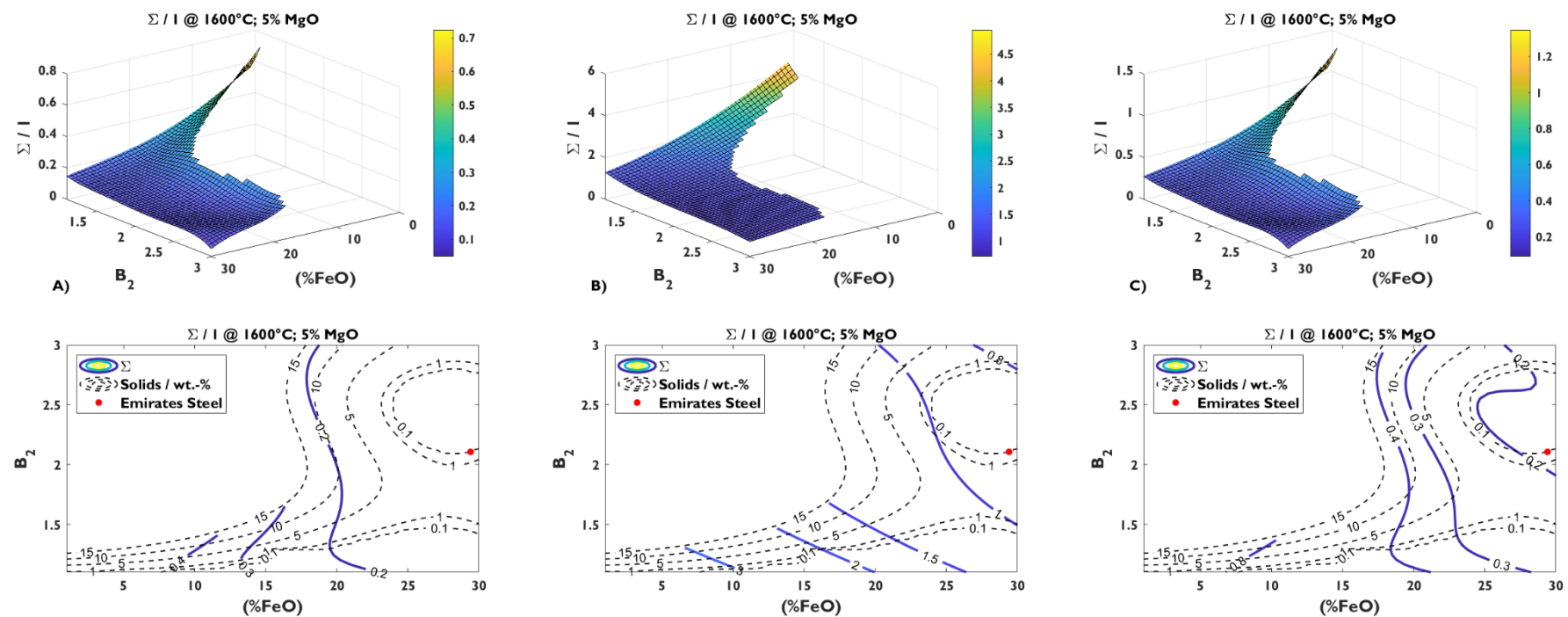


Figure A- XXXV: Surface plot and horizontal sections of Slag foaming index Σ ; 5% MgO, 1600°C; A) for bath smelting slags; B) for MgO_{sat} slags; C) for CaO-based slags; Emirates steel data from^[105]